

ECIO 2018

European Conference on Integrated Optics

Universitat Politecnica de Valencia, Spain

Collected Manuscripts

(c) Copyright 2018 The ECIO Board. All rights reserved.

Contents

ID	Author	Title
S1.1	Delphine Marris-Morini, Qiankun	We.1.1. 8-Invited Paper, Delphine Marris-Morini (Univ. Paris-Sud), “Chip-scale integrated photonics for the mid-infrared”
S1.2	Tin Komljenovic	We.1.2. 22-Invited Paper, Tin Komljenovic (UCSB), “Heterogeneous large-scale photonic integration for communications and beyond”
S1.3	Michael Liehr, Frank Tolic, Edwa	We.1.3. 30-Invited Paper, Michale Liehr (AIM Photonics) Silicon photonics open access in US
S2.1	Jaime García-Rupérez	Fr.1.A.1 26 Invited Paper, Jaime Garcia, Nanophotonics Technology Center, High sensitivity photonic configurations for biochemical detection
S2.2	Jonas Leuermann, Alejandro Sánch	Fr.1.A.2 138-Regular Paper, Towards Photonic Biosensing using a Three-Port Mach-Zehnder Interferometer in a Silicon Nitride Platform
S2.3	Sergio Lechago, Carlos García-Me	Fr.1.A.3 125-Regular Paper, Ultra-compact label-free silicon-nanoantenna-based optofluidic microflow cytometer with a high signal-to-noise ratio
S2.4	Øystein Ivar Helle, David Andre	Fr.1.A.4 28-Invited Paper, Balpreet S. Ahluwalia (University of Norway), ‘Nanoscopy-on-a-chip high-throughout super-resolution imaging’
S3.1	Mark Wade	Fr.2.1 6-Invited Paper, Mark Wade (Ayar Labs), “Zero-change photonic integration for co-integration with CMOS electronics”
S3.2	Weidong Zhou	Fr.2.2 16-Invited Paper, Weidong Zhou (Univ. Texas Arlington), “Printed active hybrid photonic crystal devices for 3D integrated photonics”
S3.3	Daniel Pérez, Erica Sánchez, D.	Fr.2.3 31-Invited Paper, J. Capmany, (Universitat Politècnica de València) ‘The COST CA16220 Action European Network on High performance Integrated Microwave Photonics’
S4.1	T. T. M. van Schaijk, D. Lenstra	Fr.1.B.1 66-Regular Paper, Analysis of the Operation of an Integrated Unidirectional Phase Modulator
S4.2	Marija Trajkovic, Fabrice Blache	Fr.1.B.2 67-Regular Paper, Low loss transmission lines in COBRA generic photonic integration platform
S4.3	Guillermo Carpintero, Robinson C	Fr.1.B.3 29-Invited Paper, Guillermo Carpintero (Universidad Carlos III), “The future of THz integrated photonics”
S4.4	Claudio Porzi, Antonella Bogoni	Fr.1.B.4 91-Regular Paper, Integrated Passband Optical Filter with High-Order Phase-Shifted Bragg Grating in Silicon-on-Insulator Technology
S4.5	Phuong T. Do, Carlos Alosno-Ramo	Fr.1.B.5 101-Regular Paper, Silicon Micro-ring Resonator Integrated in an Optoelectronic Oscillator System
S5.1	Dr. Milan L. Mashanovitch Freedo	Th.1.A.1 5-Invited Paper, Milan Mashanovitch (Freedom Photonics), “Novel high-performance lasers in InP”
S5.2	Jukka Viheriälä, Antti T. Aho, R	Th.1.A.2 96-Regular Paper, Gain characteristics of 1.3μm GaInNAs-GaAs quantum wells monolithically integrated on Ge
S5.3	Amin Abbasi, Jochem Verbist, Lei	Th.1.A.3 79-Highly Rated Paper, 100 Gb-s Duobinary Electro-Absorption Modulation of a Heterogeneously Integrated InP-on-Si DFB Laser Diode
S5.4	Tomohiro Amemiya, Daisuke Inoue,	Th.1.A.4 21-Invited Paper, Tomohiro Amemiya (Tokyo Institute of Technology), “Semiconductor membrane lasers”
S5.5	R. Loi, B. Roycroft, J. O’Callag	Th.1.A.5 15-Invited Paper, Brian Corbett (Tyndall Institute), “Micro-transfer

		printing for advanced scalable hybrid photonic integration”
S6.1	G. E. Hoefler, R. Going, R. Mahe	Th.3.1 2-Invited Paper, Gloria Hoefler (Infinera), “Large scale InP photonic integrated circuits (PICs)”
S6.2	Maxim Karpov, John Jost, Hairun	Th.3.2 10-Invited Paper, Tobias Kippenberg, EPFL, “Optical frequency combs technologies for generation and applications”
S6.3	C. Ciminelli, D. Conteduca, F. D	Th.3.3 9-IP, Caterina Ciminelli (Polit. Bari), “Silicon photonics biosensors”
S6.4	Joyce K. S. Poon	Th.3.4 14-Invited Paper, Joyce Poon (Univ. Toronto), “Monolithically Integrated 3D Silicon Photonic Platforms”
S7.1	Wim Bogaerts	We.3.A.1. 11-Invited Paper, Wim Bogaerts (Univ. Gent), “Programmable photonic integrated circuits”
S7.2	Jörn P. Epping, Denys Marchenko,	We.3.A.2. 86-Regular Paper, Ultra-low-power stress-based integrated photonic phase actuator
S7.3	Maziyar Milanizadeh, Douglas Agu	We.3.A.3. 109-Regular Paper, Automatic Hitless Tuning of Third Order Micro-Ring Resonator Add-Drop Filters
S7.4	Luis A. Bru, Daniel Pastor, Bern	We.3.A.4. 131-Regular Paper, On-chip full-field test engine for photonic integrated devices based on optical frequency domain reflectometry technique
S7.5	Antonio Ribeiro, Umar Khan, and	We.3.A.5. 64-Regular Paper, Matrix Addressing Silicon Photonics Phase Shifters using Heaters with Integrated Diodes
S7.6	Maziyar Milanizadeh, Douglas Agu	We.3.A.6. 105-Regular Paper, A tuning method for photonic integrated circuits in presence of thermal cross talk
S8.1	Yasuhiko Arakawa, Bongyong Jang,	We.2.A.1. 13-Invited Paper, Yasuhiko Arakawa (Univ. of Tokyo), “Quantum nanostructures and photonic devices”
S8.2	Caterina Taballione, Tom A. W. W	We.2.A.2. 61-Highly Rated Paper, Quantum Photonic Processor based on Silicon Nitride Waveguides
S8.3	A. Delgoffe, A. Miranda, B. Riga	We.2.A.3. 47-Highly Rated Paper, Tilted-potential Photonic Crystal Cavities for Integrated Quantum Photonics
S8.4	C. Abellan, W. Amaya, M. Rudé, D	We.2.A.4. 27-Invited Paper, Carlos Abellan (Quside), “Photonic integration of quantum random number generators”
S8.5	Carsten Schuck	We.2.A.5. 20-Invited Paper, Carsten Schuck (Univ. Munster), “Integrated quantum photonics”
S9.1	Charles Baudot, I. Charlet, M. D	Th.2.A.1 3-Invited Paper, Charles Baudot (STMicroelectronics), “High-speed Si transceiver for datacom applications”
S9.2	Chong Zhang, Di Liang, Geza Kurz	Th.2.A.2 84-Highly Rated Paper, Low-threshold and High-speed Quantum-dot Microring Lasers on Silicon
S9.3	Sarah Uvin, Sulakshna Kumari, An	Th.2.A.3 103-Highly Rated Paper, InAs-GaAs quantum dot 1.3 um DFB laser heterogeneously integrated on a silicon waveguide circuit
S9.4	Michal Lipson	Th.2.A.4 7-Invited Paper Michal Lipson (Columbia Univ.), “Next generation Silicon Photonics”
S9.5	Diego Pérez-Galacho, Laurent Bra	Th.2.A.5 44-Regular Paper, O-Band QPSK modulation based on a silicon dual-drive Mach-Zehnder
S9.6	Elena Durán-Valdeiglesias, Carlo	39 Th.2.A.6 39-Highly Rated Paper, Dual-polarization O-band silicon nitride Bragg filters with high extinction ration
S10.1	A. Raza, S. Clemmen, M. de Goede	We.2.B.1. 129-Regular Paper, The performance of High-Index-Contrast Photonics Platforms for On-Chip Raman Spectroscopy
S10.2	Mu-Chieh Lo, Robinson Guzmán, an	We.2.B.2. 45-Regular Paper, On-Chip Vernier Filtering of Colliding Pulse

		Mode-Locked Laser Coupled with Fabry-Pérot Feedback Cavity via MMI Reflector
S10.3	Alan Scott, Hugh Podmore	We.2.B.3. 4-Invited Paper, Alan Scott (Honeywell), “A Compressive Sensing Integrated Fourier Raman Spectrometer”
S10.4	Anton Vasiliev, Muhammad Muneeb,	We.2.B.4. 119-Highly Rated Paper, Integrated Silicon-on-Insulator AWG Spectrometer with Single Pixel Readout for 2.3 um Spectroscopy Applications
S10.5	Michiel de Goede, Lanthian Chang	We.2.B.5. 74-Regular Paper, Integrated Al2O3-Yb3+ Microring Laser for On-Chip Active Sensing in an Aqueous Environment
S11.1	A. Manolis, G. Dabos, D. Ketzaki	Th.1.B.1 73-Regular Paper, Water-loaded plasmonic stripe integrated with Si3N4 waveguide using gold and CMOS compatible metals
S11.2	Ali Raza, Javier Losada, Stephan	Th.1.B.2 80-Regular Paper, Surface enhanced Raman spectroscopy via isolated plasmonic nanoantennas integrated on silicon nitride waveguides
S11.3	J. H. Schmid, P. Cheben, D. Mela	Th.1.B.3 12-Invited Paper, Jens Schmid (National Research Council, Canada), “Silicon photonics and subwavelength photonic structures-metamaterials”
S11.4	José Manuel Luque-González, Alej	Th.1.B.4 53-Regular Paper, High performance and small footprint spot size converters based on SWG metamaterial lenses
S11.5	Alba Espinosa-Soria, Amadeu Grio	Th.1.B.5 121-Regular Paper, Coherent control of the absorption and scattering of an isolated plasmonic nanoantenna integrated in a silicon waveguide
S11.6	Pierre Berini	Th.1.B.6 19-Invited Paper, Pierre Berini (Univ. Ottawa), “Plasmonics for Integrated Optics”
S12.1	Jae K. Jang, Alexander Klenner,	141 Th.2.B.1 141-Regular Paper, Synchronization of Modelocked Coupled Microresonator Combs
S12.2	Juan Fernández, Rocío Baños, Dav	Th.2.B.2 110-Regular Paper, Low-loss inverted taper edge coupler in silicon nitride
S12.3	J. G. Wangüemert-Pérez, A. Sánch	Th.2.B.3 24-Invited Paper, Gonzalo Wangüemert (Univ. Málaga), “Mid-infrared suspended waveguide platform & building blocks”
S12.4	Lawrence Rosenfeld, Joshua W. Si	Th.2.B.4 94-Regular Paper, A new platform for integrated quantum optics the short-wave infrared
S12.5	Siddharth Nambiar, Abhai Kumar.,	Th.2.B.5 59-Regular Paper, High-efficiency SiN Grating Fiber-Chip Coupler with Bottom Reflector
S12.6	Marco A. G. Porcel, J. David Dom	Th.2.B.6 25-Invited Paper, David Domenech-VLC, “PIX4life developments the path towards a visible light photonic foundry”

Chip-scale integrated photonics for the mid-infrared

(Invited paper)

Delphine Marris-Morini [1], Qiankun Liu [1], Joan-Manel Ramirez [1], Vladyslav Vakarin [1], Andrea Ballabio [2], Daniel Chrastina [2], Jacopo Frigerio [2], Xavier Le Roux [1], Samuel Serna [1], Eric Cassan [1], Daniel Benedikovic [1], Carlos Alonso-Ramos [1], Laurent Vivien [1], Giovanni Isella [2]

[1] Centre de Nanosciences et de Nanotechnologies, Univ. Paris-Sud, CNRS, Université Paris-Saclay, C2N – Orsay, 91405 Orsay cedex, France

e-mail: delphine.morini@u-psud.fr

[2] *L-NESS, Dipartimento di Fisica, Politecnico di Milano, Polo di Como, Via Anzani 42, 22100 Como, Italy*

ABSTRACT

Recent works towards the development of Ge-rich SiGe photonic integrated circuits for on-chip mid-IR spectroscopy will be presented. First, the demonstration of ultra-wideband passive circuits will be discussed, followed by the first proofs of concepts towards the realization of efficient wideband active devices. The combination of on-chip integrated spectrometers with on-chip mid-IR sources will provide a solid basis for the development of a competitive mid-IR integrated platform from 3 to 15 µm wavelength.

Keywords: silicon photonics, germanium, silicon-germanium, mid infrared.

1. INTRODUCTION

Mid-infrared (mid-IR) integrated photonics undergoes a growing interest, for applications in mid-IR spectroscopy or free-space telecommunications. Silicon photonics presents strong advantages for integrated photonics as it benefits from reliable and high-volume fabrication to offer high performance, low cost, compact, low-weight and low-power-consumption photonic circuits, which can be particularly interesting for mid-IR spectroscopic sensing systems that need to be portable and cost effective [1,2]. Among the different materials available in silicon photonics, Germanium (Ge) and Silicon-Germanium (SiGe) alloys with a high Ge concentration are noticeable because of the wide transparency window of Ge up to 15 µm [3]. Furthermore, a large increase of the non-linear refractive index of $Si_{1-x}Ge_x$ alloys has been predicted for Ge concentrations x larger than 0.8 [4].

In this context, we will review our recent works towards the development of Ge-rich SiGe photonic integrated circuits for mid-IR wavelengths. The Ge-rich SiGe platform will be presented first, with the demonstration of ultra-wideband passive circuits. In a second part the strategy for the development of active devices based on non-linear effects will be presented.

2. GE-RICH SIGE PLATFORM FOR MID-INFRARED

Ge-rich SiGe materials have been used for a long time in Si photonics, for optical modulation and photodetection [5]. Due to the differences in lattice constants and thermal expansion coefficient between Si and Ge, graded buffer layers have been proposed and used to realize fully relaxed virtual substrates with a low density of threading dislocations suitable for the growth of Ge quantum wells with high crystalline quality. While this integration scheme was initially developed for near-IR wavelength range, to demonstrate electro-absorption modulator and photodetector for telecom and data com applications [6], the extension of this approach for mid-IR wavelength range has been proposed. The use of graded based SiGe layers and Ge-rich SiGe alloys can provide definite advantages for mid-IR integrate photonics. Indeed, a gradual increase of the Ge content in the SiGe graded buffer allows a smooth increase of the refractive index, thus confining the optical mode in the Ge-rich part of the epitaxial structure. Low-loss optical waveguides are thus expected, potentially up to λ = 15 µm, as the refractive index gradient allows to push the optical mode far from the Si substrate where absorption begins to be prohibitive beyond $\lambda \sim 8.5$ µm. Furthermore, confining light in Ge-rich $Si_{1-x}Ge_x$ is also beneficial for non-linear based devices, as an increase of the non-linear refractive index n_2 has been demonstrated when x is larger than 80% [7]. Finally the use of SiGe alloys allows tailoring the light propagation properties by playing on the gradient shape and layers composition. The dispersion and the modal confinement can thus be engineered very precisely.

As a first proof-of-concept of the potential of this new platform for mid-IR photonics, the first waveguide design that was investigated uses a 2 µm-thick $Si_{0.2}Ge_{0.8}$ layer on a 11 µm- thick linearly graded $Si_{1-x}Ge_x$ substrate from Si to $Si_{0.21}Ge_{0.79}$. This structure directly comes from previous work at near-IR wavelengths [6]. The waveguide design is shown in Fig 1(a). The vertical confinement is allowed by the refractive index profile (Fig 1 (b)) which increases linearly in the graded layer according to the Ge concentration. Low-energy plasma-enhanced chemical vapor deposition was used to grow the $Si_{1-x}Ge_x$ material, with a typical growth rate of 5–10 nm/s. The

waveguides were then patterned using lithography followed by inductively coupled plasma etching. The etching depth was 4 µm, and the waveguide width was 4 µm, allowing a good confinement of the fundamental TE and TM modes. As a key building block for the development of the mid-IR photonics platform, Mach-Zehnder Interferometers (MZI) have been demonstrated [8]. The asymmetric MZI have been designed with 3 mm long arms and arm length differences of 48 µm, 87 µm and 149 µm, and Multimode Interference (MMI) coupler and splitter. The characterization of the different MZIs in both polarizations is reported in Fig 1(c). Interestingly large extinction ratios of at least 10 dB between 5.5 µm and 8.6 µm wavelength are obtained for both TE and TM polarizations. In all the characterized structures the expected decrease of the free spectral range (FSR) with the increase of arm length difference ΔL and the increase of the FSR with the increase of the wavelength are observed. The unique broadband properties of the MZI and corresponding MMI are explained to be due to the vertical refractive index gradient in the graded $Si_{1-x}Ge_x$ substrate. Finally, while the reported wavelength range is limited by the available experimental set-up, numerical simulations indicate that the MZI operation can be extended up to 11 µm wavelength, being limited only by the MMI coupler bandwidth.

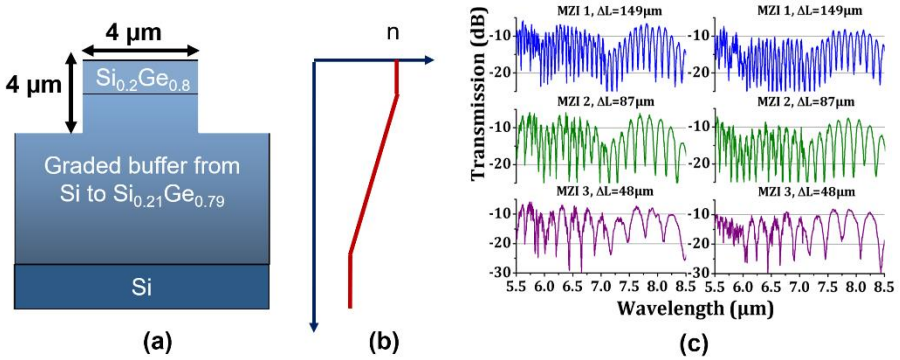


Figure 1. (a) first waveguide design; (b) refractive index profile along the vertical direction ; (c) transmission of the Mach Zehnder interferometers for different length difference between both arms, from 48 to 149 µm, in TE (left column) and TM (right column)

3. TOWARDS ACTIVE DEVICES

As a next step towards a complete integrated platform for spectroscopic applications, active devices such as wideband supercontinuum sources can be envisioned. While it has been previously demonstrated that Ge-rich SiGe alloys present a large non-linear Kerr refractive index n_2, optimising light confinement is a key parameter to achieve efficient non-linear based devices. From the initial waveguide design, two additional epitaxial layer designs have been proposed to increase light confinement. The three platforms are then compared in Fig 3, where (a) refers to the former waveguide reported in Fig. 1, the platform (b) corresponds to a reduction of waveguide thickness by using a 6 µm graded layer from pure Si to pure Ge, and the platform (c) is based on two graded layers, first a 3 µm-thick layer from Si to $Si_{0.5}Ge_{0.5}$ followed by a 1 µm-thick graded layer from $Si_{0.5}Ge_{0.5}$ to pure Ge. All three platforms have been investigated in terms of propagation losses, and the results are reported in Fig 2. Interestingly low propagation losses between 2 and 3 dB/cm are obtained with platforms (a) and (b), while the platform (c) provides prohibitive losses in the longer wavelength range, which can be correlated to an increase of the overlap of the optical mode with Si and Si-rich SiGe layer, which could be responsible for such increase of the propagation losses at long wavelengths [9].

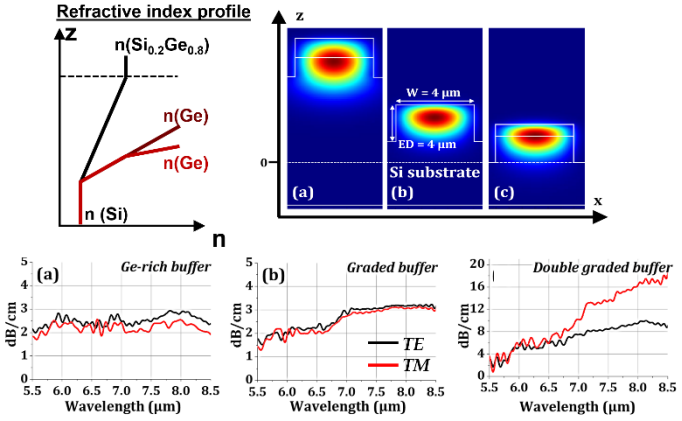


Figure 2. Different SiGe platforms investigated in this work (a) 11µm thick graded buffer followed by 2µm-thick $Si_{0.2}Ge_{0.8}$, as shown in Fig 1 ; (b) 6µm thick graded layer from Si to Ge ; (c) double graded buffer layer : 3µm thick graded layer from Si to $Si_{0.5}Ge_{0.5}$ followed by 1µm thick graded layer from $Si_{0.5}Ge_{0.5}$ to Ge . Refractive index profile, illustration of mode confinement increases when the waveguide thickness decreases, and comparison of the propagation losses determined experimentally by a non-destructive cut-back technique.

From this work it was possible to conclude that the platform (b) based on a 6 µm-thick SiGe graded layer from pure Si to pure Ge is the most promising one for active devices. The waveguide has thus been engineered to evaluate the possibility to generate a supercontinuum [10]. In addition to the good modal confinement, a flat anomalous dispersion in a wide spectral range is required. The final design is reported in Fig 3 (a). The waveguide width and etching depth are 4 µm. The optimized confinement of the optical mode which is always located in the upper part of the waveguide, overlapping with the Ge-rich part of the SiGe graded buffer waveguide is illustrated by the calculation of the modal effective area (Fig 3.(b)). The spectral dispersion characteristics of quasi-TE and quasi-TM polarizations are reported in Fig 3.(c). Both polarizations provide broadband anomalous dispersion over a 1.4 octave spanning, having the quasi-TM mode an almost flat profile with a maximum value of ≈ 14 ps/nm/km. Finally the value of n_2 as a function of the wavelength and for different Ge fraction of $Si_{1-x}Ge_x$ alloys has been used to calculate the effective nonlinear parameter (γ_{eff}) of graded $Si_{1-x}Ge_x$ waveguides (Fig 3 (e)). A maximum value of $\gamma_{eff} \approx 10\ W^{-1}m^{-1}$ is obtained at $\lambda = 3$ µm, and decreases down to $\sim 0.6\ W^{-1}m^{-1}$ for $\lambda = 8$ µm. The comparison of these values with previously reported experimental demonstrations [11] on different platforms provide an optimistic foreseeable future for the development of supercontinuum sources using such waveguide design.

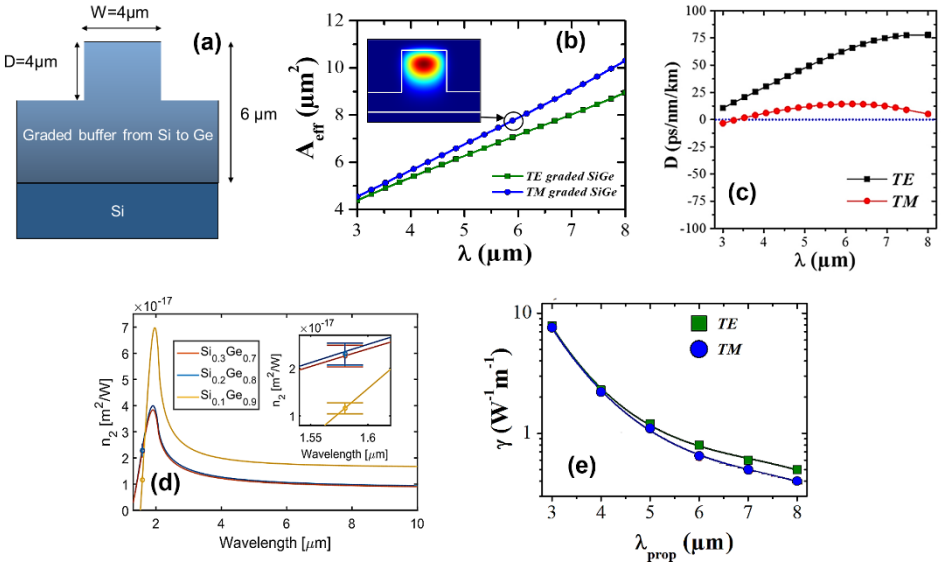


Figure 3. (a). Waveguide design for a supercontinuum source (b) optical mode effective area as a function of the wavelength; (c) dispersion properties showing flat anomalous dispersion; (d) non-linear Kerr refractive index n_2 as a function of the wavelength and for different Ge fractions; (e) effective non-linear parameter of the optical mode.

4. CONCLUSION

Recent works towards the development of Ge-rich SiGe photonic integrated circuits for mid-IR wavelength range have been reported. While passive devices have demonstrated good operation properties, current challenges are the demonstration of active devices based on non-linear effects. The design of a wideband supercontinuum source paves the way towards the demonstration of a complete mid IR photonic platform for spectroscopic applications.

ACKNOWLEDGEMENTS

The authors acknowledge funding from European Research Council (ERC) under the European Union's Horizon 2020 research and innovation program (N°639107-INsPIRE). The fabrication of the devices was performed at the Plateforme de Micro-Nano-Technologie/C2N, which is partially funded by the "Conseil Général de l'Essonne". This work was partly supported by the French RENATECH network.

REFERENCES

[1] Lin, H., et al., Nanophotonics (2017).
[2] Zhang, L., et al, Nanophotonics 3, (2014).
[3] Soref, R., Nat. Photonics 4, 495–497 (2010).
[4] Hon, N. K., et al, J. Appl. Phys. 110, 11301 (2011).
[5] Marris-Morini et al, Nanophotonics 2 (4) (2013).
[6] Chaisakul P., et al, Nature Photonics 8, 482-488 (2014)
[7] Serna, S., Scientific reports, 7, 14692 (2017)
[8] Vakarin, V., et alOptics Letters, 42 (17), 3482-3485 (2017)
[9] Ramirez et al, Optics Express, 26 (2), 870, (2018)
[10] Ramirez, J-M., Optics Express 25 (6) 6561 (2017) .
[11] Carletti, L., et al Optics express, 23(25), 32202-32214 (2015).

Heterogeneous large-scale photonic integration for communications and beyond

(Invited paper)

Tin Komljenovic
Department of Electrical and Computer Engineering
University of California, Santa Barbara, CA 93106, USA
e-mail: tkomljenovic@ece.ucsb.edu

ABSTRACT

Heterogeneous silicon photonics using bonding is reaching maturity with first commercial products for data center market being shipped in volume. Here we give an overview of recent research in the area carried out at University of California, Santa Barbara. Ability to do multiple die bonding on a single device/die with optimized epitaxially grown layer stacks was used to realize high performing photonic integrated circuits both for communications and sensing.

Keywords: silicon photonics, heterogeneous silicon photonics, integrated optoelectronics, optoelectronic devices, semiconductor lasers.

1. INTRODUCTION

Photonics integrated circuits (PIC) can be realized in a number of platforms, but for efficient on-chip light generation a direct bandgap semiconductor is needed. Historically, the first integrated photonic circuits with lasers were realized on GaAs or InP substrates. More recently, optical components are being integrated on silicon (Si) substrates where the main idea is to leverage the superiority of CMOS processing infrastructure, perfected throughout the years and billions of dollars invested by (electronics) semiconductor industry. In the past 15 years, a whole range of photonic components have been demonstrated, mostly in the silicon-on-insulator (SOI) platform. The SOI platform is especially suited for standard communication bands at 1.31 μm and 1.55 μm, as silicon and its oxide (SiO_2) are both transparent and form high-index contrast, high-confinement waveguides ideally suited for medium to high-integration PICs. However, electrically pumped efficient sources on silicon remain a challenge due to the indirect bandgap of silicon.

One of the solutions to that problem, most commonly called heterogeneous[1] integration, bonds pieces of III/V materials on patterned Si wafer and then processes them together using standard lithography tools. First demonstrated by UCSB in 2006 [2], such an approach is currently widely used by academia (e.g. UCSB [3], Ghent University [4]), research organizations (e.g. III-V lab [5]) and industry (e.g. Intel [6], Juniper Networks (former Aurrion) [7], HP Enterprise [8]) with first commercial products for data center market being shipped in volume [6]. The advantage of this approach is that the alignment tolerances are significantly reduced as devices are defined using lithography alignment marks after bonding of larger III/V pieces allowing for efficient volume scaling due to superior quality with smaller feature sizes, smoother surfaces and superior yield. This will become increasingly important as the complexity of PICs increase, as shown in Figure 1.

Heterogeneous silicon photonics works to provide the best of both worlds: high performance devices from optimized III/V materials and superior passive and waveguide technology of the SOI platform. Physically, the large mismatch in lattice constant and thermal expansion coefficient between the Si and III-V make monolithic integration very challenging, although a lot of progress has been recently reported in the area of heteroepitaxy on Si. Bonding removes, or at least relaxes, the lattice mismatch limitations to a very large degree although the thermal expansion coefficient mismatch still has to be taken care of. For this reason temperature during bonding and subsequent processing steps is typically limited to <300 °C.

In the last 10 years, many high-performing components realized in the heterogeneous silicon platform have been demonstrated, some of which outperform native III/V components such as narrow-linewidth single-frequency lasers (< 1 kHz linewidth), narrow-linewidth widely-tunable lasers (50 kHz linewidth), mode-locked lasers (900 fs pulse, 1.1 kHz RF linewidth @ 20 GHz) and high-power high-speed waveguide photodetectors (12 dBm @ 40 GHz, - 2 dBm @ 70 GHz). The record performing devices take the advantage of low and ultra-low loss waveguides in Si, efficient light generation in III/V and the ability to continuously control the confinement in active region by tapering the underlying Si waveguide width or the III/V structure on the top, or both.

[1] When the heterogeneous approach was first demonstrated, the nomenclature "hybrid III–V silicon evanescent laser" was used and often shortened to "hybrid silicon laser." In subsequent years, "heterogeneous" is more commonly used to describe this wafer scale approach to integration, and "hybrid" is more commonly used for bonding or soldering individual die onto a common substrate.

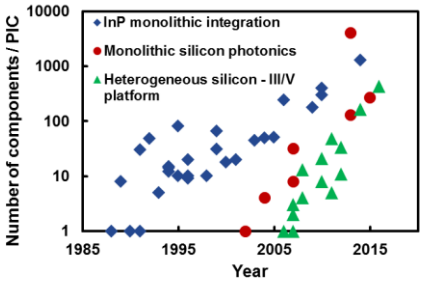


Fig. 1. Progress in photonic integration shown in terms of a number of devices optically connected on a single chip. Silicon photonic integration (red circle) represents the "passive" integration without on-chip laser solution; InP integration (blue square) and heterogeneous silicon integration (green triangle) are solutions with on-chip lasers.

2. SYSTEMS ON CHIP (SOC)

A complex PIC might require a number of different, high-performing components. The underlying Si waveguides can provide for routing, multiplexing/demultiplexing, filtering, splitting and combining, and with extra processing (implants and Ge) can also provide modulation and detection. The ability to bond different III-V epitaxially grown thin-films on a single die allows for optimization of individual device performance, so a complex PIC device might make use of optimized laser gain material, bandgap shifted modulator material as well as optimized photodetector material, all on the same SOI die with no regrowth which would be required for monolithic III-V PIC. With proper design of the III-V layer stacks, simultaneous processing of all the bonded III-V layers is possible reducing the number of processing steps, directly reducing cost and improving yield. The process also allows for fabrication of 1.31 µm and 1.55 µm devices on same wafer as demonstrated in [9], making it very powerful. A number of SOC have been demonstrated including a microwave signal generator, integrated optical driver for interferometric optical gyroscope, beam scanner and optical network-on-chip

2.1 Microwave generator

Fully integrated photonic microwave generator realized in heterogeneous silicon platform combined waveguide photodiodes with a 3 dB bandwidth of 65 GHz and 0.4 A/W responsivity with lasers that tune over 42 nm and have 150 kHz linewidth, which allowed for microwave signal generation from 1 GHz to 112 GHz. The inclusion of modulators allows for direct signal generation at the microwave frequency, or for generation of sidebands for e.g. measurement applications [9].

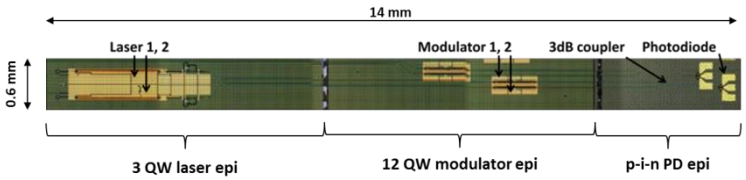


Fig. 2. Optical microscope image of the fully integrated photonic microwave generator chip realized by bonding three optimized III/V layer stacks for optical sources, phase modulators and high-speed PIN photodetectors.

2.2 Interferometric optical gyroscope driver

A chip-scale fully-integrated optical driver (IOD) that can interrogate a sensing coil and realize an interferometric fiber optical gyroscope was demonstrated. The chip comprises a light source (Fabry-Perot laser with broad optical spectrum which is beneficial for gyroscope operation), three photodiodes (7 GHz bandwidth, 0.7 A/W responsivity, 4 nA dark current), two phase modulators (V_π = 4.2 V) and two broadband 3-dB splitters (> 70 nm bandwidth) within an area of 4.5 mm^2 [10].

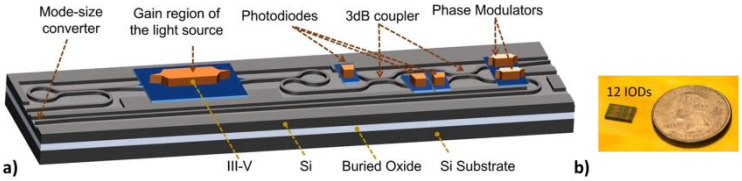


Fig. 3. (a) 3D schematic (not to scale) of the integrated optical driver (IOD) for fiber optic gyroscopes (b) A set of 12 IOD devices next to an US quarter coin for size comparison.

2.3 2D beam scanner

An integrated phased array beam steering system on a chip was demonstrated. The heterogeneous PIC consists of 164 optical components including lasers, amplifiers, photodiodes, phase tuners, grating couplers, splitters, and a photonic crystal lens in 69 mm^2. The beam scanner allows for steering over 23° x 3.6° with beam

widths of 1° x 0.6° giving a total of 138 resolvable spots in the far field with 5.5 dB background suppression [11].

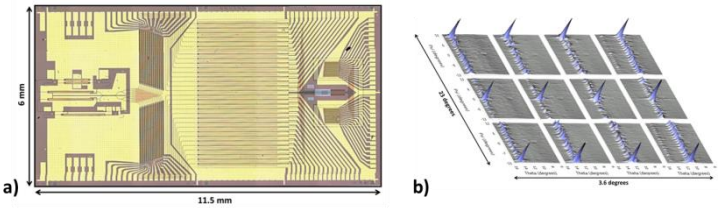


Fig. 4. (a) Microscope picture of the fully integrated beam-steering PIC (b) Two-dimensional beam-steering plots spanning 23° in ψ and 3.6° in θ planes.

2.4 Network-on-Chip (NoC)

An optical network-on-chip (NoC) that connects eight nodes, realized in heterogeneous silicon platform, has been demonstrated [12]. The NoC has 8 nodes, each node having 8 DWDM channels capable of on-off keying (OOK) data transmission of up to 40 Gbps, bringing the total on-chip capacity to 2.56 Tbps. The chip comprises of more than 400 functional components including lasers, modulators, amplifiers, detectors, switches and arrayed-waveguide gratings in an area of 176 mm^2 and uses three different III-V layer stacks for DFB lasers (7.5 mA threshold current), electroabsorption modulators (6 dB extinction @ 1 Vpp) and detectors (>20 GHz bandwidth, 10 nA dark current).

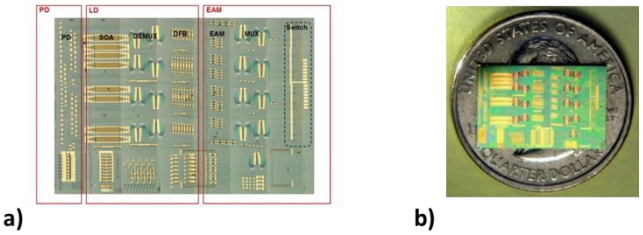


Fig. 5. (a) Microscope image of the photonic transceiver circuit (16 mm x 11 mm) (b) Size comparison with US quarter.

ACKNOWLEDGEMENTS

This work was supported by Keysight and DARPA DODOS, MOABB, SWEEPER, POEM, and iWOG contracts. The author acknowledges John Bowers and present and past members of Optoelectronics Research Group at UCSB that contributed to work presented, as well as many other individuals that offered advice, assistance and suggestions.

REFERENCES

[1] L. Coldren, S. Corzine and M. Mashanovitch, *Diode Lasers and Photonic Integrated Circuits*, 2nd ed.; John Wiley and Sons: New Jersey, United States, 2012, pp. 451-503

[2] A. W. Fang et al., "Electrically pumped hybrid AlGaInAs-silicon evanescent laser," *Opt. Express*, vol. 14, no. 20, pp. 9203-9210, 2006.

[3] T. Komljenovic et al., "Heterogeneous Silicon Photonic Integrated Circuits," *J. Lightwave Technol.*, pp. 34, no. 1, pp. 20-35, 2016.

[4] G. Roelkens et al., "III-V-on-Silicon Photonic Devices for Optical Communication and Sensing," *Photonics*, vol. 2, no. 3, pp. 969–1004, 2015.

[5] G.-H. Duan et al., "New Advances on Heterogeneous Integration of III–V on Silicon," *J. Lightwave Technol.*, vol. 33, no. 5, pp. 976-983, 2015.

[6] Intel, http://www.intel.com/content/www/us/en/architecture-and-technology/silicon-photonics/optical-transceiver-100g-psm4-qsfp28-brief.html (accessed March 3rd, 2018)

[7] B. R. Koch et al., "Integrated Silicon Photonic Laser Sources for Telecom and Datacom," in OFC 2013, OSA Technical Digest (online) (Optical Society of America, 2013), paper PDP5C.8.

[8] D. Liang et al., "Integrated finely tunable microring laser on silicon," *Nat. Photon.*, vol. 10, pp. 719-722, 2016.

[9] J. Hulme et al., "Fully integrated microwave frequency synthesizer on heterogeneous silicon-III/V," *Opt. Express*, vol. 25, no. 3, pp. 2422-2431, 2017.

[10] M. A. Tran et al., "Integrated optical driver for interferometric optical gyroscopes," *Opt. Express*, vol. 25, no. 4, pp. 3826-3840, 2017

[11] J. C. Hulme et al., "Fully integrated hybrid silicon two dimensional beam scanner," *Opt. Express*, vol. 23, no. 5, pp. 5861-5874, 2015.

[12] C. Zhang et al., "8 × 8 × 40 Gbps fully integrated silicon photonic network on chip," *Optica*, vol. 3, no. 7, pp. 785-786, 2016.

Solving Technical Challenges of PICs through the Advancement of Integrated Silicon Photonics Solutions for the 21st Century

(Invited paper)

Michael Liehr[1,2], Frank Tolic[1,2], Edward White[1,2], Erman Timurdogan[3], Benjamin Miller[4]
[1] AIM Photonics, *257 Fuller Road, Albany, NY 12203 - USA*
Tel: +15189567221, e-mail: ftolic@aimphotonics.com
[2] SUNY Polytechnic Institute, *257 Fuller Road, Albany, NY 12203 - USA*
Tel: +15189567221, e-mail: ftolic@sunypoly.edu
[3] Analog Photonics, *1 Marina Park Drive, Suite 205, Boston, MA, 02210 - USA*
Tel: +18579911120, e-mail: erman@analogphotonics.com
[4] University of Rochester Medical Center, *601 Elmwood Avenue, Box 697, Rochester, NY 14642- USA*
Tel: +15852759805, e-mail: Benjamin_Miller@URMC.Rochester.edu

ABSTRACT

In this paper, AIM Photonics describes how developing a widely accepted set of processes and protocols for the design, manufacture, and integration of silicon photonics systems not only advances this technology, but also presents a tremendous economic opportunity, with the overall global market estimated to grow to more than $795 billion by 2022. Integrated Photonics is finding use in a wide range of areas including: telecommunications, laser based radar, data communications, sensing, and many others. Integrated photonics dramatically improves the performance and reliability of electronic integrated circuits while significantly reducing size, weight, and power consumption. Integrated photonics will advance established industries and enable new ones in the 21st century in the same way that semiconductors fostered the revolution in computing, telecommunications and other fields over the past 40 years.

1. INTRODUCTION

This paper details various projects and results driving advancements of integrated silicon photonics. Recent successes are highlight in data comm, sensors, and manufacturing. AIM Photonics addresses challenges associated with key technologies and manufacturing of integrated silicon photonics. Automated electro-optical inline testing and automated fiber attach are two key volume manufacturing challenges being addressed. In addition, advancing transceiver technologies for communication, and sensors for bio medical and chemical detection purposes are presented. AIM Photonics has also worked the past two years to establish a silicon photonics Process Design Kit (PDK) to enable small to medium sized companies access to validated and tested devices for previously mentioned key technologies.

AIM Photonics partnership with EPDA industry leaders, large and small PIC companies, government institutes, and globally recognized university researchers has establish an ecosystem that provides complete access across the entire product cycle; design, research, development, proof of concept, prototyping, validation, and fast transfer to volume manufacturing. This allows AIM Photonics partners a low cost solution with quick cycles of learning, creating reduced time to market, all while advancing the broader silicon photonics manufacturing ecosystem.

2. HIGH DENSITY FIBER-CHIP INPUT/OUTPUT (I/O)

AIM Photonics and partners are developing the critical fiber-to-photonic chip coupling technology that will become the mainstay manufacturing solution at the Test Assembly and Packaging (TAP) Facility in Rochester, New York. Widespread commercial adoption of integrated photonics has been impeded by the challenges of realizing low cost scalable optical I/O packaging solutions. The fiber and fiber array connector envisioned in this PIC attach process would open a path to high volume manufacturing, with unprecedented coupling alignment tolerances for scalable, cost effective assembly. The significant reduction in the size of components, as depicted in Figure 1, will result in cost reductions for those components [1].

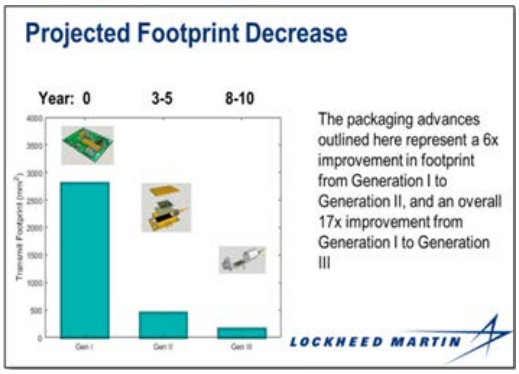


Figure 1. Timeline for reduction in packaging footprint. Credit: Lockheed Martin.

3. DEVELOPMENT OF UNIVERSAL TRANSDUCER COMPONENTS AND MICROFLUIDIC SYSTEMS

This project demonstrates photonics manufacturing processes for common detection elements of chemical and biological sensors and completed testing of photonics based components that detected simulants of the chemical warfare agent Sarin within tolerances approaching Department of Defense (DoD) requirements. This is the first time a sensor of this type, as shown in Figure 2, has been manufactured using a process that can be scaled for commercial production [1].

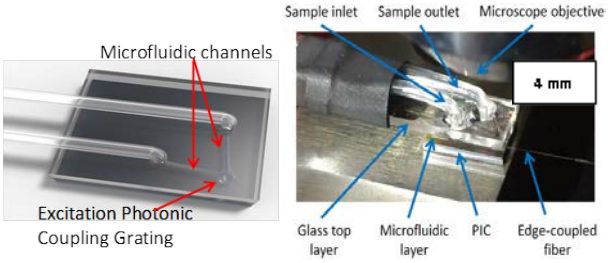


Figure 2. Schematic (left) and fabricated device (right) for microfluidic-enabled PIC for SERS. Credit: Carl Meinhart, University of Rochester.

4. HIGH CAPACITY PHOTONIC INTERCONNECTED SYSTEMS

AIM photonics recently completed set of key design deliverables, which were implemented with the assistance of products from member companies working in the AIM Photonics Data Communications Key Technology Manufacturing Area, in developing very high speed photonics-based digital and data communication links. By replacing electronic switches, which have been a major communication bottleneck and power sink in data centers, this technology will increase capacity tenfold and reduce energy consumption-per-bit transmitted by a factor of 10.

Another recent accomplishment is the completed installation of inline controls and test equipment to permit optical and electrical testing of photonic components. Such testing is a key to the improving photonics manufacturing processes. Inline testing significantly improves yield and reduces scrap loss. This will advance the development of (PIC) technology area for AIM Photonics members and other organizations by reducing cycles of learning and product development costs. The test system, shown in Figure 3, is the first of its kind [1].

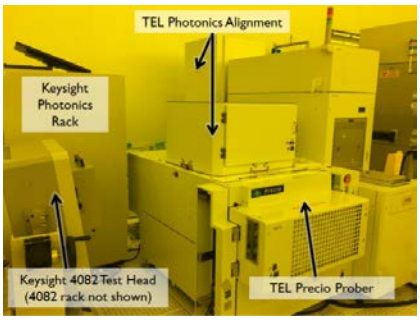


Figure 3. Newly installed electrical optical test equipment in the SUNY Poly cleanroom. The tools, part of the Inline Test Development project, will reduce the time to detect a misprocessed wafer from 4 months to a few days. Credit: AIM Photonics

5. PHOTONICS PROCESS DESIGN KIT COMPONENT LIBRARY

Analog Photonics, LLC and SUNY Poly expanded the comprehensive set of publicly available silicon PIC components in the integrated photonics process design kit (PDK). Continued development of the PDK is an essential enabler for both the baseline technology and the efficient design of products that will ultimately be manufactured. Work in 2017 provided new capabilities in optical integration, enabling reductions in the time to market, product development risk, and investment. Combined with Multi-Project Wafer (MPW) runs, this PDK will give AIM Photonics members access to silicon photonics components for the development of 100G, 200G and 400G+ optical transceivers or systems used in data centers, metro and long haul optical networks. Some features of the APSUNY_PDK are:

- 50Gbps modulation with less than one volt peak to peak drive. Low voltage drive at high bandwidth is key to enable low power applications and work with CMOS/BiCMOS drivers.
- Digital detectors with greater than 45GHz bandwidth and high responsivity, ideal for C-band receivers.
- Both polarization support for standard and low-cost single mode fibers, eliminating the need for expensive polarization maintaining fibers.
- Lower loss crossings and propagation with seamless dielectric transitions and <1% mismatch between the outputs of a 3dB splitter, leading to a high common mode rejection ratio (CMRR) [2].

6. TEST, ASSEMBLY, AND PACKAGING (TAP) FACILITY PROCESS DEVELOPMENT

The planning, construction, and implementation of the TAP Facility is near completion. Validation and testing of products for the facility are performed in advance with the help of industrial partners and their design teams. The TAP Facility, which represents an investment of $194 million by New York State for facility upgrades, equipment, installation, and lease costs, will open in the second half of 2018 [3].

7. CONCLUSIONS

Prior to the establishment of AIM Photonics, the growth of the integrated photonics industry was impeded by an immature manufacturing and design ecosystem. The ecosystem being created by AIM Photonics harnesses the combination of the nation's leading experts in photonics integration from both industry and academia.

ACKNOWLEDGEMENTS

AIM Photonics also recognizes its members and partners who are instrumental in driving the technology advancements through this national network for manufacturing innovation for integrated photonics.

REFERENCES

[1] AIM Photonics, 2017 Manufacturing USA Annual Report, *American Institute for Manufacturing Integrated Photonics*, May 2018

[2] M. Liehr, *et al.*: AIM Photonics is Ready for High-Speed Optical Communications (50Gbps) with the New Silicon Photonics Process Design Kit (PDK), *AIM Photonics News Release.*, February 1st, 2018

[3] F. Tolic, *et al.:* AIM Photonics: Meeting Challenges of the Marketplace and Providing Innovative Solutions, *OFC 2018 Show Floor Session*, San Diego, CA, March 12th, 2018

High sensitivity photonic configurations for biochemical detection

(Invited paper)

Jaime García-Rupérez
Nanophotonics Technology Center, Universitat Politècnica de València, Camino de Vera s/n - 46022, Valencia - Spain
Tel: +34 963879736, Fax: +34 963877827, e-mail: jaigarru@ntc.upv.es

ABSTRACT

In this paper, we present different approaches for the creation of high sensitivity nanophotonic-based biosensing devices that are currently being developed by our group. These approaches not only focus on the improvement of the photonic sensing structures themselves, what can have a limited effect over the sensitivity, but also on other aspects as the use of functional biomolecular receptors, the use of advanced microfluidic systems, or a proper selection of the constitutive materials of the photonic sensing structures. The aim of these approaches is being able to detect very low concentrations of biological/chemical analytes having a very reduced size and/or molecular weight, something that has a tremendous importance for many application fields as medical diagnosis, environmental control or biological/chemical threats detection, among others.

Keywords: photonic sensors, high sensitivity, PBG structures, molecular beacons, porous silicon.

1. INTRODUCTION

Photonic technology is one of the main candidates to create the core transduction elements of future high-performance analysis devices since it provides significant advantages such as high sensitivity, compactness and high integration level, short time to result, label-free detection, and use of very low sample volumes. These advantages will allow deploying compact and low cost analysis systems able to simultaneously detect hundreds/ thousands of analytes in few seconds/minutes using simply a couple of drops of the sample to be analyzed. Therefore, this type of technology will be crucial for the development of many high impact applications as for example the implementation of minimally-invasive screening programs for a higher accuracy early diagnosis of diseases as cancer or cardiovascular diseases, a better monitoring of environmental resources in order to promptly identify hazardous pollutants and to properly manage these resources, or the surveillance of public spaces in order to provide an early warning in the case of potential biological/chemical attacks.

However, despite being very high, the sensitivity provided by photonic technology is sometimes not enough to detect very low concentrations of the target analytes or to detect target analytes with a very low size and/or molecular weight. In those situations, the local variations of the refractive index that are produced by the presence of the targets analytes are almost negligible, making them practically undetectable. Unfortunately, many of the most promising applications nowadays fall in that scenario, so alternatives to further increase the sensitivity of photonic-based biosensors are required. Within this context, we present in this paper different approaches being developed in our group for increasing the sensitivity of nanophotonic-based sensing devices.

2. HIGH SENSITIVITY DETECTION APPROACHES

2.1 Use of photonic bandgap sensing structures

Our current work is specially focused on the development of photonic sensors based on 1D photonic bandgap (PBG) structures, as that shown in Fig. 1. In these structures, the periodicity in the propagation direction gives rise to the appearance of a spectral PBG region where guided modes are forbidden; the position of this PBG will be shifted when the target analytes are bound to the surface of the structure. These PBG periodic structures are also characterized by the appearance of the so-called slow-wave effect for the PBG edge modes. That slow-wave behavior translates into a higher sensitivity due to the higher interaction that is produced with the target analytes because of the group velocity reduction.

By using these 1D PBG sensing structures in combination with molecular beacon (MB) probes, we have demonstrated a very high sensitivity towards the detection of short length target oligonucleotides. Spectral shifts of the PBG edge even above 1 nm have been obtained for the detection of a 35-mer target oligonucleotide [1,2], as shown in Fig. 1. These shifts are even more than one order of magnitude higher that those typically obtained using other photonic sensing structures as ring resonators for the detection of similar targets (in the range of 50-100 pm [3]), thus demonstrating the higher sensitivity of PBG structures. Note also that a further increase of the sensitivity can be obtained by properly designing the constitutive parameters of the PBG sensing structure in order to have a better interaction with the targets to be detected.

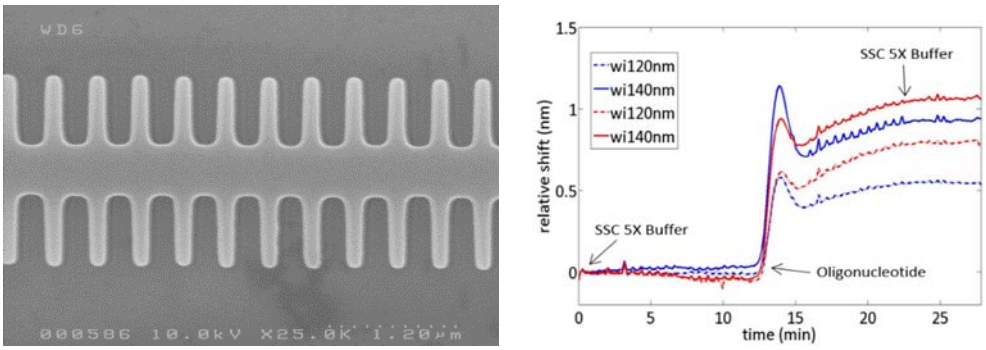


Figure 1. (Left) Scanning electron microscope (SEM) image of a 1D PBG sensing structure. (Right) Evolution of the PBG edge position for four 1D PBG sensing structures with different parameter wi (≡width of the transversal elements) being biofunctionalized with specific MB probes. The 1D PBG sensing structures respond to the presence of the target oligonucleotide when it is flowed over them.

2.2 Use of nanoparticle-labelled molecular beacon receptor probes

A molecular beacon (MB) is a special type of probe for nucleic acids detection. Its working principle is based on the conformational change that the MB probe suffers upon the recognition of its target nucleic acid: the MB probe is initially in a closed stem-loop configuration and it will open into a straight configuration when the target nucleic acid is recognized. Typical use implementations of MB probes are based on attaching a fluorophore and a quencher to their 3' and 5' terminations in order to switch on the fluorescence when the target nucleic acid is recognized (the fluorophore and the quencher are moved away when the MB changes to the straight configuration).

In our group, we are working on the use of MB probes for the biofunctionalization of photonic sensing structures. Besides using them as specific recognition elements, as for the results shown in the previous subsection, we are working on the use of nanoparticle-labelled MB probes with the objective of having additional sensing effects determined by the conformational change suffered by the MB. As it is schematically explained in Fig. 2, the conformational change of the MB can be used to move a nanoparticle away from the surface of the photonic sensing structure when the target nucleic acid is recognized. This displacement of the nanoparticle will produce an additional negative shift on the sensor response, leading to a net sensing response being combination of that negative shift and of the positive shift produced by the direct detection of the target nucleic acid. We have already demonstrated how these two effects determine the sensing response of the photonic structure by using streptavidin-labelled MB probes [2]. By properly designing the photonic sensing structure, the MB probe and the attached nanoparticle, it might be possible to have a net shift being higher than that provided for the direct detection of the target analytes, thus leading to an amplification of the photonic sensing response.

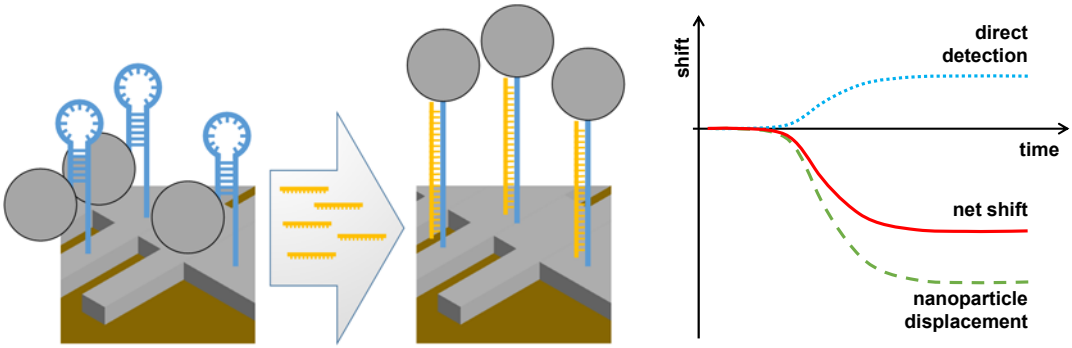


Figure 2. (Left) The nanoparticle-labelled MB probes immobilized on the surface of the photonic sensor change their shape when the target nucleic acid is recognized, leading to the displacement of the nanoparticle from the sensor surface. (Right) The measured sensing response (net shift – red solid line) will be given by the combination of the positive shift produced by the direct detection of the target analyte (blue dotted line) and the negative shift produced by the displacement of the nanoparticle from the surface (green dashed line).

2.3 Use of micro-/nanofluidic concentration systems

Another option for increasing the sensitivity of nanophotonic-based sensing systems is acting over the delivery of the target analytes towards the sensing structure in order to have a higher interaction between the sensor and those analytes. To do so, we are working on the combination of photonic sensing structures with active micro-/nanofluidic systems able to selectively stop the target analytes over the sensing structures, as shown in Fig. 3. These micro-/nanofluidic systems are based on the depletion zone isotachophoretic (dz-ITP) effect [4], which allows controlling the velocity of analytes with a given mobility by combining electroosmotic and electrophoretic

effects. In this way, the effective concentration of the target analytes to be detected can be increased by several orders of magnitude, and thus the final sensitivity of the whole photonic-based sensing system will be increased.

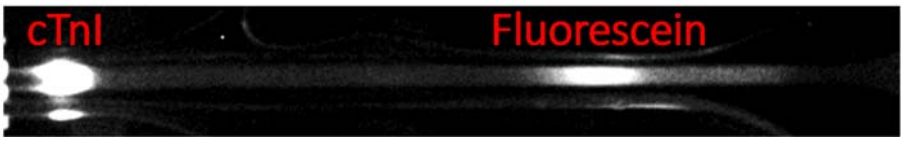


Figure 3. Fluorescence microscopy image of an experiment where cardiac troponin I (cTnI) and fluorescein are separated and concentrated. Results obtained at BIOS Lab-on-a-chip group at the University of Twente.

2.4 Use of porous silicon based sensing structures

The last approach considered to enhance the sensitivity of photonic-based sensors is changing the materials used to create the sensing structures. Typically, photonic sensors operation is based on the interaction of the evanescent field of the photonic structure with the target analytes to be detected. This fact limits the sensing performance of these sensors, since only a small amount of low intensity optical field will actually interact with the target analytes. An alternative for enhancing that interaction of the optical field with the target analytes is using porous materials for the creation of the photonic sensing structures; in that way, the target analytes can enter inside the photonic structure and thus interact with the region where the optical field is more intense. In our group, we are working on the use of porous silicon (PS) for the creation of different types of photonic sensing structures, including Fabry-Perot resonators, microcavities and ring resonators, as shown in Fig. 4. Besides the sensitivity increase produced by the infiltration of the target analytes into the photonic sensing structure, what we have experimentally confirmed by means of refractive index sensing experiments [5,6], porous silicon substrates also provide a higher surface/volume ratio, what also allows increasing the number of sensing events that can be detected, thus also improving the sensitivity.

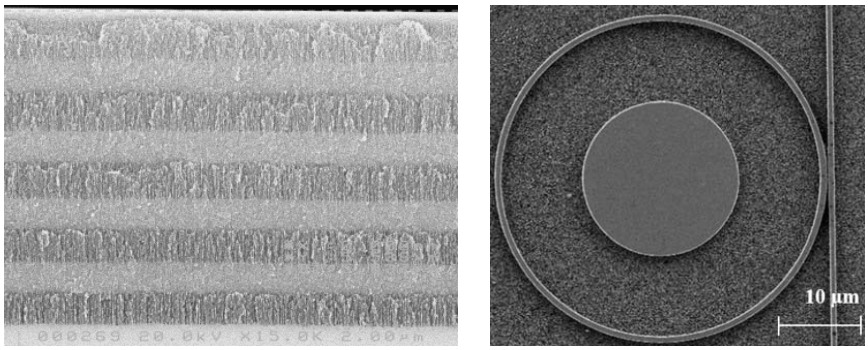


Figure 4. (Left) Cross sectional SEM image of a PS multilayer. (Right) SEM image of a PS ring resonator sensor.

ACKNOWLEDGEMENTS

Support from the European Commission through the projects H2020-644242-SAPHELY and H2020-634013-PHOCNOSIS is acknowledged. Funding from grant TEC2015-63838-C3-1-R (MINECO/FEDER, UE) is acknowledged.

REFERENCES

[1] Á. Ruiz-Tórtola, *et al.*: High sensitivity and label-free oligonucleotides detection using photonic bandgap sensing structures biofunctionalized with molecular beacon probes, *Biomed. Opt. Express*, vol. 9, pp. 1717-1727, 2018.

[2] Á. Ruiz-Tórtola, *et al.*: High sensitivity oligonucleotides photonic detection and optical characterization of molecular beacon conformational changes, *in Proc. ECIO 2018*, Valencia, Spain, May 2018.

[3] A. J. Qavi, R. C. Bailey: Multiplexed Detection and Label-Free Quantitation of MicroRNAs Using Arrays of Silicon Photonic Microring Resonators, *Angew Chem Int*, vol. 49, pp. 4608-4611, 2010.

[4] V.A. Papadimitriou, L.I. Segerink, A. van den Berg, J.C. Eijkel: Continuous Extraction Depletion Zone Isotachophoresis (edz-ITP), *in Proc. µTAS 2017*, Georgia, USA, October 2017.

[5] R. Caroselli, *et al.*: Real-time and in-flow sensing using a high sensitivity porous silicon microcavity based sensor, *Sensors*, vol. 17, pp. 2813.1-12, 2017.

[6] R. Caroselli, *et al.*: Experimental study of the sensitivity of a porous silicon ring resonator sensor using continuous in-flow measurements, *Opt. Express*, vol. 25, pp. 31651-31659, 2017.

Towards Photonic Biosensing using a Three-Port Mach-Zehnder Interferometer in a Silicon Nitride Platform

Student Paper

Jonas Leuermann[1,2,*], Alejandro Sánchez-Postigo[1], Adrian Fernandez-Gavela[3], Íñigo Molina-Fernandez[1,2] Laura M. Lechuga[4], Robert Halir[1,2]

[1] *Bionand Center for Nanomedicine and Biotechnology, Parque Tecnológico de Andalucía, 29590 Málaga, Spain*

[2] *Universidad de Málaga, Dept. de Ingeniería de Comunicaciones, ETSI Telecomunicación, Campus de Teatinos s/n, 29071 Málaga, Spain*

[3] *Universidad de Oviedo, Departamento de Física C/Federico García Lorca, 33007 Oviedo, Spain*

[4] *Nanobiosensors and Bioanalytical Applications Group. Catalan Institute of Nanoscience and Nanotechnology (ICN2), CSIC, BIST and CIBER-BBN. Campus UAB. 08193Bellaterra, Barcelona, Spain.*

[*] *Corresponding author: jleuermann@bionand.es*

ABSTRACT

Integrated photonics enables sensitive and label-free optical biosensors for the detection of chemical and biological substances and is therefore promising for future lab-on-chip solutions. In this article we present our current development of silicon nitride based integrated photonic biosensing devices working at telecom wavelengths. Our approach of three-port based interferometric sensing circumvents the issues of conventional Mach-Zehnder interferometers, providing a constant sensitivity, and allowing to use a fixed wavelength sensing scheme. Preliminary experimental results show that the fabricated devices work as expected from simulations.

Keywords: photonic biosensor, silicon-nitride, three-port Mach-Zehnder interferometer, refractive index sensing, phase detection

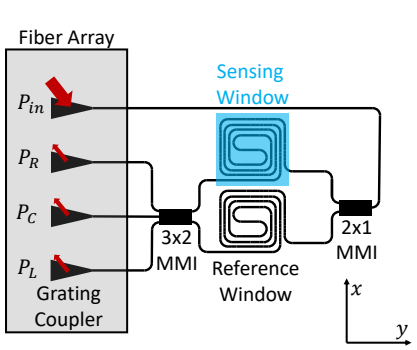
1 MOTIVATION

Integrated optical sensors, based on the interaction of the waveguide mode with the analyte, are promising candidates for lab-on-chip platforms, because they offer label-free detection, high sensitivity and low production costs [1], particularly when implemented with silicon based materials [2]. In the silicon-on-insulator (SOI) platform and at telecom wavelengths, interferometric sensors have recently been shown to achieve limits of detection below 10^{-7} refractive index units [3] when using optimized phase read-out techniques [4]. Compared to SOI, silicon-nitride waveguides offer the fundamental advantage that they remain transparent even at visible wavelength, where photo-damage to biological tissues and water absorption, which may ultimately limit sensitivity, are minimal [5]. Here we report on exploratory work on implementing advanced interferometric sensors in a silicon-nitride platform, working at telecom wavelengths as a first step to extend the operation into the visible regime.

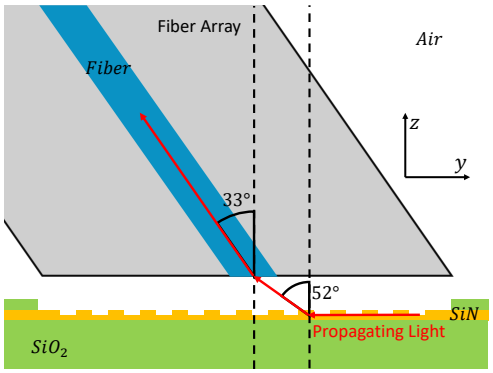
2 DESIGN

The complete sensing structure is shown schematically in Fig. 1(a). Light is coupled into the structure through a fiber array and split among the two interferometer arms with a 1x2 multimode interference coupler (MMI). Each arm consists of a spiraled waveguide, which is exposed to the analyte in the sensing arm, and covered in the reference arm. As light propagates through the sensing arm it interacts with the analyte deposited on the chip surface, thereby acquiring a phase shift with respect to the reference arm. In order to optimally detect this phase shift, light from both arms is recombined by a 2x3 MMI, which provides three output signals, shifted by 120° to each other, thereby avoiding the low sensitivity regions at the interferometric maxima and minima that arise in conventional Mach-Zehnder schemes [4]. This enables sensing without any wavelength sweeping, thus offering potentially low cost. The three output signals are coupled back to the fiber array, and can then be detected with photo-diodes. All elements were designed for TE (horizontal) polarization in $300\,\mathrm{nm}$ thick silicon nitride waveguides, with a refractive index of ~ 2.0 at telecom wavelengths. We briefly discuss the design of each element in the following.

Efficient and low cost light coupling is a key challenge for many integrated optical platforms. Surface grating couplers are widely used for this purpose, because they can be placed anywhere on the chip surface, and, due to their comparatively large size, offer relaxed alignment tolerances. Highly efficient grating couplers for the silicon nitride platform have been reported [6], but require complex dual etch structures with small feature



(a) Schematic of the sensing structure showing the gratings for coupling to a fiber array, the interferometer with the exposed sensing arm, and the 2x3 coupler for enhanced phase read-out.



(b) Illustration of the grating coupler angles. The grating radiates in an angle of around 52° in direction of the FA where it is coupled into the fiber mode according to Snell's Law at an angle of 33°. The FA is not drawn to scale.

Figure 1. Schematics of the sensing structure and the fiber-to-chip coupling solution.

sizes. Here, we designed a grating with one single shallow ($150\,\mu$m) etch step, and a period of $\Lambda = 2.1\,\mu$m with a duty cycle $DC = 50\%$, which greatly simplifies fabrication. This structure provides both minimized back reflections as well as a theoretical coupling efficiency to a standard fiber of around $-5\,$dB. The resulting radiation angle into air, measured from the surface normal, is $52°$. In order to place the fiber array close enough to the grating couplers (to avoid diffraction of the radiated beam), the fiber array has to be angle-polished. As shown in Fig. 1(b), the polishing angle is $\sim 33°$ to take into account Snell's law as the light beam couples from air into the fiber with refractive index 1.45.

The spirals forming the inteferometer should, in principle, be as long as possible to increase the interaction length of light with the analyte placed on the sensing arm. Keeping bending losses low is crucial to minimize the overall losses of the spirals. We found by simulation that a bending radius of $50\,\mu$m should yield negligible losses.

Finally, the dimensions of the multimode interference couplers were designed according to the procedure detailed in [7]. The 1x2 device used for equally splitting the power into the MZI arms is fully etched and has a footprint of $9\,\mu\text{m} \times 44\,\mu$m. The 2x3 MMI used for the recombination of the sensing and reference arm with $120°$ phase shift among the outputs, was also fully etched with a footprint of $13.5\,\mu\text{m} \times 264\,\mu$m.

3 FABRICATION

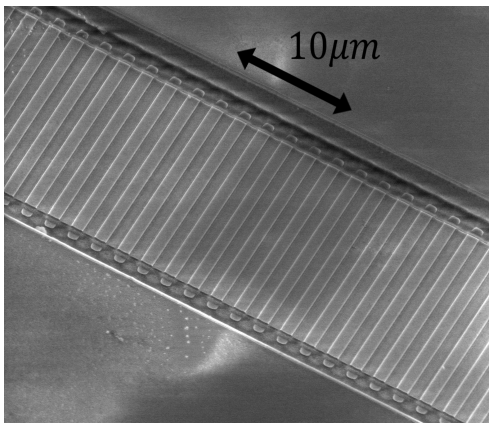
The sensing chip was fabricated at the Instituto de Microelectrónica de Barcelona, Centro Nacional de Microelectrónica (IMB-CNM), CSIC [8] through a Multi Project Wafer approach offered by VLC photonics. The $300\,$nm thick silicon nitride layer was fully etched to define the single-mode waveguides, while a shallow ($150\,$nm deep) etch was employed for the fiber-to-chip grating couplers. The material surrounding the waveguides, the 1x2 and the 2x3 MMIs is silicon-dioxide (SiO_2), whereas for the gratings and sensing arms the SiO_2 cladding is removed by two additional dry etching steps, so that light propagating in the sensing arm is able to interact with the analyte on top of it. Fig. 2(a) shows a SEM picture of the fabricated grating coupler.

4 PRELIMINARY OPTICAL CHARACTERIZATION

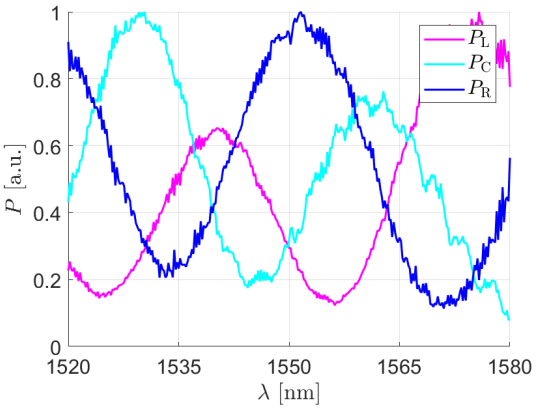
A preliminary characterization was carried out to verify the optical functionality of the chip. A tunable near infra-red laser source ($1520\,$nm to $1580\,$nm) is connected to a polarization controller, wherefrom light is coupled into a fiber array which is positioned above the grating couplers (see Fig. 1(a)). The polarization of the input light is adjusted to match the TE (horizontal) polarization state required for efficient coupling. The output fibers are attached to optical power meters.

First we measured four different test spirals with lengths ranging from $3\,$mm up to $21.5\,$mm, to estimate waveguide and bending losses. We found very low bending losses of $\sim 0.15\,\text{dB}/90°$ and $\sim 0.12\,\text{dB}/90°$ for curvature radii of $50\,\mu$m and $75\,\mu$m, respectively. Waveguide losses were found to be below $1.5\,\text{dB}/\text{cm}$ but could not be measured accurately with these test structures.

In a second experiment, the complete sensing structure as shown in Fig. 1(a) was measured, recording all three output ports (P_L, P_C, P_R) simultaneously, as the wavelength was swept. This causes a phase shift between the sensing and reference arm of the sensor, emulating a sensing experiment. The normalized measurements in Fig. 2(b) demonstrate that the three outputs show the expected sinusoidal behavior, with a phase shift of approximately $120°$ to each other.



(a) Scanning electron micrograph of the shallowly etched grating coupler.



(b) A wavelength swept measurement confirming the the chip provides the desired 120° phase shift between the three output signals of the interferometer.

Figure 2. Preliminary experimental results on the optical functionality of the chip.

5 CONCLUSIONS

The combination of SiN with a three-port phase read-out of the MZI is a promising approach for high sensitivity biosensing. We have designed, fabricated and experimentally demonstrated the optical functionality of the fabricated chips thereby paving the way for detailed sensing experiments which will be carried out in the near future.

ACKNOWLEDGMENT

This project has received funding from the European Union's Horizon 2020 research and innovation programme under the Marie Skłodowska-Curie grant agreement No 713721. We would like to acknowledge the Ministerio de Economía y Competitividad, Programa Estatal de Investigación, Desarrollo e Innovación Orientada a los Retos de la Sociedad (cofinanciado FEDER), Proyecto TEC2016-80718-R, the Ministerio de Educación, Cultura y Deporte (FPU14/06121), and the Universidad de Málaga. The NanoB2A is a consolidated research group of the Generalitat de Catalunya and has support from the Departament d'Universitats, Recerca i Societat de la Informació de la Generalitat de Catalunya (2014 SGR 624). The ICN2 is funded by the CERCA programne/Generalitat de Catalunya. ICN2 is supported by the Severo Ochoa programme of the Spanish Ministry of Economy, Industry and Competitiveness (MEIC, grant no. SEV-2013-0295). The views presented by the authors do not necessarily state or reflect the opinions of the aforementioned institutions. The authors and executors are not responsible for any use that may be made of the information in this article.

REFERENCES

[1] X. Fan, I. M. White, S. I. Shopova, H. Zhu, J. D. Suter, and Y. Sun, "Sensitive optical biosensors for unlabeled targets: a review," Analytica Chimica Acta, vol. 620, issues 1-2, pp. 8–26, Jul. 2008

[2] A. F. Gavela, D. G. García, J. C. Ramirez and L. M. Lechuga, "Last advances in silicon-based optical biosensors," Sensors, 2016, 16, 285.

[3] R. J. J. van Gulik, B. M. de Boer, and P. J. Harmsma, "Refractive index sensing using a three-port interferometer and comparison with ring resonators," IEEE Journal of Selected Topics in Quantum Electronics, vol. 23, no. 2, pp. 433-439, March-April 2017.

[4] R. Halir, L. Vivien, X. Le Roux, D. X. Xu, and P. Cheben, "Direct and sensitive phase readout for integrated waveguide sensors," IEEE Photonics Journal, vol. 5, no. 4, pp. 6800906-6800906, Aug. 2013.

[5] A. Z. Subramanian, E. Ryckeboer, A. Dhakal, F. Peyskens, A. Malik, B. Kuyken, H. Zhao, S. Pathak, A. Ruocco, A. De Groote, P. Wuytens, D. Martens, F. Leo, W. Xie, U. D. Dave, M. Muneeb, P. Van Dorpe, J. Van Campenhout, W. Bogaerts, P. Bienstman, N. Le Thomas, D. Van Thourhout, Z. Hens, G. Roelkens, and R. Baets, "Silicon and silicon nitride photonic circuits for spectroscopic sensing on-a-chip [invited]," Photon. Res. 3, B47-B59, 2015

[6] Y. Chen, T. D. Bucio, A. Z. Khokhar, M. Banakar, K. Grabska, F. Y. Gardes, R. Halir, I. Molina-Fernández, P. Cheben, and J. He, "Experimental demonstration of an apodized-imaging chip-fiber grating coupler for Si3N4 waveguides", Optics Letters, vol. 42, no. 18, pp. 3566-3569, 2017

[7] R. Halir, I. Molina-Fernández, A. Ortega-Moñux, J. G. Wangüemert-Pérez, D. Xu, P. Cheben, and S. Janz, "A design procedure for high-performance, rib-waveguide-based multimode interference couplers in silicon-on-insulator," J. Lightwave Technol. 26, 2928-2936, 2008

[8] Further information available at: http://www.imb-cnm.csic.es/index.php/en/clean-room/silicon-nitride-technology

Ultra-compact label-free silicon-nanoantenna-based optofluidic microflow cytometer with a high signal-to-noise ratio

(Student Paper)

Sergio Lechago[1], Carlos García-Meca[1], Amadeu Griol[1], Javier Martí[1]
[1] *Nanophotonics Technology Center, Universitat Politènica de València, c/ Camino de Vera s/n – 46022, Valencia - Spain*
Tel: +34963877000, Fax: +34963877827, e-mail: serlecbu@ntc.upv.es

ABSTRACT

Flow cytometry currently represents a fundamental source of progress in biomedical research and chemical diagnosis, opening new means in the treatment of diseases such as AIDS or cancer. Via this technique, flows of live cells or biotargets can be dynamically analysed via the use of optical- or impedance-based devices. In this work, an ultra-compact microflow cytometer enabled by on-chip silicon photonic antennas with an enhanced signal-to-noise ratio (SNR) is designed and experimentally demonstrated. The authors previously employed the design of these all-silicon integrated nanoantennas, allowing the realization of an optofluidic lab-on-a-chip sensor. Going a step further, here, we developed an enhanced version of this system, focusing our efforts on improving the SNR of a target in several angular positions. We find an optimal receiving angle with SNR figures higher than 14 dB, which not only overcomes our previous scheme by more than 10 dB, but also competes with the best state-of-the-art on-chip implementations, yielding the most compact footprint demonstrated so far.

Keywords: Lab-on-a-chip Devices, Integrated Optics, Nanoantenna, Sensing, Silicon Photonics.

1. INTRODUCTION

Flow cytometry allows the rapid and simultaneous analysis of multiple parameters of live cells in aqueous solutions as they flow in a stream via optical or electric signals. As mentioned before, this technique has become an essential tool in cell sorting and analysis with a notable impact in the biomedical and chemical fields. However, traditional top bench flow cytometers are expensive devices and require the presence of trained personnel in their use, implying additional indirect costs. Moreover, traditional flow cytometers demand large amounts of expensive reagents and solutions, with non-trivial post-processing steps, feature that entails high maintenance costs [1]. Along this line, lab-on-a-chip technology has arisen as a promising alternative for reducing both the cost and the bulky implementations of traditional biomedical equipment [2]. Most of the current approaches to on-chip microflow cytometry are based on the use of optical- or impedance-based technology [1, 3], as mentioned before. While both schemes offer valuable and complementary information [3], impedance-based systems present some disadvantages as compared to optical ones. For instance, an impedance-based multiparametric analysis can only be performed by using alternating electric currents with different frequencies, requiring external equipment [4]. In contrast, this can be achieved with optical cytometers just by scanning different angles at a single frequency. The integration of electrodes into the microfluidic channel, typical in these schemes, also increases the cost and complexity of the device as compared to optical approaches [1]. Those are the main reasons why most of the current approaches to on-chip microflow cytometry are based on optofluidic devices [1]. Within the optical approach, fluorescence-based flow cytometry has proved its suitability to identify and classify biotargets. However label-free systems -as those based on scattering biotarget analysis- are currently preferred [5], as they avoid the cost, time, and the use of fluorescent biomarkers that could potentially damage the analyte.

In this paper, we propose a novel antenna-based approach -able to radiate sharp beams thanks to its high directivity- that avoids the use of non-compact structures such as fibres or microlenses, usually in the mm-scale, to illuminate the targets and collect the scattered light, commonly used at previous lab-on-a-chip designs [1]. Thus, we get rid of the previously mentioned bulky structures enabling an ultra-compact on-chip nanoantenna-based optical subsystem ($0.64 \times 14\ \mu m^2$ for a single nanoantenna) able to yield the most compact implementation of microflow cytometers demonstrated so far. Moreover, this reduced footprint, together with the fact that the proposed structures can be fabricated using standard CMOS-compatible silicon-on-insulator (SOI) technology, shows the low-cost nature of this approach. This scheme provides a notable advance in portability, fabrication automation and cost reduction not only respect to standard top bench cytometers but also to previous integrated approaches [1]. Outstandingly, thanks to the high-directive nature of the nanoantennas, we can achieve an enhanced SNR in the target detection as passing in front of the emitting antenna regarding our previous design [6], also rendering a very low coefficient of variation (CV) for specific angular directions. All designs and experiments were carried out at the wavelength $\lambda = 1550$ nm, for the target illumination.

2. THEORY AND SIMULATIONS

The main building block of our microflow cytometer is an all-silicon highly-directive photonic nanoantenna. Specifically, we used the antennas proposed in [6], which are based on open-ended strip waveguides. The directivity of these structures was modelled via the Huygens' principle (typically used in classic antenna theory [7]) to achieve sharp radiation beams in the fluidic channel. In the final configuration of the microflow cytometer we use an antenna consisting of a transition from a standard 450-nm-width 220-nm-height strip silicon wire to a 150-nm-width silicon tip through an inverted taper, which already achieves a directivity as high as 54 (linear units), see Figure 1A. Several additional elements (the so-called directors) were placed in front of the antenna to further improve its directivity [6]. Figure 1A additionally shows the impact of the number of directors on the antenna directivity. In Figure 1B, the final configuration of the antenna and the directors is depicted.

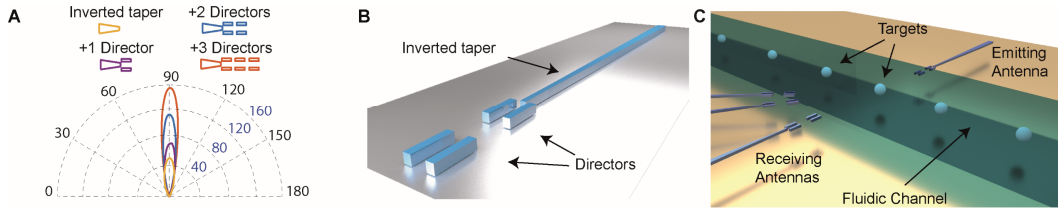


Figure 1. A) Polar directivity diagram of the designed antennas as a function of the number of directors. Blue numbers represent the directivity. B) Artwork displaying the final antenna and two directors used for the experimental microflow cytometer. A 2-µm thick layer of SiO_2 covered the antennas in the simulations and experiments. C) Scheme of the proposed microflow cytometer based on the use of the designed antennas.

A given particle scatters light differently in each direction when illuminated by a light beam, providing a traceable time-dependent pulse shape. Therefore, the power intensity detected by the receiving antenna depends on the angle at which it is placed. The goal of this work was to optimize this angle in order to maximize the SNR in the target detection. To this end, we simulated the power received in a set of antennas placed at different angular directions, which were normalised to the power received in the baseline configuration (i.e., that in which there is no particle in the channel between antennas). To design the system, we used a similar arrangement to that employed in [6], which is made up by an emitting antenna, a 10-µm-wide 4-µm-deep fluidic channel filled with an aqueous solution where the particles flow and the aforementioned set of receiving antennas, see Figure 1C. Following this previous experiment, we used the system to explore the scattered-power signature of polystyrene microspheres with a diameter of 2 µm. Polystyrene beads were placed in the middle of the microfluidic channel (x-direction), while different positions in the flowing direction (y-axis) were considered, see Figure 2A.

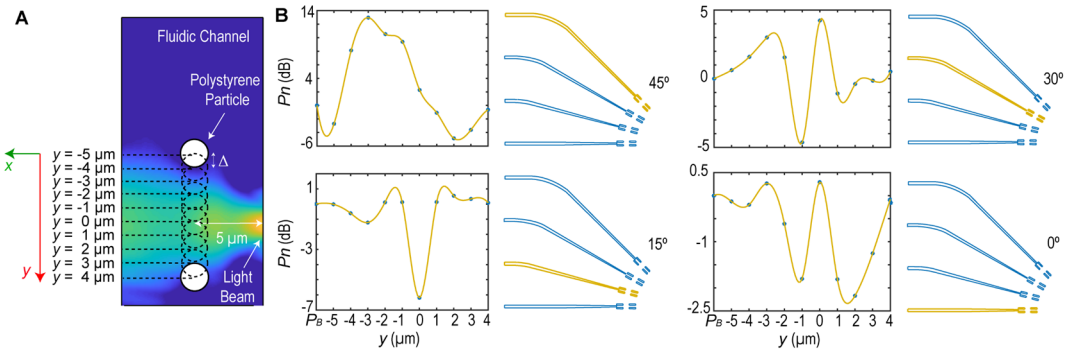


Figure 2. A) Schematic top view of a microfluidic channel where a polystyrene bead is flowing. The light beam radiated by the emitting antenna illuminates the targets (at the centre of the channel in the transverse or x-direction) for ten different longitudinal positions, from y = -5 µm to y = 4 µm, with steps of Δ = 1 µm. In an experiment, a flowing particle will be in a different position at each instant. B) The power scattered from the target at each position are retrieved for each receiving antenna. P_B accounts for the power of the baseline configuration when no targets are within the channel. $P_n = 10 \cdot \log10(P/P_B)$, where P represents the power value of a target measured in a specific position.

As can be seen in Figure 2B, there are different and characteristic pulses depending on the direction from which the scattered field of the particle is retrieved. Clearly, the better SNR was attained for the 30º and 45º directions, with an amplitude of 8 dB for the former and an outstanding 17-dB figure for the latter.

3. EXPERIMENTAL MEASUREMENTS

Taking into account the previous discussion, we conducted an experiment to demonstrate the sensing ability of the proposed antenna-based microflow cytometer. In our final device, the wireless deployment is made up of the highly-directive emitting antenna considered above and two other identical antennas measuring the scattered field

at 30º and 45º (the angles for which a better numerical SNR was obtained), see Figure 3A. To build the fluidic subsystem, a 10-µm-wide 4-µm-deep trench was directly opened in the SiO_2 region in between the antennas. This subsystem is completed with the incorporation of two inlet and outlet reservoirs, where the solutions containing the microparticles (10 µl volume, concentration of 0.1 % solids) are drop cast with a precision micropipette. The two receiving antennas located at 30º and 45º simultaneously measured the characteristic time-dependant scattered-field pulses of these microspheres as passing in front of the emitting antenna. On the 45º direction, a well-defined pulse is displayed when the target is detected, see Figure 3B, yielding figures of SNR as high as 14 dB. Outstandingly, there is and almost qualitative and quantitative perfect agreement between the simulations (where 17-dB SNR pulses were retrieved) and the experimental results. Additionally, we calculated the experimental CV at both directions, yielding values of 28.17 % and 6.64 % in the 45º and 30º directions, respectively. This last figure (at 30º) represents a record regarding the reported CV for previous microflow cytometers where the light signal is retrieved on-chip.

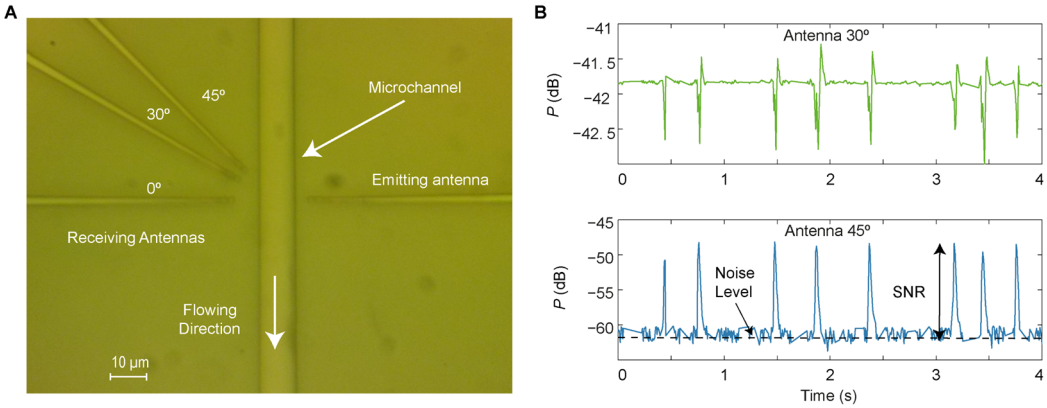


Figure 3. A) Optical microscope image of the fabricated microflow cytometer. B) Power efficiency (P) simultaneously measured at 30º and 45º during a four-second interval. In this case, P = 10·log10 (PRX/PTX), where PTX is the power injected to the emitting antenna, and PRX is the power retrieved at the receiving antennas. Very similar pulse shapes are measured if compared with those calculated numerically (Figure 2). The SNR level at the 45º configuration also matches the results anticipated by the simulations.

4. CONCLUSIONS

In this work, we have experimentally demonstrated the realization of an on-chip silicon photonic antenna-based microflow cytometer with a notably improved SNR in the target detection regarding our previous scheme [6], yielding figures as high as 14dB. Outstandingly, this design is achieved with a dramatically reduced footprint (0.64 ×14 µm^2 for a single antenna), as compared with current state-of-the-art approaches [1]. The combination of this antenna-based photonic subsystem together with integrated microfluidic deployment, paves the way towards the realization of cost-effective lab-on-a-chip flow cytometers and POC sensing devices with a direct impact for biological, chemical and medical diagnosis.

ACKNOWLEDGEMENTS

We acknowledge support from the Spanish Ministry of Economy and Competiveness under project TEC2015-73581-JIN (AEI/FEDER, UE).

REFERENCES

[1] Y.S. Zhang *et al.*: Optofluidic device based microflow cytometers for particle/cell detection: a review, *Micromachines*, vol. 6, 70, Apr. 2016.

[2] D. Psaltis, S.R. Quake, C. Yang: Developing optofluidic technology through the fusion of microfluidics and optics. *Nature*, vol. 442, pp. 381-386, Jul. 2006.

[3] K.C. Cheung *et al.*: Microfluidic Impedance-Based Flow Cytometry. *Cytom. Part. A*, vol. 77A, pp. 648-666, Jul. 2005.

[4] K.C. Cheung, S. Gawad, P. Renaud: Impedance Spectroscopy Flow Cytometry: On-Chip Label-Free Cell Differentiation. *Cytom. Part. A*, vol. 65A, pp. 124-132, Jun. 2005.

[5] T. Blasi *et al.*: Label-free cell cycle analysis for high-throughput imaging flow cytometry. *Nat. Comms.*, vol. 7, 10256, Jan. 2016.

[6] C. García-Meca *et al.*: On-chip wireless silicon photonics: from reconfigurable interconnects to lab-on-chip devices, *Light Sci. Appl.*, vol. 6, e17053, Sept. 2017.

[7] C.A. Balanis: Aperture Antennas, in *Antenna Theory: Analysis and Design*. 3rd Ed., New York: Wiley, 2005.

Nanoscopy-on-a-chip: high-throughput super-resolution imaging

(Invited paper)

Øystein Ivar Helle[1], David Andre Coucheron[1], Jean-Claude Tinguely[1], Firehun Tsige Dullo[1], Cristina Ionica Øie[1,2] and Balpreet Singh Ahluwalia[1]*

[1] Department of Physics and Technology, UiT, The Arctic University of Norway, Klokkargådsbakken N-9019, Tromsø, Norway

[2] Department of Medical Biology, UiT – The Arctic University of Norway, Tromsø, N-9019, Tromsø, Norway

Tel: +77645185, e-mail: balpreet.singh.ahluwalia@uit.no

ABSTRACT

Fluorescence based super-resolution optical microscopy, commonly referred to as optical nanoscopy, enables visualization of nanoscale biological events and structures in living cells. Although optical nanoscopy offers unprecedented opportunities, the widespread adoption of nanoscopy is presently hindered by system-complexity, high-cost, lack of multi-modality and slow imaging speed of present nanoscopy techniques.

Here, we report chip-based nanoscopy (CbN). To achieve super-resolution, our main idea consists in taking the generation, the steering and the delivery of the laser illumination pattern from the microscope and transferring it to the photonic chips. Using the principle of single molecule localization, we demonstrate CbN with a resolution of 50 nm. Furthermore, wedemonstrate the capability of CbN to acquire super-resolved images over millimetre field-of-view scale; a 100-fold increase in imaging area as compared to other nanoscopy solutions.

The waveguide platform has been developed using high-refractive index material such as silicon nitride (Si_3N_4) and tantalum pentoxide (Ta_2O_5). High-index contrast materials enable tight confinement of the light inside the waveguide, allowing for ultra-compact waveguide structures with small footprint benefitting from high intensity in the evanescent field.

Keywords: Optical nanoscopy, super-resolution microscopy, bio-imaging, silicon nitride, tantalum pentoxide

1. INTRODUCTION

Fluorescence based optical microscopy has emerged as a vital tool in modern bio-medical imaging and diagnosis[1-3]. Different labelling strategies allow high specificity towards the enabling fluorescence microscopes to generate images with excellent signal to noise ratio and high specificity. However, the optical resolution of the fluorescence microscopy is limited due to the diffraction limit, i.e. around 200-250 nm and 500 nm along the lateral and the axial directions, respectively.

During the last decade, there has been a significant growth in the field of super-resolution optical microscopy [1-3] to image targets with resolution below the diffraction limit. The field is referred to as optical nanoscopy. Optical nanoscopy has revolutionized bio-imaging and provided insights into structures and phenomena that were previously only accessible with electron microscopy on fixed specimens. The methods of optical nanoscopy include techniques such as structured illumination microscopy (SIM), stimulated emission depletion microscopy (STED); single molecule localization microscopy (SMLM) techniques such as photo-activated localization microscopy (PALM), and (*direct*) stochastic optical reconstruction microscopy ((*d*)STORM); and fluctuation based optical nanoscopy techniques such as super-resolution optical fluctuation imaging (SOFI), multiple signal classification algorithm (MUSICAL), and entropy-based super-resolution imaging (ESI).

SMLM and STED provide the best resolution (20-50 nm), but they are slow and require special dyes. SIM is a wide-field technique, thus faster, works with common dyes, and is suitable for imaging of live cells. However, SIM provides optical resolution only upto 100 nm with a practical speed is in the range of 0.1-1 Hz, which is much slower than the imaging speed of commonly used diffraction-limited live cell microscopy (up to 300 Hz).

Chip-based nanoscopy (CbN): In optical nanoscopy, the illumination path is as important as the detection path in order to provide images of high quality. One of the main tricks behind breaking the optical diffraction limit is to tailor the laser illumination pattern and emission collection. Conventional optical nanoscopy techniques use a complex microscope for imaging and a simple glass slide solely to hold the sample. Here, we report the inverse configuration: a complex but mass-producible photonic chip (optical waveguides) to both hold the sample and generate and deliver the illumination pattern needed to acquire super-resolved images, and a standard optical microscope to acquire a super-resolved image.

2. Development of the waveguide chip platform

The waveguide platform should be optimized for the visible wavelengths (405-780 nm) for optical nanoscopy. It is desirable to use a material having low propagation losses**,** low absorption and low auto-fluorescence at visible wavelengths. The *d*STORM [3] rely on most of the fluorophores to be forced into long-lived dark states, where

only sub-sets are allowed to return to the fluorescent state resulting in blinking of the fluorescent molecules. When the blinking is sufficiently sparse, a high-resolution image can be built up over several thousand individual sub-sets (individual images). The *d*STORM technique requires a high intensity evanescent field of around 1-10 kW/cm^2. The high intensity is required to enable blinking of the fluorophores, a key requirement in SMLM. We employ thin (150-200 nm) optical waveguide made of high-refractive index contrast (HIC) materials such as silicon nitride (Si_3N_4) [4] and tantalum pentoxide (Ta_2O_5) [5] to achieve such high power intensities. For such a waveguide, up to 10-15% of the guided power can be then made available in the evanescent field.

When single mode conditions are required, we employed shallow rib geometry, i.e. 2-4 nm etched rib heights out of a total height of 150 nm [4]. Multimode waveguides do not directly provide homogeneous illumination on the surface due of interference between several guided modes inside the guiding layer. However, by oscillating the input-coupling beam combined with averaging the acquired image stacks helped to generate acceptable homogeneous illumination (around 15% intensity modulation). Strip geometry was employed in this work, with a waveguide width of 100-250 µm and total thickness of 150-220 nm.

3. Super-resolution imaging using chip-based nanoscopy platform

In chip-based nanoscopy, the generation of the illumination light (evanescent field) is independent of the collection objective lens, which gives several advantages compared over other nanoscopy systems. The experimental-setup is compact and stable; pre-aligned for easy multi-color imaging without additional optical alignment and mechanical adjustments; and simple changing of the magnification/imaging objective lens without influencing the illumination.

Figure 1 shows the experimental set-up that consists of an upright microscope, laser coupling unit and the photonic chip. The photonic chip is used as a substrate, and the laser light is coupled into the waveguide either through an objective lens or by using optical fiber. The cells are illuminated using the evanescent field present on top of the waveguide surface. The fluorescence light is collected using an upright microscope, fitted with several objective lenses of different magnification.

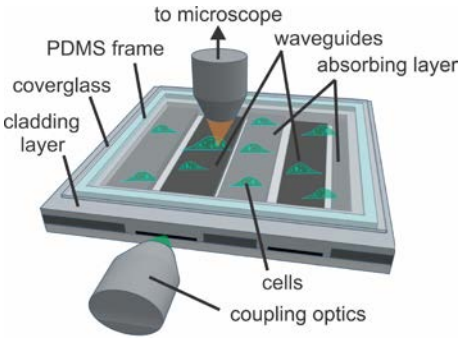


Figure 1 Experimental set-up of chip-based optical nanoscopy. The sample is placed directly on top of waveguide and is illuminated by the evanescent field. The optical waveguide is made of high refractive index contrast material. The fluorescence light from the waveguide surface is collected by an upright microscope.

The evanescent field decays exponentially from the waveguide surface, illuminating only a thin section of the cells (around 150 nm) close to the waveguide surface. The illumination from the waveguide-chip therefore enables total internal reflection fluorescence (TIRF) microscopy. Images acquired using chip-based TIRF microscopy are shown in Figure 2. Liver sinusoidal endothelial cells (LSECs) were seeded directly on top of the photonic-chips and stained with fluorescent dyes. The cells were fixed on the chips and first imaged at low magnification (4x) to locate isolated specimens and to find regions of interest (top image of Figure 2A). Once the region of interest was found, imaging of the fluorophores was done with a higher resolution objective at three different wavelengths, 488 nm, 561 nm and 660 nm (cell membrane in green, actin in blue, and proteins undergoing endocytosis in red – bottom image of Figure 2B). The chip-based TIRF microscopy decouples the illumination and the collection light path, allowing changing the magnification of the imaging objective lens without altering the TIRF illumination generated by the optical waveguide, as shown in Figure 2. The optical waveguide platform supports multiplexing, i.e. generation of TIRF illumination for different wavelengths without the need of additional optical components or adjustments to the set-up.

Figure 3 shows chip-based nanoscopy using *d*STORM principle [6] on LSECs. Figure 3a shows diffraction-limited TIRF image and Figure 3b shows *d*STORM image, both acquired using the waveguide-chip platform. The LSECs possess a unique structure on its membrane, nano-sized holes (50-200 nm) commonly referred to as fenestrations. The size of fenestration is below the diffraction limit (200 nm). The fenestration is therefore not visualized using diffraction limited TIRF microscopy but can be imaged using chip-based *d*STORM. A high numerical aperture and high magnification objective lens (60x/NA1.2) is used in Figure 3. As the evanescent

field is present over the entire surface of the optical waveguide, TIRF illumination can be achieved over large surface areas by simply using a wide optical waveguide (e.g. 200-500 µm). Recently, chip-based *d*STORM using a 20x/NA0.45 objective lens was shown capable of imaging field-of-view of 0.5x0.5 mm^2 covering more than 50 cells with a resolution of 140 nm [6].

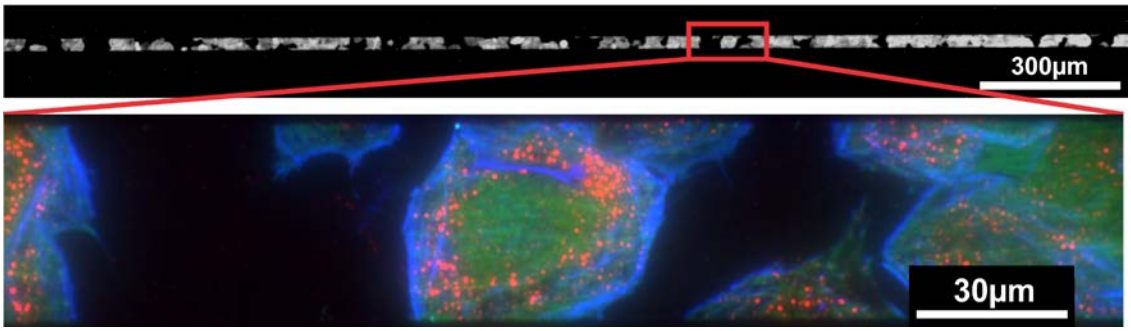


Figure 2 Chip-based TIRF microscopy of liver sinusoidal endothelial cells (LSECs). The top image is acquired using an objective lens with 4X magnification and bottom image is acquired using an objective lens with 60X magnification. A low magnification objective lens is used to scan large areas. As evanescent field is generated by the waveguide, the imaging objective lens can simply be changed without altering the illumination light path. Staining represents: plasma membrane (in green), actin (in blue), and an endocytosed protein (in red)

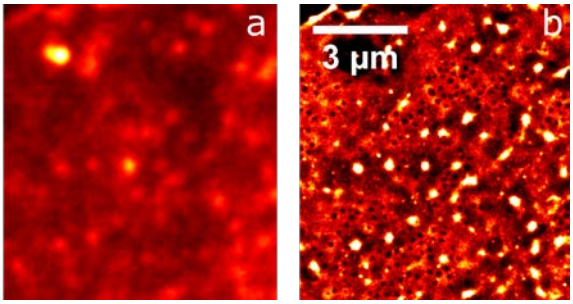


Figure 3 a) Chip-based TIRF and (b) chip-based dSTORM of liver sinusoidal endothelial cells (LSECs).

4. CONCLUSIONS

The Photonic-chip offers great miniaturization of versatile sets of design to shape and control optical beams that can be barely engineered with conventional far-field optics. Development of nanoscopy using waveguide chips opens a new research activity in bio-imaging, as the chip-platform can easily be integrated (retrofit) into conventional microscopes. In addition, CbN can enable integration of multiple nanoscopy modalities onto a single waveguide-chip using a standard microscope. The compatibility of CbN with optical fibre components will enable easy wavelength multiplexing and an alignment-free illumination light path. In addition CbN is shown to surpass the technical capabilities of present day optical nanoscopy in terms of large field-of-view, high-throughput imaging and simplicity. Development of on-chip TIRF microscopy and optical nanoscopy is flexible towards future integration with other integrated photonic-chip based functions such as on-chip sensing, spectroscopy [7], and particle tracking and trapping [8].

ACKNOWLEDGEMENTS

B.S.A acknowledges the funding from the European Research Council, (project number 336716).

REFERENCES

[1] Lothar S. et.al, “A guide to super-resolution fluorescence microscopy”, J. *Cell Biol*, **190**, 165, 2010.
[2] Betzig, E. et al. Imaging intracellular fluorescent proteins at nanometer resolution. Science 313, 1642-1645, (2006).
[3] Hell, S. W. & Wichmann, J. Breaking the diffraction resolution limit by stimulated emission: stimulated-emission-depletion fluorescence microscopy”, *Opt Lett* **19**, 780-782 (1994).
[4] J-C Tinguely et al., “Silicon nitride waveguide platform for fluorescent microscopy of living cells“, Optics Express **25 (22)**, 27678-27690 (2007)
[5] Ahluwalia, B. S. *et al.* Fabrication of submicrometer high refractive index Tantalum Pentoxide waveguidesfor optical propulsion of microparticles. *IEEE Photonics Technology Letters* **21**, 1408-1410 (2009).
[6] R. Diekmann et al., “Chip-based wide field-of-view nanoscopy”, Nature Photonics **11**, 322 (2017)
[7] Pål Løvhaugen, Balpreet Singh Ahluwalia, Thomas R. Huser, and Olav Gaute Hellesø, "Serial Raman spectroscopy of particles trapped on a waveguide," Opt. Express **21**, 2964-2970 (2013)
[8] Helle, Ø. I., et.al. Optical transport, lifting and trapping of micro-particles by planar waveguides. *Opt Express* **23**, 6601-6612 (2015).

Single-chip Electronic-Photonic SoCs in a 45nm High-Volume CMOS Foundry: A Platform for Next-Generation Integrated Optics

Mark Wade
Ayar Labs, Inc., Emeryville, CA - USA
e-mail: mark@ayarlabs.com

ABSTRACT

Driven by relentless increases in high-performance ASICs (switches, GPUs, CPUs, DRAM, etc.), the electrical I/O roadmap is nearing its end, and the ASIC industry is looking for a ubiquitous replacement to electrical I/O escaping chip packages. To meet such demands, a photonics technology with massive bandwidth density, high energy efficiency, and low cost must be used. These requirements necessitate unprecedented levels of integration between electronics and photonics and require rethinking traditional communication architectures. In this talk, I will present a new class of optical devices integrated directly into a high-volume 300mm 45nm SOI CMOS process and how these devices enable new SoC's to solve the bandwidth bottleneck in the ASIC industry. Examples include a 400Gbps microring-based DWDM transmitter, a low latency RapidIO optical engine, and the first CPU chip with optical I/O.

Printed active hybrid photonic crystal devices for 3D integrated photonics

(Invited paper)

Weidong Zhou
[1] *University of Texas at Arlington, Arlington, Texas, USA*
Tel: +0018172721227, e-mail: wzhou@uta.edu

ABSTRACT

Free-space coupled membrane photonic devices are highly desirable for 3D integrated photonics, free space communications, imaging, sensing, and ranging applications. [1] Based on transfer printing processes, heterogeneously integrated active photonic crystal devices can be built on the common silicon platform. [2] In this talk, I will review progresses made on photonic crystal based lasers, modulators, and related high quality factor resonant structures. [3-6] The progresses towards emerging low dimensional 2D materials for active devices will also be reported.

Keywords: Lasers, silicon photonics, integrated photonics, optical interconnect, free-space communications, hybrid integration.

Selected references

[1] W. Zhou, D. Zhao, Y.-C. Shuai, H. Yang, S. Chuwongin, A. Chadha, *et al.*, "Progress in 2D photonic crystal Fano resonance photonics," *Progress in Quantum Electronics*, vol. 38, pp. 1-74, 2014.

[2] B. Corbett, R. Loi, W. Zhou, D. Liu, and Z. Ma, "Transfer print techniques for heterogeneous integration of photonic components," *Progress in Quantum Electronics*, 2017.

[3] H. Yang, D. Zhao, S. Chuwongin, J.-H. Seo, W. Yang, Y. Shuai, *et al.*, "Transfer-printed stacked nanomembrane lasers on silicon," *Nature Photonics*, vol. 6, pp. 615-620, 2012.

[4] D. Zhao, S. Liu, H. Yang, Z. Ma, C. Reuterskiöld-Hedlund, M. Hammar, *et al.*, "Printed Large-Area Single-Mode Photonic Crystal Bandedge Surface-Emitting Lasers on Silicon," *Scientific reports*, vol. 6, 2016.

[5] Y.-C. Shuai, D. Zhao, Y. Liu, C. Stambaugh, J. Lawall, and W. Zhou, "Coupled Bilayer Photonic Crystal Slab Electro-Optic Spatial Light Modulators," *IEEE Photonics Journal*, vol. 9, pp. 1-11, 2017.

[6] Y. Liu, W. Zhou, and Y. Sun, "Optical Refractive Index Sensing Based on High-Q Bound States in the Continuum in Free-Space Coupled Photonic Crystal Slabs," *Sensors*, vol. 17, p. 1861, 2017.

Silicon Nitride Tunable Directional Coupler for programmable waveguide meshes

Daniel Pérez[1], Erica Sánchez[1], D. Doménech[2], P. Muñoz[1,2] & José Capmany[1,2]
[1] Universitat Politècnica de València (UPV), *c/ Camino de Vera s/n – 46022, Valencia - Spain*
e-mail:dapelo2@iteam.upv.es
[2] VLC Photonics S.L, *c/ Camino de Vera s/n – 46022, Valencia - Spain*

ABSTRACT

Emerging programmable multifunctional integrated photonic circuits rely on different topologies of waveguide mesh arrangements of beamsplitters with additional phase shifting capabilities. The optimization of these basic units is essential to increase the versatility, performance and potential scalability of photonic signal processing structures. In this paper, we propose and experimentally demonstrate a thermally-tuned photonic directional coupler in a silicon nitride platform. The trade-offs of this approach and their potential impact is addressed.

Keywords: integrated photonics, programmable photonics, optical switches.

1. INTRODUCTION

During the last 30 years, photonic integrated circuits (PICs) have been shown for a wide range of applications. Most of the devices are specifically designed, manufactured and, in some cases, packaged to perform one single application. However, a new generation of programmable PICs proposes a paradigm shift where a common hardware structure is configured to enable multifunctional designs that potentially offer more versatile cost-effective solutions and reduce the time-to market [1]-[5]. Most of them are based on arrangements of 2x2 beamsplitters with additional phase shifting capabilities allowing either only-forward [2,3], or both forward and backward signal propagation and routing [1,4,5].

All the proposed demonstrators rely on using balanced Mach-Zehnder Interferometers (MZIs) closed by 3-dB couplers as their Tunable Basic Unit (TBU), offering wideband operation but limiting the scalability of the circuit due to the accumulated insertion losses (IL). Optimizing the TBU by miniaturizing the basic delay and the IL is essential to achieve high-frequency operation as well as reducing the footprint of the circuit. However, in principle, the time-step resolution of the mesh and the total accumulated losses are both related to a miniaturization of the TBU, since for MZI-based TBU, losses are dominated by the two 3-dB beamsplitters, [5].

Recently, standalone Tunable Directional Couplers (TDC) have been demonstrated in polymer materials [6] and in Silicon on Insulator [7], providing a reconfigurable splitting ratio by adding a propagation constant difference in the pair of waveguides with a thermal-tuner on top of one of the parallel waveguides. In this paper, we propose a Tunable Directional Coupler (TDC), which is able as a TBU providing both the beamsplitting and the additional phase shifting capabilities by inducing a differential and common phase shift, respectively. As a proof-of-concept, the thermally-tuned device is integrated in a silicon nitride platform and we analyse the potential benefits and weaknesses when acting in waveguide mesh arrangements.

2. PROGRAMMABLE WAVEGUIDE -MESH ARRANGEMENTS

In a similar way to the operating mode of electronic Field Programmable Gate Arrays, programmable photonic integrated circuits can be configured by discretising conventional circuits into a previously fabricated waveguide mesh arrangement of TBUs. By configuring each TBU, constructive, destructive or intermedium interference can be achieved at each complementary output port, leading to the routing of the signal and the definition of the circuit topology and design parameters. Figure 1 illustrates different combinations and waveguide mesh topologies that have been proposed in the literature for this purpose. A common feature is that their demonstrators have employed balanced MZIs to implement the TBUs, either using multimode interference or directional couplers for the two required 3-dB couplers. These, limit the miniaturization of the TBU and dominate the total accumulated insertion losses for a defined path. With this approach, a programmed waveguide length containing N TBUs will always have $2N\ IL_{coupler}$ additional losses compared to that of a standard waveguide in the same integration platform.

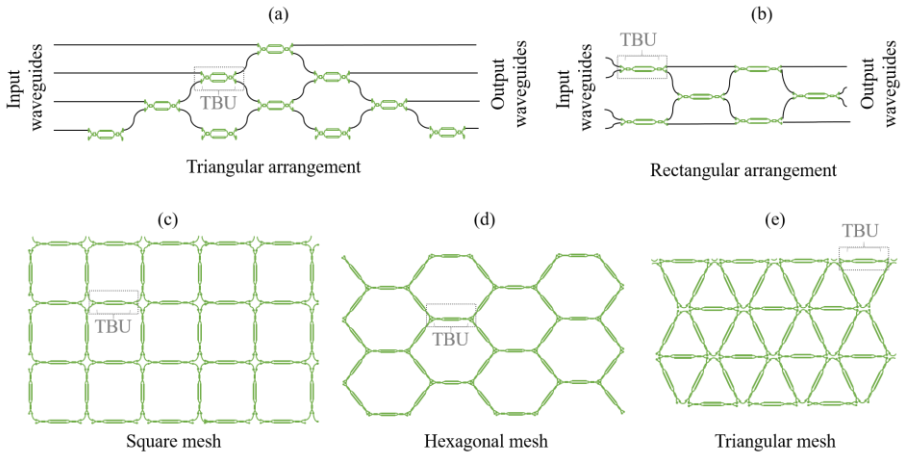


Figure 1. Different waveguide mesh arrangements of beamsplitters: (a)Triangular Feedforward [2], (b)Rectangular Feedforward [3], (c)Squared Feedforward/backward [4], (d)Hexagonal Feedforward/backward [1,5], (d) Triangular Feedforward/backward [1].

3. TUNABLE DIRECTIONAL COUPLER

The directional coupler is one of the most employed building block present at any PIC. The signal of one waveguide is transferred to a parallel waveguide if they are close enough to partially couple their signal field distribution. At a certain length, *Lc*, the signal is transferred totally from the first waveguide to the second one. However, this structure suffers from fabrication errors that change the designed wavelength of operation. As demonstrated in [6,7], a change in the propagation constant difference between waveguide 1 and 2 origins a change in the amplitude splitting ratio of the device (*K*), defined as the optical power ratio coupled to the cross port.

While by employing one phase shifter in one of the waveguides produces a differential phase shift that changes the amplitude splitting ratio, an additional common phase shift will keep constant the value of *K* while adding an independent common phase shift if required. This common phase shift is essential for implementing tunable optical filters, waveguide mesh arrangements and for correcting errors during fabrication. As an example, Figure 2a illustrates a possible implementation of a hexagonal waveguide mesh employing tunable directional couplers as their TBU. Figure 2b describes the structure topology and Figure 2c the different splitting ratios.

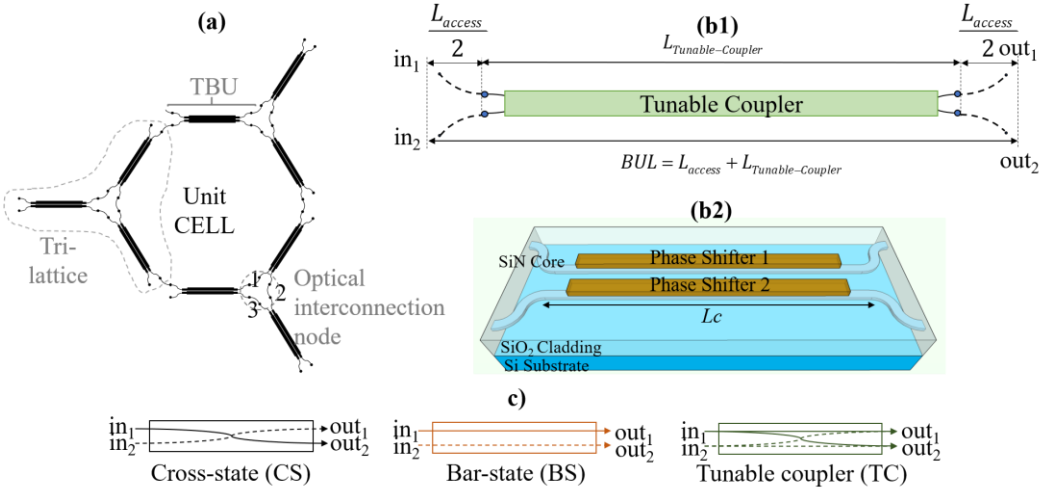


Figure 2. (a) Labelled Hexagonal waveguide-mesh cell, (b1) Tunable Basic Unit definition, (b2) Tunable Directional Coupler illustration, (c) modes of operation representing different splitting ratios.

For the experimental demonstration, we have designed and fabricated under a Multi Project Wafer (MPW) run offered by the Centro Nacional de Microelectronica (CNM) and VLC Photonics a standalone Tunable Directional Coupler in a silicon nitride platform. For the measurements we employed a tunable laser sweeping from 1520 to 1620 nm, followed by a polarization controller before accessing the chip by means of lensed fibres. The data was acquired by an optical spectrum analyser for each programmed electrical power value.

In this case, a single-mode waveguide of 1 µm width and 300 nm height was employed to propagate a TE field. As illustrated in Figure 3a (crossection inset), the gap between the waveguides (*g*) was set to 1.5 µm, leading to a

theoretical total coupling length of 717 µm. However, we decided to increase the final coupler length *L* to 1235 µm to increase the safety of the thermal tuners before proceeding to an optimization round. For the phase shifters, we exploited the thermo-optic effect. For the metal layer, a distance between heaters *(d)* of 2 µm was considered. The optical crosstalk was kept between 15-21 dB for the cross and bar operations while obtaining a bandwidth > 5 nm for a ±2% uniformity. The *total excess loss* was negligible and estimated to be under 0.1 dB. Figure 3b illustrates the change of *K* versus applied electrical current at four different wavelengths.
For this particular proof of concept device, the power consumption needed for the coupling factor reconfigurability from 1 to 0 is greater than in a MZI approach if a thermal tuning mechanism is employed (i.e we measured a power consumption of 270 mW for the MZI approach and 460 mW for the TDC approach in the same integration platform). The reason behind this is the proximity of the two waveguides and the resulting unoptimized thermal crosstalk that impacts more seriously the common rather than the differential phase shift. However, if the structure is optimized accordingly changing *d* and *g*, the electrical power consumption can be considerably reduced [6,7]. Moreover, this concept can be exploited with alternative tuning mechanisms like electromechanical, piezoelectrical or electrooptical effects. Furthermore, a lot of publications aims to increase the fabrication failure tolerance and bandwidth of directional couplers by optimizing the waveguides geometries. With the state-of-the-art, TDCs with phase shifting capabilities of less than 700 µm and 100 µm in silicon nitride and silicon on insulator platforms could be achieved, respectively, which represent more than a three-fold decrement with respect to the MZI-based TBU approaches.

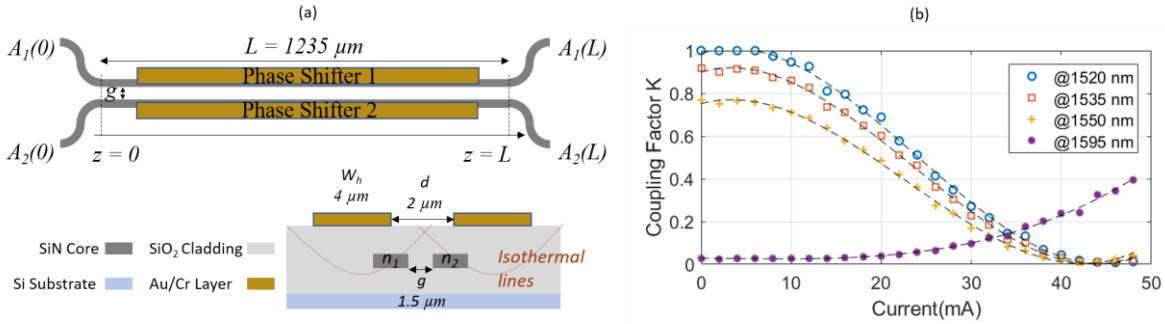


Figure 3. (a) Schematic topview of the fabricated tunable directional coupler and labelled crossection where d represents the distance between the metal layers and g the distance between the waveguides. (b) Experimental results of the tunable directional coupler coupling factor versus current applied to one of the phase shifters for different wavelengths. A cubic fitting is added for each trace (dashed).

4. CONCLUSIONS

We have proposed a new photonic 2x2 building block that allows both beam-splitting and phase shifting of light in a compact design, based on inferring a differential and common phase shift to each waveguide of conventional directional couplers. Once optimized, this component represents a promising TBU alternative for programmable waveguide meshes and for conventional PICs.

ACKNOWLEDGEMENTS

This research was supported by the ERC Adv. Grant 741415 UMWP-CHIP, the COST Action CA16220 EUWMP, the Spanish MINECO Projects TEC2014-60378-C2-1-R and the Gen. Valenciana PROMETEO Project 2017/103. Authors specially acknowledge C. Domínguez from the Centro Nacional de Microelectronica for the access to the Multi Project Wafer (MPW) run.

REFERENCES

[1] D. Pérez, I. Gasulla, J. Capmany, and R. A. Soref: Reconfigurable lattice mesh designs for programmable photonic processors, *Optics Express*, vol. 24, pp. 12093-12106, 2016.
[2] M. Reck, A. Zeilinger, H. J. Bernstein, and P. Bertani: Experimental realization of any discrete unitary operator, *Phys. Rev. Lett.* vol. 73, pp. 58–61, 1994.
[3] W.R. Clements, P.C. Humphreys, B.J. Metcalf, W.S. Kolthammer and I.A. Walsmley: Optimal design for universal multiport interferometers, *Optica*, vol. 3, pp. 1460–1465, 2016.
[4] L. Zhuang et al.: Programmable photonic signal processor chip for radiofrequency applications, *Optica*, vol. 2, pp. 854-859, 2015.
[5] D. Perez, et al.: "Multipurpose silicon photonics signal processor core, *Nat. Commun*., vol. 8, n. 636, 2017.
[6] A. S. M. Supa'at: Implementation of thermo-optic waveguide photonics switch using polymer material, *in IEEE ICP 2013*, Melaka, Malaysia, Oct. 2013.
[7] P. Orlandi, et al.: Tunable silicon photonics directional coupler driven by a transverse temperature gradient, in *Optics Letters*, vol. 38, n.6, pp. 863-865, 2013.

Analysis of the Operation of an Integrated Unidirectional Phase Modulator

T. T. M. van Schaijk, D. Lenstra, K. A. Williams and E. A. J. M. Bente
Eindhoven University of Technology, Den Dolech 2, 5612AZ Eindhoven, The Netherlands
Tel: +31402473728, Email: p.v.schaijk@tue.nl

ABSTRACT

In this paper we present a model and experimental verification of a unidirectional phase modulator realised in InP. We show that non-linearity in the phase-voltage dependance of the electro-refractive modulators has to be taken into account. It limits the isolation that can be obtained using the device and it introduces modulation on the forward propagating wave. Finally we derive minimum requirements for the electrical driving signals that allow operation of the unidirectional phase modulator close to this optimal performance such that its performance is limited by non-linearity only. In this way, we find for our device a maximum tolerable imbalance in modulation amplitude of $2\,\%$, a phase error of $0.18°$ and an error in the summed modulation amplitude of the two driving signals of $2.8\,\%$. These values are feasible with current electronics.

Keywords: integrated isolator, optical isolator, unidirectional phase modulator, photonic integration

1 INTRODUCTION

Many optical circuits require a strong optical isolator to prevent the deleterious effects on the performance of the system that are caused by light that is reflected back into the circuit. Most notably optical isolators are used to protect lasers from external optical feedback (EOF), requiring as much as $60\,\mathrm{dB}$ isolation. Deployed photonic circuits require isolation against reflections and optical disturbances from outside the chip. It has proven difficult to achieve strong isolation in a monolithically integrated platform using magneto-optic effects [1], mainly because the required magnetically active materials strongly attenuate the light and are often incompatible with clean room processes used for fabricating photonic integrated circuits (PICs).

A different approach to realizing an integrated isolator using directionally dependent properties of tandem sinusoidally driven phase modulators is presented in [2]. The tandem phase modulators we shall refer to as a unidirectional phase modulator (UPM) and are schematically depicted in Fig. 1. Combining the UPM with a spectral filter yields a significant difference in directionally dependent loss for light of a single optical frequency, e.g. as from a single mode laser. Using this approach, [2] demonstrated $10.8\,\mathrm{dB}$ of isolation. This is insufficient to protect lasers from strong EOF when the isolator is placed in series with the laser. However, we have predicted that this amount of isolation can be used within an integrated, unidirectional ring laser to create greatly enhanced reflection tolerance [3]. In such a laser, the performance of the UPM, when integrated into the laser cavity, has a big impact on quality of the emitted laser light. It is therefore important to characterize the performance of the UPM in detail and derive its optimal parameters for operation.

2 UPM MODEL AND VERIFICATION

We start our model with the description of individual InP-based ridge wave guide phase modulators. Then the model is extended to two modulators. Each phase modulator is implemented using a voltage controlled electro-refractive modulator (ERM) and is modeled as a time-dependent, non-linear, local variation of the refractive index that is a function of the applied voltage. Non-linear effects are taken into account up to second order.

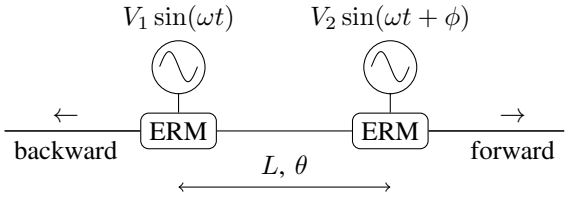


Figure 1. Schematic representation of a UPM consisting of two tandem ERMs. Both modulators are driven by an RF signal with potentially different amplitude and at a phase difference ϕ. The modulators are spaced by a distance L. Due to the finite group velocity, the electrical signal has gained $\theta \equiv \omega L / v_g$ phase while the light is traveling this distance.

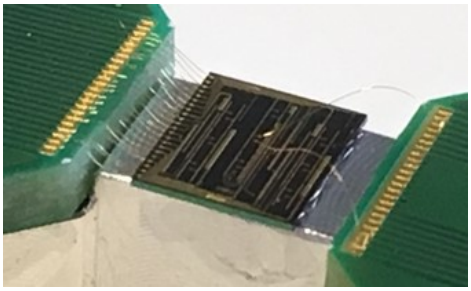


Figure 2. Photograph of the fabricated PIC which contains a number of devices among which the UPM presented here. The structure connected to the PCB on the right is the UPM described in this paper.

Residual amplitude modulation (RAM) is assumed to scale linearly with refractive index modulation. On the fabricated PIC both modulators are positioned $300\,\mu\mathrm{m}$ apart, so their characteristics are assumed to be identical.

The electrical signals driving the ERMs are assumed to have the same frequency. In practice this assumption can be satisfied relatively easily if both electrical signals are derived from the same source or from two phase locked sources. As can be seen in Fig. 1, there is a phase difference ϕ between the driving signals and there is a length L of waveguide separating the two ERMs. It takes the light a finite amount of time to travel between these two modulators and therefore the time at which the light is modulated is different for each modulator. We assume the waveguide separating the ERMs has no effect on the light other than the time delay. This allows us to model both ERMs as if they are located at the same physical location by introducing an additional effective phase delay $\theta \equiv \pm\omega L/v_g$ which is positive for light propagating in the forward direction and negative for light propagating in the backward direction. We model the complete UPM as the sum of two ERMs driven by sinusoidal voltages with phase difference $\psi \equiv \phi + \theta$, which is dependent on the propagation direction of the light. This direction dependence is the effect that is used to ultimately obtain isolation using the UPM and it is therefore crucial to its operation.

From the effective modulation of the refractive index follows the phase modulation amplitude $2\pi L n(t)/\lambda$ where $n(t)$ is the change in refractive index at time t and λ is the wavelength of the light. The phase modulation amplitudes imposed by both modulators are called A_1 and A_2 respectively. From this we define the average modulation amplitude $A \equiv (A_1 + A_2)/2$, the modulation imbalance $\alpha \equiv (A_1 - A_2)/(A_1 + A_2)$, the proportionality constant for RAM γ and the proportionality constant for non-linearity β. It can be shown that the modulated spectrum is a frequency comb with peaks spaced at the electrical frequency ω. The intensity of the comb lines depend on the properties of the UPM and its driving signals and is found as

$$P_k \equiv P\left|\sum_{m=-\infty}^{\infty} i^m J_{k-2m}(B_1) J_m(B_2) \exp\left((k-2m)\Psi_1 + m\Psi_2\right)\right|^2 \tag{1}$$

where

$$B_1 \equiv A(1-j\gamma)\sqrt{2+2\alpha^2+2(1-\alpha^2)\cos\psi}, \tag{2}$$

$$B_2 \equiv -\frac{1}{2}A(1-j\gamma)\beta\sqrt{2+2\alpha^2+2(1-\alpha^2)\cos(2\psi)}, \tag{3}$$

$$\tan\Psi_m \equiv \frac{(1-\alpha)\sin m\psi}{(1+\alpha)+(1-\alpha)\cos m\psi} \tag{4}$$

represent the effective first and second order modulation amplitudes and the effective modulation phase respectively, P is the input power and k denotes the order of the side band as counted from the center.

3 EXPERIMENTAL VERIFICATION

Our model was verified using a UPM that was manufactured in the SMART photonics InP based platform [4] and that is shown in Fig. 2. The ERMs were deeply etched, had a length of $1\,\mathrm{mm}$ and were separated by deeply-etched waveguide such that the spacing of their centers was $L = 4167\,\mu\mathrm{m}$. This optimizes operation for $5\,\mathrm{GHz}$. In the experiments, the ERMs were connected to two signal generators via bond wires, a PCB and coaxial cables. Two signal generators were phase-locked to each other with a controllable RF phase difference ϕ. The electrical modulation frequency ω corresponded to $3.5\,\mathrm{GHz}$ because of limitations in the transmission of the electrical connections. The output from a tunable laser (HP 81940A) set at $1550\,\mathrm{nm}$ and $10\,\mathrm{mW}$ was coupled into the PIC via a lensed fibre and was sent through the UPM. The comb generated by the UPM was measured using an optical spectrum analyser with $20\,\mathrm{MHz}$ resolution (APEX 2641-B).

In the experiments the ERMs were biased at $-6\,\mathrm{V}$. One of the signal generators was set at a modulation amplitude of $3.2\,\mathrm{Vp}$, while the other was swept from $2.1\,\mathrm{Vp}$ to $3.2\,\mathrm{Vp}$ in steps of $0.16\,\mathrm{Vp}$. Subsequently the second modulator was kept at $3.2\,\mathrm{Vp}$ while the other was swept in amplitude. For each set of modulation amplitudes the phase difference between the signal generators was swept over 360° in steps of 10°. Finally, the whole procedure was performed four additional times to determine the non-systematic errors. Fig. 3 shows the mean and standard deviation of the measured values as error bars for two settings of the modulation amplitude. The solid line in this figure shows the result of a fit of the modeling parameters to all experimental data simultaneously. Very good agreement is obtained, validating the model.

4 REQUIREMENTS ON ELECTRICAL DRIVING SIGNALS

The model allows one to study the effects of the electrical signals driving the ERMs on the performance of the UPM. Non-linearity in the phase response of the ERMs mainly influences the suppression of the central band of a backward propagating wave, as well as the power in the even side bands for a forward propagating wave. It can be neglected for other properties of the UPM.

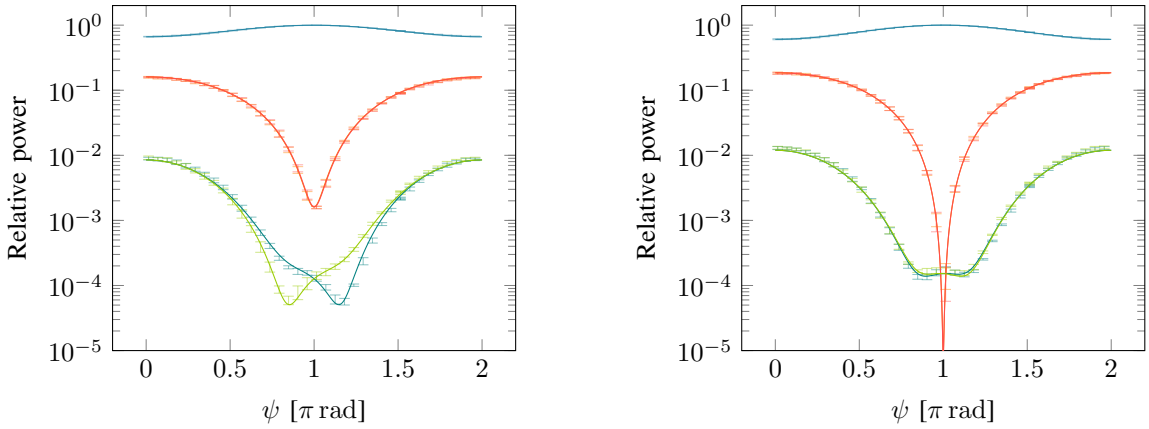


Figure 3. Relative intensity of the sidebands as measured at the output of the UPM as a function of the effective phase difference for $\alpha = -0.09$ (left) and $\alpha = 0.005$ (right). The sidebands are centered at the optical input frequency and spaced by the electrical driving frequency. Sidebands $-2, \ldots, 2$ are presented in green, orange, blue, red and cyan respectively. The error bars indicate the mean and standard deviation of the experimental data, the solid line is the fitted data. Our model captures the characteristics of the UPM very well as can be seen from the good fit.

From our experiment, we find that non-linearity limits isolation to approximately $26\,\mathrm{dB}$, taking all other values optimal. Allowing other effects to reduce this number by $1\,\mathrm{dB}$ we find a maximum tolerable imbalance in the modulation amplitudes of both ERMs of $\alpha = 0.02$, a maximum error in the phase difference of $\psi = 0.18°$ and a maximum error in the modulation amplitude of $A = 2.5\,\%$ or $1.46°$ at the optimum modulation amplitude.

For the forward direction Fig. 3 shows that non-linearity in the ERMs causes second order side bands at approximately $-40\,\mathrm{dB}$. For optimal isolation the ERMs need to be driven at a higher voltage, increasing these sidebands to approximately $-24\,\mathrm{dB}$. We take this value as the maximum allowable power for the first order side bands. From (1) and using $B_2 = 0$, we find a requirement on the modulation amplitude for light propagating in the forward direction, which is satisfied if $A\sqrt{2 + 2\alpha^2 + 2(1-\alpha^2)\cos\psi} < 0.13\,\mathrm{rad}$. From this we find the maximum tolerable modulation imbalance $\alpha < 0.054$ and the maximum tolerable error in the electrical phase difference ψ of $6.2°$. Any error in A does not affect the first order side bands up to a first order approximation.

5 CONCLUSION

A UPM was fabricated and characterized and a phenomenological model was derived to describe the performance of the UPM. Very good agreement was found between the experimental data and the model. It was shown that non-linearity in the phase transfer function of the ERMs limits the isolation that can be achieved using such a UPM as well as the maximum suppression of side bands generated in the forward propagating light. We derived minimum requirements on the electrical driving signals that do not deteriorate the isolation and the level of the generated side bands by more than $1\,\mathrm{dB}$ and find that these requirements can be met using current electronics. The UPM presented here can thus be used in combination with a filter to form an integrated optical isolator.

REFERENCES

[1] B. J. H. Stadler and T. Mizumoto, "Integrated magneto-optical materials and isolators: a review," IEEE Photon. J. **6**, 1–15 (2014).

[2] C. R. Doerr, N. Dupuis, and L. Zhang, "Optical isolator using two tandem phase modulators," Opt. Lett. **36**, 4293–4295 (2011).

[3] T. T. M. van Schaijk, D. Lenstra, E. A. J. M. Bente, and K. A. Williams, "Theoretical analysis of a feedback insensitive semiconductor ring laser using weak intracavity isolation," IEEE J. Sel. Topics Quantum Electron. **24**, no. 1 (2018).

[4] L. M. Augustin *et al.*, "InP-based generic foundry platform for photonic integrated circuits," IEEE J. Sel. Topics Quantum Electron. **24**, no. 1 (2018).

Low loss transmission lines in COBRA generic photonic integration platform

Marija Trajkovic[1], Fabrice Blache[2], Helene Debregeas[2], Xaveer Leijtens[1], Kevin Williams[1]
[1]Eindhoven University of Technology, *Institute for Photonic Integration (previously COBRA research center), 5600 MB Eindhoven, the Netherlands*
Tel: +33182720455, e-mail: m.trajkovic@tue.nl
[2]III-V Lab, *joint laboratory between Nokia Bell Labs, Thales Research and Technology, and CEA Leti Campus de Polytechnique, 1 avenue Augustin Fresnel, 91767 Palaiseau-Cedex, France*

ABSTRACT

Delivering unperturbed radio-frequency signal to the components on densely packed photonic integrated chip is an important aspect for circuits needed to operate at high bit rates. Efficient, low-loss routing of a high-speed electrical signal from the driver to the photonic chip can be a challenge. Therefore, the design of transmission lines for intra-chip connection, with low microwave loss and matched characteristic impedance to the rest of the circuit is important. We have characterized transmission lines on two different substrates, n-InP doped and semi-insulating. Low-loss transmission lines in the COBRA generic integration platform are fabricated and measured up to 65 GHz.

Keywords: transmission line, radio-frequency, n-doped substrate, semi-insulating substrate, microwave loss, characteristic impedance

1. INTRODUCTION

The integration of a large number of optical components on a single chip is currently one of the main research objectives for data communications and networking applications. Radio-frequency (RF) propagation on photonic integrated circuits (PICs) has received substantial attention with the bandwidth scaling up. The use of on-chip transmission lines enables important design freedom for highly integrated PICs [1]. Keeping the electrical losses low and the characteristic impedance (Z_C) of the lines matched to the driver input ensures efficient propagation of the electrical signals. As most commercially-available, broad-bandwidth drivers are standardized to 50 Ω, it is desired that the on-chip lines have the same value.

Providing electrical signals to components on a photonic chip is often done via bond pads placed at the edge of the chip. However, with increasing component densities, also the distance of some components to the edge of the chip is increasing. To bridge the distance, electronic interconnects are needed, but especially for RF-components, this may degrade the signal quality.

The properties of the substrate play a key role in this degradation, as it determines the microwave loss of transmission lines and the parasitic capacitance of access pads [2]. A doped substrate is preferred when it comes to biasing lasers and modulators, as it offers straightforward current/voltage application. However, it introduces more losses for the radio-frequency signal. We investigated different designs of transmission lines in the COBRA generic integration platform [3], on n-doped and semi-insulating (SI) substrate, demonstrating very low losses in a large frequency range for the SI-substrate.

2. TRANSMISSION LINE DESIGN

An ideal transmission line is an interconnect whose conductors are perfect with zero resistance and a lossless dielectric. In this scenario, a voltage at the input of the ideal transmission line would propagate without distortion or attenuation [4]. However, in reality each type of transmission line exhibits a certain attenuation, yet depending on its type this can be minimized.

Two types are mostly in use: microstrip line due to its simple fabrication, and coplanar waveguide (CPW) exhibiting lower losses as the mode propagates partly in air. The corresponding electro-magnetic field is shown in Figure 1. The microstrip mode is confined between the upper metal line and the highly doped n-InP substrate acting as a conductor, $\varepsilon_r = 12.5$, while the CPW mode is propagating between the metals on top of the dielectric, $\varepsilon_r = 3.5$, and partially in the air. Design parameters for microstrip line are signal width (w) and dielectric height (h) and for CPW line are signal width (w) and signal-ground separation (g), as indicated in Figure 1. In order to realize the CPW transmission line, the signal-ground separation needs to be smaller than the height of the dielectric. This is not always possible due to fabrication limitations, therefore we examine transmission line design on two different substrates, aiming at low-losses and matched characteristic impedance at 25 GHz operation.



Figure 1: Microstrip (left) and coplanar waveguide (right) transmission line behaviour, with the important parameters for their design.

2.1 N-doped substrate

For a n-doped substrate in the COBRA platform, the transmission line acts as a microstrip line, as the condition $g < h$ cannot be satisfied due to fabrication limitations. In the COBRA platform, the nominal height of the polyimide is $h = 2 \pm 0.5$ μm, depending on the position on the wafer and neighbouring topology. We examine the influence of this tolerance on the characteristic impedance, shown in in Figure 2 [5]. We observe that for a change of ± 0.5 μm, Z_C changes by ± 5 Ω. Aiming at $Z_C = 50$ Ω and fixing the polyimide height at 2 μm, the signal width needs to be as narrow as 4 μm. However, this value is dependent on the exact dielectric height.

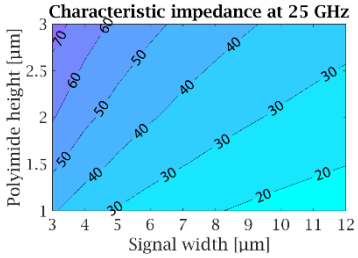


Figure 2: Microstrip line characteristic impedance dependence on w *and* h *at 25 GHz.*

Another problem which exists with the doped substrate is the high parasitic capacitance of the access pad. The design of the access pad is made in ground-signal-ground (GSG) configuration, in order to transfer the ground plane via wire bonds to the photonic chip and to allow direct on-chip measurements with RF probes. For a pad of 60×60μm^2, the value of pad capacitance is about 60 pF and can limit the bandwidth of the photonic components.

2.2 Semi-insulating substrate

In order to solve the problem of the access pad parasitic capacitance, we have also designed the transmission lines on semi-insulating substrate. Elimination of the parasitic capacitance of the pad is solved by placing it directly onto the SI-substrate. As the line is placed on top of a polyimide (Figure 1), there is a transition between the pad and the transmission line, bringing the metal gradually from the substrate to the top of the polyimide layer.

The parameters which influence the characteristic impedance of the line are signal width (w) and signal-ground gap (g). Previous work on electro-refractive modulators in the COBRA platform has showed that for a combination of values w = 10 μm and g = 10 μm, the obtained loss was minimal and the characteristic impedance was around 30 Ω [6]. Here we examine slight variations of this case, having the same mask set for both n-doped and semi-insulating substrate. Keeping the gap constant at g = 10 μm, we change the signal width w = 4-10 μm to obtain the optimal performance for both substrates.

3. TRANSMISSION LINE CHARACTERIZATION

The fabrication on both substrates is done through the JePPIX foundry services [7]. We used a 2-port vector network analyser to obtain the scattering (S) parameters of the network. The ABCD de-embedding technique [8] allows us to extract parameters of the line: Z_C, losses and microwave propagation index. Transmission lines on 2 μm polyimide with a gap g = 10 μm and varying signal widths w were characterized. The extracted microwave loss and characteristic impedance are shown in Figure 3.

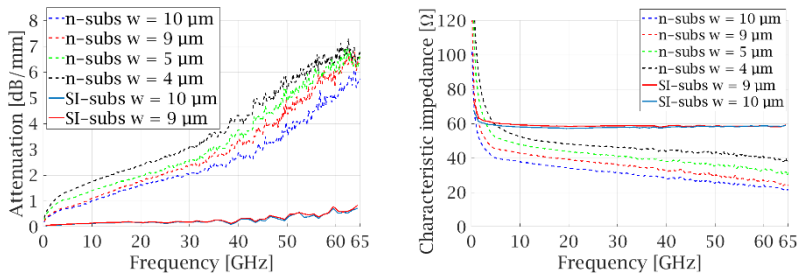


Figure 3: Extracted microwave loss (left) and characteristic impedance (right) of transmission lines on two different substrates from the measured S-parameters.

The microwave losses on n-doped substrate are 2-3 dB/mm at 25 GHz, rising up to 6-7 dB/mm at 65 GHz. Two origins are responsible for these losses: electrical loss, coming from the fact that the conductor is not perfect, and dielectric losses, as the mode is confined. With the frequency increase the microstrip line is

dispersive and the characteristic impedance is frequency dependent on n-substrate. For the microstrip line the characteristic impedance changes rapidly with the geometry change: varying w by 5 µm Z_C changes by 10 Ω.

The main advantage of the semi-insulating compared to the doped substrate is low microwave loss, as low as 0.2-0.6 dB/mm in the whole measured frequency range, for w = 10µm and g = 10 µm. This value is an order of magnitude lower than the one obtained for the doped substrate. Additionally, the characteristic impedance is independent of the frequency, and in our case is 58 Ω. In the interest of reaching exactly 50 Ω, the gap needs to be lowered.

Owing to low losses, transmission lines can be made long up to several mm, therefore facilitating the design of compact photonic circuits adding a level of freedom in placing the components anywhere on the chip, while maintaining the integrity of driving signal.

4. CONCLUSION

Transmission lines for intra-chip connection in COBRA generic integration platform have been designed, fabricated and characterized on two different type of substrate, n-doped and semi-insulating. The choice of substrate highly influences the performance of the high frequency signal on chip, as the electrical signal propagates differently.

In case of a doped substrate, the line behaves as a microstrip waveguide and the optimal value for loss is w = 10 µm and h = 2 µm in COBRA platform. Nevertheless, its characteristic impedance slightly depends on the frequency and the losses are 2 dB/mm at 25 GHz. On the other side, the transmission line on SI-substrate acts as a coplanar waveguide, with parameters w = 10 µm and g = 10 µm, showing as low as 0.2 dB/mm loss at 25 GHz.

Another important aspect of undoped substrate is the removal of the access pad parasitic capacitance. All of this together will allow more freedom in placing other building blocks in the platform which operate at high speed, as the introduction of a transmission line on SI-substrate will not degrade the transmitted electrical signal to the component.

ACKNOWLEDGEMENTS

The devices reported in this work were fabricated by Smart Photonics through the JePPIX.eu MPW service. The authors would like to thank the European Commission for partly funding this research through the Marie Curie GeTPICs project, funded under FP7-PEOPLE under grant agreement no 317316.

REFERENCES

[1] F. A. Kash et al, "Current Status of Large-Scale InP Photonic Integrated Circuits," *IEEE Journal of Selected Topics in Quantum Electronics*, vol. 17, no. 6, pp. 1470-1489, 2011.

[2] M. Trajkovic, W. Yao, H. Debregeas, K. A. Williams, and X. J. M. Leijtens, "High speed electroabsorption modulator in the generic photonic integration platform," in *20th Annual Symposium of the Benelux IEEE Photonics Society*, Brussels, Belgium, 2015.

[3] M. Smit et al, "An introduction to InP-based generic integration technology," *Journal Semiconductor Science and Technology*, no. 8, pp. 1-41, 2014.

[4] D. M. Pozar, Microwave Engineering, John Wiley & Sons, Inc., 1997.

[5] "Advanced Design System (ADS)," [Online]. Available: https://www.keysight.com/en/pc-1297113/advanced-design-system-ads?cc=FR&lc=fre.

[6] W. Yao, G. Gilardi, M. Smit, and M. J. Wale, "Microwave Modeling and Analysis of an InP based Phase Shifter from a Generic Foundry Process," in *18th Annual Symposium of the IEEE Photonics Society Benelux Chapter*, Eindhoven, the Netherlands, 2013.

[7] "JePPIX," [Online]. Available: http://www.jeppix.eu/.

[8] A. M. Mangan, S. P. Voinigescu, M. Yang, and M. Tazlauanu, "De-Embedding Transmission Line Measurements for Accurate Modeling of IC Designs," *IEEE Transactions on Electron Devices*, vol. 53, no. 2, pp. 235-241, 2006.

The heterogeneous future of integrated Millimeter- and Terahertz-wave photonics

(Invited paper)

Guillermo Carpintero[1], Robinson C. Guzmán[1], Mu Chieh Lo[1], Muhsin Ali[1], Alberto Zarzuelo[1], Luis Enrique García-Muñoz[1], Daniel Segovia[1], Elliott Brown[2], David de Felipe[3], Norbert Keil[3]

[1] *Universidad Carlos III de Madrid, Av. de la Universidad, 30 – 28911, Leganés, Madrid - Spain*
Tel: +34916249427, Fax: +34 916249430, e-mail: guiller@ing.uc3m.es
[2]*Wright State University, 3821 Colonel Glenn Hwy, Room 109, Dayton, OH 45435-0001 USA, email elliott.brown@wright.edu*
[3] *Fraunhofer Heinrich Hertz Institute, Photonics Components Department, Einsteinufer 37 – 10587 Berlin, Germany, email: david.felipe@hhi.fraunhofer.de*

ABSTRACT

High frequency generation using photonic techniques combines the best of two worlds, photonics with RF electronics. Photonic integration technology has been shown effective in order to reduce size and cost of this approach. More recently, heterogeneous integration is bringing the advantage of choosing the integration substrate material to optimize the performance of each components for the function that performs, instead of having to compromise the epitaxial structure of different components with different function.
Keywords: microwave photonics, THz signal generation, photonic integration

1. INTRODUCTION

Photonic techniques are leading the access to the millimetre (MMW) and Terahertz (THz) frequency bands of the electromagnetic spectrum, ranging from 30 GHz to 300 GHz and from 300 GHz to 3 THz respectively. Compared with electronics techniques, photonics offers a range of advantages, benefiting from the low loss of optical fibers to transport these frequencies over long distances and the extremely wide modulation bandwidth of photonic components. These are key requirements for beyond 5G wireless communications, which need access to broad bandwidth regions to meet the ever-increasing demand for higher data rates, available only at carrier wave frequencies above 275 GHz [1]. It has been recognized that integration and packaging technologies are among the future issues for MM-wave and THz-wave systems [2].

Among the different photonic schemes to continuous wave (CW) signal generation of frequencies within the Terahertz range, the most advantageous in terms of frequency tuning range is optical heterodyning. This scheme uses a dual wavelength source, emitting at two wavelengths λ_1 and λ_2, which are mixed on a photodiode or photoconductor to generate an electrical beat note with frequency given by the difference among the two wavelengths, $f_{beat} = c|\lambda_1 - \lambda_2|/(\lambda_1 \cdot \lambda_2)$. There have been different solutions being proposed to achieve a dual wavelength source, the simplest being combining the output of two single wavelength tunable lasers as shown in *Figure 1*. To date, the widest frequency tuning range was provided by complex and costly external-cavity diode lasers. A simpler approach uses thermal wavelength tuning of distributed feedback (DFB) lasers, which through the combination of multiple DFBs, a tuning range of 2750 GHz was achieved without gaps [3].

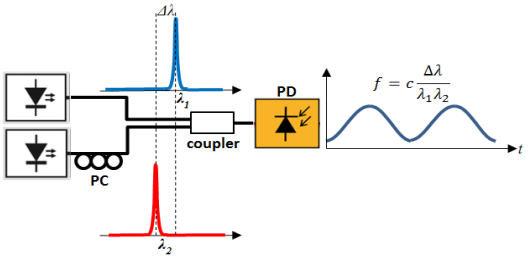


Figure 1. Photonic components required for the optical heterodyne signal generation scheme.

2. PHOTONIC-BASED INTEGRATED TERAHERTZ SIGNAL GENERATION

It is the common sense of photonic integration to use it whenever the number of components starts to increase, to keep size and cost at bay. Not being so numerous the number of components required for the optical

heterodyne signal generation technique, it turns that using photonic integration techniques produces significant improvements in the quality of the generated signal. The reason is that when fiber-based components are used (including optical fibers to interconnect them), the phase noise fluctuations in the generated signal are affected from changes in the optical path length difference between the lasers and the coupler due to temperature fluctuations or other external effects, such as vibrations [4]. In photonic signal generation applications, even moderate integration efforts have an impact on the quality of the signal. This is probably the main driver for the photonic integration efforts of photonic-based millimetre- and Terahertz wave signal generation, as placing all the critical components on the same chip will make them experience the same environmental fluctuations [5]. Additionally, photonic integration makes the optical heterodyne system more compact, which is advantageous to improve efficiency of delay sensitive feedback loops of noise reduction schemes.

We have already approach the integration of a photonic-based millimetre-wave transmitter module using Indium Phosphide (InP) monolithic integration. All the required components are grown on the same chip, including two DFB lasers, an optical wavelength combiner (a multimode-interference coupler), an electro-absorption modulator (EAM) for data, as well as various semiconductor optical amplifiers (SOA) to boost the optical signal through the chip, leading to a high-speed photodiode for wireless transmission [6]. We must highlight that this photonic chip enables to package a photonic-based signal generation system packaged in a module with electrical accesses only. Avoiding the need to assemble fiber optic accesses allows to decrease the packaging costs. In addition to the DC ports, the package includes an SMA connector for the input data signal towards the EAM and a WR-10 (75 GHz – 110 GHz) rectangular waveguide output to radiate the modulated millimetre-wave carrier wave signal. The advantage of placing all the components in the same substrate comes at the expense of making performance compromises to the components on the chip.

3. HETEROGENEOUS INTEGRATION PLATFORMS

To avoid the compromises among the different components, heterogeneous integration techniques must be employed. These enable using the principle of the 'best substrate for the function', which becomes advantageous when combining photonics with RF electronics.Recently, a similar chip to the monolithic integrated photonic-based millimetre-wave transmitter demonstrated on InP in [6] was demonstrated using a heterogeneously integrated silicon/InP integration technology [7]. This heterogeneous integration platform shows waveguide photodiodes with 65 GHz 3-dB bandwidth and 42 nm wavelenth tuning range lasers with lower than 150 kHz optical linewidth (one order of magnitude smaller than the DFB lasers). Recently, high speed uni-traveling carrier photodiode (UTC-PD) structures have been demonstrated on silicon using InP-based photonic membrane heterogeneous integration on silicon, with 3-dB bandwidth beyond 67 GHz with responsivity of 0.7 A/W [8].

A novel heterogeneous integration platform that we have demonstrated for photonic-based signal generation is the PolyBoard InP/Polymer heterogeneous photonic integration platform, developed by HHI's Hybrid PICs Group [9]. This platform offers hybrid InP/Polymer DBR tunable lasers comprising a 400 µm long InP gain element, and polymer thermo-optically tunable 200 µm long phase and 1000 µm long Bragg reflector sections as shown in *Figure 2(a).* Frequency tuning (wavelength shifting) can be achieved through current injection in the gain, or heating the phase and DBR sections. The widest tuning range, in excess of 34.6 nm (~4.3 THz), is achieved with the DBR grating tuning as shown in *Figure 2(b). Figure 3(a)* shows the tuning achieved through the gain and phase section, with different tuning sensitivity. It is worth to mention that the tuning steps are in the MHz range for the gain and in the GHz range for the phase. The beat note when the phase current section is varied from 16 mA down to 10 mA with a current step of 1 mA. Under this variation, the beat note frequency changed from 322 GHz to 337 GHz. It can be observed on *Figure 3(b)* that the wavelength step is not linear with the electrical current, as the tuning depends on thermal effects which are proportional to the electric power.

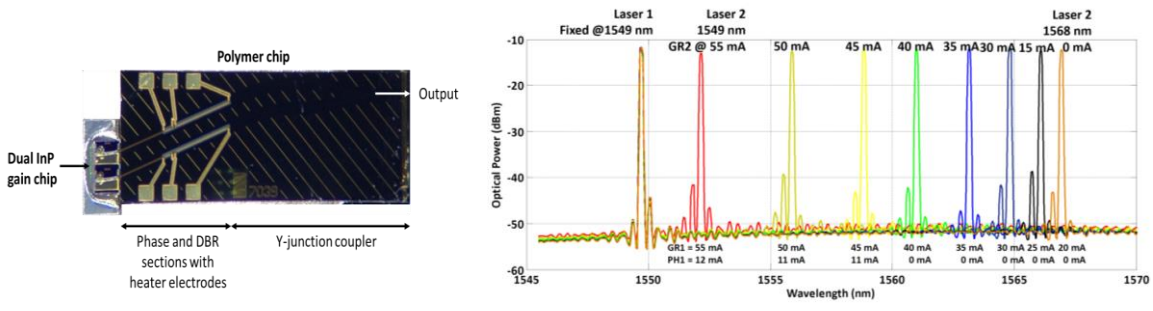


Figure 2. (a) Microscope photograph of the InP/Polymer chip, and (b) Wavelength tuning one InP polymer DBR laser varying the current injected into the DBR grating heater.

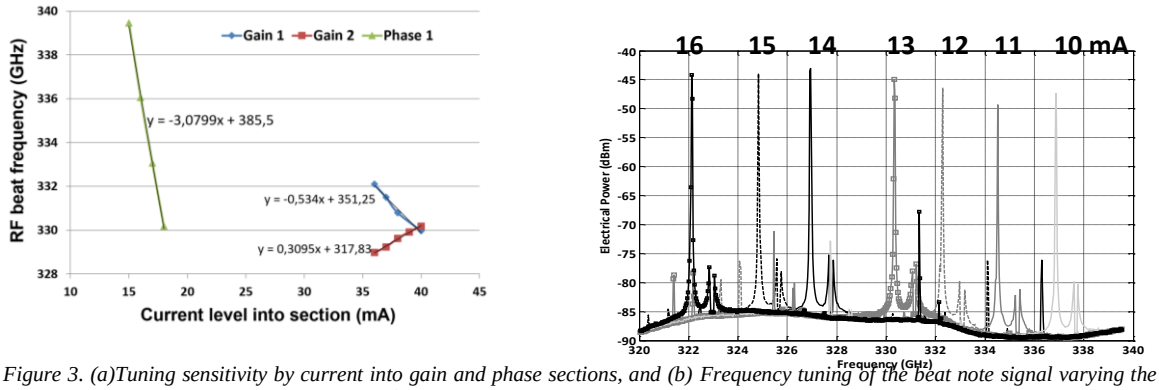


Figure 3. (a)Tuning sensitivity by current into gain and phase sections, and (b) Frequency tuning of the beat note signal varying the phase section heater current at 1 mA current steps, from 16 mA (322 GHz) down to 10 mA (337 GHz).

4. CONCLUSIONS

We present the potential of heterogeneous photonic integration technology for photonic-based signal generation, specially an InP/Polymer heterogeneous platform.

ACKNOWLEDGEMENTS

Universidad Carlos III de Madrid authors would like to acknowledge support from Spanish Ministerio de Economia y Competitividad thourgh Programa Estatal de Investigación, Desarrollo e Inovación Orientada a los Retos de la Sociedad thougth grant iTWIT, TEC2016-76997-C3-3-R.

REFERENCES

[1] H.-J. Song and T. Nagatsuma, “Present and future of terahertz communications,” IEEE Trans. Terahertz Science and Technology, vol. 1, pp. 256-263, 2011

[2] T. Nagatsuma, S. Hisatake, M. Fujita, H.H.N. Pham, K. Tsuruda, S. Kuwano, J. Terada "Millimeter-Wave and Terahertz-Wave Applications Enabled by Photonics," in *IEEE Journal of Quantum Electronics*, vol. 52, no. 1, pp. 1-12, 2016.

[3] A.J. Deninger, A. Roggenbuck, S. Schindler, S. Preu, “2.75 THz tuning with a triple-DFB laser system at 1550 nm and InGaAs photomixers” J Infrared Milli Terahz Waves, vol. 36, pp. 269-277, 2015

[4] T. Nagatsuma, H. Ito, and K. Iwatsuki “Generation of Low-phase Noise and Frequency-tunable Millimeter-/terahertz-waves Using Optical Heterodyning Techniques with Uni-traveling Carrier Photodiodes” Proceedings of the 36th European Microwave Conference, pp. 1103-1106, 2006.

[5] F. van Dijk, A. Accard, A. Enard, O. Drisse, D. Make, F. Lelarge “Monolithic dual wavelength DFB lasers for narrow linewidth heterodyne beat-note generation” 2011 International Topical Meeting on Microwave Photonics, pp. 73-76, 2011.

[6] G. Carpintero, K. Balakier, Z. Yang, R. C. Guzm’an, A. Corradi, A. Jimenez, G. Kervella, M. J. Fice, M. Lamponi, M. Chitoui, F. van Dijk, C. C. Renaud, A. Wonfor, E. A. J. M. Bente, R. V. Penty, I. H. White, and A. J. Seeds “Microwave photonic integrated circuits for millimeter-wave wireless communications,” J. Lightw. Technol., vol. 32, no. 20, pp. 3495–3501, 2014.

[7] J. Hulme, MJ Kennedy, R.L. Chao, L. Liang, T. Komljenovic, J.-W. Shi, B. Szafraniec, D. Baney, and J. E. Bowers, "Fully integrated microwave frequency synthesizer on heterogeneous silicon-III/V," Opt. Express 25, pp. 2422-2431, 2017.

[8] L. Shen, Y. Jiao, W. Yao, Z. Cao, J. P. van Engelen, G. Roelkens, M. K. Smit, and J. J. G. M. van der Tol, "High-bandwidth uni-traveling carrier waveguide photodetector on an InP-membrane-on-silicon platform," Opt. Express 24, 8290-8301, 2016.

[9] Z. Zhang, D. Felipe, V. Katopodis P. Groumas C. Kouloumentas H. Avramopoulos, J.Y. Dupuy, A. Konczykowska, A. Dede, A. Beretta A. Vannucci, G. Cangini, R. Dinu, D. Schmidt, M. Moehrle, P. Runge J.H. Choi, H.G. Bach, N. Grote, N. Keil, M. Schell, “Hybrid Photonic Integration on a Polymer Platform” *Photonics*, pp. 1005-1026, 2015.

Integrated Passband Optical Filter with High-Order Phase-Shifted Bragg Grating in Silicon-on-Insulator Technology

Claudio Porzi[1], Antonella Bogoni[1,2]
[1] TeCIP – Scuola Superiore Sant'Anna, Via Moruzzi 1 – 56124, Pisa - Italy
e-mail: claudio.porzi@sssup.it
[2] CNIT – National Photonics Labs, Via Moruzzi 1 – 56124 Pisa - Italy
e-mail: antonella.bogoni@cnit.it

ABSTRACT

An integrated passband optical filter based on a high-order phase-shifted Bragg grating (BG) realized in silicon-on-insulator technology is presented. Five half-wave cavities are placed between six BG mirrors defined by laterally corrugating a strip silicon waveguide through electron-beam lithographic process. The BG mirrors are dimensioned in order to provide the proper reflectivity at Bragg wavelength such to tailor the spectral transmission of the multi-cavity filter. A passband window within a 1 THz stopband region having nearly-Gaussian transfer function with a -3dB bandwidth of ~25 GHz, low insertion loss of less than 1 dB, minimum stopband attenuation of ~35 dB, and a passband-to-stopband transition bandwidth of ~30 GHz is observed. These features, which are unreported for such class of structures, illustrate the potentials of this approach for realizing FSR-free bandpass optical filters with arbitrary bandwidth, strong out-of-band rejection, and fast roll-off. Effects of waveguide corrugation depth on the stopband width has also been investigated.

Keywords: Integrated optical filters, silicon photonics, Bragg gratings, Fabry-Perot filters.

1. INTRODUCTION

Tunable optical passband filters based on silicon waveguides enhance the flexibility and the operation of photonic integrated circuits (PICs) in a variety of applications for silicon photonics systems. As such, a large amount of research has been spent in the last decade in designing and fabricating optical filters in silicon-on-insulator (SOI) technology realizing advanced passband transfer functions (TFs). For a given filter bandwidth, desirable additional features are: strong stopband rejection (SBR), flat passband and low insertion loss, sharp passband-to-stopband transition, and wide free-spectral-range (FSR). Microring resonators (MRR)-based approaches proofed excellent performances for applications spanning from microwave photonics [1] to optical communications [2] and sensing [3] systems. Yet, it is challenging to achieve high FSR-to-bandwidth ratios (namely, high values of the filter finesse) unless increasing filter complexity, like resorting to Vernier-operation [3], where MRRs with different FSRs are combined to suppress as much as possible resonances but the operating one.

A FSR-free passband TF can be obtained by collecting the light reflected from a Bragg grating (BG), which can be realized in SOI technology by laterally corrugating either strip or rib silicon waveguides. However, minimum achievable reported bandwidths are greater than ~50 GHz [4], [5], and the SBR is typically limited to ~10 dB, if no apodization is employed in the grating design. Alternatively, phase-shifted (PS) BGs exhibit a sharp passband window within the grating stopband [6]-[8] with additional advantages of transmission-mode operation and large SBR with no need of apodization. By using a contra-directional coupler architecture, the device can also operate as a narrow-band add-drop filter [8]. Similarly to serially-coupled MRRs, the spectral transmission of a PSBG passband window can be tailored using a multi-cavity design in which several PS sections are encompassed between different BG mirrors, each with proper reflectivity at the Bragg wavelength. Away from Bragg condition, incident light is strongly attenuated over a stopband region whose extension is determined by the grating coupling coefficient, which is set by the waveguide corrugation depth. This approach thus enables in principle the realization of optical filters with arbitrary bandwidth, large stopband-to-passband ratio, strong SBR, and sharp transition band, and we recently reported a 6-th order SOI PSBG exhibiting a transmission window with a -3dB bandwidth of ~100 GHz, a 40dB attenuation over a 120 THz-wide stopband region, and a ~300 dB/nm roll-off [8].

Here, a 5-th order cavity design producing a 25 GHz passband window within a 1 THz stopband is reported and experimentally characterized. Thermal tunability, as well as the influence of the waveguide corrugation depth on the stopband width for the employed fabrication process are also investigated

2. PSBG FILTER DESIGN, FABRICTION, AND CHARACTERIZATION

The schematic structure of the proposed high-order PSBG is reported in Fig. 1(a). Five quarter-wave phase-shift sections are placed between six BG mirrors defined by producing periodic variations in the width of a silicon strip waveguide through electron-beam lithographic process on a SOI wafer. The average waveguide width is

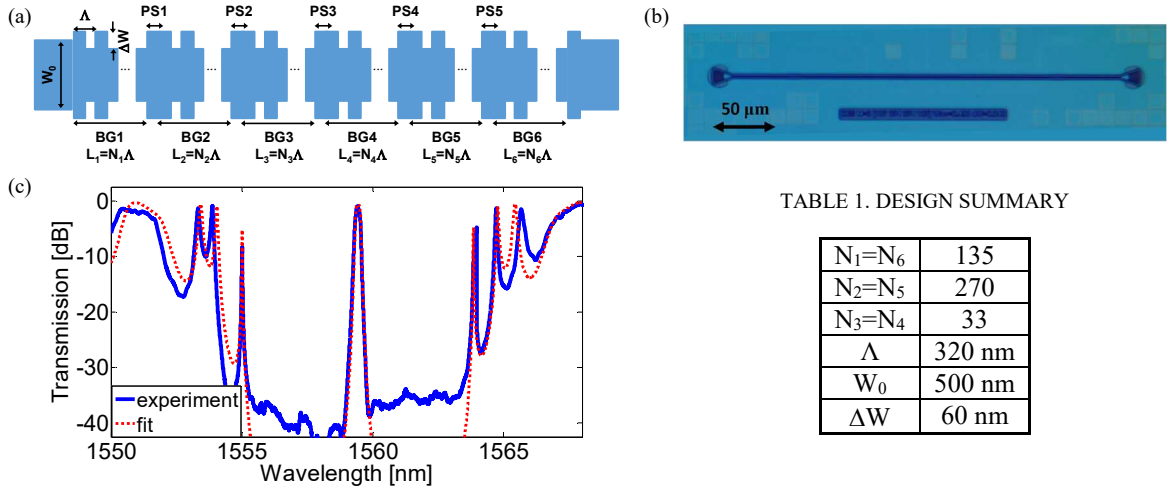


TABLE 1. DESIGN SUMMARY

$N_1=N_6$	135
$N_2=N_5$	270
$N_3=N_4$	33
Λ	320 nm
W_0	500 nm
ΔW	60 nm

Figure 1. (a): High-order phase-shifted Bragg Grating (BG) schematic structure; (b): Picture of the fabricated device; (c): Measured spectral transmission and numerical fit.

W_0=500 nm; the corrugation has a period Λ=320 nm and an ideally rectangular shape, with a depth ΔW=60 nm on each sidewall of the grating. An image of the fabricated device is shown in Fig. 2(b). The summary of the design is also reported in Table I, for a total device length of ~280 μm. Grating couplers (GCs) are used for vertical coupling with input/output optical fibers.

The measured transmission spectrum of the structure, after normalization to the transmission of a reference GC pair, is shown in Fig. 1(c) where a sharp passband window within an 8 nm (1 THz) stopband region is observed. The passband window transmission peak is ~-0.7 dB, whereas the out-of-band rejection is more than ~35 dB over the whole stopband region. The measured spectrum has been fit using a model based on transmission matrix method (TMM). From the fit, also shown in the figure, the effective coupling coefficient of the fabricated grating is extracted. The details of the passband window are illustrated in Fig. 2(a), together with the fitting curve, exhibiting a -3dB bandwidth of 26 GHz, and a -3dB to -30dB transition bandwidth of 27.5 GHz on the steeper edge. The mismatch between the measured transfer function and the simulated response, where the design of Table I for the number of periods in the BGs is used, is ascribed to random oscillations of the BG wavelength along the structure, due to fabrication imperfections. This also produces a slower filter roll-off at the high-frequency detuning. Flatter passband response and steeper roll-off could be in principle achieved by controlling the effective index in the PS sections through local heaters. Thermal tuning of the filter response has been assessed by changing the chip temperature; the results, in Fig. 2(b), indicate a spectral shift of about 0.075 nm/°C.

3. EFFECT OF CORRUGATION DEPTH

A wide stopband region is desirable in several applications, such as OSNR monitoring or single-channel extraction in WDM multichannel system, with the passband width depending on the specific application. As such, the effect of the waveguide corrugation depth ΔW on the stopband width has been investigated by using 1st-order PSBG, where a single half-wave cavity is embedded between two BG mirrors, for three different values of waveguide corrugation depths: 46, 60, and 72 nm. The number of periods in the BGs is 250 for all the considered samples. The measured spectra are shown in Fig. 3(a), along with the corresponding fitting curves, from which an estimate of the grating coupling coefficients for each considered ΔW is retrieved. These values, reported in Fig. 3(b), are compared with those obtained from coupled-mode theory (CMT), in which the results of modal analysis are used for the two waveguide sections in the grating with nominal widths $W_0 \pm \Delta W$, assuming no smoothing effect due to fabrication process. Although the approximated CMT is expected to overestimate the coupling coefficient, the

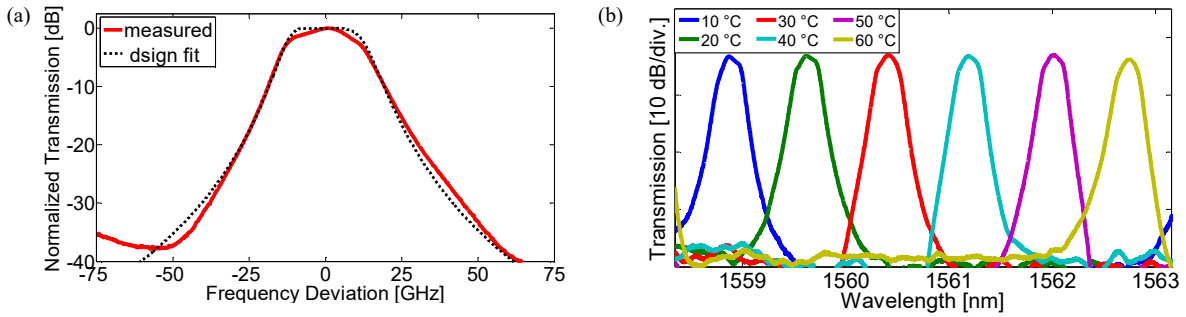


Figure 2. (a): Measured passband transmission window from the high-order PSBG and numerical fit; (b): Thermal dependence of the spectral transmission around the passband window.

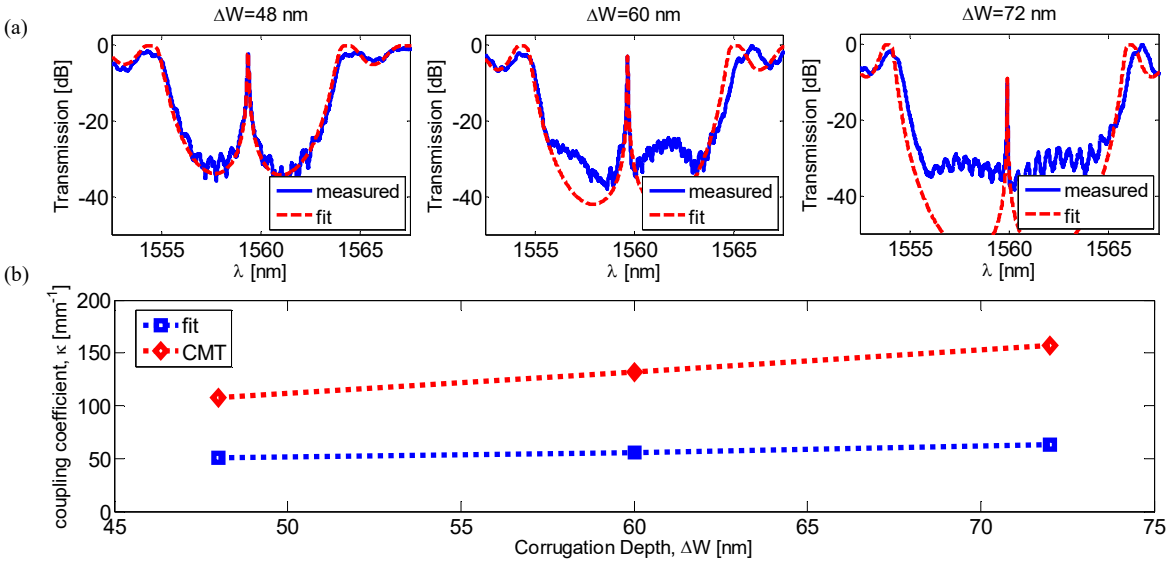


Figure 3. (a): Measured transmission of 1st order PSBGs with different values of corrugation width ΔW. (b): Estimated and calculated grating coupling coefficient versus waveguide corrugation width.

effect of residual lithographic smoothing is evident from Fig. 3(b). Nevertheless, the results from the fitting can be used for design calibration, by acting on the number of periods to compensate the effect on passband window due to reduced coupling coefficient. The estimated propagation loss, obtained by fitting the peak transmission and 3dB bandwidth of the passband windows are comprised between 3 and 4 dB/cm for all the samples. The highest ΔW value exhibits a stronger sensitivity to propagation loss due to the corresponding increase of cavity Q-factor.

4. CONCLUSIONS

A thermally-tunable integrated passband optical filter based on a high-order phase-shifted Bragg grating in silicon-on-insulator technology has been designed, fabricated and characterized. A 25 GHz bandwidth passband transfer function with out-of-band rejection exceeding 35 dB over 1 THz stopband and low insertion loss of ~1 dB is reported in an ultra-compact footprint of less than 150 μm^2. Effect of grating corrugation on the stopband width has been investigated, and the coupling strength reduction due to lithographic smoothing has been estimated through a fitting procedure. Integrated high-order phase-shifted Bragg gratings in silicon waveguide may be of practical interest in microwave-photonics applications and optical network technologies for future 5G systems.

ACKNOWLEDGEMENTS

This work has been supported by the national projects Phood, Prevention, and Divine. The device has been fabricated at the Integrated Photonics Technologies Center (InPhoTec) within the TeCIP institute of Scuola Superiore Sant'Anna, Pisa, Italy. The authors thank Prof. Marc Sorel of University of Glasgow for discussions.

REFERENCES

[1] P. Dong, *et al.*: GHz-bandwidth optical filters based on high-order silicon ring resonators, *Opt. Express*, vol. 18, pp. 23784–23789, Oct. 2010.

[2] J. R. Rong, *et al.*: Ultra-high-contrast and tunable-bandwidth filter using cascaded high-order silicon microring filters, *IEEE Photon. Technol. Lett. Vol.* 25, pp. 1543-1546, Aug. 21013.

[3] T. Claes, *et al.*: Vernier-cascade label-free biosensor with integrated arrayed waveguide grating for wavelength interrogation with low-cost broadband source, *Opt. Lett.*, vol. 36, pp. 3320-3322, Sept. 2011.

[4] X. Wang, *et al.*: Narrow-band waveguide Bragg gratings on SOI wafers with CMOS-compatible fabrication process, *Opt. Express*, vol. 20, pp. 15547-15558, Jul. 2012.

[5] I. Giuntoni, *et al.*: Tunable Bragg reflectors on silicon-on-insulator rib waveguides." *Opt. Express* vol. 17, pp. 18518-18524, Oct. 2009.

[6] P. Prabhathan, *et al.*: Compact SOI nanowire refractive index sensor using phase shifted Bragg grating, *Opt. Express*, vol. 17, pp. 15330–15341, Aug. 2009

[7] X. Wang, *et al*: Narrow-band transmission filter using phase-shifted Bragg gratings in SOI waveguide, in *Proc. IEEE Photonic Society 24th Annual Meeting*, Arlington, VA, paper ThZ1, Oct. 2011.

[8] C. Porzi, *et al.*: Integrated SOI High-Order Phase-Shifted Bragg Grating for Microwave Photonics Signal Processing, *J. of Lightw. Technol.*, vol. 35, pp. 4479-4487, Oct. 2017.

[9] Shi, Wei, *et al.*: Silicon photonic grating-assisted, contra-directional couplers, *Opt. Express*, vol. 21, pp. 3633-3650, Feb. 2013.

Silicon Micro-ring Resonator Integrated in an Optoelectronic Oscillator System

(Student paper)

Phuong T. Do[1], Carlos Alosno-Ramos[2], Diego Pérez-Galacho[2], Xavier Le Roux[2], Pascal Landais[2], Laurent Vivienn[2], Isabelle Ledoux-Rak[1], Bernard Journet[1] and Eric Cassan[2]

[1] *LPQM (CNRS UMR-8537) École Normale Supérieure de Cachan, Centrale Supelec, Université Paris-Saclay, 61 avenue du Président Wilson, 94235 Cachan Cedex, France*

[2] *C2N (CNRS UMR-9001), Univ. Paris-Sud, Université Paris-Saclay, Bât 220, rue André Ampère, 91405 Orsay Cedex, France*

Tel: +33758866710, e-mail: tdo01@ens-paris-saclay.fr

ABSTRACT

In this paper, we present our recent results on the integration of an add-drop silicon micro-ring resonator in an optoelectronic oscillator (OEO) system for the generation of low phase noise RF signal at around 16 GHz. The add-drop ring serves as a selective band pass microwave filter in the OEO, being the frequency operation of the loop defined by the resonator free spectral range (FSR). The investigated micro-ring resonators have been fabricated using a standard silicon-on-insulator (SOI) substrate with 450-nm-wide Si waveguides and an unfolded physical length of 4.7 mm. To reduce the footprint of the device, a spiral arrangement was chosen with a total footprint of 500 µm by 500 µm. After fabrication, samples were tested using input and output grating couplers. The measured micro-ring resonators exhibited typical loaded qualities factors of around 120 000 at 1.55 µm wavelength. Optimized resonators were then introduced in the OEO system, to generate a RF signal around 16.2 GHz matching well the designed resonator FSR. These results constitute the first demonstration of an OEO RF oscillator integrating such a long SOI add-drop silicon ring resonator, paving the way for the future integration of an OEO system on a single chip.

Keywords: Function integration, silicon micro-ring resonator, microwave photonic filter, optoelectronic oscillator.

1. INTRODUCTION

Since the first introduced by X.S Yao and L.Maleke in 1994 [1], the optoelectronic oscillator (OEO) system is known for its ability to generate spectrally pure microwave signals. By using a long length optical fiber with extremely low losses to introduce a large delay to propagate microwave by an optical wave, this system has also potentials for providing tunability and the possibility of microwave comb-type generated RF frequency bands [2]. Because of these advantages, OEO has widespread applications in many fields of science and technology ranging from metrology to communications, radar and even sensing [3]-[5]. However, an OEO has some problems related to the optical fiber delay line that are difficult to solve. First of all, the use of long length optical fiber leads to a large number of RF frequencies satisfying the 2π phase oscillation condition of the loop. This may result in detrimental mode hoping from one of these frequencies to another. Moreover because of the dependence of the refractive index on temperature, the optical fiber delay line has to be placed into a temperature controlled box, which makes the system become bulky. An alternative approach to solve these problems of optical delay line in OEO has been proposed as early as 1999 [6] and consists in replacing the optical fiber by an optical resonator. Nowadays, many types of optical resonators have been proposed for use in OEO such as a whispering gallery mode (WGM) micro or mini-disk resonator [7, 8], optical fiber ring resonator [9]. However, these approaches are realized with a lack of integration, which makes them hardly transferrable to real applications. Here we present experiment results dedicated to an OEO loop in which a silicon micro-ring resonator is employed in order to replace the optical fiber delay line and that also acts as a selective microwave photonic band pass filter. This resonator has been fabricated based on silicon fabrication processes including electron beam (e-beam) lithography and inductively coupled plasma (ICP) etching.

2. OPTICAL RESONATOR FABRICATION AND CHARACTERIZATION

An overall view of the fabricated ring resonator is given in figure 1(a). The ring fabrication started by using silicon on insulator (SOI) wafer with 220 nm of silicon and a 2 µm buried oxide. The patterns were lithographically defined in a 100 nm of photoresist ZEP-520A by using e-beam lithography. After lithography,

the patterns were transferred using ICP etching with Sulfur hexafluoride SF_6 and Octafluorocyclobutane C_4F_8 gas. After patterning, a top cladding of Poly methyl methacrylate (PMMA) was deposited. No additional post processing was done. The spirals consisted entirely of photonic wires with a width of 450 nm. Light was coupled in and out of the chip using vertical grating couplers, as shown in figure 1(d), that were optimized for transverse magnetic-polarized (TM) mode at 1550 nm wavelength. Several spirals with different combinations of coupling gaps/coupling lengths were fabricated with 500 µm x 500 µm footprints.

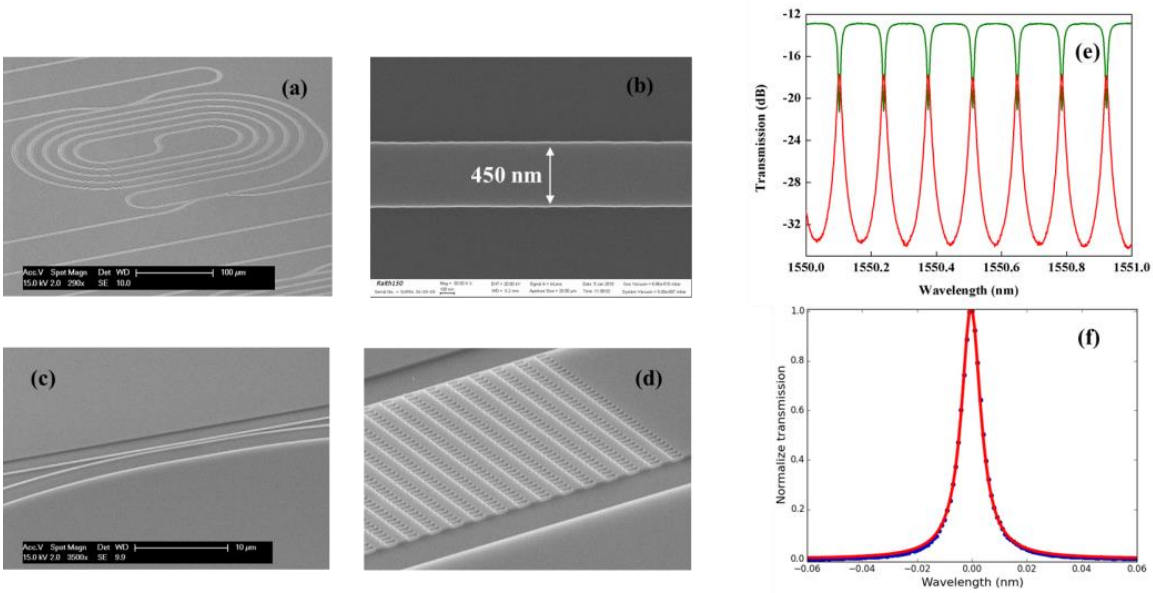


Figure 1. SEM pictures (a,b,c,d) and transmission spectrum (e,f) of an add-drop ring resonator

Figure 1(e) shows the transmission spectrum measured at the through and the drop ports of the add-drop ring resonator having a coupling gap of 400 nm and a linear coupling length of 17.5 µm. Figure 1(e) shows a Lorentzian curve fit of a single resonance peak, from which the loaded quality factor, Q_L, was determined to be 120 000. The *FSR* estimated from the transmission spectrum was 0.137 nm, which corresponds with 16.2 GHz. Moreover, from the transmission spectrum at both through and drop port, we estimated the intrinsic losses of 2.3 dB/cm based on the theory introduced by by Shijun Xiao [10].

3. DEDICATED OF MICRO-RING RESONATOR IN OEO LOOP

The schematic of the integration of the micro-ring resonator that we have performed into an OEO loop is shown in Figure 2(a). A CW laser beam at around 1.55 µm wavelength was modulated by the intensity modulator, with a frequency matching the FSR of the ring, and injected into the micro-ring resonator. The output signal at the drop port of the resonator was applied to the photo-detector, performing optical to electrical conversion. Due to the periodical spectrum of the resonator, a microwave signal of frequency corresponding with the optical ring FSR was generated. This RF signal is then amplified by a RF amplifier and split by an RF coupler (see Fig 2(a)). One part of the signal is sent to the electrical signal analyzer (ESA) while another is sent back to the modulator to form a closed loop OEO.

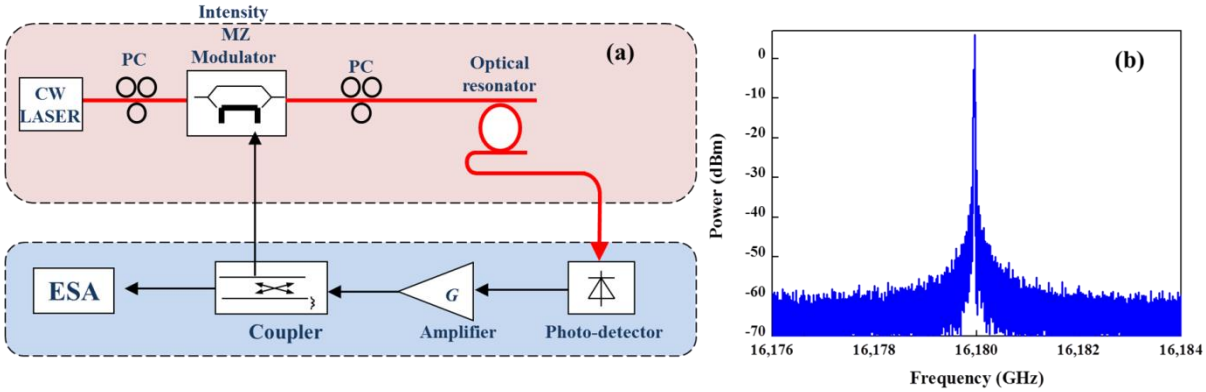


Figure 2. Experiment setup (a) and oscillation spectrum of OEO with integration of silicon ring resonator (b).

A typical generated microwave oscillation spectrum characterized is shown in Figure 2(b). The oscillation frequency observed of around 16.2 GHz, which corresponds to the FSR of the SOI photonics resonator. This result constitutes first observation of an OEO RF oscillator integrating such a long SOI add-drop silicon ring resonator.

4. CONCLUSIONS

We have successfully integrated a 16 GHz-FSR silicon add-drop ring as a microwave photonic band pass filter in an OEO system. As many optoelectronic elements in an OEO loop such as the modulator and the photodetector are now classical parts of the silicon photonics-tools and as other elements such as the RF amplifier and filter can be straightforwardly fabricated in CMOS lines, this work contributes to show the potential of fully integrated OEO systems in a single chip. Cost efficiency and scalability of such systems are envisioned to broaden their application in many fields.

REFERENCES

[1] X. S. Yao and L. Maleki: High frequency optical subcarrier generator, *Electron. Lett*., vol. 30 pp. 1525-1526, Sept. 1994.

[2] L. Bouchier, *et al.*: Theoretical and experimental study of the phase noise of opto-electronic oscillators based on high quality factor optical resonators, *in Proc. 2010 IEEE International Frequency Control Symposium*, Newport Beach, USA, Jun. 2010**.**

[3] X. S. Yao, *et al.*: Progress in the opto-electronic oscillator - a ten year anniversary review, *in Proc. 2004 IEEE MTT-S International Microwave Symposium Digest*, Fort Worth, USA, Jun. 2004, paper 04CH37535.

[4] L. Maleki: The opto-electronic oscillator (OEO): Review and recent progress, *in Proc. 2012 European Frequency and Time Forum*, Gothenburg, Sweden, Apr. 2012.

[5] L. D. Nguyen, *et al.*: Refractive index measurement by using an optoelectronic oscillator, *IEEE Photon. Technol. Lett.*, vol. 22 pp. 857-859, Jun. 2010.

[6] L. Maleki, *et al.:* New schemes for improved opto-electronic oscillator, *in Proc. Microwave Photonics, 1999. MWP '99. International Topical Meeting on*, Melbourne, Australia, Nov. 1999.

[7] V. S. Ilchenko, *et al.:* Miniature oscillators based on optical whispering gallery mode resonators, *in Proc. 2008 IEEE International Frequency Control Symposium*, Honolulu, USA, May 2008.

[8] P. H. Merre, *et al. :* High-Q optical resonators for stabilization of high spectral purity microwave oscillators, *in Proc. 2009 IEEE International Frequency Control Symposium Joint with the 22nd European Frequency and Time forum*, Besancon, France, Apr. 2009.

[9] K. Saleh, *et al.:* Optoelectronic oscillator based on fiber ring resonator: Overall system optimization and phase noise reduction, *in Proc. 2012 IEEE International Frequency Control Symposium*, Baltimore, USA, May 2012.

[10] S. Xiao, *et al.:* Modeling and measurement of losses in silicon-on-insulator resonators and bends, *Opt. Express.*, vol. 15 pp. 10553-10561, Aug. 2007.

Novel high-performance lasers in InP

(Invited paper)

Dr. Milan L. Mashanovitch
Freedom Photonics LLC, *41 Aero Camino, Santa Barbara, CA 93117 - USA*
Tel: +18059674900, e-mail: info@freedomphotonics.com

ABSTRACT

In this paper, we provide an overview of a variety of novel, high-performance lasers and PICs in InP that Freedom Photonics has developed and commercialized over the past several years. Those include lasers in several different wavelength ranges: 1300nm, 1550nm and 1650nm. The applications for these devices span high-performance sources for Datacom systems, integrated optical transmitters for telecom applications, lasers for optical sensing as well as lasers for free-space optical communications.

Keywords: lasers, tunable lasers, photonic integrated circuits, Indium Phosphide.

1. INTRODUCTION

New and existing applications drive the demand for innovation in the area of monolithic laser technology in InP. In this paper, we are describing a number of different advanced monolithic semiconductor lasers and related PICs in InP, developed for a variety of markets and applications in the 1270nm – 1680nm wavelength range.

2. High-Performance Lasers at 1300nm

At Freedom Photonics, we have developed widely tunable monolithic semiconductor lasers operating in the O-band wavelength range, and these devices, described in [1] are available as standard products, with 3 different central wavelengths.

More recently, a new DFB laser technology at 1300nm has been developed for high output power and high wall-plug efficiency. Figure 1 left shows the output power and efficiency for one particular laser implementation, where the back facet is high-reflectivity (HR) coated for improved front-facet efficiency. Peak wall plug efficiency around 36% is observed at ~4x threshold current, and peak power >200mW. Figure 1 (right) shows lasing spectral obtained at room temperature at different laser bias. Stable and highly single-mode emission is demonstrated.

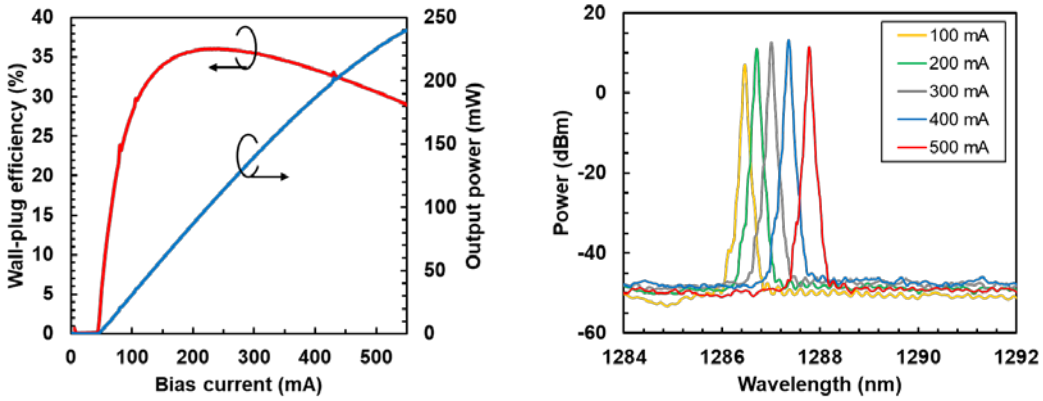


Figure 1 – Left - Output power and efficiency of a DFB laser. Back facet is HR coated such that the light primarily exits from the front facet and is detected. Right - Single-mode operation with laser bias. Data taken with temperature-controlled stage at 20ºC.

3. Integrated Optical Transmitters at 1550nm

Tunable chip-scale optical transmitter devices have revolutionized the pluggable module telecom market, by enabling excellent performance with great cost and size reduction. We have developed a novel, patented tunable transmitter device, based on a dual output tunable laser, and a pair of modulators which are interferometrically combined (Tunable Interferometric Transmitter, TunIT) [2]. This unique device architecture allows for improved performance in terms of the side-mode suppression ratio, and tuning current needed for laser tuning. TunIT image is shown in Figure 2 (left), and results of transmission experiments, are shown in Figure 2 (right).

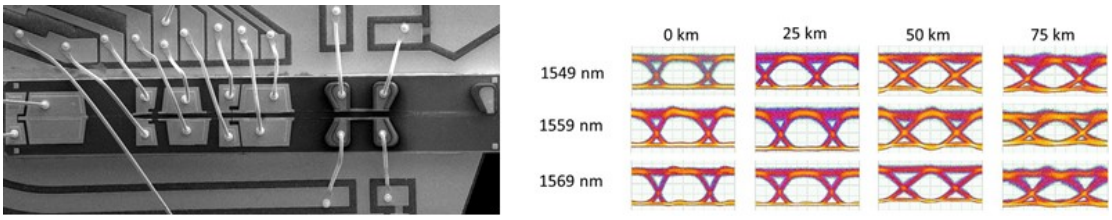


Figure 2 – (left) Scanning Electron Microscope (SEM) image of a TunIT laser chip mounted on an AlN carrier, with wirebonds connecting the contact pads on the chip to metal traces on the carrier. Sections include an HR coating rear mirror, gain section, and two output arms, each with phase control, Vernier mirrors, SOAs, and high speed modulators. In this implementation, the device has a common phase control electrode inside the laser cavity, as well as phase electrodes that control the phase of the interferometer. (right) Eye diagrams for a single TunIT device, measured over a 20 nm wide wavelength range. Eye diagrams are shown for operation at 1549 nm (top), 1559 nm (middle), and 1569 nm (bottom).

We have also developed a novel, 4-channel, monolithic widely tunable transmitter device (QUAD) in Indium Phosphide [3]. This device is based on monolithic integration of 4 widely tunable externally modulated lasers, with a single output waveguide. The QUAD device is designed to operate at 55 ˚C, in order to reduce the power consumption of the cooler. A completed, wire-bonded QUAD is shown in Figure 3 (left), with eye diagrams (middle) from a module (right).

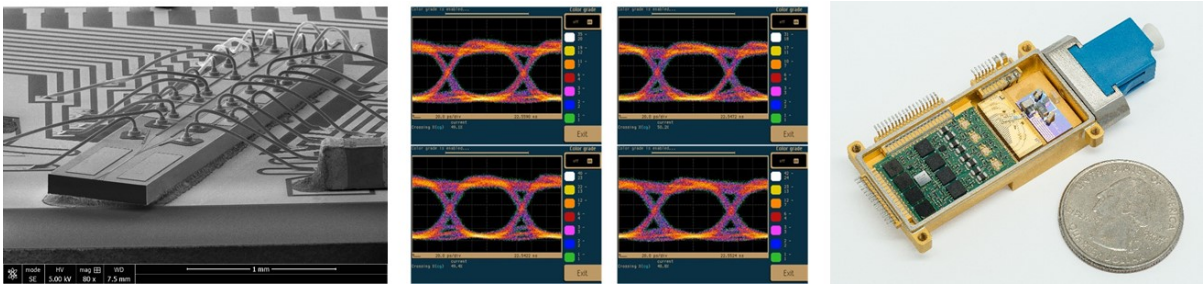


Figure 3 – (left) Scanning Electron Microscope (SEM) image of a QUAD transmitter chip mounted on an AlN carrier, with wirebonds connecting the contact pads on the chip to metal traces on the carrier. The device consists of 4 functionally equivalent widely tunable optical transmitters, connected to a single output multimode interference coupler (middle) Representative eye diagrams, at 10 Gbps, for all 4 transmitters working simultaneously. (right) QUAD module.

Please check spelling in your paper and do not use automatic hyphenation. Additionally, be sure your sentences are complete and that there is continuity within your paragraphs. Check the numbering of your graphics and make sure that all appropriate references are included.

4. Lasers and PIC for gas sensing at 1650nm

Methane is about 23 times more potent at trapping infrared radiation than carbon dioxide. The development of low-cost, accurate remote methane sensing technologies is becoming increasingly critical in order to analyze methane concentrations and distributions throughout the atmosphere.

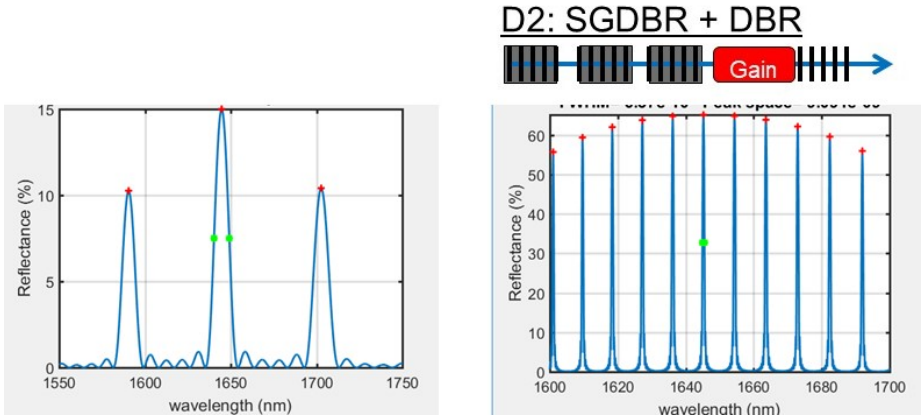


Figure 4 – Patent-pending, Comb-Optimized DBR concept: a DBR laser that uses two different DBR mirrors, one broad-band DBR mirror, and a sampled grating mirror, where sampling is used to control the shape of the DBR peaks, and allow for narrow filter response, and long DBR cavity.

LIDAR based methane spectroscopy at 1651nm presents an opportunity to perform these measurements remotely over localized areas without the need to sample the atmosphere. Majority of these techniques require tunable lasers.

Some of the key requirements for a tunable laser used in spectroscopy applications are fast tuning speed, and laser linewidths less than 10 MHz. The simplest way to realize a semiconductor tunable laser is using a Distributed Bragg Reflector laser architecture [4]. To achieve further control over design space, and decouple the dependence between the DBR laser gain section length and laser modal purity, a DBR laser can be realized using 2 different DBR mirrors, at both sides of the cavity, which allow for more precise cavity mode filtering. We have used one such novel approach, a proprietary Comb-optimized (COMBO) DBR design, to design and implement 1650nm COMBO-DBR lasers for gas sensing. An example COMBO design is shown in Figure 4, where one broad-band DBR mirror, and a sampled grating mirror are used, and where sampling is used to control the shape of the DBR peaks and allow for narrow filter response [5]. This approach allows for tuning ranges on the order of 8nm. For wider tuning ranges, more complex dual mirror DBR laser designs can be used, including varieties using Vernier tuning, as described in [4].

At Freedom Photonics, we have developed and commercialized one such laser implementation at 1650nm, which shows more than 70nm of continuous tuning range, and is now available in butterfly packaging, Figure 5.

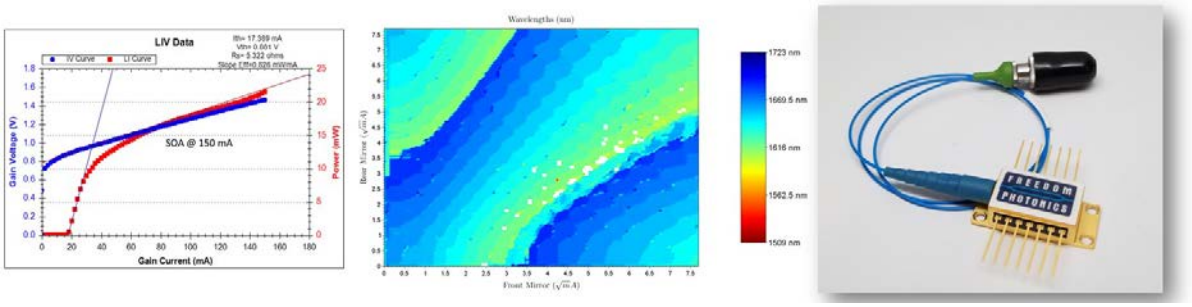


Figure 5 – (left) Light-current-voltage characteristic of a widely-tunable 1650nm laser (right) Laser tuning map, showing >70nm of laser tuning range

CONCLUSIONS

New and existing applications drive the demand for innovation in the area of monolithic laser technology in InP. In this paper, we have provided an overview of a variety of novel, high-performance lasers and PICs in InP that we at Freedom Photonics have developed and commercialized in the past couple of years. Those include lasers at several different wavelength ranges: 1300nm, 1550nm and 1650nm. The applications for these devices span high-performance sources for Datacom systems, integrated optical transmitters for telecom applications, lasers for optical sensing as well as lasers for free-space optical communications.

REFERENCES

[1] M. L. Mašanović and L. A. Johansson, "Widely tunable semiconductor lasers and transmitters," 2015 IEEE Photonics Conference (IPC), Reston, VA, 2015, pp. 611-612.

[2] M. L. Mashanovitch et al., "Monolithic Tunable Interferometric Transmitter (TunIT) in Indium Phosphide," in IEEE Journal of Selected Topics in Quantum Electronics, vol. 23, no. 6, pp. 1-5, Nov.-Dec. 2017.

[3] D. J. Kebort et al., "Monolithic Four-Channel (QUAD) Integrated Widely Tunable Transmitter in Indium Phosphide," in IEEE Journal of Selected Topics in Quantum Electronics, vol. 24, no. 1, pp. 1-7, Jan.-Feb. 2018.

[4] L. Coldren, S. Corzine, M. Mashanovitch, “Diode Lasers and Photonic Integrated Circuits”, Book, Wiley and Sons, 2012

[5] Gordon B. Morrison et al., "New semiconductor laser technology for gas sensing applications in the 1650nm range", Proc. SPIE 10406, Lidar Remote Sensing for Environmental Monitoring 2017, 1040605 (30 August 2017)

Gain characteristics of 1.3μm GaInNAs/GaAs quantum wells monolithically integrated on Ge

Jukka Viheriälä, Antti T. Aho, Riku Isoaho, Arto Aho, Antti Tukiainen, Mircea Guina

Optoelectronics Research Centre, Tampere University of Technology, Korkeakoulunkatu 3, Tampere, Finland,

ABSTRACT

Gain characteristics of quantum-well laser diodes monolithically integrated on Ge substrate are reported. The gain is provided by two GaInNAsSb/GaAs quantum-wells with emission at 1.2 μm–1.3 μm. The diode exhibits continuous-wave operation with mW-level output power at room temperature.

Keywords: Monolithic integration, laser diode, gain, GaInNAs quantum well

1. INTRODUCTION

Silicon photonics offers the most advanced and versatile, integration of a large variety of passive optical components. On the other hand, Si lacks the ability to generate light requiring integration with III-V optoelectronics emitter. Amongst various platforms targeting for Si/III–V convergence, monolithic integration enables highest level of scalability. The main issues preventing developments in this direction are related to the large lattice mismatch between Si and III–V compounds, and formation of antiphase domains at the interface between group IV and III–V layers. An interesting possibility to mitigate the lattice mismatch issue has emerged recently owing to developments of Ge/SiGe/Si epitaxy. In turn, this allows integration of GaAs optoelectronics components on artificial Si/Ge substrates, since Ge and GaAs-based compounds have similar lattice constants. This approach has been recently pursued in demonstration of 1.3 μm InAs/GaAs QD lasers on Ge/Si [1], [2]. On the other hand, attempts to integrate InGaAs/GaAs quantum-well (QW) emitters have been limited to a wavelength range below 1.1 μm due to the strain associated with In [3].

Recently, we proposed a new approach for the fabrication of gain structures at 1.2 – 1.3 μm monolithically integrated on an artificial Ge substrate (i.e. incorporating a GaAs-based buffer) [4], which takes advantage of recent progress in epitaxy of GaInNAs/GaAs compounds [5], [6] . Compared with QD gain structures monolithically integrated on Ge/Si, QW technology should provide higher single-pass gain increasing the density of integration, the operation speed, and reducing the power consumption. Here we report the gain characteristics of GaInNAs/GaAs/Ge quantum well laser diodes operating at 1.3 μm.

2. EPTAXIAL STRUCTURE

The general structure is depicted in Figure 1. The laser was grown by plasma-assisted molecular beam epitaxy (MBE) onto a 4” artificial Ge substrate. The epitaxial growth was started with a GaAs buffer layer followed by a thick n-GaAs contact layer. Then we grew the laser structure that consisted of two dilute-nitride QWs embedded within a 250 nm GaAs waveguide and surrounded by 1 μm AlGaAs claddings. Finally, a p++ contact GaAs layer was deposited on top. Following the epitaxy we assessed the photoluminescence (PL) emission of the laser diode grown on the Ge substrate and compared it with the signal obtained from a similar structure grown on n-GaAs (100) substrate. As shown in Figure 1, the two type of structures provide similar level of PL, with slight difference in the peak wavelength, possibly due to a difference in composition. The difference in the background signal is due to different types of substrates. Moreover, the morphology of the structure was assessed by microscopy (both optical and atomic force). Again, we did not observe significant changes in quality besides an increase in roughness of a structure grown on Ge.

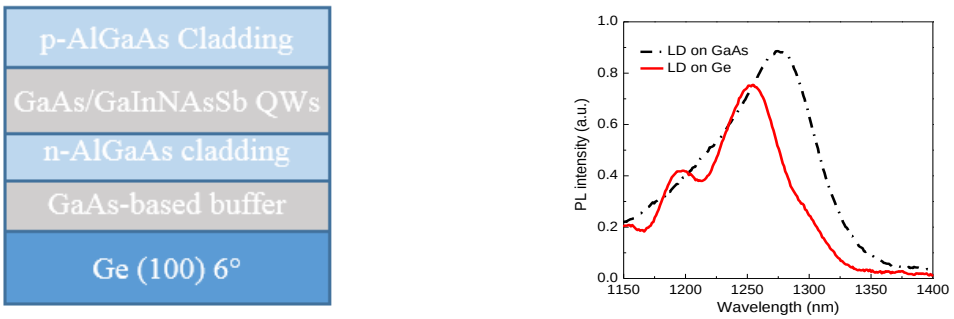


Figure 1. Left: General schematics of the laser structure. Right: PL signal for GaInNAsSb QWs on Ge and GaAs [4].

3. LASER DIODE PROCESSING AND PERFORMANCE

Laser diodes with a ridge waveguide (RWG) geometry were fabricated with both p- and n- contacts on the top. Finally, laser bars were cleaved and some of the bars were HR/HR coated to allow operation with reduced current. The coatings consisted of two pairs of SiO_2/TiO_2 for the front mirror and 6 pairs for the back mirror, ensuring 75% and 99.5% nominal reflection, respectively. The devices were glued epi-side up on AlN-submounts. Room temperature *cw* operation with mW-level output power for a component as short as 250-µm is shown in Figure 2 (left). Temperature dependent LI-characterization (not shown) reveals a characteristic temperature above 125 K and continuous wave lasing up to 120 °C.

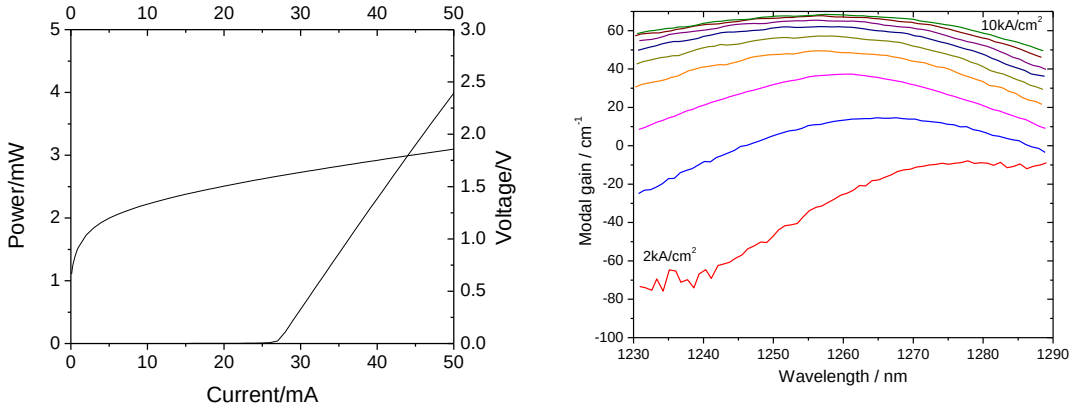


Figure 2. Left: Room temperature output characteristics of the GaInNAs/GaAs/Ge 1.3 µm laser. Results are shown for 250µm long transversely single mode LDs at room temperature. Right: Modal gain vs wavelength at different current densities from 2 kA/cm² to 10 kA/cm² with 1kA intervals.

Gain characteristics were determioned using Hakki-Paoli method [7] for AR/AR-coated and as cleaved devices. Figure 2 (right) shows the spectarl gain curve under different levels of injection for 2 µm wide and 250 µm long waveguide. The device exhibited a modal gain of up to 68 cm^{-1} at a current density of 10 kA/cm^2. At moderate injection level of 5 kA/cm2 full width half maximum of modal gain curve is around 70 nm.

4. CONCLUSIONS

We report gain characteristics of a 1.3 µm dilute-nitride QW laser integrated on Ge substrate. Laser diode demonstration reveal excellent output and temperature characteristics, wide gain spectrum capable to support multiple channels and high gain. Compared to InAs/GaAs QD lasers at similar wavelength range grown on Ge, our approach enables higher gain and hence efficient operation of short components (potentially below 200µm chip length). This is an advantageous feature for higher density of integration, higher speed, and lower power consumption.

ACKNOWLEDGEMENTS

We wish to thank Mervi Koskinen for support in processing and characterization.

REFERENCES

[1] A. Y. Liu *et al.*, "High performance continuous wave 1.3 µm quantum dot lasers on silicon," *Appl. Phys. Lett.*, vol. 104, no. 4, p. 041104, Jan. 2014.

[2] H. Liu *et al.*, "Long-wavelength InAs/GaAs quantum-dot laser diode monolithically grown on Ge substrate | Nature Photonics," *Nat. Photonics*, vol. 5, pp. 416–419, Jun. 2011.

[3] V. Y. Aleshkin *et al.*, "Monolithically integrated InGaAs/GaAs/AlGaAs quantum well laser grown by MOCVD on exact Ge/Si(001) substrate," *Appl. Phys. Lett.*, vol. 109, no. 6, p. 061111, Aug. 2016.

[4] M. Guina, R. Isoaho, J. Viheriälä, A. Aho, A. Aho, and T. Antti, "Quantum-well laser emitting at 1.2µm–1.3µm window monolithically integrated on Ge," presented at the ECOC 2017, Gothenburg, Sweden, 2017.

[5] H. Virtanen *et al.*, "Spectral Characteristics of Narrow-Linewidth High-Power 1180 nm DBR Laser With Surface Gratings," *IEEE Photonics Technol. Lett.*, vol. 29, no. 1, pp. 114–117, Jan. 2017.

[6] V.-M. Korpijärvi, J. Viheriälä, M. Koskinen, A. T. Aho, and M. Guina, "High-power temperature-stable GaInNAs distributed Bragg reflector laser emitting at 1180 nm," *Opt. Lett.*, vol. 41, no. 4, pp. 657–660, Feb. 2016.

[7] B. W. Hakki and T. L. Paoli, "Gain spectra in GaAs double−heterostructure injection lasers," *J. Appl. Phys.*, vol. 46, no. 3, pp. 1299–1306, Mar. 1975.

100 Gb/s Duobinary Electro-Absorption Modulation of a Heterogeneously Integrated InP-on-Si DFB Laser Diode

Amin Abbasi[1+], Jochem Verbist[1,2], Leila A. Shiramin[1], Michiel Verplaetse[2], Timothy De Keulenaer[3], Ramses Pierco[3], Arno Vyncke[3], Guy Torfs[2], Geert Morthier[1], Johan Bauwelinck[2], Gunther Roelkens[1*]

[1] Photonics Research Group, *INTEC, Ghent University-IMEC, 9000 Ghent - Belgium*

[2] IDLab, *Ghent University - IMEC, 9000 Ghent, Belgium*

[3] BiFast, *9000 Ghent, Belgium*

[+] *currently at Antwerp Space, Antwerp, Belgium*

**corresponding author e-mail: gunther.roelkens@ugent.be*

ABSTRACT

We demonstrate for the first time a serial 100 Gb/s transmission with a heterogeneously integrated InP/Si DFB laser by operating the InP tapers – used to couple to the underlying silicon waveguide- as electro-absorption modulators. An in-house developed driver IC, fabricated in a 0.13µm SiGe BiCMOS technology, employing a 4x1 multiplexer and an analog six tap feedforward equalizer was used to generate a duobinary modulated signal at 100 Gb/s on the tapers, requiring no power-consuming digital signal processing (DSP) or digital-to-analog converters (DAC). With these devices, open eyes and a bit-error ratio (BER) down to 1.6E-3 at 100 Gb/s electrical duobinary are obtained. As the DFB consists of 2 independent tapers and emits light from both ends, this laser can be used to generate 2x 100 Gb/s data streams from a single transmitter, leading to a reduction in area, power and packaging cost over a 2-laser approach. Such a transmitter would be an attractive solution for 200 GbE and 400 GbE transceivers in short-reach optical interconnects.

Keywords: Semiconductor Lasers, IIIV-on-Si, Silicon Photonics, Electro-absorption modulation, Optical Interconnects

1. INTRODUCTION

The increasing growth of internet traffic driven by high-definition video-streaming and cloud computing pushes the requirements on inter and intra-datacenter optical interconnects. The use of lower line rates (e.g., 25 or 50 Gb/s) requires a relatively large number of lanes to achieve 400GbE transceivers and beyond, making integrated transmitters for high aggregate bit rates more complex, which impacts the cost. While bit rates per wavelength beyond 100 Gb/s are very well possible using quadrature amplitude modulation (QAM), coherent transmission is considered less viable for intra-datacenter links. Therefore there is an interest in transceivers that allow for 100Gbit/s operation per wavelength using an intensity modulation / direct detect format.

Electrical duobinary (EDB) modulation is an intensity modulation format that relaxes the bandwidth requirements on the optical components and still offers a simple demodulation scheme. EDB was used to demonstrate real time 100 Gb/s transmission based on an InP travelling-wave electro-absorption modulator with integrated DFB laser [1]. However, the 50 Ω termination for this transmission line structure increases the power consumption. Using a silicon-organic Mach-Zehnder modulator (MZM) 100 Gb/s electrical duobinary transmission was demonstrated [2]. The combination of state-of-the-art SiGe electro-absorption (EA) modulators

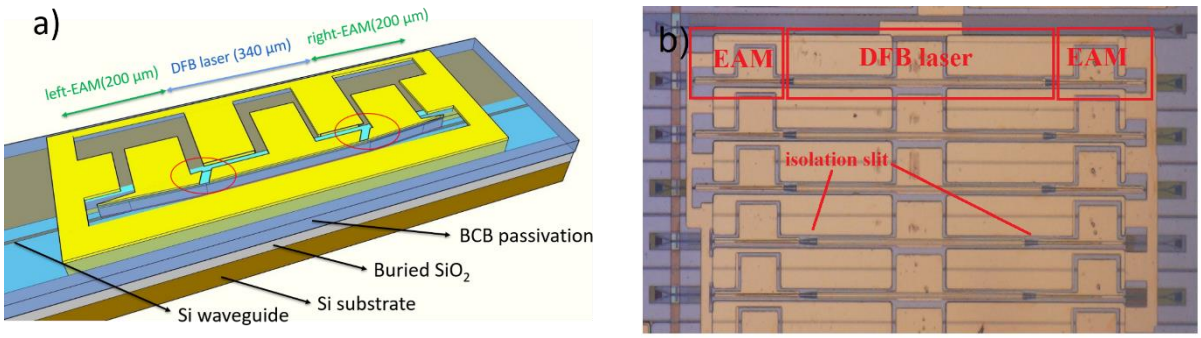


Figure 1. a) Schematic of the heterogeneously integrated InP-on-Si externally modulated laser (tilted isolation slits' position are indicated by red circles); b) Microscope image of the fabricated device showing the DFB laser in the middle and the tapers used as EAMs.

on a silicon photonics platform with state-of-the-art modulator drivers has resulted in a first real-time serial 100 Gb/s NRZ-OOK transmission on a silicon platform without any DSP, DAC or power-hungry travelling wave structures [3]. At the same time, both direct and EA modulation of heterogeneously integrated InP-on-Si lasers were shown up to 56 Gb/s [4,5].

Here we present the first demonstration of the generation and transmission of a 100 Gb/s electrical duobinary signal using a heterogeneously integrated InP-on-Si externally modulated DFB laser (EML) combined with an in-house designed transmitter (TX-IC) chipset in a SiGe BiCMOS technology, without the need for any digital signal processing (DSP).

2. DEVICE STRUCTURE, STATIC AND SMALL-SIGNAL CHARACTERISTICS

The EML was realized through adhesive die-to-wafer bonding on a silicon photonic integrated circuit, schematically illustrated in Fig. 1(a). A DFB laser structure, with the grating defined in the silicon waveguide layer, is coupled to the silicon waveguide using a III-V/Si taper structure. The EAMs are implemented in this taper structure. In our devices, the active layer for the DFB laser and the EA modulators (or tapers) is identical, which eases the fabrication process. The active region consists of 8 InAlGaAs quantum wells emitting in the C-band. The taper is electrically isolated from the laser by etching the InGaAs contact layer (200 nm) and part of the p-InP cladding layer (125 nm). 8 kΩ electrical isolation between both is obtained. The realized devices are shown in Fig. 1(b). Each row consists of one DFB laser (340 µm long) and two EAMs (200 µm long) coupled to a silicon waveguide. The output power of the laser can be collected using two grating couplers on each side. The structure is identical to the heterogeneously integrated DFB lasers that have been discussed in [5].

Threshold currents at room temperature of 20 mA, output powers in the silicon waveguide above 3 mW at 100 mA bias current, and a series resistance of 7 Ω were measured for the lasers. Single mode emission at 1567 nm with 40 dB side mode suppression ratio is obtained. Lasers operating on the long wavelength side of the gain spectrum are used as this reduces the insertion loss of the EAM, which uses the same active region as mentioned before. Fig. 2(a) shows the normalized output power versus the reverse (DC) bias applied to the EAM. An extinction ratio of 15 dB is obtained for a voltage swing of 1.5 V. This measurement was done at the different DFB laser bias currents and we observed that there is little dependence on the laser bias current, indicating that absorption saturation is not occurring. The small signal characteristics, measured at 80 mA bias current to the DFB laser and for a bias voltage of -0.8 V to the EAMs, are shown in Fig. 2(b). An RC-limited 3 dB bandwidth of around 20 GHz is obtained with a slow roll-off at higher frequencies.

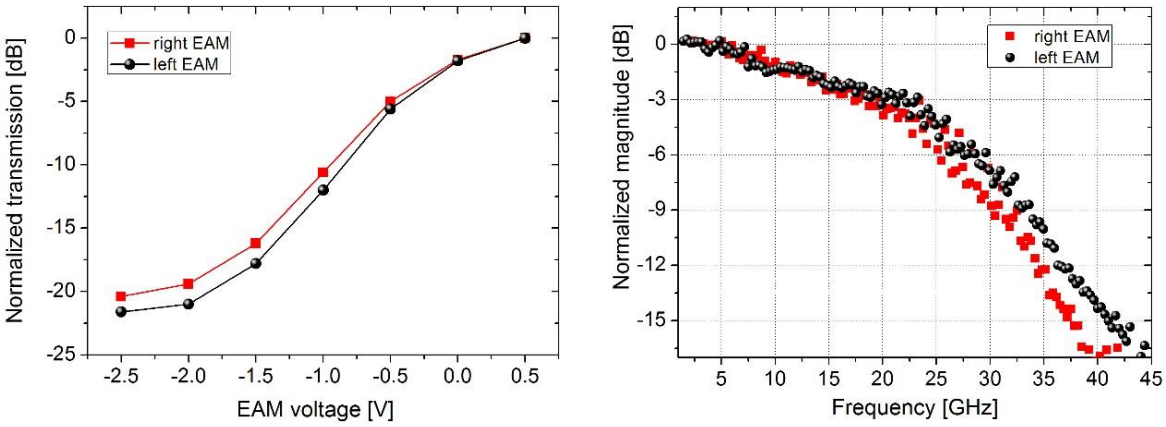


Figure 2. Normalized output power versus the reverse (DC) bias applied to the EAM (left); small signal modulation characteristics for a bias voltage of -0.8V to the EAMs and 80 mA bias current to the DFB laser (right).

3. LARGE SIGNAL MODULATION CHARACTERISTICS AND TRANSMISSION EXPERIMENT

To characterize the device's large signal performance the setup shown in Fig. 3 is used. A XilinX FPGA-board generates four 25 Gb/s binary data streams with 2^7-1 long pseudo-random bit sequences (PRBS), which are multiplexed on the TX-IC with the required delays to again form a 2^7-1 long PRBS at 100 Gb/s. Next, a six tap analog feed forward equalizer (FFE) is used to compensate frequency roll-off of the following components in

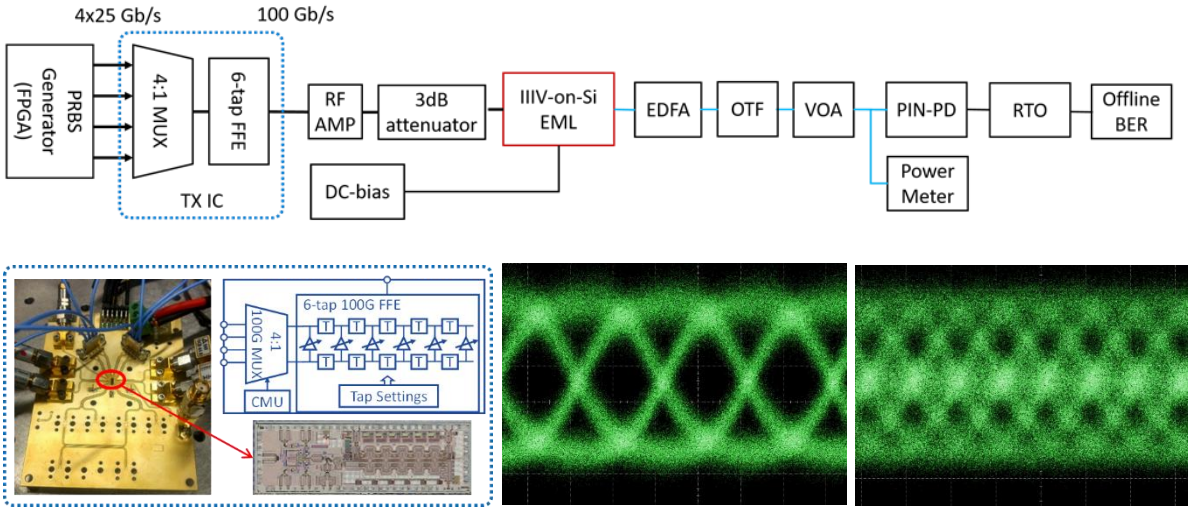


Figure 3. Schematic of the measurement setup (top), schematic and die micrograph of the TX-IC (bottom left); eye diagrams at 50 Gb/s NRZ-OOK(bottom middle) and 100 Gb/s EDB (bottom right), the DFB laser is biased at 80 mA and the EAM at -0.8 V .

the link. The TX-IC consumes less than 0.9W. An RF amplifier with bias-T delivers the signal with a swing of ~2.5 Vpp to the EML via an RF-probe. To reduce back reflection to the RF amplifier, a 3 dB attenuator is placed at the output of the RF AMP. During bit-error rate (BER) measurements the laser was biased at 80 mA and the EAM was biased at -0.8 V. As no high-speed transimpedance amplifier was available during testing, an erbium-doped fiber amplifier (EDFA) had to be used to increase the signal power to ~9 dBm before entering a commercial PIN-photodiode (BW=45 GHz). An optical tunable filter is used to minimize the EDFA-noise. Finally, the signal is captured by a 63 GHz 160 GSa/s real-time oscilloscope (RTO). The BER is determined offline by resampling the captured signal. The optimal sampling point is determined by visual inspection of the eye diagram, no equalization or other DSP is used. For more than 100,000 symbols a BER of 1.6E-3 was measured which is below the hard decision forward error coding limit with 7% overhead (3.8E-3).

4. CONCLUSIONS

We demonstrated for the first time the generation of a 100 Gb/s electrical duobinary signal using a heterogeneously integrated InP-on-Si externally modulated DFB laser without having to rely on any DSP. Since the device consists of two identical EAMs on each side, we can use each side to generate 2 independent 100 Gb/s EDB data streams resulting in a single laser 200 Gb/s transmitter [4]. Combining two of these devices could be low-cost and compact option for 400 GbE transceivers for short-reach optical interconnects.

ACKNOWLEDGEMENTS

The authors acknowledge 3-5 Lab for supplying the III-V epitaxial wafer.

REFERENCES

[1] M. Chacinski, U. Westergren, B. Stoltz, and L. Thylén, “Monolithically Integrated DFB-EA for 100 Gb/s Ethernet”, IEEE Electron Device Lett, 2008.

[2] H. Zwickel, et al, “100 Gbit/s serial transmission using a silicon-organic hybrid (SOH) modulator and a duobinary driver IC”, OFC 2017.

[3] J. Verbist, et al, “First Real-Time 100-Gb/s NRZ-OOK Transmission over 2 km with a Silicon Photonic Electro-Absorption Modulator”, Proc. OFC 2017 .

[4] A. Abbasi, L. Abdollahi Shiramin, B. Moeneclaey, J. Verbist, X. Yin, J. Bauwelinck, D. Van Thourhout, G. Roelkens, G. Morthier, “2x56 Gbps Electroabsorption Modulated III-V-on-silicon DFB Laser”, European Conference on Optical Communication (ECOC), 2017.

[5] A. Abbasi, B. Moeneclaey, J. Verbist, X. Yin, J. Bauwelinck, G.-H. Duan, G. Roelkens, G. Morthier, “Direct and electro-absorption modulation of a III-V-on-silicon DFB laser at 56 Gb/s”, IEEE JSTQE special issue on Semicond. Lasers, Vol. 23, Iss. 6, Art. 1501307, Nov.-Dec. 2017.

GaInAsP/InP Membrane Lasers for On-chip Applications

(Invited paper)

Tomohiro Amemiya[1,2] Daisuke Inoue[1] Takuo Hiratani[2†] Takahiro Tomiyasu[2‡]
Tatsuya Uryu[2] Nagisa Nakamura[2] Nobuhiko Nishiyama[1,2], and Shigehisa Arai[1,2]
[1] *Institute of Innovative Research (IIR), Tokyo Institute of Technology, Tokyo 152-8552, Japan*
[2] *Department of Electrical and Electronic Engineering, Tokyo Institute of Technology, Tokyo 152-8552, Japan*
Tel: +81357342555, e-mail: amemiya.t.ab@m.titech.ac.jp, arai@pe.titech.ac.jp
[†]*Currently in Sumitomo Electric Industries, Ltd*
[‡]*Currently in Furukawa Electric Co., Ltd*

ABSTRACT

Toward the practical use of on-chip optical interconnection in LSIs, we developed an ultralow-power DR laser made in an InP-based membrane on a silicon substrate. The device showed a low threshold current of 0.21 mA, a high differential quantum efficiency of 32 %, and a maximum light output of 0.5 mW. Demonstration of data transmission confirmed a small energy cost of 93 fJ/bit at 20 Gbps operation.

Keywords: Semiconductor laser, III-V semiconductors, Optical interconnection, Photonic integrated circuits.

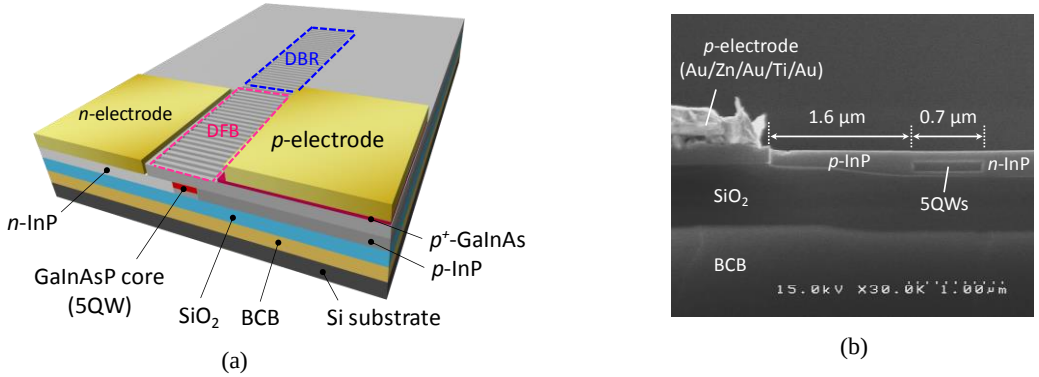
1. AIMING FOR ON-CHIP OPTICAL INTERCONNECTN

Silicon LSIs have rapidly advanced their performance by increasing the degree of their integration. In consequence, the interconnection delay of inter-block data communication (especially between CPU and memory) in a chip is becoming a dominant limiting factor on LSI performance, which is known as an 'interconnect bottleneck'. To overcome this problem, several potential countermeasures have been proposed. Especially the on-chip optical interconnection is very promising because it has less transmission delay and electromagnetic interference.

A laser is a key device for this purpose and has to satisfy several requirements for on-chip operation. First, it must be compatible with a silicon platform. Second, it must operate with low driving energy. Considering various factors, the allowable driving energy for on-chip data communication has been estimated to be 100 fJ/bit or less [1]. Thirdly, the laser must produce sufficient light output for high-speed communication with a low bit error rate (BER). For example, light output is needed to be 0.16 mW or more for 10 Gbps transmission with BER of 10^{-9} or less, a GaInAs PIN photodetector, and an intra-chip link loss of 5dB. To meet these requirements, we have developed a distributed-reflector laser (DR laser) made in a GaInAsP membrane on a silicon platform. The details are described below.

2. STRUCTURE OF MEMBRANE DR LASER WITH LOW POWER CONSUMPTION

The point of our idea is to make the core of waveguides (active region of lasers) in a form of a GaInAsP/InP membrane sandwiched between air and SiO_2 layers (see Fig. 1(a)). Strong optical confinement can be achieved in the core because the refractive indices of air and SiO_2 are far smaller than that of III-V semiconductors. This enables laser operation at very low input power as compared to ordinary semiconductor lasers [2]. We made actual devices on a SiO_2/Si substrate. Typical structural parameters of the device were: 32-μm-long distributed feedback (DFB) region, 50-μm-long distributed Bragg reflector (DBR), 296-nm grating period, and 0.7-μm grating stripe



(a) (b)

Fig. 1. (a) Structure of membrane distributed-reflector (DR) laser, (b) Cross sectional SEM image near *p*-electrode and quantum-well (QW) gain region.

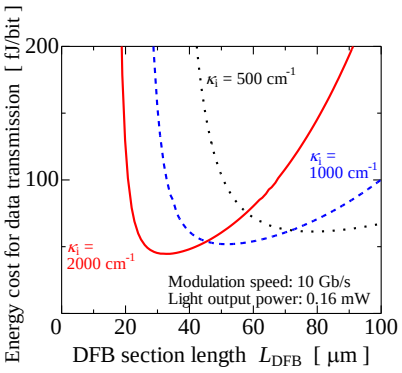


Fig. 2. Energy cost calculated for various index coupling coefficient as a function of DFB length [4].

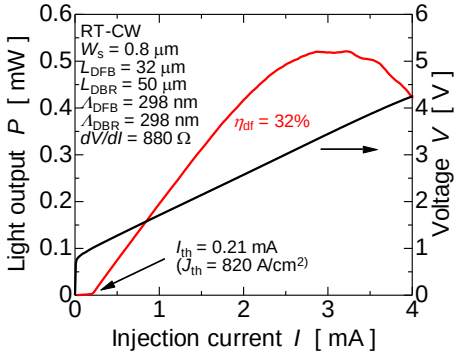


Fig. 3. Light output and bias voltage characteristics of device, measured as a function of injection current [7].

width. The active region consists of five GaInAsP strained quantum wells sandwiched by InP layers with a total thickness of 270 nm. Figure 1(b) shows part of the cross section of the device.

Figure 2 shows the energy cost as a function of the length of the DFB region, calculated for various values of the index coupling coefficient, assuming 10-Gbps operation and 0.16-mW light output power. Other structural parameters were set equal to the typical values mentioned above. As DFB length decreases, the energy cost increases because of increases in differential resistance and threshold current of the device. And as DFB length increases, the energy cost again increases because of a decrease in differential quantum efficiency and an increase in threshold current. There is therefore an optimal DFB length that minimizes the energy cost. The optimal DFB length depends on the index-coupling coefficient, but the minimum energy cost is almost the same value. For the index-coupling coefficient of 1000 cm^{-1}, the energy cost can be reduced to 52 fJ/bit, using 50-μm DBR length.

3. STATIC CHARACTERISTICS OF FABRICATED MEMBRANE LASERS

Figure 3 shows the light output and bias voltage characteristics of the DR laser, measured under room-temperature continuous-wave (RT-CW) condition. The threshold current I_{th} was 0.21 mA (threshold current density J_{th} = 820 A/cm^2). The light output increased linearly with injection current, showing an external differential quantum efficiency of front-side output, η_{df}, of 32% for injection current I < 1.5 mA and a maximum power conversion efficiency (wall-plug efficiency), η_{PC}, at an output power 0.16 mW of 12.2% [3]. They were slightly improved to η_{df} of 36% and η_{PC} of 14.6% in a different device [4].

4. DYNAMIC OPERATION OF MEMBRANE LASERS

From the small-signal modulation response, we obtained the relaxation oscillation frequency f_r and 3dB bandwidth f_{3dB} as a function of the square root of injection current. Figure 4 shows the result. The slope of f_r curve (i.e. modulation current efficiency factor) and that of f_{3dB} were 12 and 15 GHz/mA$^{1/2}$, respectively.

We demonstrated high-speed direct modulation of the DR laser at a data rate of 20 Gbps. Figure 5 shows the bit error rate (BER) as a function of average received power after amplification by an EDFA. Bias current for the DR laser were set to 1.06 mA (bias voltage = 1.76 V). The minimum BER of 6.4×10^{-10} was obtained at an average

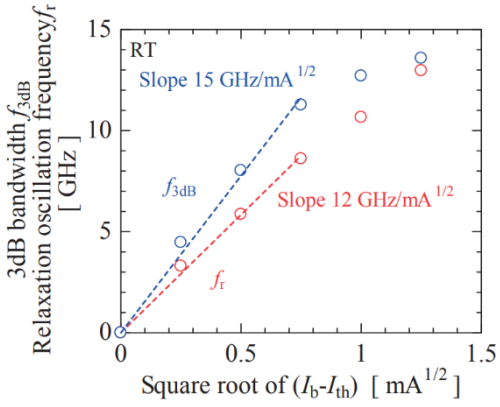


Fig. 4. Relaxation oscillation frequency f_r and 3dB bandwidth f_{3dB} vs. square root of effective injection current (I - I_{th}) [7].

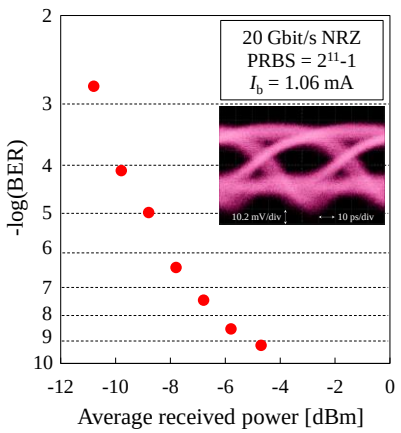


Fig. 5. Bit error rate vs. receiver input power measured for 20 Gbps operation with injection current I = 5I_{th}. Inset is eye diagram at BER of 6.4 ×10^{-10} [7].

Table I. Performance of various DFB/DR lasers made on Si substrate

Structure	Area [μm^2]	Ith [mA]	DQE [%/facet]	Max. output power [mW]	Mod. speed [Gb/s]	Energy cost [fJ/bit]	Group [ref.]	year
DFB†	800	8.8	~7	3.75	12.5	~11000	UCSB [8]	2014
DFB‡	73	0.9	~11	0.93	25.8	171	NTT [9]	2015
DFB†	~1100	17	~15	6	40	~5000	Ghent Univ. [10]	2016
DR‡	40	0.6	~21	~0.65	25.8	132	NTT [11]	2016
DFB‡	30	0.21	5	~0.05	10	230	Tokyo Tech [12]	2016
DR‡	67	0.21	32	~0.5	20	93	Tokyo Tech [7]	2018

† Laser is combined with Si waveguides.
‡ Laser is monolithically integrated with InP/GaInAsP waveguides.

received power of -4.8 dBm. This result shows the feasibility of using the membrane DR laser as an ultralow-power light source for on-chip optical interconnections. Inset in Fig. 5 shows the 20-Gbit/s eye diagram measured at an average received power of -4.8 dBm, where eye opening can be confirmed. Noise was moderately suppressed because the absorption region at the rear of the laser prevented signal reflection back to the cavity. The energy cost was 93 fJ/bit. To the best of our knowledge, it is the lowest value reported for membrane-based DFB and DR lasers.

5. COMPARISON OF VARIOUS DFB/DR LASERS MADE ON SI SUBSTRATE

The performance of our membrane laser is summarized in Table I, compared with those of other DFB lasers and DR ones made on Si substrate. DFB lasers hybrid-coupled with Si waveguides have too energy cost for on-chip application. In contrast, lasers combined monolithically with InP/GaInAsP waveguides can achieve low energy cost, and especially our device (bottom in the table) has achieved the minimum value of energy cost. DR lasers (DFB lasers combined with DBR) has a relatively high differential-quantum-efficiency (DQE) because DBR suppresses the unnecessary reflection of light, and our device has achieved the highest DQE. We expect that the energy cost of our device can be lowered down to 50 fJ/bit at 20 Gbps by improving the device structure, especially around the electrodes, to reduce the parasitic resistance of the device.

ACKNOWLEDGMENTS

This research was financially supported by JST-CREST (JPMJCR15N6) and JSPS KAKENHI (#15H05763, #16H06082, #17H03247).

REFERENCES

[1] D. A. B. Miller, "Rationale and challenges for optical interconnects to electronic chips," *Proc. IEEE*, vol. 88, no. 6, pp. 728-749, June 2000. [CrossRef]
[2] S. Arai *et al.*, "GaInAsP/InP Membrane Lasers for Optical Interconnects," *IEEE J. Sel. Top. Quantum Electron.*, vol. 17, no. 5, pp. 1381-1389, Apr. 2011. [CrossRef]
[3] T. Tomiyasu et al., "High-differential quantum efficiency operation of GaInAsP/InP membrane distributed-reflector laser on Si," *Appl. Phys. Express*, vol. 10, no. 6, 062702, June 2017. [CrossRef]
[4] T. Hiratani et al., "High Efficiency Operation of GaInAsP/InP Membrane Distributed-Reflector Laser on Si," *IEEE Photon. Technol. Lett.*, vol. 29, no. 21, pp. 1832-1835, Nov. 2017. [CrossRef]
[5] T. Hiratani *et al.*, "High Efficiency Operation of Membrane Distributed-Reflector Lasers on Silicon Substrate," *IEEE J. Sel. Top. Quantum Electron.*, vol. 23, no. 6, 3700108, Nov. 2017. [CrossRef]
[6] D. Inoue *et al.*, "Integrated Optical Link on Si Substrate Using Membrane Distributed-Feedback Laser and *p-i-n* Photodiode," *IEEE J. Sel. Top. Quantum Electron.*, vol. 23, no. 6, 3700208, Nov. 2017. [CrossRef]
[7] T. Tomiyasu *et al.*, "20-Gbit/s direct modulation of GaInAsP/InP membrane distributed-reflector laser with an energy cost of less than 100 fJ/bit," *Appl. Phys. Express*, vol. 11, no. 1, 012704, Jan. 2018. [CrossRef]
[8] C. Zhang *et al.*, "Low threshold and high speed short cavity distributed feedback hybrid silicon lasers," *Optics Express*, vol. 22, no. 9, pp. 10202-10209, May 2014. [CrossRef]
[9] S. Matsuo *et al.*, "Directly modulated DFB laser on SiO_2/Si substrate for datacenter networks," *IEEE J. Lightwave Technol.*, vol. 33, no. 6, pp. 1217-1222, Mar. 2015. [CrossRef]
[10] A. Abbasi *et al.*, "High speed modulation of a heterogeneously integrated InP/SOI DFB laser," *IEEE J. Lightwave Technol.*, vol. 34, no. 8, pp. 1683-1687, Apr. 2016. [CrossRef]
[11] H. Nishi *et al.*, "Membrane distributed-reflector laser integrated with SiOx-based spot-size converter on Si substrate," *Optics Express*, vol. 24, no. 16, pp. 18346-18352, Aug. 2016. [CrossRef]
[12] D. Inoue *et al.*, "Low-bias current 10 Gbit/s direct modulation of GaInAsP/InP membrane DFB laser on silicon," *Optics Express*, vol. 24, no. 16, pp. 18571-18579, Aug. 2016. [CrossRef]

Micro-transfer printing for advanced scalable hybrid photonic integration

(Invited paper)

R. Loi[1], B. Roycroft[1], J. O'Callaghan[1], J. Justice[1], A. Gocalinska[1], E. Peluchi[1], A. J. Trindade[2], C. A. Bower[2], G. Roelkens[3], B. Corbett[1]

[1] Tyndall National Institute, University College Cork, *Lee Maltings, Cork - Ireland*

Tel: +353212346380, e-mail: brian.corbett@tyndall.ie

[2] X-Celeprint Limited, *Lee Maltings, Cork, - Ireland*

[3] Ghent University-Imec, *Technologiepark-Zwijnaarde 15, Ghent,- Belgium*

ABSTRACT

Integrated photonics has lagged the complexity possible with electronics by orders of magnitude. This is changing with the development of photonic integrated circuits on silicon photonics which has allowed thousands of optical components to be integrated and where many applications in communications and sensing can be addressed. Nevertheless, the key component of a gain block is missing while other functions can have better performance with separately optimised materials. Micro-transfer printing is emerging as an effective, accurate and massively parallel technique for the heterogeneous integration of photonic and electronic devices to different platforms including silicon photonics. We describe some recent development in this technology.

Keywords: Heterogeneous integration, photonic devices, lasers, coupling, silicon photonics.

1. INTRODUCTION

The optimal device structures are distinct for different photonic functions which makes their co-integration challenging. While excellent progress has been made with photonic integrated circuits (PICs), especially using InP platforms for telecommunications, these PICs are expensive to produce due to the limited wafer sizes and complexity of the manufacturing processes. Silicon photonics has now emerged as a scalable large-area platform for integrating photonic devices where waveguides, multiplexing, routing, detection and modulation can be performed [1]. The light source or an optical amplification function has yet to be monolithically integrated on the platform though advances are been made with selective area epitaxy. In the meantime the laser light has to be provided to the silicon waveguides from a separate InP (or GaAs) based material structure. Laser light can be coupled to these silicon waveguides using grating, evanescent or edge coupling. Associated methods to achieve these couplings are, respectively, fibre coupling of an external laser, integration using wafer/die bonding or flip-chip of laser devices.

An alternative approach that is being investigated is the use of the micro-transfer technique [2], [3]. This technique involves the formation and registration of thin (typically < 5 μm thick) coupons of a material structure, releasing these coupons from their source wafer, the sequential, parallel transfer of stamp-selected arrays of the coupons and their bonding to selected matching locations on a target substrate. The technique requires that there is a means to separate the coupons from the source wafer which is achieved with a buried release layer in the layer structure. The process is indicated schematically in Fig. 1. Note that the technique transfers the coupons in an 'epitaxial-side-up' configuration. The primary requirement for bonding on the new substrate is that the mating surfaces are locally flat and co-planar. This can be achieved by a coating the surface of the target substrate with a thin layer of polymer which also assists the bonding. A direct bond can also achieved between the semiconductor surfaces through van der Waals forces that are particularly enabled for thin and small dimensioned coupons. The micro-transfer printing approach allows the material to be transferred to structured substrates such as fully processed target wafers. The source coupons can be unprocessed material or part / fully processed into devices with the appropriate structuring and contacts present. In the former case the coupons have to be structured into the appropriate devices post transfer. This then requires compatibility between the process technologies and material compatibility in the foundry. However, this approach allows for lithographic alignment between waveguides [4]. In the latter case the devices can be tested before transfer and only known-good-die transferred. This also allows the source wafers to be processed in their optimum environment – ie without process limitations. Additional stresses due to the process technology need to be managed in order to prepare the flattest coupons. Transfer print has been demonstrated for multiple materials including III-V devices (InP, GaAs, InAs, GaN), silicon, graphene, and dielectrics. One example of the integration of large numbers of different

components on a single substrate is with displays where separate red, green and blue LED together with a control circuit have been integrated for each pixel in the display [5].

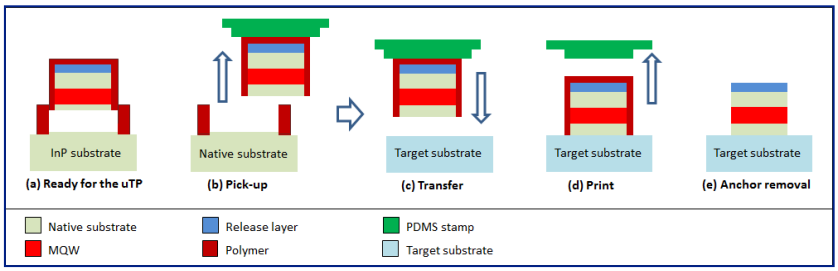


Figure 1. Schematic of the micro-transfer print process indicating the preparation, pick-up and transfer of a single coupon.

2. Transfer of InP lasers to Si

The transfer of InP devices to Si wafers is a pertinent example. InP is the material of choice for lasers, modulators and detectors operating in the 1300 nm to 2000 nm wavelength range. The device structures are typically grown on 50 mm or 75 mm diameter wafers. The wafer size is clearly not compatible with 200 mm or 300 mm diameter wafers from silicon foundries. Yet, the resulting InP wafers are very valuable as many thousands of high performance devices can be made with the material. For example, one 75 mm wafer can easily produce lasers with a total bandwidth of >200 Tb/s. The transfer print process allows an increase in number of lasers with the aim to distribute these lasers so that they can be integrated and aligned with appropriate waveguides.

It is necessary to include a release layer early in the epitaxial structure. The layer should be lattice-matched and its release chemistry be compatible with the other layers within the structure. We compared InGaAs and InAlAs as release layers using a dilute $FeCl_3$ etching solution which is compatible with the standard resists that act as tethers to hold the coupons in place while being undercut. Both release layers are etched with a high selectively with respect to the surrounding InP material. We found that the InGaAs etch rate is highly crystallographic with the etch proceeding along the <010> directions [6]. If the eventual ridge waveguides need to be aligned along the <011> directions, as is used in conventional device processing, then the releasing etch takes several hours with some resultant dishing of the release InP surface. In that case the width of the devices can be limited. On the other hand, the etching of InAlAs has low crystallographic selectivity and also much reduced times to release the coupons. As a result wider coupons can be more easily accommodated with the InAlAs release layer.

We have considered two situations for integrating the laser with silicon waveguides. The first is to use evanescent coupling to an underlying waveguide which couples to gratings in the silicon which provide the feedback [7]. A second approach is to produce stand-along lasers which can be integrated by butt coupling (see below). In that case the laser is fabricated with etched facets to provide feedback [8]. The width of the laser coupons are 60 μm and have a metal-coated rear facet. The device length is 500 μm while the coupon length is longer in order to accommodate bond pads on the chip. Figure 2 shows an optical image of the 1550 nm emitting devices after transfer to a flat silicon substrate and the temperature-dependent light-current characteristics. The performance after transfer is superior to that before transfer due to an improvement in the heat sinking.

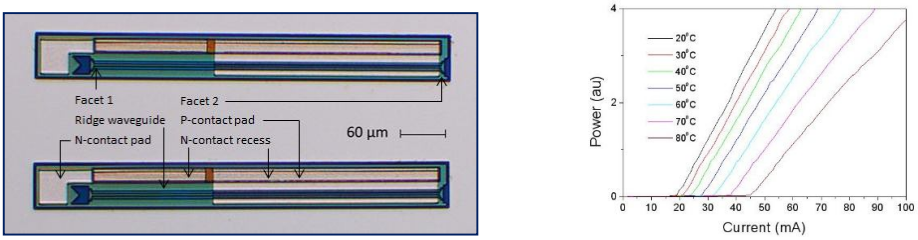


Figure 2. Optical image of transferred etched facet lasers on silicon (left) and temperature-dependent light-current characteristics of transferred 1550 nm ridge waveguide laser (right)

3. Integration with Si waveguide

We are developing a butt coupling approach where the lasers are to be aligned with respect to waveguides on a silicon photonic platform. This requires that there be alignment of the laser and silicon waveguides. The height dimension on the silicon side is controlled by the thickness of the buried oxide layer. A facet is etched at the waveguide end using a chrome mask with the etching stopped at the interface with the thermally-conductive silicon substrate. The laser waveguide height is then referenced with respect to this surface. To obtain the highest potential coupling efficiency the laser mode field should be matched to that of the Si waveguide. The lateral alignment of the laser relies on high contrast fiducials present on both the laser and on the target substrate. Figure 3 shows a schematic of the concept for the laser alignment together with an optical microscope image of the aligned laser. The laser is recessed from the waveguide facet by ~3 micron. The figure shows the spectrum from the laser when out-coupled using the grating on the waveguide.

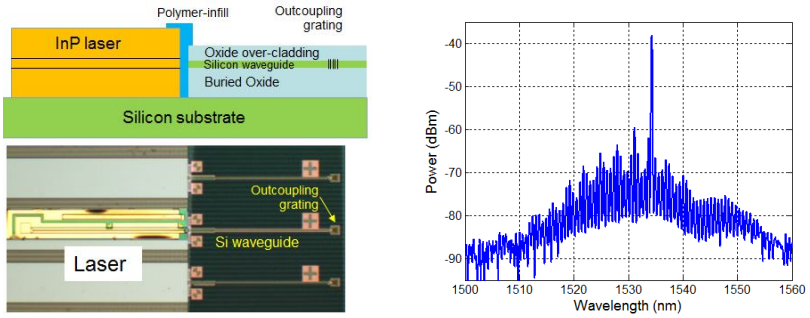


Figure 3. Schematic cross-section of heterogeneously integrated InP laser butt coupled to a silicon photonics platform; optical image of the printed laser aligned to Si waveguide and the out-coupled spectrum

4. CONCLUSIONS

The technology for transfer printing of InP based devices is being developed. Solutions for the transfer of many other thin and small materials can be achieved by engineering. Transfer printing has the potential to be a game changing technology for the heterogeneous integration of components for scalable smart photonic systems.

ACKNOWLEDGEMENTS

This work is part-funded by the European Union's Horizon 2020 Research and Innovation Programme under Grant agreement No. 645314 (TOP-HIT) and by Science Foundation Ireland under 12/RC/2276 (IPIC). We acknowledge the valuable contributions from our many collaborators in those consortia.

REFERENCES

[1] G. Roelkens *et al*., "III-V/silicon photonics for on-chip and intra-chip optical interconnects," *Laser Photon. Rev*., 4, 1–29, 2010.

[2] M. A. Meitl, *et al*, "Transfer Printing by Kinetic Control of Adhesion to an Elastomeric Stamp," *Nature Materials* 5, 33-38, 2006.

[3] B. Corbett, *et al*, "Transfer print techniques for heterogeneous integration of photonic components," *Prog. Quantum Electron.*, 52, 1–17, 2017.

[4] J. Justice, *et al*, "Wafer-scale integration of group III–V lasers on silicon using transfer printing of epitaxial layers," *Nat. Photon*. 6, 612, 2012.

[5] C. A. Bower *et al*, "Emissive displays with transfer-printed assemblies of 8 μm×15 μm inorganic light-emitting diodes," *Photonics Research* A24 5, 2327, 2017.

[6] J. O'Callaghan *et al*, "Comparison of InGaAs and InAlAs sacrificial layers for release of InP-based devices," *Opt. Mat. Expr*., 7, 4408-4414, 2017.

[7] J. Zhang, *et al*, "Transfer-printing-based integration of a III-V-on-silicon distributed feedback laser," *Opt. Exp*., 2018.

[8] R. Loi *et al.*, "Transfer Printing of AlGaInAs/InP Etched Facet Lasers to Si Substrates," *IEEE Photon. J.* 8, 1-10, 2016.

Tb/s-Class InP-Based System-On-Chip Photonic ICs

G. E. Hoefler, R. Going, R. Maher, M. Lauermann, A. Hosseini, M. Lu, N. Kim, P. Studenkov, , S. Corzine, J. Summers, M. Anagnosti, M. Montezari, H. Tsai, J. Zhang, B. Behnia, J. Tang, S. Buggaveeti, T. Vallaitis, J. Osenbach, M. Kuntz, X. Xu, K. Croussore, V. Lal, P. Evans, J. Rahn, T. Butrie, A. Karanicolas, K.-T. Wu, M. Mitchell, M. Ziari, D. Welch, and F. Kish

Infinera Corporation, 140 Caspian Court, Sunnyvale CA 94089
ghoefler@infinera.com

(Invited paper)

Abstract: State-of-the-art monolithically integrated, multi-channel InP-based system on chip (SOC) photonic ICs have been developed to implement Tb/s class coherent transmitters and receivers with extended C-band tunability. A 14-channel PIC architecture is demonstrated enabling 4.9 Tb/s total capacity using 44 Gbaud 16-QAM coherent modulation. Furthermore, multi-channel coherent transmitter PIC with hybrid integrated with SiGe drivers capable of operating up to 1.0 Tb/s per wave, utilizing 100 GBaud, 32QAM modulation are demonstrated.

OCIS codes: (250.0250) Optoelectronics; (060.0060) Fiber optics and optical communications; (250.5300) Photonic integrated circuits; (060.1660) Coherent Communications

1. Introduction

The development of fully integrated optical system-on-chip (SOC) transmitter and receiver solutions has resulted in significant benefits to the economics, power consumption, density, and reliability of high capacity DWDM systems. Traditionally, the use of photonic integrated circuits (PICs) reduces costs by minimizing electrical and optical assembly processes, test apparatus and time. Furthermore, PICs mitigate potential performance degradation due to the many optical couplings required in a discrete component system and enable efficient creation of super-channels, helping the increase of the DWDM line card capacity while reducing operational complexity.

Photonic integrated circuit technologies have contributed to more than an order of magnitude increase in capacity every decade, a trend that started with electroabsorption-modulated lasers [1] and continued through with the commercial introduction of the first fully integrated multi-channel optical SOC 100 Gb/s transmitter and receiver PICs in 2004 [2]. Several generations of commercial SOC InP-based PIC transmitters and receivers have been deployed based on a compact platform that leverages coherent modulation with unique scalability, efficiency and security. A large scale fully integrated optical SOC InP-based coherent PIC platform was demonstrated in a research setting in 2014, by monolithically integrating 40 wavelength channels and over 1700 optical functions on a single chip. The PIC platform demonstrated a 2.25 Tb/s PM-QPSK transmitter with over a 1 THz optical bandwidth [3]. A 6-channel implementation of with C-Band tunable 1.2 Tb/s transceiver modules operating at 33Gbaud, 16-QAM was also developed and transitioned into manufacturing in 2016. Each channel on the PIC comprises of an integrated widely-tunable laser capable of continuous tuning over the extended C-band (4.8 THz). The progression in performance of system-on-chip PICs has resulted in the demonstration and deployment of multiple generations of optical engines [3-7].

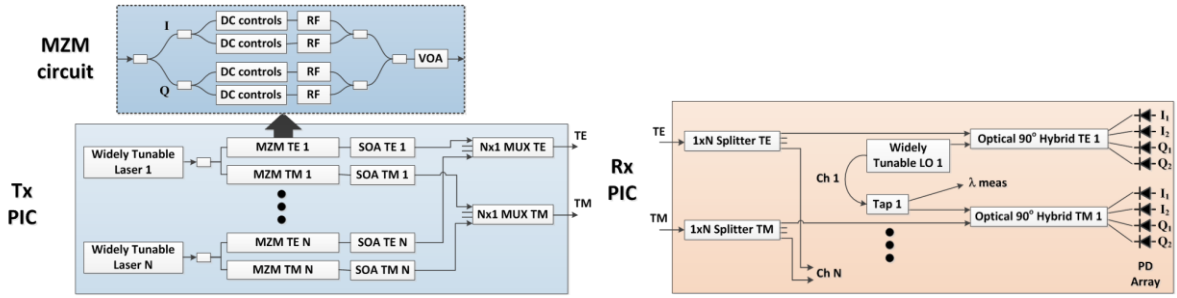
A fully integrated InP-based coherent transmitter PIC with extended C-Band tunability architecture was recently shown to support 14 channels on a single chip operating at 33 and 44 Gbaud per channel under 16-QAM dual polarization [6]. To further scale the platform beyond 44Gbaud, a 2-channel Tx PIC and Rx PIC assembly was realized with hybrid integrated SiGe drivers and amplifiers. This test vehicle was used to demonstrate transmission between TxPIC and RxPIC over a variety of distances, from 200 Km to 1400 Km and with a variety of symbol rates and modulation formats. Up to 1 Tb/s per wavelength capacity is shown by operating at 100Gbaud under 32-QAM (back-to-back). Additionally, 100Gbaud under 16-QAM signals generated with an integrated TxPIC assembly are transmitted over a distance of 1400 Km using a reference receiver. We believe this are the highest data-rate and capacity coherent PIC results to date and demonstrate the viability of 100Gbaud operation of fully integrated multi-channel InP-based PICs and SiGe electronic assemblies [7].

The ability to monolithically integrate lasers, optical amplifiers, saturable absorbers, modulators and low-loss passive waveguides on an InP-based platform enables the realization of systems on chip for a variety of applications. In this paper, we present an overview of the architecture of extended C-Band tunable coherent transmitter and receiver

PICs, representing the state-of-the-art for functional integration of InP-based transmitter technology [2-6].

2. Multi-Tbps System-on-Chip Architecture

Figure 1 (a) shows a schematic of the multi-channel Tx PIC integration, up to 14-channels were realized and reported in [5]. Each channel includes an independently controlled, widely-tunable laser (WTL) providing continuous tuning over the entire extended C-band (4.8 THz). The output from each laser is split into two nested Mach-Zehnder Modulators (IQ-MZMs). At the output of the MZM, a variable optical attenuator (VOA) and a semiconductor amplifier (SOA) is used to provide additional power balancing and amplification of the output power from the Tx PIC. DC control elements in each of the four arms of the nested MZM are used for power balancing and biasing the modulator to the required phase condition. Each MZM on these PICs is designed to run at symbol rates of up to 100 Gbaud and support modulation formats with variable spectral efficiency.



a) b)

Fig. 1 (a) Schematic of the multi-channel widely tunable coherent Tx PIC architecture. (b) Schematic of the Rx PIC architecture.

The corresponding receiver (Rx) PIC architecture is shown in Fig. 1(b). The monolithically integrated InP receiver PIC accepts two inputs polarized to be TE on chip from free space optics that rotate one signal path polarization from TM to TE. Each polarization signal path is split with a multi-mode interference coupler (MMI) based 1xN power splitter to feed N 90° optical hybrids. The optical hybrids mix the incoming signals with one of the independently controlled, integrated widely tunable local oscillator laser outputs. MMI-based optical taps on the laser output paths are used to couple light out from the chip to measure wavelength over the extended C-band (>40 nm). The PICs described herein enable each channel on the multi-channel PIC to span the entire extended C-band (40 nm), maximizing optical channel utilization and capacity as well as enabling reconfigurability on a super-channel or on a per-channel basis [5].

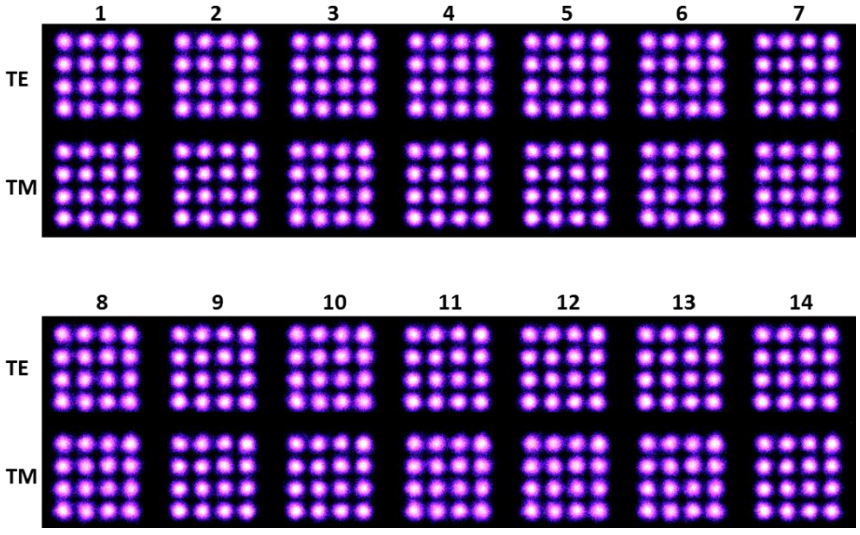


Fig. 2: Back-to-back 44 Gbaud constellations for all 14 channels on a Tx PIC as measured using an Rx PIC-based receiver. The figure shows only the outermost sub-carrier on each polarization for a dual-pol 16-QAM signal.

The 14-channel Rx and Tx PICs were mounted and wire-bonded to ceramic carriers with a multi-channel high-speed trans-impedance amplifier (TIA) ASIC and MZM driver, respectively. The RF elements on the PIC were

directly probed with a custom high-speed probed card. An arbitrary waveform generator and amplifier were used to provide the RF signals to the modulator. Figure 2 shows the recovered 44 Gbaud x 16-QAM constellations for two polarizations and all 14 channels integrated on the widely tunable coherent transmitter PIC. All channels on the PIC achieved performance above the required FEC limit, demonstrating a capacity capability of 4.9 Tb/s for a single PIC operating at 44 Gbaud data rates [6].

To demonstrate transmission between TxPIC and RxPIC platforms, a 2-channel SOC test vehicle was assembled with hybrid integrated 180 nm SiGe BiCMOS electronic drivers and amplifiers. The Tx and Rx PICs were mounted on a carrier with a two-channel MZMD and TIA, respectively. Each driver and amplifier supplied 8-high-speed streams. A commercial line system was used to generate and transmit data signals at various formats and symbol rates. Utilizing the TxPIC assembly, 100 Gbaud x 32-QAM signals were transmitted to the reference receiver in a back-to-back configuration. Figure 3 shows the transmitted signals, with a total data rate capability of 1 Tb/s on a single wavelength, and a Q^2-factor above 6.2 dB, using SD-FEC[6] with 25% overhead allows for 800 Gb/s per wavelength. Furthermore, a net payload transmission in excess of 600Gb/s was obtained with three different combinations of symbol rates and modulation formats (data not shown) at 66Gbaud x 64-QAM, 88Gbaud x 16-QAM, 100Gbaud x 16-QAM. Each demonstration with successively longer distance 200, 600, 1400Km [7].

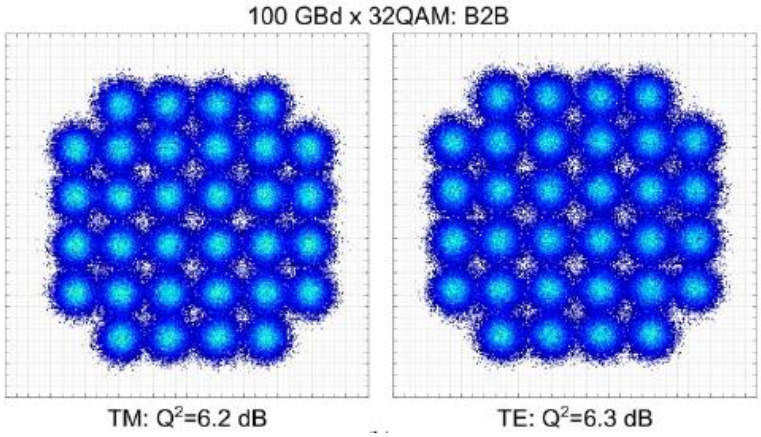


Fig. 3: Constellations of the received 100 Gbaud, 32QAM signal from the TxPIC assembly to a reference receiver in back-to-back configuration.

3. Conclusion

We have presented an overview of the state-of-the-art functional integration of system-on-chip utilizing InP-based PICs to realize multi-channel transceivers with extended C-band tunability for optical communication applications. The Tx and Rx PICs described in this paper are scalable, up to 1700 optical functions were integrated in a 40-channel PIC. A multi-channel architecture has been commercialized using a 6-channel transceiver module that integrates extended C-Band widely tunable lasers and with 1.2 Tb/s total payload capacity. Furthermore, using SOC Tx and Rx PICs we have demonstrated data rates of up to 100 Gbaud per channel under 32-QAM dual-polarization modulation, achieving up to 1 Tb/s per wavelength. The utility of integrated multi-channel InP-based PICs to achieve high-baud rates and high order modulation formats over a wide range of distances has been demonstrated. The InP-based SOC integration platform and multi-channel architecture offers commercial solutions that deliver multi-terabit scalability with security, simplicity, and operational efficiency.

4. References

[1] Y. Kawamura et al., ‘‘Monolithic integration of InGaAsP/InP DFB lasers and InGaAs/InAlAs MQW optical modulators,’’ Electron. Lett., vol. 22, pp. 242–243, 1986.
[2] R. Nagarajan et al., “Large scale photonic integrated circuits,” IEEE J. Sel. Top. Quantum Elec., vol. 11, no. 1, pp. 50–65, Jan/Feb. 2005.
[3] J. Summers et al., “40 Channels x 57 Gb/s monolithically integrated InP-based coherent photonic transmitter,” in 2014 ECOC, Cannes, France.
[4] F. Kish et al., “From Visible Light-Emitting Diodes to Large-Scale III–V Photonic Integrated Circuits,” Proc. of the IEEE, vol. 101, no. 10, pp. 2255-2270 (2013).
[5] V. Lal et al., “Full C-Band Tunable Coherent Transmitter and Receiver InP Photonic Integrated Circuits,” in 2016 ECOC, Dusseldorf, Germany.
[6] V. Lal et al., "Extended C-Band Tunable Multi-channel InP-based Coherent Transmitter PICs," in J. Lightwave Tech, Feb 2017, no.99.
[7] Going, Ryan, et al. "Multi-channel InP-based Coherent PICs with Hybrid Integrated SiGe Electronics Operating up to 100 GBd, 32QAM," in 2017 ECOC, Los Angeles, USA.

Microresonator soliton frequency combs

Maxim Karpov[1], John Jost[1], Hairun Guo[1], Martin H.P. Pfeiffer[1], Erwan Lucas[1], Junqiu Liu[1], Miles Anderson[1], Arslan S. Raja[1], Bahareh Ghadiani[1], Anton Lukashschuk[1], Wenle Weng[1], Romain Bouchand[1], Jia-Jung Ho[1], Michael Geiselmann[1,2], Tobias J. Kippenberg[1,*]

[1]*Laboratory of Photonics and Quantum Measurements (LPQM), École Polytechnique Fédérale de Lausanne (EPFL), Lausanne, CH-1015, Switzerland*

[2]*LiGenTec SA, CH-1015 Lausanne, Switzerland*

[*]*e-mail: tobias.kippenberg@epfl.ch*

ABSTRACT

Microresonator frequency combs provide access to compact, photonic-integrated optical comb with large mode spacing operating in a soliton regime. We will discuss the physics of such solitons and their applications in telecommunication and distance measurements.

Keywords: Integrated photonics, nonlinear optics, optical frequency combs, microresonators, optical solitons.

1 INTRODUCTION

Optical frequency combs [1], [2] provide equidistant markers in the IR, visible and UV and have become a pivotal tool for frequency metrology and constituted the underlying principle of optical atomic clocks. They are also finding use in other areas, such as broadband spectroscopy or low noise microwave generation. In 2007 a new method to generate optical combs was discovered based on high-Q optical microresonators[3], [4]. Such microresonator frequency combs have since then emerged as a new and widely investigated method with which combs can be generated via parametric frequency conversion of a continuous wave (CW) laser inside a high-Q resonator via the Kerr nonlinearity.

Over the past years the detailed understanding of the microresonator-based comb formation process has been gained, and regimes where such nonlinear driven dissipative microresonator system can support the formation of intracavity pulses - dissipative Kerr solitons (DKS), that not only provide low-noise optical frequency combs, but moreover give access to femtosecond pulses. Such DKS have unlocked the full potential of soliton microcombs by providing access to fully coherent and broadband combs obtained via soliton broadening effects. Dissipative Kerr solitons have now been generated in a wide variety of resonators, including crystalline microresonators and planar platfroms which are compatible with photonic integration based on silicon or silicon nitride (Si_3N_4). We will discuss the regime of dissipative Kerr solitons (DKS), first discovered in crystalline resonators [5], and our current understanding including its formation dynamics and behaviour under different effects, such as the impact of Raman scattering of the microresonator medium [6] and higher-order dispersion effect, including the emission of soliton dispersive waves (soliton-induced Cherenkov radiation)[7]. We also demonstrate a rich panel of instabilities available for DKS states due to their nonlinear origin, which includes the observation of different types of breathers [8], the influence of avoided mode crossings on breather and the repetition rate [9], [10], as well as methods to deterministically access the single soliton regime[11]. Taken together this has enabled to reliably access single soliton states in photonic-chip-based resonators, in particular those utilizing the photonic Damascene process [12].

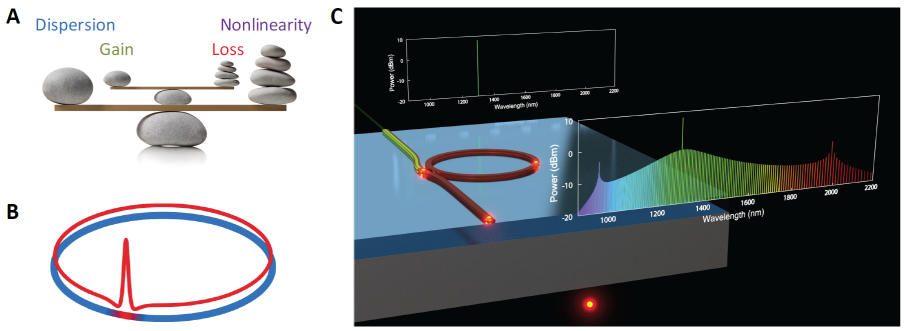


Figure 1. **Dissipative Kerr solitons** (a) Double balance between dispersion, nonlinearity, pump and cavity losses that is achieved for stable dissipative Kerr solitons generated in nonlinear Kerr cavity. (b) Intracavity waveform of the dissipative Kerr soliton. (c) Dissipative Kerr soliton formation in CW-driven on-chip nonlinear microresonator.

Dissipative Kerr solitons enable optical frequency combs that can span more than a full octave using soliton-induced Cherenkov radiation, which extends the combs bandwidth and power in the spectral wings via dispersive

waves. Such DKS have been enabled to count the cycles of light[13], allow 2f-3f self referencing [14]. Using such soliton Kerr optical frequency combs in a SiN microresonator we have recently demonstrated with the group of C. Koos (KIT) massively parallel coherent communication, with dual combs for both the source and as massively parallel LO for the coherent receiver[15]. Moreover, using a pair of photonic-chip-based frequency combs, we have demonstrated dual-comb distance measurements, with record acquisition rates due to the combs large mode spacing (100 GHz). Our recent work moreover has shown that DKS can be extended to the biological imaging window at 1 micron, relevant for e.g. Raman spectral imaging or OCT [16]. Soliton microcombs have the potential to advance timekeeping, metrology or telecommunication by providing a technology amenable to full photonic integration, low power consumption and large comb bandwidth with high repetition rates.

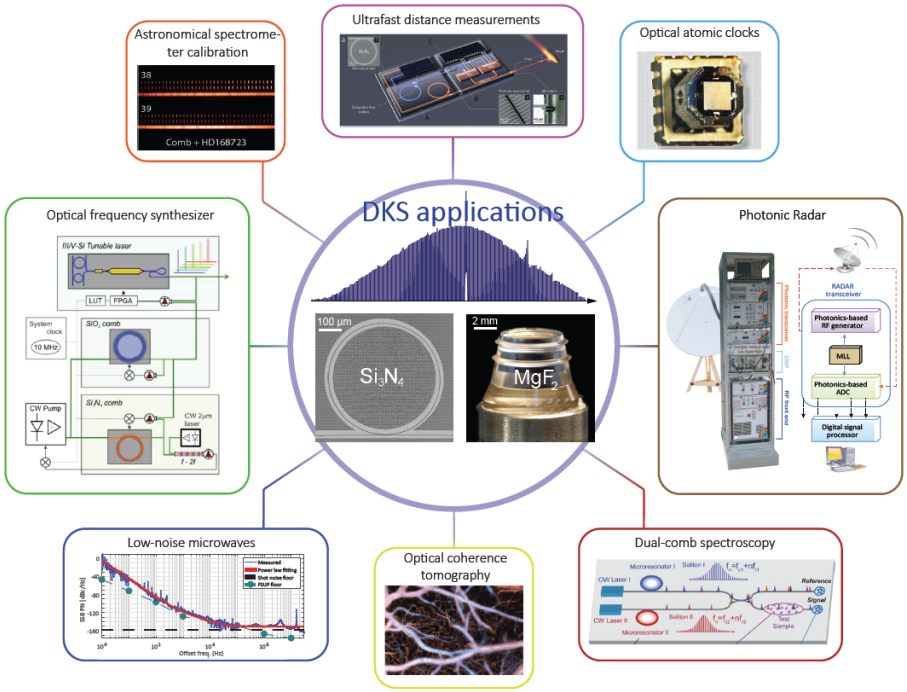


Figure 2. **Application of dissipative Kerr solitons**

REFERENCES

[1] S. T. Cundiff and J. Ye, "Colloquium: Femtosecond optical frequency combs," Reviews of Modern Physics, vol.75, (2003)

[2] T. Udem, R. Holzwarth, and T. W. Hänsch "Optical frequency metrology," Nature vol.416, p.6877 (2002).

[3] P. Del'Haye et al, "Optical frequency comb generation from a monolithic resonator," Nature vol.450, p.7173 (2007).

[4] T. J. Kippenberg, R.Holzwarth and S.Diddams, "Microresonator-based optical frequency comb," Science vol. 332, p.6029 (2011).

[5] T. Herr et al, "Temporal solitons in optical microresonators," Nat.Phot. Vol.8, p.2 (2014).

[6] M. Karpov et al, "Raman self-frequency shift of dissipative Kerr solitons in optical microresonator," Phys.Rev.Lett. 116(10), (2016).

[7] V. Brasch et al, "Photonic chip-based optical frequency comb using soliton Cherenkov radiation," Science vol.351, p.6271 (2016).

[8] E. Lucas et al, "Breathing dissipative solitons in optical microresonators," Nat.Comm 8(1), (2017).

[9] H. Guo et al, "Intermode breather solitons in optical microresonators," Phys.Rev.X 7(4) (2017).

[10] E. Lucas et al, "Detuning-dependent properties and dispersion-induced instabilities of temporal dissipative Kerr solitons in optical microresonators," Phys.Rev.A. 95(4) (2017).

[11] H. Guo et al, "Universal formation and deterministic switching of dissipative Kerr solitons in optical microresonators," Nat.Phys. 13 (2017).

[12] M. H. P. Pfeiffer et al, "Photonic Damascene process for integrated high-Q microresonator based nonlinear photonics," Optica 3(1), (2016).

[13] J. D. Jost et al, "Counting the cycles of light using a self-referenced optical microresonator," Optica 2(8), (2015).

[14] V. Brasch et al, "Self-referenced photonic chip soliton Kerr frequency comb," Light: Science & Applications 6(1), (2017).

[15] P. Marin-Palomo et al, "Microresonator-based solitons for massively parallel coherent optical communications," Nature 546, p.7657, (2017).

[16] M. Karpov et al, "Photonic chip-based soliton frequency combs covering the biological imaging window," Nat.Comm 9(1) (2018).

Silicon photonic biosensors

Invited paper

C. Ciminelli, D. Conteduca, F. Dell'Olio, M.N. Armenise
Polytechnic University of Bari, Via Edoardo Orabona, 4, 70126 Bari - Italy
Tel: +390805963404, e-mail: caterina.ciminelli@poliba.it

ABSTRACT

Silicon-based optical biosensors used for biomedical applications are described. In particular, integrated optical devices and their advantages, in terms of high performance and compactness, and also high reliability and long life term, have been reported. Since the last years, these features have been allowing to realize high-efficiency biosensing platforms with on-chip integration of several biosensors for a multi-analyte detection. Many lab-on-chip systems integrated in portable medical instruments have been proposed in literature and already commercialized in the worldwide market, so reaching extraordinary improvements in the early detection and monitoring of several diseases. Therefore, fast and accurate self-tests achievable with silicon photonic biosensors are remarkably opening new possibilities and applications in the healthcare industry.

Keywords: Biosensors, Silicon Photonics, Biophotonics

1. INTRODUCTION

In the last decades a strong effort has been observed in the healthcare industry to improve the quality of services for patients, in order to reduce the number of deaths and improve the outcomes in a shorter time. This corresponds to a better patients' life quality and also remarkably reduced costs for Health System. In particular, many advantages have been achieved by adopting electronic patient records and by developing a better organization and management of first aid centres and hospitals to reduce the average hospitalization period for each patient with a continuous monitoring at home after the hospital discharge without requiring expert users. The recent spread of point-of-care (POC) technologies is enabling such change in the worldwide Health Systems, because high performance and accuracy are guaranteed by the biosensors integrated in these biomedical systems together with high portability and ease of handling, so allowing their use also by not expert users in every place with no laboratory infrastructures [1]. Many improvements have been reached for several widespread diseases to detect viral infections and allergies, but many farther results can be also obtained for many stigmatized diseases for which the absence of fast and cheap tests still represent one of the first causes of death.
A further step for the next generation of biosensors in POC systems is to reach a stronger efficiency with a better resolution, with the aim of enabling their use also for other dangerous and deadly human diseases, such as cancer, cardiovascular diseases and genetics [2], for which the prevention at first stages represents the first reason of survival. Nowadays, similar diseases can be detected and monitored with bulky and expensive medical instruments and long and complex processes carried out by expert users are also necessary. Therefore, novel techniques and devices have been investigated to overcome such limitations in the last years.

2. STATE-OF-THE-ART OF SILICON-BASED PHOTONIC BIOSENSORS

An ultra-compact footprint and high resolution together with reliability and versatility represent the main features required to biosensors, in order to facilitate their integration in portable instruments.
The best performance in terms of resolution, compactness and reliability have been obtained with optical biosensors also due to the ease of on-chip integration with microfluidics, so opening new opportunities and applications for diseases detection and drug delivery [3].

Several configurations, technologies and materials have been proposed to realize high-efficiency optical biosensors. In particular, silicon technology is the most largely used due to the extraordinary improvements observed in nanofabrication, that makes possible to obtain high control and high reliability for the final pattern of the silicon-based optical biosensors with remarkable advantages in terms of cost-efficiency and mass production, together with a stability much better than other materials, such as polymers. Furthermore, the CMOS compatibility of silicon enables the on-chip integration of electronic components together with the optical biosensors, which is necessary to realize lab-on-chip systems for the real-time analysis and data transfer to a database of patient records or medical centres, besides low cost, low power consumption and long life term [4].

The lowest values of limit of detection (LOD) have been obtained with silicon optical devices based on Mach-Zehnder (MZI) [5], Bimodal Waveguide and Young interferometers [6]. In particular, a value of LOD up to 10^{-7} RIU has been achieved with the MZI configurations [5] and even lower (LOD < 10^{-8} RIU) with the latter ones [6]. These very-low resolution values provide an extraordinary mass sensitivity, as demonstrated in [5], where the DNA hybridization of the BRCA-1 gene has been obtained, which is involved in breast cancer development, with a detection limit of this biological element up to 0.06 pg/mm^2. The limitation of the interferometric structures is mainly related to their large footprint with a length also of 1.5 cm [5], which makes difficult their on-chip integration in particular with an array of biosensors for a multi-analyte detection. Significant improvements have been realised with integrated label-free optical biosensors in silicon technology, and particularly, with resonant cavities, because light-matter interaction is stronger in optical resonators than conventional optical waveguides and this allows higher sensitivity together with small volumes [2]. Photonic crystal (PhC) cavities and microring resonators (MRR) have demonstrated the highest values of the figure of merit *S/A*, where *S* is the device sensitivity and *A* is the device footprint. A values of LOD ~ 10^{-5} RIU has been already demonstrated with PhC cavities with ultra-compact device footprints (< 10 μm^2), up to 5 orders of magnitude smaller than interferometers. Further improvements have been attained by including a slotted waveguide in the PhC structures, because of an enhancement of the *Q/V* ratio, which is strongly related to light-matter interactions [7]. In particular, Di Falco et al. in [7] have demonstrated a LOD ~ 10^{-6} RIU with a PhC slotted cavity and such performance can provide the detection and the monitoring of low concentrations of DNA and proteins, such as BSA, streptavidin and biotin.

Higher performance have been also obtained with silicon microring resonators, with a device footprint slightly larger than that typically obtained with PhC cavities, but several orders of magnitude smaller than interferometers, so facilitating their on-chip integration with ultra-high sensitivity [3]. A resolution of 0.3 pg/mm^2 has been obtained with conventional microring resonators with $A \sim 10^3$ μm^2, enabling the detection of low concentration of proteins [8]. Dell'Olio et al. in [3] have proposed a novel configuration of a slotted microring resonator (see Fig. 1).

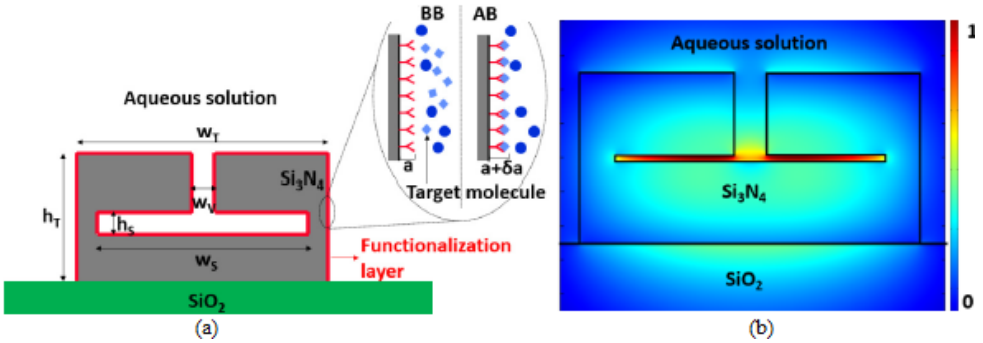


Fig. 1. (a) Cross-section of the waveguide of the slotted MRR configuration and (b) fundamental quasi-TM mode distribution.

The biosensors allows to strongly confine the optical energy at resonance in the ultra-small slot with a consequent enhancement of light-matter interaction, so obtaining an ultra-high resolution of 0.2 ng/mL, corresponding to a value of LOD up to 0.06 pg/mm^2, with an improvement of 5 times the state-of-the-art of integrated silicon optical biosensors with MRR devices. Similar performance makes microring resonators suitable to realize a high-efficiency biosensing platform with an on-chip integration of several biosensors for a multi-analyte detection. For instance, the biosensing platform proposed in [3], made by an array of different microring resonators, potentially allow the monitoring of several biomarkers for early detection of lung cancer.

High performance of optical biosensors, confirmed by the very-low values of LOD, have been also proposed with plasmonic structures [9]. In particular, Surface Plasmon Resonance (SPR) configurations based on the well-known Kretschmann configuration have demonstrated a LOD < 10^{-7} RIU [9]. Such structures are realized by a properly-functionalized thin metal film on a prism glass and they are excited by a light beam passing through the glass prism. These configurations are very sensitive to any molecular interaction in close proximity of the functionalization layer that can be monitored by the plasmon resonance shift. However, SPR instruments are bulky and their miniaturization is challenging due to the optics required to couple light into the metal film, therefore, new plasmonic technologies at the nanoscale for biosensing, e.g. those based on localized SPRs excited in metal nanoparticles or plasmonic nanopores and nanoholes in thin metal films, are currently under investigation for lab-on-chip microsystems. Among those technologies, planar resonant structures where light is confined in surface plasmon polariton (SPP) waveguides are very advantageous because a planar resonant biosensor can be easily arrayed due to a footprint of a few μm^2, and exhibits a resolution that is compliant to the requirements of many

applications in the biomedical environment. A strong advantage of planar metal cavities used as biosensors is the compatibility with a silicon-based optical chip, so including the possibility to be manufactured by the standard fabrication tools and techniques widely utilized in micro and nanoelectronics. In the last years, several silicon-based biosensing platforms with the integration of plasmonic cavities have been proposed aiming at improving the sensor resolution and obtaining ultra-compact devices to carry out a multi-analyte detection with a large array of biosensors in the same platform [10]. In particular, Dell'Olio et al. have proposed in [10] a bio-multisensing platform for the selective label-free detection of protein biomarkers. Several biosensors have been included in the platform and each of them is based on a plasmonic nanocavity consisting of a periodic metal structure (see Fig. 2).

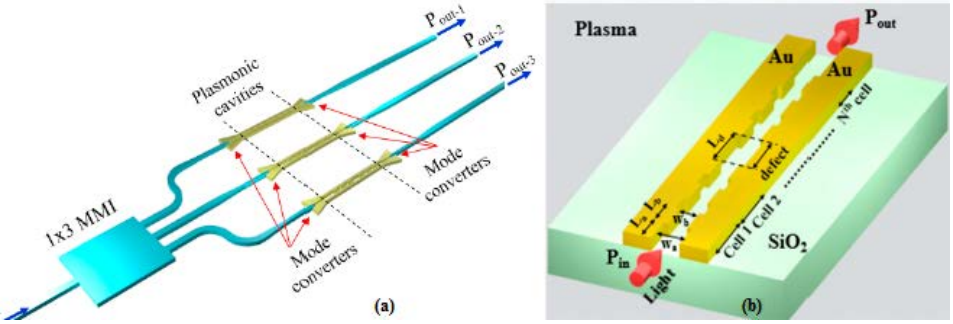


Fig. 2. (a) Silicon-based biosensing platform with (b) a zoom of the plasmonic cavity as sensing element [10]

The extreme energy confinement in an ultra-small region allows to enhance light-matter interaction, and a LOD = 0.42 μg/mL has been obtained. Such performance is not comparable to the state-of-the-art of integrated photonic biosensors, because the resolution is 128 pg/mm^2 (4 orders of magnitude lower than performance obtained with slotted MRR [3]), but very suitable for some medical applications, such as the study of coronary artery diseases, because the risky levels of the main biomarkers are at least one order of magnitude higher than the device resolution. The main advantage of the proposed biosensing platform is the high compatibility to the silicon technology. In fact, each sensor is connected to a hybrid converter that enables the conversion of the plasmonic mode in an optical one propagating in conventional low-loss silicon-based waveguides. The sensors and the converters have a very-compact device, so enabling the integration of all optical components and, potentially, also the electronic ones in the same optical chip to obtain a high-efficiency LOC system as biosensing platform.

CONCLUSIONS

A description of the state-of-the-art of silicon optical biosensors has been proposed with a focus on their features and advantages in terms of efficiency, resolution and compactness compared to the performance obtained with the commercialized biosensors with different configurations and materials. A strong improvement obtained by silicon technology is the availability to realize biosensing platforms with on-chip integration of several biosensors for a multi-analyte detection, facilitating the spread of new high-efficiency portable medical instruments that can improve the early detection and monitoring of several diseases with fast and accurate self-tests without requiring expert users or laboratory infrastructures.

References

1) S. A. Soper et al., "Point-of-care biosensor systems for cancer diagnostic/prognostics", *Biosensors and Bioelectronics*, vol. 21, no. 10, pp. 1932-1942, April 2006.
2) C. Ciminelli et al., "High performance SOI microring resonator for biochemical sensing", *Optics and Laser Technology*, vol. 59, pp. 60-67, July 2014.
3) F. Dell'Olio et al., "New ultrasensitive resonant photonic platform for label-free biosensing", *Optics Express*, vol. 23, no. 22, pp. 28593-28604, October 2015.
4) A. F. Gavela et al., "Last advances in silicon-based optical biosensors", *Sensors*, vol. 16, no. 3, 285, 2016.
5) S. Dante, "All optical phase modulation for interdigitated interferometric biosensors", *Opt. Exp.*, vol. 20, no. 7, 2012.
6) D. Duval et al., "Nanophotonic lab-on-a-chip platforms including novel bimodal interferometers, microfluidics and grating couplers", *Lab on Chip*, vol. 12, pp. 1987-1994, 2012.
7) A. Di Falco, "Chemical sensing in slotted photonic crystal heterostructure cavities", *Appl. Phys. Lett.*, vol. 94, no. 6, 2009.
8) D.-X. Xu et al., "Label-free biosensor array based on silicon-on-insulator ring resonators addressed using a WDM approach", *Optics Letters*, vol. 35, no. 16, pp. 2771–2773, 2010.
9) E. Homola et al., "Surface Plasmon Resonance Based Sensors", Springer: New York, NY, USA, 2006.
10) F. Dell'Olio et al., "Design of a New Ultracompact Resonant Plasmonic Multi-Analyte Label-Free Biosensing Platform", *Sensors*, vol. 17, no. 8, 1810, 2017.

Monolithically Integrated 3D Silicon Photonic Platforms

(Invited paper)

Joyce K. S. Poon[1]
[1] Department of Electrical and Computer Engineering, University of Toronto,
10 King's College Road, Toronto, Ontario, M5S 3G4, Canada
joyce.poon@utoronto.ca

ABSTRACT
This talk presents my group's progress in foundry-compatible, monolithically integrated multilayer silicon nitride-on-silicon (SiN-on-Si) photonic platforms. These SiN-on-Si photonic platforms contain several waveguide levels, and light can be routed vertically between the layers to realize 3D photonic devices and circuits. I will present our work on passive and active elements, including ultra-low-loss waveguide crossings, multi-layer grating couplers, polarization management components, and ultra-efficient Si depletion modulators. These advancements make possible the implementation of very large-scale photonic circuits for applications such as optical switching, phased arrays, and dense sensor systems.

Keywords: Integrated optics, silicon photonics, photonic devices

Large-scale Programmable Silicon Photonics

(Invited paper)

Wim Bogaerts

[1] Ghent University – IMEC. Department of Information Technology, Photonics Research Group.
Technologiepark-Zwijnaarde 15, 9052 Gent, Belgium - e-mail: wim.bogaerts@ugent.be
[2] Center for Nano- and Biophotonics, *Ghent University, Belgium.*

ABSTRACT

In the past few years, new concepts for general-purpose, programmable photonic integrated circuits have been proposed. These stand in contrast to custom-designed, *application-specific photonic integrated circuits* (ASPIC), in a similar way as electronic *field-programmable gate arrays* (FPGA) and microcontrollers stand in contrast with *application-specific integrated circuits* (ASIC). Several programmable PIC concepts have already been experimentally demonstrated on a modest scale, reproducing functionality in programming that was hitherto limited to custom-designed hardware. The PhotonicSWARM project looks into the scaling potential of such programmable PICs, combining distributed optical paths with distributed control algorithms to keep larger circuits manageable. We will discuss these concepts and the recent results in this project, implemented using silicon photonics technology.

Keywords: Programmable Photonics, Photonic Integrated Circuits.

1. INTRODUCTION

Photonic Integrated Circuit (PIC) technology today has reached a point where large-scale integration has become a technological possibility. Especially with silicon photonics, chips with >10000 optical elements can be fabricated with acceptable quality. This has resulted in demonstrations of large-scale switches, or optical phased array components, but most photonic circuit demonstrations remain much smaller in scale. They are typically designed to perform a single function with best efficiency, similar to electronic ASICs. In contrast, new photonic circuit concepts have emerged in the past years that have the ambition to be more generic in applicability, and reconfigurable to perform a multitude of different optical functions [1]–[4]. Such *programmable PICs* bear a resemblance with electronic FPGAs. These new programmable PICS, or photonic processors, consist of regular arrangements of optical waveguides and couplers to realize arbitrary connectivity and distribution of light on the chip. Combined with active functionality such as modulation, detection and gain, they can perform different operations in incoming light and/or electrical of *radio-frequency* (RF) signals. A conceptual schematic of such a generic programmable PIC is shown in Figure 1. Optical inputs/outputs are connected to a reconfigurable linear circuit. This circuit provides connectivity to active optical elements such as electro-optic modulators or high-speed photodetectors (which provide the inputs and outputs for RF signals).

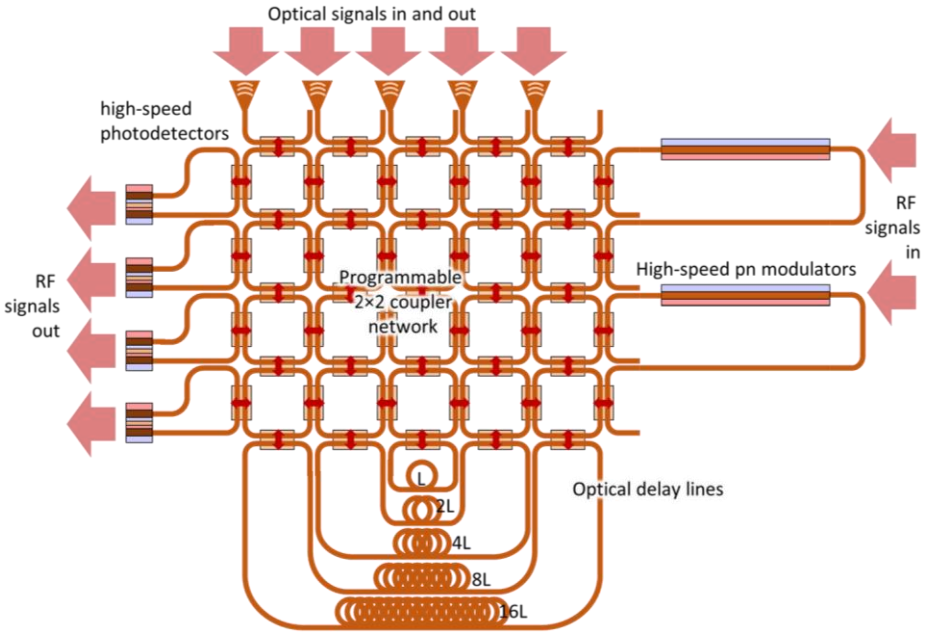


Figure 1: Conceptual schematic of a programmable photonic IC. A programmable linear circuit connects optical input/outputs with RF modulators and photodetectors. The linear circuit can perform arbitrary linear transformations between its input/output ports and perform wavelength filtering functions, either using the 'edge' delay lines, or by configuring a path in the mesh.

2. LINEAR PHOTONIC PROCESSORS

The linear circuit (or linear processor) is the heart of the programmable PIC. It is essentially a N-port linear circuit of which the scatter matrix (S-matrix) can be reconfigured to perform connectivity functions, but also wavelength filtering operations between the different ports. This is done by a cascade of tunable optical couplers and tunable optical phase shifters. Simple switchings is not sufficient, as the multiple inputs can interfere and control of both amplitude and phase in the circuit is essential to obtain the desired coupling ratios between inputs and outputs. The most straightforward implementation of such a circuit was already proposed in 1994 [5]: It consists of a cascade of tunable balanced *Mach-Zehnder interferometers* (MZI) and phase shifters. In 2013, this concept was extended to include simple control algorithms that allow the circuit to configure itself to certain functions [4]. Experimental demonstrations show that these circuits can be used to demonstrate adaptive beam coupling [3] and different linear transformations [2], [6].

By incorporating optical delays in such a linear circuit, programmable wavelength filters can be constructed. The delays can be simple waveguides, but a lot more flexibility is gained by creating programmable loops in the circuits, effectively creating a mesh of coupled ring resonators. Such meshes can have different topologies, based on square or hexagonal unit cells [7], [8].

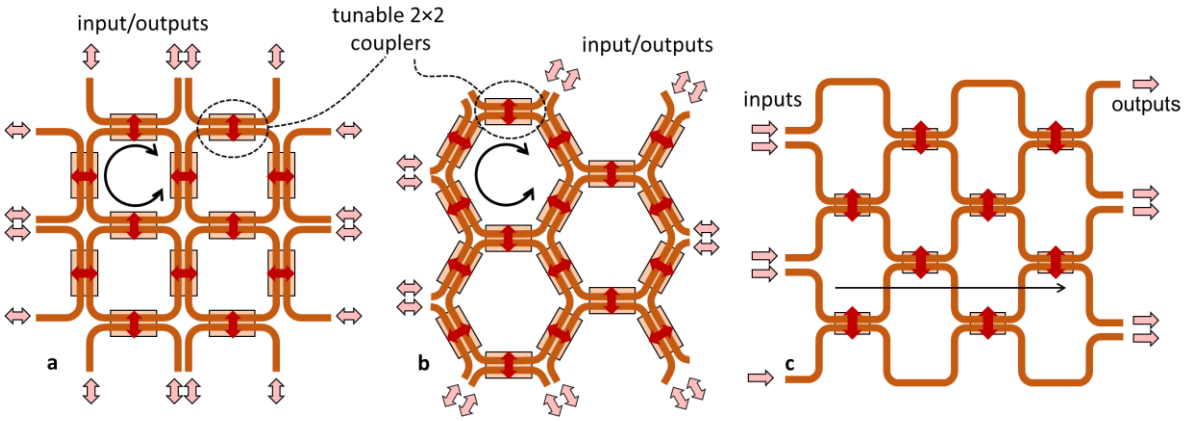


Figure 2: Different architectures for linear photonic processors. (a) Rectangular meshes form a network of ring resonators [7] *(b) Hexagonal lattices offer richer connectivity and clockwise/counterclockwise coupling* [8], *(c) Unidirectional Mach Zehnder interferometer networks map inputs to a different set of outputs* [5], [9] .

3. A NEW FIELD WITH NEW CHALLENGES

The field of programmable photonic circuits is only just taking off. The first demonstrations show the potential of the technology and the concept, but with these new concepts come new challenges. The reconfigurability implies that the circuits are much larger than non-reconfigurable circuits that should perform similar optical tasks: they contain an order of magnitude more building blocks. This imposes requirements on the technology in terms of integration density and the performance of the individual building blocks. Imperfections and parasitic effects (e.g. loss, backscattering) will accumulate much faster in a programmable circuit. Also, as any function in such a circuit needs actuation, there is a constant power consumption. All implementations of programmable photonic circuits today use thermal tuners, with a tuning efficiency of 10-50mW per π phase shift. Scaling up to thousands of tuners becomes impractical in terms of power consumption. Alternative low-power tuning methods, such as photonic MEMS are not yet available on large-scale integration platforms, but are actively studied, for instance in the European project MORPHIC.

All these tuners need to be controlled, which imposes strong requirements on the electronics. As the number of elements grows beyond the scale of traditional lab equipment, custom driver circuits based on ASICs or FPGAs are needed. The precision of this control is not straightforward: small imperfections can lead to parasitic coupling and interferences that can significantly alter the circuit's function. Therefore the control also requires monitoring of the circuits, and different architectures are possible, inserting monitors either inside the circuit or on the edge. In any case, monitors should induce a minimum of optical losses. Non-invasive techniques such as CLIPP probes [10] can help. Finally, how the control reconfigures and stabilizes the operation of the circuit determines the functionalities that the circuit can accomplish. For instance, an adaptive beam coupler is fairly easy to configure and control [3], [4]. Arbitrary transformations between inputs and outputs require more complicated setup algorithms [9]. Because these circuits are interferometric, small changes in the control can induce large changes in a monitoring response. Control algorithms should therefore be carefully tuned to maintain stability. This can be done either on a global scale for the entire circuit, or on a local scale where only neighbouring circuit elements are taken into consideration. The choice of control algorithm goes hand in hand with the waveguide architectures and the connectivity of the mesh. These considerations are studied in the PhotonicSWARM project.

4. A NEW ECOSYSTEM AROUND PROGRAMMABLE PHOTONIC CHIPS

Programmable photonic chips have the potential to radically change the use of photonic integrated circuits. This is similar to the adoption of FPGAs in electronics. Today, the cost of entering the world of photonic integration is prohibitively high. While the cost of multi-project-wafer runs is still acceptable, the time from design start to packaged chip is usually larger than one year. This stifles development. Programmable PICs, on the other hand, can be available off the shelve and supplied (including standard packages) in a matter of days or weeks. With such chips, the intellectual effort shifts from chip design to programming the functionality. This higher level of abstraction presents new opportunities for innovation. Because programmable PICs can be used in a variety of applications, they can also be fabricated in higher volumes, which will offset the higher cost of the chip (because of its larger complexity and footprint). Like FPGAs and ASICs in electronics, programmable chips will not replace dedicated photonic ICs, which will always have a better performance.

Programmable PICs can find their applications in many domains. Notable are the fields of microwave photonics, where photonic circuits can process RF signals much more efficiently, or quantum optics, where linear processors can perform operations on entangled qubits. But essentially every application field that currently uses dedicated photonic chips or discrete optics could benefit from readily available programmable PICs.

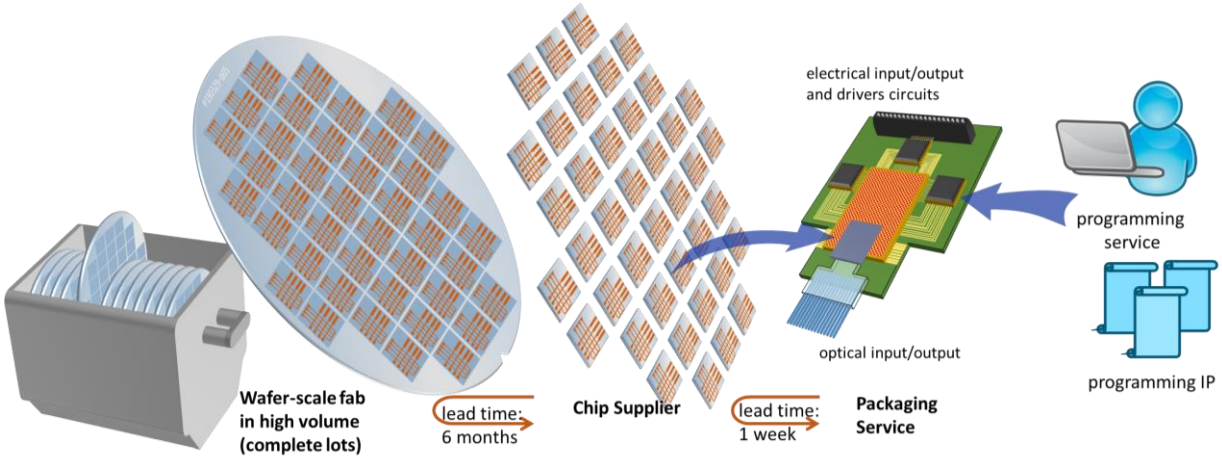


Figure 3: Generic programmable photonics can seed a different ecosystem, providing fabs with regular, homogeneous large-volume manufacturing, while giving end-users customized functionality and a short lead time.

5. SUMMARY

The field of programmable photonic circuits in only just taking off, but there have already been a number of convincing demonstrations. The flexibility of these chips can dramatically lower the barrier of entry in integrated photonics, and create a new ecosystem around the software-defined functionality.

ACKNOWLEDGEMENTS

This project has received funding from the European Union's Horizon 2020 research and innovation programme under grant agreement No 780283 (MORPHIC – www.h2020morphic.eu) and the European Research Council under grant agreement No 725555 (PhotonicSWARM).

[1] D. Perez, I. Gasulla, and J. Capmany, "Photonics Processors," vol. 36, no. 2, pp. 519–532, 2018.
[2] J. Carolan *et al.*, "Universal linear optics," *Science (80-.).*, vol. 349, no. 6249, pp. 711–716, 2015.
[3] A. Ribeiro, A. Ruocco, L. Vanacker, and W. Bogaerts, "Demonstration of a 4 X 4-port universal linear circuit," *Optica*, vol. 3, no. 12, p. 1348, 2016.
[4] D. a B. Miller, "Self-aligning universal beam coupler.," *Opt. Express*, vol. 21, no. 5, pp. 6360–70, 2013.
[5] M. Reck, A. Zeilinger, H. J. Bernstein, and P. Bertani, "Experimental realization of any discrete unitary operator," *Phys. Rev. Lett.*, vol. 73, no. 1, pp. 58–61, Jul. 1994.
[6] J. Wang *et al.*, "Multidimensional quantum entanglement with large-scale integrated optics," vol. 7053, no. March, pp. 1–14, 2018.
[7] L. Zhuang, C. G. H. Roeloffzen, M. Hoekman, K. Boller, and A. J. Lowery, "Programmable photonic signal processor chip for radiofrequency applications," vol. 2, no. 10, pp. 1–6, 2015.
[8] J. Capmany, I. Gasulla, and D. Pérez, "Microwave photonics: The programmable processor," *Nat. Photonics*, vol. 10, no. 1, pp. 6–8, 2015.
[9] D. A. B. Miller, "Self-configuring universal linear optical component," *Photonics Res.*, no. 1, pp. 1–15, 2013.
[10] F. Morichetti *et al.*, "Non-invasive on-chip light observation by contactless waveguide conductivity monitoring," *IEEE J. Sel. Top. Quantum Electron.*, vol. 20, no. 4, pp. 292–301, 2014.

Ultra-low-power stress-based integrated photonic phase actuator

Jörn P. Epping[1], Denys Marchenko[1], Arne Leinse[1], Richard Mateman[1], Marcel Hoekman[1], Lennart Wevers[1], Chris G. H. Roeloffzen[1], Matthijn Dekkers[2], and René G. Heideman[1]

[1] LioniX International BV, P.O. Box 456, Enschede 7500 AL, The Netherlands

Tel.: +31 53 20 30 053, Fax: +31 53 20 11 303, e-mail: j.p.epping@lionix-int.com

[2] SolMateS BV, Drienerlolaan 5, Enschede 7522 NB, The Netherlands

ABSTRACT

In this work, we present recent improvements on the stress-optic actuator on the silicon nitride-based waveguide platform (TriPleX) in the telecommunication C-band. In our stress-optic phase modulator the refractive index of the waveguiding materials is controlled by the stress-optic effect induced by actuating a 2 µm thick PZT (lead zirconate titanate) layer on top of the TriPleX waveguide geometry. The efficiency of the modulator is optimized by, amongst others, focusing the applied stress in the waveguide core region through a local increase of the top cladding. Using a Mach-Zehnder interferometer, we measured a phase shift of π, i.e. the half-wave voltage, V_π, at 12 V and even a phase shift of 2 π at 25 V at a wavelength of 1550 nm using a modulator with a total length of 15 mm. Even smaller voltages were measured for devices using a reduced top cladding. The measured static power consumption of our stress-optic modulator is well below 1 µW as it is only determined by small leakage currents (< 0.1 µA) and, therefore, more than 5 order of magnitude lower than that of conventional thermo-optic phase actuators. The total footprint of the stress-optic actuator is similar to that of thermo-optic actuators due to lower cross-talk to neighboring actuator. These specifications along with minimal excess losses make stress-optic actuator an excellent choice for next generation integrated photonic circuits that require a large number of actuators in silicon photonics in general and in the TriPleX platform in particular.

Keywords: Integrated Optics, Microwave Photonics, Actuator, PZT, Silicon nitride, TriPleX™

1. INTRODUCTION

For integrated photonics circuits with complex function, such as optical beam forming networks (OBFN) [1,2] or microwave photonic signal processing [3,4], large amounts of phase actuators are mandatory. In the silicon nitride and similar platforms today's phase modulation depends solely on thermo-optic phase shifters[5], which are reliable, straightforward to manufacture, and offer tuning speeds around 1 ms. However, thermo-optic modulators suffer from huge power dissipation, in the order of 300 mW per π phase-shift per modulator, and thermal cross-talk from neighboring heaters. While their tuning speed is sufficient to drive the envisioned applications, the constant power dissipation of thermo-optic modulators makes them less suitable to support large scale waveguide-based matrices.

Recently, we have demonstrated that low-power modulation is feasible for visible light as well as near-infrared light by using stress-optic modulators in the silicon nitride platform[6,7,8]. The stress-optic modulator was realized by harnessing the stress from an actuating piezoelectric material (lead zirconate titanate, PZT) on top of a standard silicon nitride-based TriPleX geometry. The major advantage of such stress-optic modulators over thermo-optic modulators for future applications is their ultra-low power dissipation in a static state, where no high speed tuning is required. The static power consumption is solely determined by tiny leakage currents through the piezoelectric layer resulting in a dissipated power in the µW-region. Here, we present recent advances in the stress-optic actuator in the telecommunication C-band using the silicon nitride-based waveguide platform, TriPleX. We employ a stress-focusing geometry on top of the waveguide core region, while at the same time allowing for a thinner top cladding to further increase the stress at the waveguide core and keeping the excess loss per modulator minimal. Using a Mach-Zehnder interferometer, we measured a half-wave voltage, V_π, at 12 V at a wavelength of 1550 nm using a modulator with a total length of 15 mm.

2. STRESS-OPTIC ACTUATOR

We fabricated a stress-optic modulator using a standard double stripe TriPleX™ geometry[9], which is also offered via a Process Design Kit (PDK) and Multi Project Wafer (MPW) access. To evaluate the dependence of the stress-optic effect with the top cladding thicknesses, t_c, we deposited top claddings with a thickness of 2 µm and 3 µm on two wafers. Afterwards a bottom electrode consisting of a 10 nm thick Ti adhesive layer and a 100 nm thick Pt layer was deposited. The PZT layer with t_{PZT} = 2 µm was grown on top of this electrode using Solmates SMP-700 pulsed laser deposition (PLD) equipment. PZT deposited by PLD allows for the growth of high-quality layers which has recently become available for large wafer sizes and at commercial throughput[10]. To ensure the quality of the deposited PZT layer, we measured the transverse piezoelectric coefficient, e_{31}, of -18 to -20 C/m^2, using

simultaneously produced test structures from the same wafer. Finally, a Pt top electrodes with a thickness of 100 nm were deposited with various widths, w, and lengths, l. A scanning electrode microscope (SEM) picture of the resulting structure can be seen in Fig. 1a).

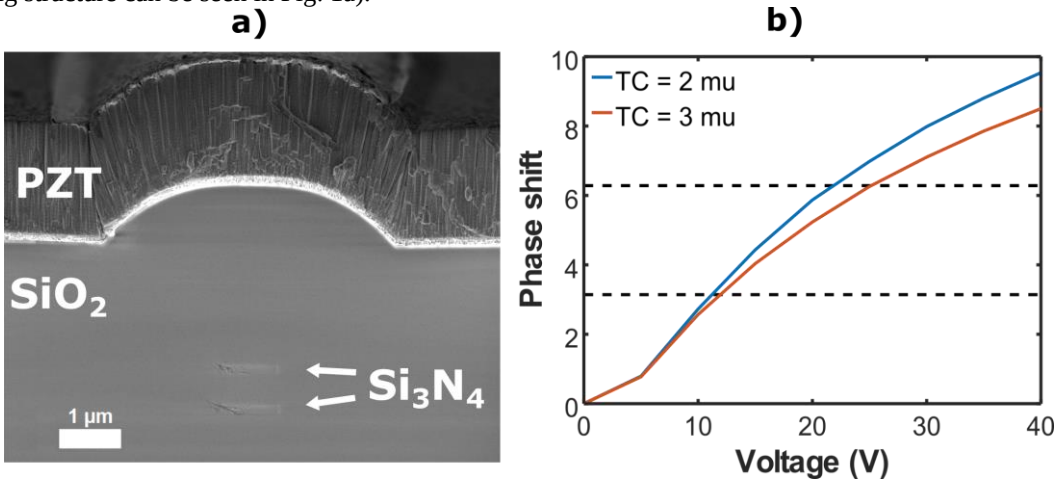


Figure 1. a) SEM picture of the stress-optic actuator on a symmetric double-stripe waveguide with a top cladding of 3 µm and a PZT thickness of 2 µm. b) Phase shift a function of applied voltage for stress-optic actuators analogue to a) with l = 1.5 cm, w = 7.5 mm, and a top cladding thickness (TC) of 2 µm (blue) and 3 µm (orange), respectively. Dashed horizontal lines indicate a applied phase shift of π and 2π, respectively.

To determine the phase shift of the stress-optic actuator, we use an asymmetric Mach-Zehnder interferometer filter (aMZI), where a top electrode in one arm was deposited to actuate the PZT layer. The top electrode has a width, w, of 7.5 µm, which was calculated to give the highest stress in the waveguide core, and a length, l, of 15 mm resulting in a measured capacitance of the modulator of 3 nF. We used a superluminescent diode with a -3 dB bandwidth of 50 nm at a wavelength around 1550 nm and an optical spectrum analyzer (HP 70951A) to measure the spectral shift in the response of the fabricated aMZI devices with a free spectral range of around 14 nm. To calculate the phase shift of the modulator as a function of voltage we measured the spectral shift for a set of applied dc-voltages, which is shown in Fig.1 b). We measured a half-wave voltage, V_π, (i.e. a phase shift of π) at 12 V and 11 V for t_C = 3 µm and 2 µm, respectively. A phase shift of 2π was measured V = 25 V and 22 V for t_c = 3 µm and 2 µm, respectively. It can be seen that the response of the stress-optic actuator has a proportional regime between 5 and 15 V, for higher voltages the slope of the curve decreases with increasing voltages. The reason for the decrease in modulation strength is the decrease of the transverse piezoelectric coefficient of the PZT layer after it reached its maximum at electric field strengths of around 10 V/µm. This decrease matches with the measured hysteresis-curve of PZT test structures that were fabricated on the same wafer.

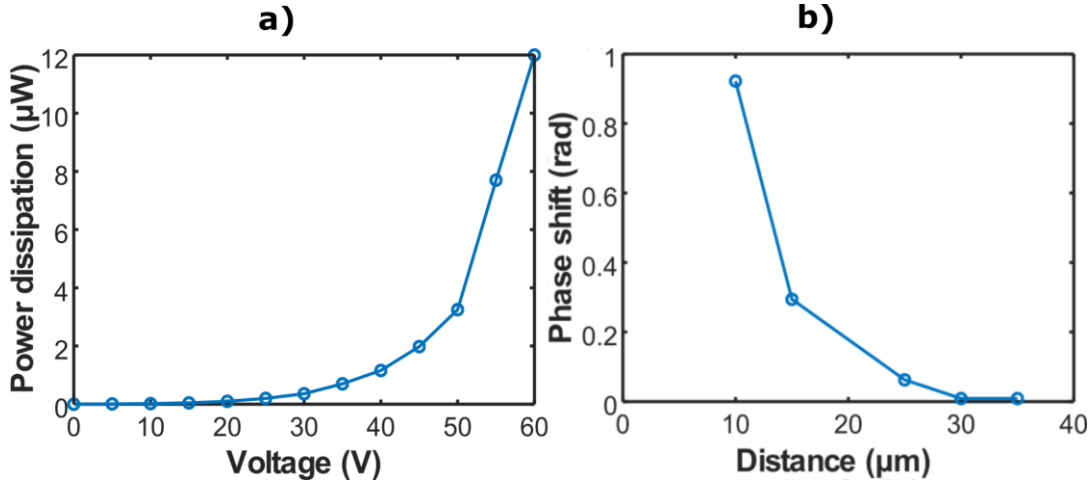


Figure 2. a) Static power dissipation of a stress-optic actuator as a function of applied voltage by measuring the leakage current. The leakage current was measured to be 0.08 µA at 25 V resulting in a power consumption well below 1 µW and went up to 0.2 µA at 60 V (P_{diss} = 12 µW).

To determine the dissipated power of the stress-optic actuator, we measured the leakage current as a function of applied voltage. The calculated dissipated power from this measurement is shown in Fig.2 a). It can be seen that for voltages needed to reach a full 2π phase shift (V>30 V) the dissipated power is well below 1 µW and, hence, is more than 5 order of magnitude lower than that of thermo-optic actuators. The power consumption of these devices with a driving frequency of 1 kHz (comparable to thermo-optic) is calculated to be below 1 mW [7].

The cross-talk from one actuator to a neighboring devise is an important parameter as it provides how densely devices can be packed on a chip. Fig.2 b) shows the measured cross-talk, i.e. induced phase shift, of a stress-optic modulator over a length of 1 cm as a function of distance between the waveguides. It can be seen that the cross-talk decays exponentially with increasing distance and starting from a distance of 30 µm the cross-talk was too low to be measured. The measured cross-talk of the stress-optic actuator is about 8 times smaller when compared to thermo-optic actuators. Due to the small cross-talk stress-optic actuators can be packed more densely on chip and when considering their current length (about 15 mm), stress-optic and thermo-optic actuators have a similar effective device footprint.

3. CONCLUSSION

In conclusion, we presented the recent improvements on stress-optic modulators for the telecommunication C-band, i.e. a wavelength around 1550 nm, in silicon nitride-based integrated circuits. The measured (static) power consumption characteristics of below 1 µW in the static case, make it an ideal actuator to realize sophisticated optical beamforming networks with 100s and even 1000s of modulators. In this work, we measured a half-wave voltage at 12 V using an electrode with a width of 7.5 µm and a length of 15 mm. The actual footprint of stress-optic modulators is measured to be the same as conventionally used thermo-optic modulators. The increase in modulator length of stress-optic modulators goes in hand with a decrease of cross-talk to neighboring devices when compared with thermo-optic modulators due to the confined actuation of the PZT. To further improve the devices, it is favorable to deposit PZT layers that are thicker than 2 µm. An improved PZT layer thickness should lead to both a higher stress induced into the waveguide core and, as well, an extension of linear modulation regime of the PZT.

ACKNOWLEDGEMENTS

This project has received funding from the European Union's Horizon 2020 research and innovation program under grant agreement No 688750 (HAMLET) and No 688519 (PIX4LIFE).

This work is supported by NanoNextNL, a micro and nanotechnology consortium of the Government of the Netherlands and 130 partners.

REFERENCES

[1] D. Marpaung, C.G.H. Roeloffzen, R.G. Heideman, A. Leinse, S. Sales, and J. Capmany: Integrated microwave photonics, *Laser Photon. Rev.* VOL. 7. pp. 506–538, 2013.

[2] C.G.H. Roeloffzen, L. Zhuang, C. Taddei, A. Leinse, R.G. Heideman, P.W.L. van Dijk, R.M. Oldenbeuving, D.A.I. Marpaung, M. Burla, and K.-J. Boller: Silicon nitride microwave photonic circuits, *Opt. Express* vol. 21 pp. 22937-22961 2013.

[3] L. Zhuang, C.G.H. Roeloffzen, M. Hoekman, K.-J. Boller, and A.J. Lowery: Programmable photonic signal processor chip for radiofrequency applications, *Optica* vol. 2 pp. 854-859 2015.

[4] D. Pérez, I. Gasulla, J. Capmany, and R.A. Soref: Reconfigurable lattice mesh designs for programmable photonic processors, *Opt. Express* vol. 24 pp. 12093-12106 2016.

[5] D. Pérez, J. Fernández, R. Baños, J.D. Doménech, A.M. Sánchez, J.M. Cirera, R. Mas, J. Sánchez, S. Durán, E. Pardo, C. Domínguez, D. Pastor, J. Capmany, and P. Muñoz: Thermal tuners on a Silicon Nitride platform", arXiv:1604.02958 2016.

[6] N. Hosseini, R. Dekker, M. Hoekman, M. Dekkers, J. Bos, A. Leinse, and R.G. Heideman: Stress-optic modulator in TriPleX platform using a piezoelectric lead zirconate titanate (PZT) thin film, *Opt. Express* vol. 23 pp. 14018-14026 2015.

[7] J.P. Epping, D. Marchenko, A. Leinse, R. Mateman, M. Hoekman, L. Wevers, E.J. Klein, C.G.H. Roeloffzen, M. Dekkers, R.G. Heideman: Ultra-low-power stress-optics modulator for microwave photonics, *Proc. SPIE 10106, Integrated Optics: Devices, Materials, and Technologies XXI*, 101060F February 2017.

[8] W. Jin, E.J. Stanton, N. Volet, R.G. Polcawich, D. Baney, P. Morton, and J.E. Bowers: Piezoelectric tuning of a suspended silicon nitride ring resonator, *IEEE Photonics Conference* October 2017.

[9] K. Wörhoff , R.G. Heideman, A. Leinse, and M. Hoekman: TriPleX: a versatile dielectric photonic platform, *Adv. Opt. Technol.*, vol. 4 pp. 189–207 2015.

[10] D.H.A. Blank, M. Dekkers, and G. Rijnders: Pulsed laser deposition in Twente: from research tool towards industrial deposition, *J. Phys. D: Appl. Phys.* vol. 47 pp. 034006 2014.

Automatic Hitless Tuning of Third Order Micro-Ring Resonator Add-Drop Filters

Maziyar Milanizadeh, Douglas Aguiar, Emanuele Guglielmi, Francesco Zanetto,
Marco Sampietro, Francesco Morichetti and Andrea Melloni
Dipartimento di Elettronica, Informazione e Bioingegneria - Politecnico di Milano, Milano, 20133 Italy.
maziyar.milanizadeh@polimi.it

ABSTRACT

The tuning and locking of a silicon photonics third order microring based filter suitable for hitless operation is presented. The filter has 8 nm Free Spectral Range (FSR) and operates in L band with a bandwidth of 42.5 GHz and isolation better than 20 dB. A novel channel labelling scheme is proposed and demonstrated to enable applications in add-drop reconfigurable architectures.

Keywords: Hitless Ring Resonator Filters, Automatic Control, Tuning, Locking.

1 INTRODUCTION

Node reconfigurability in optical telecomunication networks allows multiple data carrying wavelengths to be added and/or dropped from a communication system. Such functionality is a mandatory feature for capacity growth and management of core networks, 5G back-haul networks, optical interconnects and datacenters. Moreover, reconfigurable optical networks are based on the premise that newly provisioned channels must not affect already established ones. Photonic integrated circuits (PICs) have been demonstrated as a promising technology to implement flexible and hitless reconfigurable devices for telecom and interconnect applications [1]. However, the automatic calibration and control of such architectures during their operation is still an open challenge.

In this work, we demonstrate the automatic tuning of a third-order hitless filter based on silicon photonics (SiP) coupled Micro Ring Resonators (MRR). The filter is suitable for the implementation of multichannel add-drop reconfigurable architectures. A closed-loop control layer is implemented by using integrated transparent power monitors [2], integrated thermo-optic actuators and FPGA-embedded control algorithms. To identify the desired channel within a Dense Wavelength Division Multiplexing (DWDM) comb, a novel channel labeling strategy based on the use of a pilot tone generated locally at the node site is used, enabling to tune and lock the filter with telecommunication-graded characteristics. The experimental hitless reconfiguration is demonstrated by using single polarization 10 Gbit/s and 50 Gbit/s signals.

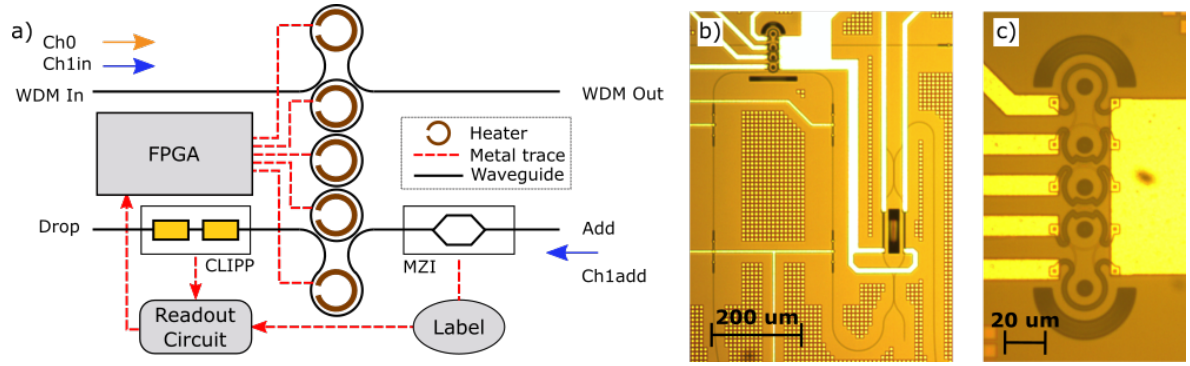


Figure 1. a) Schematic of 3rd order MRR filter with tuneable couplers in bus and add-drop waveguides, CLIPP monitor and MZ for labeling; b) micro-photograph of the 3rd order MRR filter with integrated CLIPP and labeling MZ modulator, c) detail on a 3rd order MRR filter showing heaters, waveguides, metal layer and deep trenches for heat management.

2 CHANNEL LABELING AND FILTER ARCHITECTURE

The schematic of the complete 4-ports filtering element is shown in Fig. 1a). The hitless filter consists of three directly coupled MRRs with unbalanced Mach-Zehnder (MZ) based tuneable couplers on the bus waveguides, according to the design proposed in [1]. In order to operate the filtering unit in presence of multiple DWDM channels, a weak pilot tone (channel label) is added onto the optical signal by a MZ modulator integrated on the Add port. This labeling operation is necessary to single out the Add channel from the Drop channel sharing

the same wavelength. This “labeler” is typically operated at few kHz and provides an intensity modulation of few percent ($< 8\%$) that does not impair the system quality [3]. A channel label at the remote transmitter is not required and the pilot tone can be periodically switched on/off depending on the stability of the system. An all-silicon sub-band gap transparent detector (CLIPP) [2] placed at the Drop port provides the feedback error signal to be used by the control algorithms embedded in the FPGA that drives the five integrated heaters. We use the CLIPP technique and a dual demodulation scheme, as schematically shown in Fig. 1a) [3].

Fig. 1b) shows a micro-photograph of the SiP device, which was fabricated on a commercial foundry, and in Fig. 1c) a detail of the hitless filter. The silicon channel waveguide is 490 nm wide and is buried in a silica cladding. Deeply etched trenches are used to confine the heat generated by the thermo-optic actuators around the silicon waveguides in order to increase the efficiency and mitigate thermal crosstalk effects. The filter design is optimized to have 1 THz (8 nm) FSR, 40 GHz 3dB bandwidth, and 20 dB in-band isolation. The bus to ring power coupling coefficient was chosen to guarantee a good compromise between spectral characteristics and robustness to fabrication tolerances. In the fabricated device, the channel labeler is integrated on chip by using a thermally tuneable MZ modulator; however other on-chip modulators technologies, based for instance on pn-juctions, as well as off-chip modulators could be used.

The monitoring of the channel power is made with the CLIPP device already demonstrated in commercial SiP foundries. The CLIPP monitors the light intensity in a waveguide by measuring the change in the resistance of the core segment between two metal pads. This change is induced by free carrier generation, which in turn is due to photon absorption occurring in the semiconductor waveguide core. The relation between resistance variation and optical intensity depends on the number of free carriers generated by either Surface State Absorption (SSA) or Two Photon Absorption (TPA) [4].

3 AUTOMATED HITLESS TUNING

Filter tuning in presence of neighbor DWDM channels requires the filter to be optically disconnected from the bus to prevent impairments on the other channels. This operation is usually named hitless channel tuning. In our device, hitless operation is achieved by simultaneously switching both MZ tuneable couplers connecting the filter to the line bus and to the add-drop bus, respectively.The process of decoupling, tuning and recoupling can be decomposed in four steps: switching off both tuneable couplers, tuning both rings and MZs using a look-up table (LUT), switching on both tuneable couplers and finally performing automatic continuous tuning of the filter.

The filter unit shown in Fig. 1a) can be cascaded with other units to realize a multichannel reconfigurable add-drop architectures operating on several wavelengths at the same time and the various units can be used independently one from the others. The weak pilot tone is strategical to recognize the Add channel from the Drop one, since they share the same wavelength. Moreover, it permits to tune the filter optimizing the match of the filter spectral transfer function with respect to the channel spectral shape.

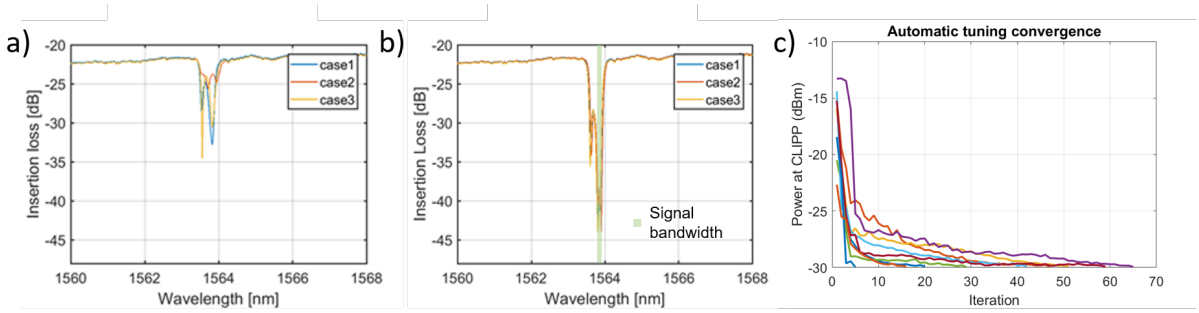


Figure 2. a) initial random spectral responses of the filter, b) tuned response of the filter and c) convergenge of the tuning algorithm.

To demonstrate the operation of the filtering unit we show that our algorithm is able to tune the filter to the wavelength of a labeled added channel and adapt its shape around the desired channel spectral shape. The automatic tuning algorithm makes use of an original transformed coordinate method [5] to tune and lock the MRRs. With this technique, the thermal phase controller of all the MRRs are tuned simultaneously at each iteration of the algorithm to minimize the target error function, which in this case is the label power at the CLIPP. A channel centered at 1563.9 nm, is split in two parts: the first one, which is provided at the Add port, has to be directed to the ”WDM Out” port of the filter unit; the second part, after being decorrelated by several kilometers of fiber, is coupled at the ”WDM In” port and has to be dropped from the Drop port. Filter tuning is performed automatically: the tuning algorithm exploits the pilot tone on the labelled channel to discriminate it from the other channel at the ”WDM In” port, brings the filter at the wavelength of 1563.9 nm, and keeps it locked. The spectral response of the automatically tuned filter is shown in Fig. 2b). As the bandwidth of the signal is much narrower than the filter, a very deep notch is created in the filter response at the expense of a slightly lower isolation at the band edges.

The power monitored by the CLIPP at the Drop port is shown in Fig. 2c).Note that only a small portion of added channel arrives at the Drop port, about 20 dB below the input power, corresponding to the isolation of the filter. For every tested starting condition the filter locking converge in few tens of iteration, each one corresponding to around 0.1 seconds.

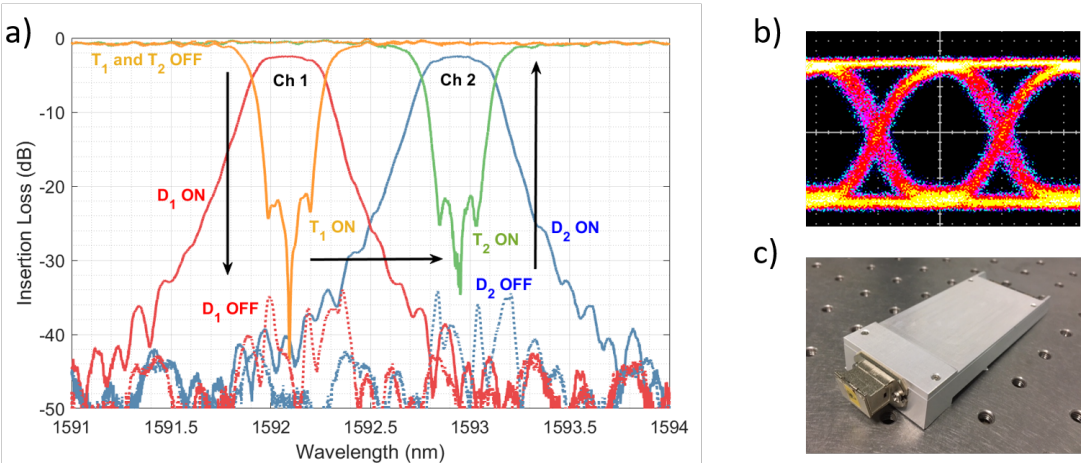


Figure 3. a) Experimental results of the hitless reconfiguration of the filter, b) eye diagram of the Ch.0 during the hitless reconfiguration of the filter and c) optical chip and control electronics assembled in a CFP2 package.

To evaluate the filter performance in the L band the filter is initially configured to Ch. 1 at 1592.1 nm (curves "D_1 ON" and "T_1 ON" Fig. 3a)), being the "WDM In to Drop" and "WDM In to WDM Out" spectral response, respectively. The tuning procedure starts with the detuning of the two MZs based tuneable couplers in order to isolate the filter from the line bus. The curve "D_1 OFF" is the spectral response between the ports "In" and "Drop" after this step, giving more than 35 dB of isolation. Next the controller is free to modify the MRRs and MZs working points without impacting other channels. Thus, the second step consists of using a pre-calculated LUT to change the voltages of the heaters corresponding to the desired channel (Ch. 2. at 1592.9 nm). Fig. 3a) shows the spectral measurements related to this steps in curves "D_2 OFF" and "T_1 and T_2 OFF ". As third step, both tuneable couplers are connected to the bus and the filter is automatically tuned to Ch. 2. The spectral response of the tuned filter is centered around Ch. 2 with an in-band isolation $>$ 20 dB ("T_2 ON") and off-band isolation $>$ 25 dB ("D_2 ON") at 50 GHz spacing from the central wavelength. Thanks to the high off-band rejection (more than 25 dB at 50 GHz from the center wavelength), the filter does not impact on the 50 GHz spaced channels. It should be noted that the filter tuning between two adjacent channels is the worst case; therefore similar, or even better, performance can be achieved for largely spaced channels.

To evaluate the effectiveness of the hitless tuning a reference channel (Ch. 0) centered at the wavelength 1592.5 nm is transmitted from the "WDM In" and "WDM Out" ports of the unit during the tuning procedure. The eye diagram of Ch. 0 was monitored and is shown in Fig. 3b). It remains almost unchanged during the tuning of the filter, demonstrating that hitless tuning can be performed. As shown in Fig. 3c) the optical chip and all controling electronics were assembled in a CFP2 package.

4 CONCLUSIONS

In this paper a hitless filtering unit suitable to be exploited in reconfigurable add-drop network nodes has been evaluated. We demonstrated the automatic tuning of a hitless reconfigurable silicon filter operating on 50-GHz-spaced DWDM channels in the L band. The control technique used is embedded in a FPGA to suit integration needs for high capacity networks, compact enough to possibly be packaged in a pluggable device. In addition, the filter unit can be cascaded with other units to realize a multichannel reconfigurable add-drop architecture operating independently on several wavelengths at the same time.

REFERENCES

[1] M. Popović et.al., "Hitless-reconfigurable and bandwidth-scalable silicon photonic circuits for telecom and interconnect applications," Proceed. Optical Fiber Communication Conference, OSA Technical Digest (CD) (Optical Society of America, 2008), paper OTuF4

[2] F. Morichetti et.al., "Non-invasive on-chip light observation by contactless waveguide conductivity monitoring," IEEE Journal of Selected Topics in Quantum Electronics, vol. 20, no. 4, pp. 292-301, 2014.

[3] A. Annoni et.al., "Automated routing and control of silicon photonic switch fabrics," IEEE Journal of Selected Topics in Quantum Electronics, vol. 22, no. 6, pp. 169–176, Nov 2016.

[4] S. Grillanda and F. Morichetti, "Light-induced metal-like surface of silicon photonic waveguides," Nature Communications, vol. 6, 2015.

[5] M. Milanizadeh et.al., "A tuning method for photonic integrated circuits in presence of thermal cross talk," submitted to ECIO 2018.

On-chip full-field test engine for photonic integrated devices based on optical frequency domain reflectometry technique

(Student paper)

Luis A. Bru,[1] Daniel Pastor,[1] Bernardo Gargallo,[2] David Doménech,[2]
Carlos Domínguez,[3] and Pascual Muñoz[1]
[1]*Universitat Politècnica de València, c/ Camino de Vera s/n - 46021 Valencia - Spain*
pascual.munoz@upv.es
[2]*VLC Photonics S.L., c/ Camino de Vera s/n - 46021 Valencia - Spain*
[3]*Institut de Microelectrònica de Barcelona CNM-CSIC - 08193 Cerdanyola del Vallès - Barcelona - Spain*

ABSTRACT

In this work we report on a fully integrated photonic chip test structure, providing optical amplitude and phase, frequency and time domain resolution for on-chip devices under test. The structure is based on optical frequency domain reflectometry, and compared to previous approaches, and by suitable design, it allows for retrieving full-field information on the device under test through a single pair of input/output optical ports, with inherent waveguide dispersion de-embedding. As a proof of concept, an experimental demonstration is performed for an arrayed waveguide grating fabricated on a silicon nitride photonic integration platform.

Keywords: optical frequency domain reflectometry, integrated test device, dispersion compensation, interferometry, arrayed waveguide grating, silicon nitride.

1 INTRODUCTION

In the world of modern integrated photonics, devices and circuits are getting more and more complex and posing increasing demands to characterization. Hence, optical frequency domain reflectometry (OFDR) [1]–[3] comes up as a very convenient technique due to its relatively simple implementation, still holding a good balance between accuracy, sensitivity, length range and time/spatial resolution [3]. Recently, approaches involving the integration on-chip of interferometric parts have appeared in the literature [4]–[6], showing improvements in terms of test setup compactness. In our previous work [5], we intendedly proposed to integrate OFDR Mach-Zehnder interferometers (MZI) as such (IOFDR), with the added advantages of extended versatility (holding any chip coupling strategy, accurate design of interferometer delays, as well as reflectometry and transmission arrangements). Remarkably, the approach inherently incorporates a (universal) dispersion de-embedding mechanism as well, something demonstrated for an arrayed waveguide grating (AWG) as a device under test (DUT). An important drawback in IOFDR is the simultaneous detection from two optical ports, something specially cumbersome on passive integrated optics having to employ a fiber array. In this work, we propose a device addressing this issue, by making use of a modified OFDR-based structure, but still preserving characteristics from our previous approach. We shall discuss this matter in section 2, to then show the experimental proof-of-concept in section 3, and finally draw our conclusions in section 4.

2 INTEGRATED TEST DEVICE

OFDR is a well-known homodyne interferometric technique providing both amplitude and phase, frequency and time domain resolution. It draws on two interferometers (typically MZI) to get interferogram data (containing amplitude and phase spectral information of the DUT) and correcting signal for proper triggering (TRIG) and therefore linearization of the optical frequency scan, indispensable to properly apply inverse fast Fourier transform (IFFT) algorithm and obtain time domain response.

The simultaneous detection of two optical ports in OFDR technique is quite an inconvenience from a practical point of view, when the signals have to be gathered from integrated waveguides on passive chip technologies, which require a fiber array as it happens for our IOFDR approach in [5]. A more straightforward single input/output detection arrangement is always preferable, so an advance interferometric system configuration is required, in order to be able to collect all the information of both conventional interferometers. In the test engine we propose hereby, these conditions are met with a 3-way interferometer (3-MZI), conveniently involving a single pair of input/ouput optical ports, and thus enabling single optical detection. An sketch of the proposed test structure is included in Fig. 1(a), where the lengths for the corresponding 3 different arms are L_1, L_2 and L_3 (being $L_1 < L_2 < L_3$, by convention). The 3-MZI can be conceived to be composed by 3 conventional 2-way interferometers which path length differences (PLDs) correspond to the following combinations of designed lengths:

$$\Delta L_{\text{DUT}} = L_2 - L_1,\ \Delta L_{\text{TRIG}} = L_3 - L_2 \text{ and } \Delta L_{\text{ADD}} = L_3 - L_1, \tag{1}$$

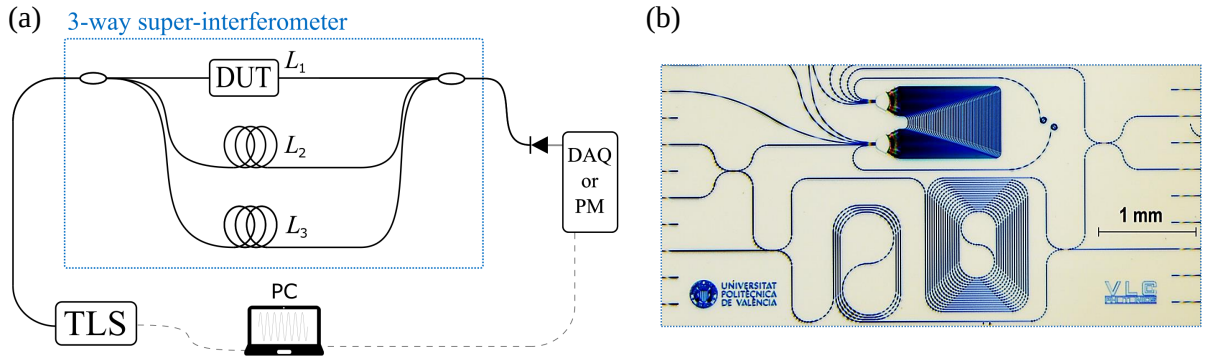


Figure 1. (a) A sketch of the proposed device and setup. In (b) a microscope photograph of the fabricated device.

i.e. the two firsts are for the DUT and TRIG interferograms as already reported, and an additional one (ADD) is incorporated. At this point, let us note that 3-MZI interferogram is not properly linearized, so it contains all the 'raw' information about interferograms including phase scanning error and dispersion. In spite of it, IFFT can be applied anyhow and identify the desired $\Delta L_{\text{DUT}}, \Delta L_{\text{TRIG}}$ contributions in the impulse domain. Then, by individually slicing contributions can be filtered, and by applying FFT to them, the interferograms are separately recovered. This in turn requires an additional processing step, and where PLDs have to be carefully designed: given a ΔL_{DUT}, applying the Nyquist criterion results into $\Delta L_{\text{TRIG}} \geq 2\Delta L_{\text{DUT}}$ (e.g. $\Delta L_{\text{TRIG}} = 4\Delta L_{\text{DUT}}$ places DUT in the center of the (semi) time window) and the third contribution ΔL_{ADD} will appear at a 'distance' ΔL_{DUT} away from ΔL_{TRIG}, so ΔL_{DUT} (and hence ΔL_{TRIG}) must account for it to prevent overlapping in the impulse domain.

Further, the proposed test device remarkably incorporates an inherent dispersion de-embedding system as in IOFDR [5]. The same waveguides for the involved MZIs and the DUT are influenced by the same dispersion phase chirp in the corresponding interferograms, in such a way that they are cancelled in the linearization process. Dispersion-free resolved time domain response is particularly convenient in the case of integrated devices, for which maximizing spatial resolution of the system (ultimately given by scanning span [2]) is crucial to indentify specially nearby events taking place in waveguides which very oftenly present high dispersion.

3 EXPERIMENTAL RESULTS

The employed setup for the measurements consists of simply introducing light in and out of the chip, as shown in Fig. 1(a): a tunable laser source (TLS) provides a continuous scanning signal at speed $v = 20$ nm/s and 80 nm span centered @1550 nm feeding the chip by horizontal coupling through one of the available inputs. Light goes over the 3 different paths, as depicted in Fig. 1(b) (Si_3N_4 waveguides of 280×1000 nm film height and width and group index $n_g^{\text{TE}} = 1.86$ for the TE mode [7]), splitting in amplitude by 2×2 multimode interferometers (MMI) and finally being combined the same way and collected at one of the outputs. The resulting signal is photodetected by a PIN (InGaAs) photodiode and acquired by a data acquisition card (DAQ) (at a rate of 100 kS/s) to be stored and post-processed. In Fig. 2(a) the generated 3-MZI interferogram is plotted: as described in section 2, IFFT algorithm is performed to the raw data so that desired contributions of the conventional interferograms, which are placed where designed (physical PLDs of $\Delta L_{\text{DUT}} = 1$ and $\Delta L_{\text{TRIG}} = 3.5$ cm), can be filtered back by FFT to the frequency domain. The result of this double transformation operation

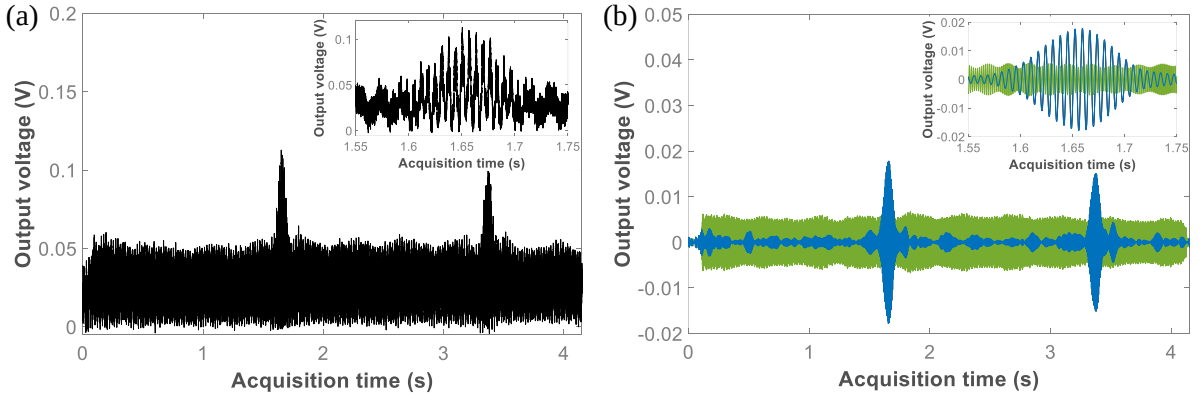


Figure 2. (a) The 3-MZI interferogram from where conventional DUT and TRIG interferograms are filtered and shown in (b). In the insets, a zoomed view of the first strong peak around 1.65 s is provided.

is shown in Fig. 2(b), in blue and green for the DUT and the TRIG, respectively.

From this point, we proceed as usual for the OFDR technique. After properly linearizing the DUT interferogram with the TRIG data, the time domain response for the AWG is retrieved by an IFFT, and plotted in Fig. 3(a). The AWG was designed with 59 waveguides in the array and a free spectral range (FSR) of 32 nm (4 THz), same as in [5] and manufactured in the silicon nitride process of CNM-VLC [8]. Most of the waveguides can be perfectly identified, with a time separation of 0.24 ps ($\sim 38\,\mu$m) as expected. This is possible because of the dispersion de-embedding of on-chip OFDR. Otherwise with the existing waveguide dispersion of $D = -1.32$ ps/nm·m (see [7]), the associated temporal broadening of $\Delta T = 0.95$ ps ($\sim 153\,\mu$m) corresponds to almost 4 times the actual peak spacing, and peak visibility would be blurred. The AWG contributions in time

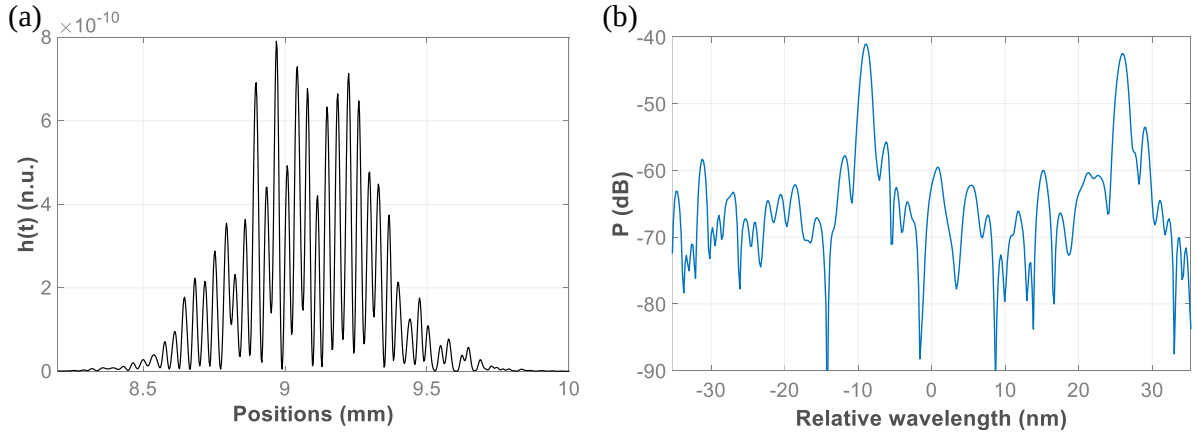


Figure 3. (a) Time domain response of the AWG, where the compensated different contribution peaks for the waveguides of the array can be perfectly distinguished. In (b), the frequency domain spectral amplitude of the AWG obtained by bandpass filtering.

domain, or position as depicted in Fig. 3(a), are extracted by slicing at the proper time/space range (besides removing detection noise and spurious time events on the chip) and the FFT is applied again to obtain the AWG spectral response in Fig. 3(b).

4 CONCLUSIONS

We have reported on a novel integrated test structure based on OFDR technique, inheriting all the capabilities from our previous work device, the IOFDR in [5] (remarkably, the mentioned dispersion compensation mechanism). The device is able to work in a single pair input/output detection arrangement so suitable in integrated optics, by translating part of the complexity to the post processing. Promising experimental results have been also reported, demonstrating the validity of the technique through the proposed test structure, by testing a designed AWG as a DUT on a silicon nitride platform. The dispersion-compensated time domain response of the AWG has been successfully resolved as expected, from which the spectral response of the AWG can be reconstructed as well.

ACKNOWLEDGMENT

The authors acknowledge financial support through projects, TEC2015-69787-REDT PIC4TB, TEC2016-80385-P SINXPECT, TEC2014-54449-C3-1-R BIOSENSLOC and GVA PROMETEO 2017/103. L.A.B. also acknowledges PTA2015-11309-I.

REFERENCES

[1] W. Eickhoff and R. Ulrich, "Optical frequency domain reflectometry in single-mode fiber," Appl. Phys. Lett. 39(9), pp. 693-695, 1981.

[2] U. Glombitza and E. Brinkmeyer, "Coherent frequency-domain reflectometry for characterization of single-mode integrated-optical waveguides," J. Lightwave Technol. 11, pp. 1377-1384, 1993.

[3] B. J. Soller, D. K. Gifford, M. S. Wolfe and M. E. Froggatt, "High resolution optical frequency domain reflectometry for characterization of components and assemblies," Opt. Express 13, pp. 666-674, 2005.

[4] D. Melati, "A design kit perspective in InP-based photonic integrated circuits," Ph.D. Thesis, Polytechnic University of Milan, 2014.

[5] L. A. Bru et al., "Fully Integrated Optical Frequency Domain Reflectometry," in proceedings of European Conference on Integrated Optics (ECIO) 2017, paper M3.5 (April 2017).

[6] D. Zhao, D. Pustakhod, K. Williams, and X. Leijtens, "High resolution optical frequency domain reflectometry for analyzing intra-chip reflections," IEEE Photon. Technol. Lett., vol. 29, no. 16, pp. 1379–1382, 2017.

[7] G. Micó et al., "Silicon nitride photonics: from visible to mid-infrared wavelengths," in proceedings of SPIE Photonics West 2018: Silicon Photonics XIII, pp. 10537-9, 2018.

[8] Silicon Nitride Photonic Integration Platform, http://www.imb-cnm.csic.es/index.php/en/clean-room/silicon-nitride-technology

Matrix Addressing Silicon Photonics Phase Shifters using Heaters with Integrated Diodes

Student paper

Antonio Ribeiro[1,2], Umar Khan[1,2], and Wim Bogaerts[1,2]

[1]*Ghent University - IMEC, Photonics Research Group, Department of Information Technology, Ghent, Belgium*
[2]*Center for Nano and and Biophotonics (NB-Photonics), Ghent, Belgium*

ABSTRACT

We present a matrix addressing approach to drive thermo-optic silicon phase shifters with integrated diodes, allowing time-multiplexed access to the heaters, which reduces the number of pads necessary to drive large silicon photonics circuits. We also demonstrate that such heaters can be driven using digitally modulated signals, which increases the linearity of the phase shift response of the device.

Keywords: heater, phase shifter, diode, multiplexed, SOI.

1 INTRODUCTION

With the increase in complexity and number of elements of large scale photonics circuit, the interfacing with electronics for controlling and read-out can become a limiting factor for the scalability of the system. A circuit with hundreds of phase shifters would need an equally large number of contact pads and voltage sources for driving. This can be challenging to the development of large scale integrated circuits once such contact pads are usually large and occupy a large space in the photonics chip. Also, a great number of wires are needed to connect the active devices to their bondpads, which can add another layer of complexity in the design of the optical device. To circumvent this issue we propose a matrix-based topology for driving thermo-optic phase shifters with integrated diode [1] in the silicon on insulator (SOI) platform. Such approach can reduce the total number of contact pads (and, consequently, of voltage sources) needed to drive large number of phase shifter. The proposed approach permits to drive up to N^2 heaters with $2 * N$ pads, while the conventional approach uses one pad per phase shifters plus one extra pad for common ground.

2 HEATERS WITH INTEGRATED DIODES

One approach to implement a thermo-optic phase shifter in SOI is adding a side strip of doped silicon close to the target waveguide and using it as a resistor. On a typical side heater, the silicon strip is doped with either *P-type* or *N-type* dopants to increase its conductivity. In our design we doped the main body of the heater using *N-type* dopants, and near one of the electrical contacts we used a *P-type* dopant, creating a *PN* junction inside the heater. This approach converts the standard heater to a diode in series with a high resistivity strip. The total length of our heater is $50\mu m$, where $8\mu m$ is used for the *P-type* doped region. The width of the heater is $1.2\mu m$. The heaters are placed close to the target waveguide [Fig. 1(a)], keeping a gap of $0.75\mu m$ between the heater and the waveguide. The gap was chosen to be close enough to increase the power efficiency of the heater and yet avoid the optical mode to leak from the waveguide to the heater. The heater and the waveguide have a different width to minimize coupling due to phase matching.

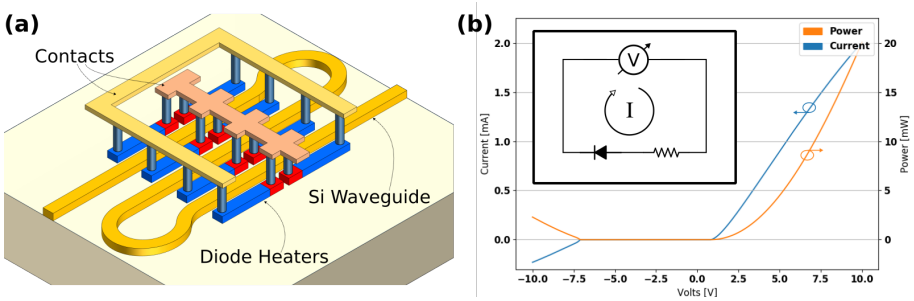


Figure 1. (a) The phase shifter implemented with eight diode heaters placed in parellel. (b) The IV curve showing the diode characteristic of the phase shifter. The measured devices yields negligible when reverse biased up to $-7V$. (b-inset) The equivalent electric circuit of the heater.

2.1 Phase-shifter Characterization

The I-V curve of the fabricated heater [Fig. 1(b)] shows a clear diode behavior, with negligible current flow in reverse bias, before the breakdown point, at around $-7V$. From this values, we assume that it is safe to operate the heaters in the $\pm 7V$ range without inducing any phase shift in the heaters connected to the same pads, but with opposite polarity.

The measured resistance at $5V$ was $5.3k\Omega$ and the electrical power delivered at $7V$ was $9.6mW$ per heater. To achieve higher power output without compromising the operational range of $\pm 7V$ we can drive multiple heaters in parallel. We constructed the phase shifter by placing eight heaters in parallel [Fig. 1(a)]. The phase shifter can deliver up to $76.8mW$ at $7V$.

To increase the power efficiency of the phase shifter we routed the waveguide around the heater [Fig. 1(a)] instead of having a single parallel placement. This design ensures that mostly of the heat generated by the heater is applied to the waveguide.

To extract the efficiency of the heater we designed a Mach-Zehnder interferometer (MZI) using the phase shifter as its arm and monitored the power necessary to switch the state of the MZI. From the obtained values we report a πrad phase shift at $20.9mW$, which is a result compatible with the reported values for this technology[2].

2.2 Time-domain Analyses of the Phase Shifters

Heaters are inherently slow when compared to other phase-shifting approaches such as free-carrier modulators[3]. The presented phase shifter has a measured time constant of $97\mu s$ [1]. The plot in Fig.2 shows the induced phase shift for a given driving signal with different frequencies. It is visible from the plot that for driving frequencies above $500KHz$ we don't notice any fluctuations in the induced phase shift over the time. The reason for that is that, for higher frequencies, the signal changes much faster than the thermal constant of the device, which behaves as a low-pass resistor-capacitor (RC) circuit.

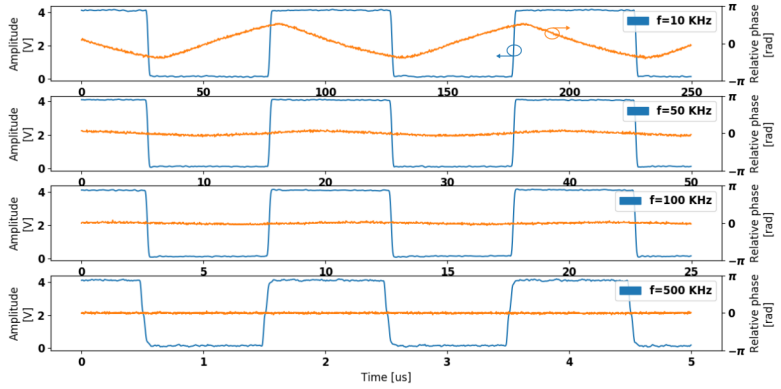


Figure 2. Induced phase shift for a driving signal with different frequencies.

The high time-constant of the heater can be used to operate it using a noncontinuous signal, such as Pulse Width Modulation (PWM). In a PWM-based driving, the delivered power is not proportional to the amplitude of the driving signal (which is constant) but proportional to the duty cycle of the PWM signal instead. To change the induced phase shift we tune the duty cycle of the driving signal. This makes the phase shift linear to the driving parameter (duty cycle), once in a PWM signal the total porwe grows linear to the duty cycle of the signal. This characteristic improves the control of the phase shifter.

3 MATRIX ADDRESSING

To multiplex the addressing of the heaters using a minimum number of pads we designed them in a matrix topology as shown in Fig.3(a). To address a given heater in the matrix it is necessary that the row linked to the respective heater to be placed in low state ($0V$) while the column, connected to the anode of the diode, is set to the required voltage to yield the desired phase shift. To achieve the multiplexing effect it is necessary to synchronize the selection of the row to be addressed with the signal applied to each channel (column) of the matrix in such way that we constantly change which row we are addressing. If such switching is made fast enough (much faster than the time constant of the heaters) each heater will see only the average power delivered over time, allowing us to drive multiple heaters in the same channel.

For a better phase shift control, the signal applied to each subchannel is not a amplitude variable signal, but a PWM signal with constant amplitude and variable duty cycle. To obtain maximum phase shift with minimum duty cycle we set the value of the amplitude of the PWM signal to the maximum voltage allowed by the diode

without reaching the breakdown region when reverse biased ($-7V$). For such configuration we were able to obtain πrad phase shift with a PWM signal with a duty cycle of 27%.

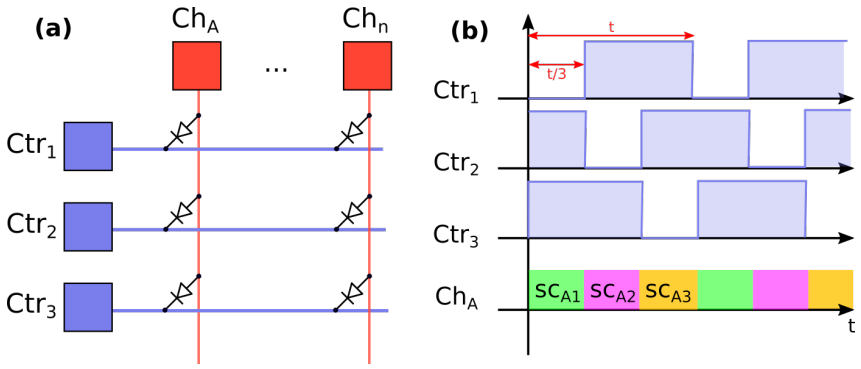


Figure 3. (a) Schematic of a matrix addressing circuit with three control lines (rows) and n channels (columns). (b) Signal representation for the three control lines (Ctr_1,Ctr_2, and Ctr_3) and the signal applied to channel A. The channel signal is subdivided in three subchannels, each synchronized to its respective control line. Each subchannel comprehends an independent PWM signal that controls its respective phase shifter.

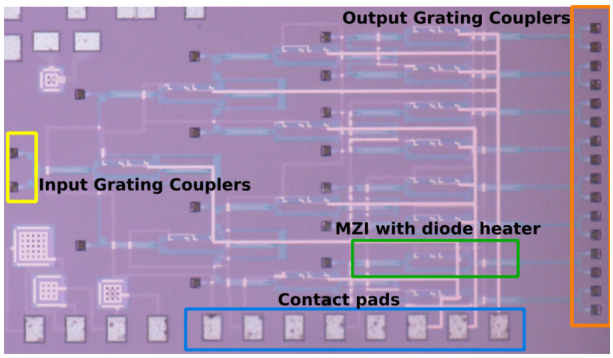


Figure 4. 1×16 multiplexer device fabricated with 15 MZIs. Each MZI is controlled by a phase shifter with integrated diode. The circuit is arranged in a matrix configuration, which allows the control of the 15 phase shifters with 8 pads.

A limiting factor that dictates how many rows can share the same channel is the duty cycle needed for the heater to delivery the maximum desired phase shift. To operate a MZI circuit in a three-rows matrix (such as the fabricated device, shown in Fig.4, and the schematic in Fig.3(a)) the heater has to be able to delivery the πrad phase shift with at most 33% of its duty cycle (as the other two-third of the time will be dedicated to the remaining rows linked to the same channel). As the fabricated device can yield πrad phase shift with a 27% duty cycle, it puts it within the limit for a three rows multiplexing scheme.

3.1 Driving Electronics

The main requirement to drive the circuit is the delivery of the signal that comprehend all the three subchannels synchronized with the control lines. Such circuit can be implemented with a standard Field Programming Array (FPGA). To boost up the output signal to meet the requirement levels ($7V$ amplitude, $20mA$ current) the signal can be amplified using an operational amplifier.

4 CONCLUSIONS AND FUTURE WORK

We demonstrated that the use of heaters with integrated diodes to allow matrix-like addressing for thermo-optic phase shifters in silicon photonics circuits is possible. The high thermal-constant of the phase shifters allows a digital (PWM) driving and also time-multiplexing the actuation of the circuit. A dedicated electronic driver is needed to control the circuit, which can be implemented with standard (FPGA) and a voltage amplifier.

REFERENCES

[1] A. Ribeiro, and W. Bogaerts, "Digitally controlled multiplexed silicon photonics phase shifter using heaters with integrated diodes," Opt. Exp. **25**, 2017.

[2] A. Masood, M. Pantouvaki, G. Lepage, P. Verheyen, J. Van Campenhout, P. Absil, D. Van Thourhout, W. Bogaerts, "Comparison of heater architectures for thermal control of silicon photonic circuits," Group IV Photonics, South Korea, p.ThC2 (2013).

[3] M. R. Watts, J. Sun, C. DeRose, D. C. Trotter, R. W. Young, and G. N. Nielson, "Adiabatic thermo-optic Mach-Zehnder switch," Opt. Lett. **38**, 733-735 2013.

A tuning method for photonic integrated circuits in presence of thermal cross talk

(Student Paper)

Maziyar Milanizadeh[1], Douglas Aguiar[1], Sara Ahmadi[1], Francesco Morichetti[1], Andrea Melloni[1]
[1]*Dipartimento di Electtronica Informazione e Bioingegneria -*
Politecnico di Milano, Piazza Leonardo da Vinci, 32 - 20133 Milano - Italy
Tel: +39223998979, e-mail: maziyar.milanizadeh@polimi.it

Abstract
We present a novel method to perform tuning and locking of photonic integrated circuits (PICs) in presence of thermal cross-talk. The unwanted phase coupling among different elements of the circuit is canceled via exploiting the eigen-vectors of the thermally coupled system. The effectiveness of the proposed method is proved on PIC architectures, based on microring resonators (MRRs) and Mach-Zehnder interferometers (MZIs).

Keywords: Tuning, Locking, Resonance alignment, Thermal cross-talk, phase coupling, Microring resonators

1 INTRODUCTION

In photonic integrated circuits (PICs), fabrication tolerances appear in the form of phase errors. Owing to the sensitivity of the effective index of the optical waveguides to nanometer-scale dimensional variations, these effects are particularly pronounced in high index contrast photonic platforms. Furthermore, phase drifts may be also caused during the device operation by temperature changes introduced in neighboring systems on the same chip.

Thermal actuators integrated in optical waveguides are a well-established approach to compensate against phase errors and to reconfigure the PIC responses. However, mutual thermal crosstalk between neighbour waveguides of the same PIC or among different PICs integrated onto the same chip may cause unwanted phase perturbations and impair control procedures. This phenomenon leads to increase of required iterations or even divergence in control algorithms employed to modify or maintain a status of the device.

In this contribution we present a novel method, named *Transformed Coordinate method* (TCM), that can be used to circumvent thermal cross talk effect and allows to automatically configure and stabilize PICs with no penalties introduced by thermal coupling between different actuators. The effectiveness of the proposed method is demonstrated by numerical simulations and experiments carried out on different PIC architectures, based on different arrangements of microring resonators (MRRs) and Mach-Zehnder interferometers (MZIs).

2 TRANSFORMED COORDINATE METHOD

To illustrate the TCM, let us consider the scheme of Fig. 1(a) showing an arbitrary integrated optic device with N thermal actuators for reconfiguration and tolerance compensation. When an electrical signal is applied to the $i-th$ actuator, it is expected to introduce a desired phase change $\delta\phi_i$ to the $i-th$ waveguide where it is integrated, with no effects on the surrounding waveguides. However, due to thermal cross-talk, some phase perturbations are also introduced in the other waveguides too. The actual phase shift $\Delta\phi_i$ induced in each waveguide is thus given by the phase coupling matrix:

$$\begin{pmatrix} \Delta\phi_1 \\ \Delta\phi_2 \\ \Delta\phi_3 \\ \vdots \\ \Delta\phi_n \end{pmatrix} = \begin{pmatrix} 1 & \mu_{12} & \mu_{13} & \cdots & \mu_{1n} \\ \mu_{21} & 1 & \mu_{23} & \cdots & \mu_{2n} \\ \mu_{31} & \mu_{32} & 1 & \cdots & \mu_{3n} \\ \vdots & \vdots & \vdots & \ddots & \vdots \\ \mu_{n1} & \mu_{n2} & \mu_{n3} & \cdots & 1 \end{pmatrix} \begin{pmatrix} \delta\phi_1 \\ \delta\phi_2 \\ \delta\phi_3 \\ \vdots \\ \delta\phi_n \end{pmatrix} \tag{1}$$

where the phase coupling coefficient μ_{nm} between the $m-th$ actuator and the $n-th$ waveguide depends on the PIC topology. Due to this phase coupling, individual modification of phases $\delta\phi_i$ is not an effective method for controlling the system, because the vector $\delta\phi$ of the desired phase shift is perturbed via this mapping matrix.

To counteract phase coupling, the TCM exploits the eigen-modes of the thermally coupled PIC. Mathematically this means that the phase change vectors that are utilized, correspond to the eigen-vectors of the unwanted phase coupling matrix extracted from (1). Orthogonality of these vectors enable to apply decoupled phase modification to the system, as shown in Fig. 1 . In principle, if the phase coupling coefficients μ_{nm} in a system of N elements are all known, TCM can reaches the optimum point in only N operations.

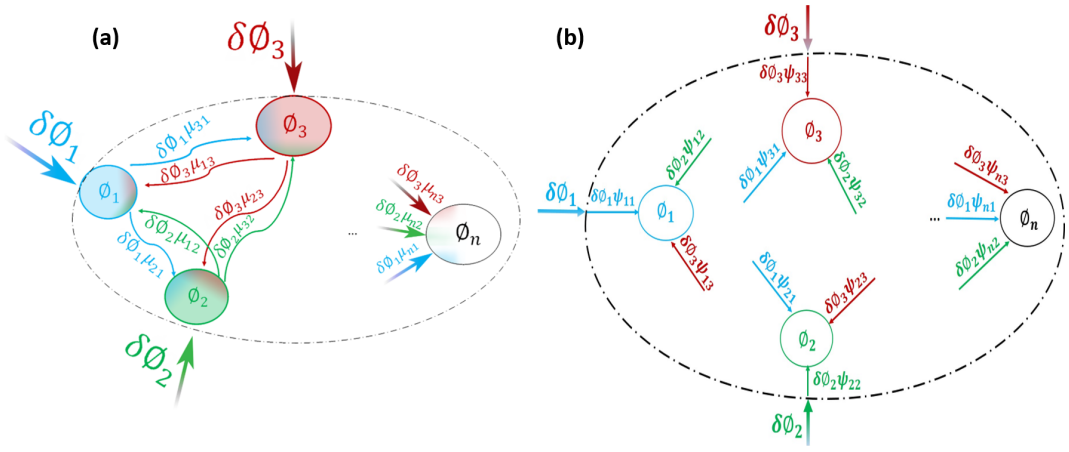


Figure 1. **(a)** Schematic representation of a PIC in the presence of phase coupling due to thermal crosstalk. $\delta\phi_i$ is the desired phase change and $\Delta\phi_i$ is the actual one. **(b)** Phase de-coupling achieved by applying TCM in control of the PIC. $\psi_{j,i}$ is the $j-th$ eigen-vector applied to $i-th$ actuator phase change $\delta\phi_i$

2.1 Numerical simulations

To show the effectiveness of the TCM method, we present its use on two different PIC architectures. The first one is the 3rd order coupled MRR filter shown in Fig. 2.(a), where 3 actuators are used to modify the round trip phase ϕ_i of each ring. Proposed tuning methods for this kind of filters exploit sequential sweeping of the individual resonance of each MRR for aligning it to the desired wavelength [1],[2] and are therefore vulnerable to phase coupling effects. In TCM all the MRRs are simultaneously modified. Considering only thermal cross-talk induced by neighboring MRRs, the thermally-coupled system can be modeled as

$$\begin{pmatrix} \Delta\phi_1 \\ \Delta\phi_2 \\ \Delta\phi_3 \end{pmatrix} = \begin{pmatrix} 1 & \mu & 0 \\ \mu & 1 & \mu \\ 0 & \mu & 1 \end{pmatrix} \begin{pmatrix} \delta\phi_1 \\ \delta\phi_2 \\ \delta\phi_3 \end{pmatrix} \tag{2}$$

Phase changes are applied sequentially but according to the eigenvectors of unwanted phase coupling matrix. These eigen-vectors are $\psi_{1,i} = [-1, 0, 1]$, $\psi_{2,i} = [1, \sqrt{2}, 1]$, $\psi_{3,i} = [1, -\sqrt{2}, 1]$ respectively with $i = 1, 2, 3$. To test the convergence of the TCM, we considered a randomly perturbed filter, where phase errors as large as

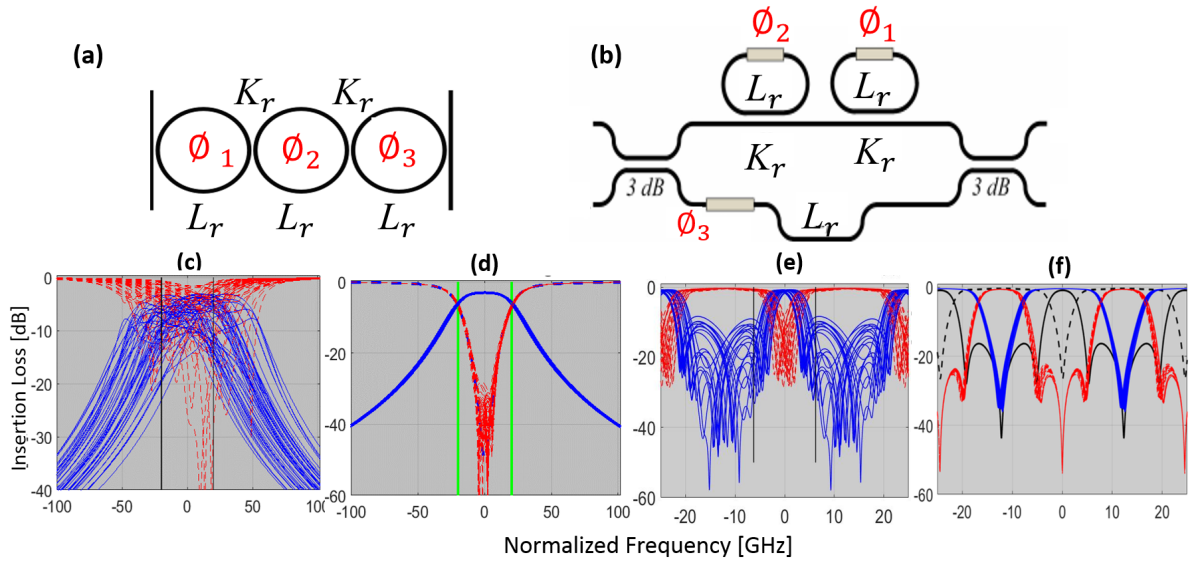


Figure 2. **(a)** 3^{rd} order MRR filter, $40GHz$ BW and $1THz$ of FSR where ϕ_i are the round trip phase of each rings. **(b)** Unbalanced Mach-Zehnder loaded with two rings to perform as tunable bandwidth filter with FSR of $25GHz$ and BW tune-ability of 0.1*FSR-0.9*FSR **(c)** Through (red-dashed) and drop(blue-solid) ports of 3^{rd} oder MRR filter for 50 cases of random perturbations. **(d)** Through and drop ports of 3^{rd} order MRR filter tuned using TCM **(e)** Bar (blue-solid) and cross (red-dashed) port of tunable Bandwidth filter for 30 cases of random perturbations as initial status of simulations. **(f)** Filters started from fig(e) are tuned and adapted to wider signal. Black curves shows tuned filter for narrow signal

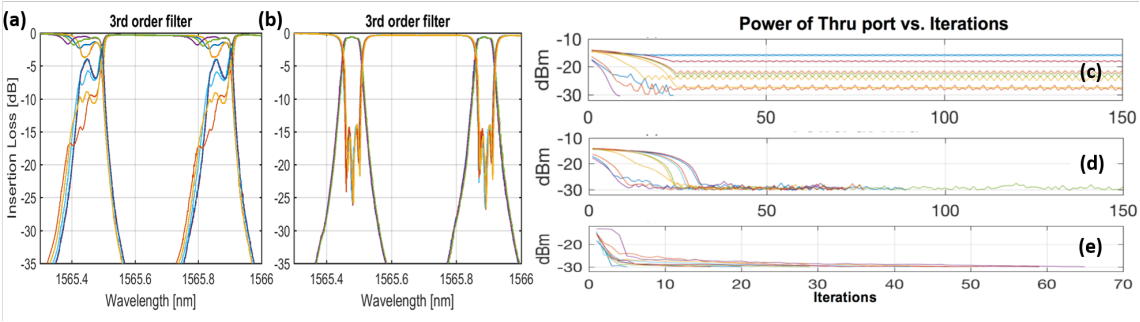


Figure 3. Experimental tuning based on the transform coordinate method. Frequency domain response of **(a)** a randomly perturbed 3^{rd} order MRR filters in SiON technology (through and drop ports) and of **(b)** the filter after TCM-based tuning. Optical power at through port of the filter during **(c)** conventional sequential tuning of resonators, **(d)** TCM with constant phase steps and **(e)** TCM with adaptive phase steps.

$\pm\pi/16$ ($\pm 31GHz$ versus $40GHz$ of filter BW) were deliberately introduced in each MRR (50 random initial conditions shown in Fig.2.(c)). Using the algorithm to minimize the optical power at the through port, fine tuned filters with almost overlapping frequency responses were achieved in all the cases of study [see Fig.2.(d)].

The second PIC architecture is an unbalanced MZI loaded with two MRRs in the shorter arm, this architecture implementing a tunable bandwidth filter [3]. Bandwidth tuneability is achieved by controlling the three phase shifters ϕ_i. The tuning of $\phi_1 - \phi_2$ allows the control of the 3 dB bandwidth of filter while the condition $\phi_3 = m\pi + (\phi_1 + \phi_2)/2$ allows the filter transfer function to be always symmetric with respect to filter central frequency. Considering all the actuators to introduce same mutual thermal cross-talk to each other, the phase coupling matrix is given by

$$\begin{pmatrix} \Delta\phi_1 \\ \Delta\phi_2 \\ \Delta\phi_3 \end{pmatrix} = \begin{pmatrix} 1 & \mu & \mu \\ \mu & 1 & \mu \\ \mu & \mu & 1 \end{pmatrix} \begin{pmatrix} \delta\phi_1 \\ \delta\phi_2 \\ \delta\phi_3 \end{pmatrix} \tag{3}$$

By distinguishing the unwanted phase coupling matrix, eigen-vectors are calculated as $\psi_{1,i} = [-1, 1, 0]$, $\psi_{2,i} = [-1, 0, 1]$, $\psi_{3,i} = [1, 1, 1]$ respectively with $i = 1, 2, 3$. In this example we start from a tuned filter for a specific channel (black curves in Fig.2.(e,f)). Random phase errors are introduced in ϕ_i as large as $\pm\pi/10$ ($\pm 1.25GHz$ versus $5GHz$ BW of filter). When the signal bandwidth is increased, not only the algorithm compensates the perturbations, but it adapts the filter to the broader signal bandwidth. Blue curves in Fig.2.(f) show transfer function of converged filters which is adapted to the wider signal bandwidth.

3 EXPERIMENTAL RESULTS

The TCM-based tuning was experimentally tested on a 3rd order MRR based filter fabricated in high-index-contrast silicon oxynitride (SiON) waveguides [4]. Different initial perturbations were intentionally introduced as random errors in the voltages driving the heaters around their optimum tuning point, resulting in a resonance spread as large as $100pm$ ($12.5GHz$ versus $6.5GHz$ BW of the filter). Fig.3.(a) shows through and drop port of the perturbed filter. By applying the TCM to minimize the power in through port at 1565.47 nm, the filter was tuned to the same shape regardless of the initial condition, as shown in Fig.3.(b).

Fig.3.(c) shows that sequential tuning of individual resonators may not converge in many cases. In contrast, the TCM tuning converged in all the considered cases, as shown in Fig.3.(d). Results in (e) show that the TCM convergence is accelerated by adopting an adaptive phase steps, leading to a reduction in the required iterations.

ACKNOWLEDGMENT

This work was supported in part by the EU H2020 Program under Grant STREAMS (no. 688172) and by Fondazione Cariplo under Project ACTIO (no. 2016-0881)

References

[1] J. C. C. Mak and W. D. Sacher and T. Xue and J. C. Mikkelsen and Z. Yong and J. K. S. Poon, "Automatic Resonance Alignment of High-Order Microring Filters" *IEEE Journal of Quantum Electronics*, vol. 51, no. 11, pp. 1-11, Nov. 2015.

[2] Hasitha Jayatilleka, Kyle Murray, Miguel Ángel Guillén-Torres, Michael Caverley, Ricky Hu, Nicolas A. F. Jaeger, Lukas Chrostowski, and Sudip Shekhar, "Wavelength tuning and stabilization of microring-based filters using silicon in-resonator photoconductive heaters," *Opt. Express 23, 25084-25097 (2015)*

[3] P. Orlandi, F. Morichetti, M. J. Strain, M. Sorel, P. Bassi and A. Melloni, "Photonic Integrated Filter With Widely Tunable Bandwidth," in Journal of Lightwave Technology, vol. 32, no. 5, pp. 897-907, March1, 2014. doi: 10.1109/JLT.2013.2294345

[4] A. Melloni, F. Morichetti, G. Cusmai, R. Costa, A. Breda, C. Canavesi, and M. Martinelli, "Progress in large integration scale circuits in SiON technology," in *Proc. 9th Int. Conf. Transp. Opt. Netw.*, vol. 1, pp. 223-226, Rome, Italy, Jul. 1-5, 2007.

Advances in Quantum Dot Lasers for Silicon Photonics

(Invited paper)

Yasuhiko Arakawa, Bongyong Jang, and Jinkwan Kwoen

Institute for Quantum Nano Infromation Electronics, The University of Tokyo
4-6-1 Komaba, Meguro-ku, Tokyo 153-8505 Japan
Tel: +81354526245 Fax: +81354526246, e-mail: arakawa@iis.u-tokyo.c.

ABSTRACT

High temperature stability and high feedback-noise tolerance of the quantum dot lasers are advantageous features for silicon photonics. In this paper, we discuss recent progresses in quantum dot laser on silicon substrates. A silicon optical interposer incorporating InAs/GaAs quantum dot laser arrays via a flip-chip bonding method was demonstrated with the bandwidth-density of 15Tbps/cm^2 at 125 °C. In addition, we report the first demonstration of a hybrid silicon quantum dot laser, evanescently coupled to a silicon waveguide. InAs/GaAs quantum laser structures are transferred, by means of direct wafer bonding, onto silicon waveguides defining cavities with adiabatic taper structures and distributed Bragg reflectors. Lasing operation has been realized above 100°C . Finally, we show an InAs/GaAs quantum dot laser directly grown on Si on-axis (100) substrate by the molecular beam epitaxy.

Keywords: quantum dot lasers, silicon photonics, integrated photonics, molecular beam epitaxy

ACKNOWLEDGEMENTS

This presentation is based on results obtained from a project commissioned by the New Energy and Industrial Technology Development Organization (NEDO).

Quantum Photonic Processor based on Silicon Nitride Waveguides

Student Paper

Caterina Taballione[1], Tom A. W. Wolterink[2], Andreas Eckstein[2], Jasleen Lugani[2], Robert Grootjans[3], Ilka Visscher[3], Jelmer J. Renema[2], Dimitri Geskus[3], Chris G. H. Roeloffzen[3], Ian A. Walmsley[2], Pepijn W. H. Pinkse[4] and Klaus-Jochen Boller[1]

[1] *Laser Physics and Nonlinear Optics (LPNO), University of Twente, PO Box 217, 7500 AE Enschede, The Netherlands. Tel: +31 53 489 5278, e-mail: c.taballione@utwente.nl*

[2] *Ultrafast Quantum Optics and Optical Metrology, University of Oxford, Clarendon Laboratory, Parks Road, OXI 3PU Oxford, UK*

[3]*Lionix International BV, PO Box 456, 7500 AL Enschede, The Netherlands*

[4]*Complex Photonic Systems (COPS), University of Twente, PO Box 217, 7500 AE Enschede, The Netherlands*

ABSTRACT

Stoichiometric high-index-contrast silicon nitride waveguides can accomplish some of the important needs of photonic quantum information processing, such as high complexity and low loss. We demonstrate a versatile linear optical photonic processor for quantum information processing based on stoichiometric silicon nitride waveguides. The photonic processor is fully programmable and remotely controllable. The 8×8 unitary network is the largest fully programmable universal quantum photonic processor, based on silicon nitride waveguides realized so far. Demonstrating its versatile functionality we observe on-chip two-photon interference of high visibility, i.e., about 80%, with less than 10% variation in visibility between various nodes, i.e., beam splitters, of the photonic processor. Our findings show that stoichiometric silicon nitride is a promising platform for integrated, programmable quantum information processing.

Keywords: quantum information processing, linear optical processor, stoichiometric silicon nitride, two-photon interference.

1. INTRODUCTION

Integrated linear optical processors have become, in the recent past years, instrumental in the development and success of quantum information processing (QIP), enabling the realization of compact and stable quantum gates [1] and showing great potential for the study of quantum walks [2] and quantum key distribution [3]. The development of integrated quantum optics applications requires a significant increase of the circuit functionality, which is only possible with a dense concentration of long and complex pathways on the same photonic chip. However, at the same time, the overall optical chip size is limited due to fabrication constrains while waveguide platforms with insufficient index contrast or low optical transparency threaten to wash out quantum interference via curvature and propagation loss. These limitations highlight the need of a low-loss high-index-contrast material platform.

Stoichiometric silicon nitride (Si_3N_4) grown with low-pressure chemical vapor deposition (LPCVD), different from other types of silicon nitride [4], offers the unique combination of high index contrast ($\Delta n \sim 25\%$), ultralow straight-propagation loss (0.0004 dB/cm [5]), low insertion loss (<0.5 dB [6]), and spectrally wide transparency (from 400 nm to 2.5 µm).

Here, we present a universal linear optical photonic processor for QIP which is the largest so far realized in Si_3N_4 with low propagation losses and a high component density, on par with the state of the art [1]. The photonic processor is a fully tunable, reprogrammable and remotely controllable optical 8×8 Blass matrix [7], which implements an 8×8 universal unitary network. We demonstrate the proper functioning of the photonic processor for QIP via observing on-chip two-photon quantum interference with high visibility, programmable towards multiple nodes within the matrix.

2. QUANTUM PHOTONIC PROCESSOR

The architecture of the quantum photonic processor is given in Fig. 1. It is a realization of an optical 8×8 Blass matrix and comprises 64 unit cells each of which are composed of a phase shifter (in red) and a tunable beam splitter (in blue), enabling thus any 8×8 unitary transformation. The 128 tunable elements (64 tunable beam splitters and 64 phase shifters) enable each a 0-to-2π phase shift, i.e., ideally a 0-to-100% splitting ratio for the beam splitter. Due to technical reasons (enabling microwave-photonic applications as well) only the waveguides

at the bottom were directly accessible. Nevertheless, the full 8×8 matrix, i.e., the whole depth of the circuit, can be accessed by routing the light from the bottom inputs to all the beam splitters.

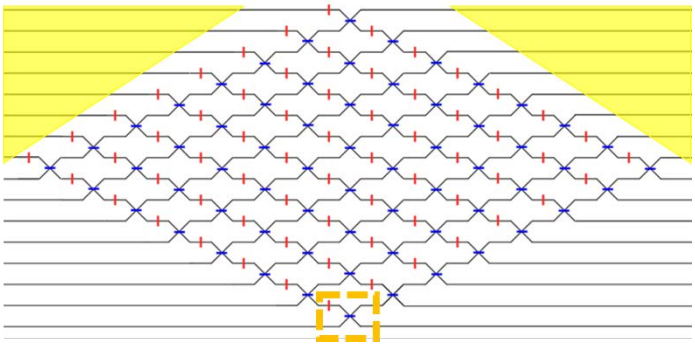


Figure 1 Schematic of the optical 8×8 Blass matrix. The orange box indicates one of the 64 unit cells: a phase shifter (red vertical line) and a tunable beam splitter (blue horizontal line). Although the top waveguides are not accessible (yellow triangles), the top part of the chip can be exploited by routing light from below.

To ensure propagation losses as low as 0.2 dB/cm and single-mode propagation at telecom C-band wavelengths (around 1550 nm) a double-stripe waveguide cross section is chosen [8]. The total on-chip propagation losses are bounded to less than 35%, a value that corresponds to the longest-possible on-chip geometrical path length (about 10 cm). A polarization maintaining fiber array is bonded to the chip to give access to the waveguides. The processor is overall temperature-stabilized by a Peltier element and an independent tuning of the 128 phase shifters is accomplished thermally via USB controlled drivers. The entire assembly comprising the chip, fiber array and electronics is packaged into a single portable box with a USB and power socket at its back, and with 16 standard fiber sockets at the front panel. After transportation of the box from Twente to the single-photon source in Oxford, there was no need for recalibrating the tuning elements on chip. After plugging in the single-photon source, the experiments were carried out straightforwardly via computer control of the USB input.

3. EXPERIMENTAL RESULTS

The single-photon source is composed of two periodically poled $KTiOPO_4$ (PP-KTP) single-mode waveguides (~10 mm long) [9] each pumped with spectrally filtered 1 ps long pulses centered at 775 nm with a repetition rate of 250 kHz from a Ti:Sapphire mode-locked laser providing an average power of 600 mW. In order to simultaneously pump both PP-KTP waveguides, the main beam from the Ti:Sapphire laser is divided into two equally long branches. An adjustable and programmable delay line (≈ 3 cm) is present in one of the two branches in order to enable Hong-Ou-Mandel-type quantum interference experiments [10]. Each PP-KTP waveguide generates, via type II parametric down-conversion, orthogonally-polarized photon pairs at telecom wavelengths (signal and idler at 1553 nm and 1547 nm, respectively) that are separated by polarizers and collected by single-mode fibers. The collection fibers are connected either directly to the detectors (idlers) or after injecting the single photons (signals) through the processor. Single photons leaving the processor were sent to a set of fiber-coupled superconducting single-photon detectors (niobium-based nanowires, efficiency 85%) and the counts were analysed with programmable electronic correlators. A total of four detectors were used: one for each generated photon.

First, we performed a reference Hong-Ou-Mandel (HOM) experiment using a fiber beam splitter with tunable splitting ratio. The signal photons from both waveguide sources are made indistinguishable by setting the delay line to zero. The measured two-photon interference for the reference experiment yields a visibility V_{ref} of about 80%.

Second, on-chip two-photon interference is performed in the form of HOM-type quantum interference. The two signal photons are now coupled into the photonic processor by polarization-maintaining fibers and are let to interfere at the first accessible tunable beam splitter (Fig. 2 (left) green circle). A variable delay is introduced between the signal photons via the aforementioned delay line. The splitting ratio of the tunable beam splitter is optimized to its ideal value, i.e., of 50%, performing a minimization of the coincidence count rate for indistinguishable input photons (i.e., zero delay). The coincidence count rate versus the relative delay of the two single photons is recorded (Fig. 2(right)) showing again a visibility of about 80%, which indicates an excellent fidelity.

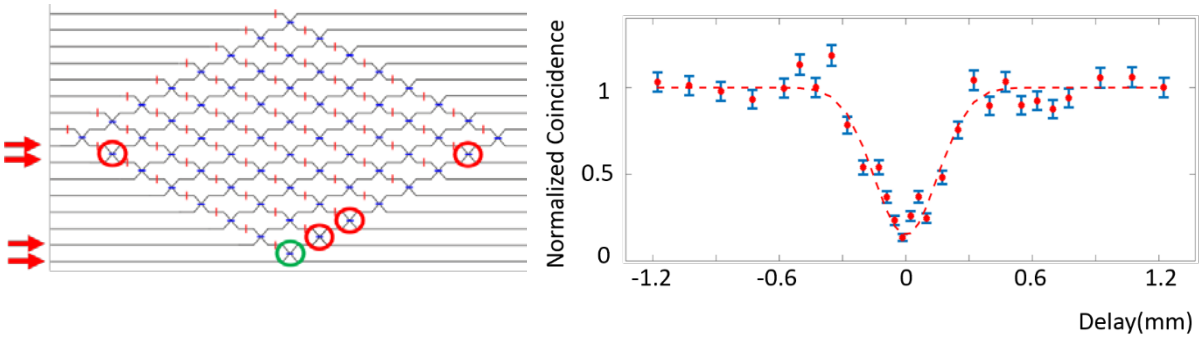


Figure 2 Left: location of various processor nodes (red circles) that where programmed to show two-photon interference, also indicating the used input waveguides (arrows). The green circle indicates the first accessible processor node. Right: two-photon-interference vs delay measured at that node. The dashed curve indicates a Gaussian fit to the data.

To further investigate the flexibility and configurability of our processor, we repeated the experiment of two-photon interference on various on-chip tunable beam splitters (Fig. 2(left) red circles), obtaining similar visibilities. We noticed a variation of the two-photon interference visibility of about ~10% between the first- and last-accessible processor nodes. This variation may have resulted either from slight path length differences between different beam splitters, which can be compensated, or from a deviation of the ideal 50% splitting ratio, which can be optimized.

4. CONCLUSIONS

We have demonstrated two-photon quantum interference on a Si_3N_4 photonic processor with results that compare well with those of an off-chip reference experiment, yielding a visibility of ~80%. The processor provides consistent results, with a variation of 10%, in terms of two-photon quantum interference visibility over its whole extension. Our findings demonstrate the suitability, reliability and, importantly, size-scalability for functionality upscaling at low loss of an integrated linear optical photonic processor based on Si_3N_4 waveguides.

REFERENCES

[1] J. Mower, N. C. Harris, G. R. Steinbrecher, Y. Lahini, and D. Englund: High-fidelity quantum state evolution in imperfect photonic integrated circuits, *Phys. Rev. A* vol. 92, pp. 032322, Sept. 2015.

[2] N. C. Harris, G. R. Steinbrecher, M. Prabhu, Y. Lahini, J. Mower, D. Bunandar, C. Chen, F. N. C. Wong, T. Baehr-Jones, M. Hochberg, S. Lloyd, and D. Englund: Quantum transport simulations in a programmable nanophotonic processor, *Nat. Photon.* vol. 11, pp. 447-452, June 2017.

[3] P. Sibson, J. E. Kennard, S. Stanisic, C. Erven, J. O'Brien, and M. G. Thompson: Integrated silicon photonics for high-speed quantum key distribution, *Optica* vol. 4, pp. 172-177, Feb. 2017.

[4] A. Peruzzo, M. Lobino, J. C. F. Matthews, N. Matsuda, A. Politi, K. Poulios, X.-Q. Zhou, Y. Lahini, N. Ismail, K. Wörhoff, Y. Bromberg, Y. Silberberg, M. G. Thompson and J. L. Obrien: Quantum Walks of Correlated Photons, *Science* vol. 329, pp. 1500-1503, Sept. 2010.

[5] J. F. Bauters, M. J. R. Heck, D. D. John, J. S. Barton, C. M. Bruinink, A. Leinse, R. G. Heideman, D. J. Blumenthal, and J. E. Bowers: Ultra-low-loss high-aspect-ratio Si_3N_4 waveguides, *Opt. Express* vol. 19, pp. 24090-24101, Nov. 2011.

[6] K. Wörhoff, R. G. Heideman, A. Leinse, and M. Hoekman: TripleX: a versatile dielectric platform, *Adv. Opt. Technol.* vol. 4, pp. 189-207, Apr. 2012.

[7] F. Casini, R. V. Gatti, L. Marcaccioli and R. Sorrentino: A novel design method for Blass matrix beam-forming networks, in *Proc. EuRAD, Munich, Germany, 2007.*

[8] K. Wörhoff, R. G. Heideman, A. Leinse and M. Hoekman: TripleX: a versatile dielectric platform, *Adv. Opt. Techn.* vol. 4, pp. 189-207, Apr. 2015.

[9] A. Eckstein, A. Christ, P. J. Mosley, and C. Silberhorn: Highly Efficient Single-Pass Source of Pulsed Single-Mode Twin Beams of Light, *Phys. Rev. Lett.* vol. 106, pp. 013603, Jan. 2011.

[10] G. Grynberg, A. Aspect, and C. Fabre: Nonlinear optics. From the semi-classical approach to quantum effect, in *Introduction to Quantum Optics: From the Semi-classical Approach to Quantized Light,* Cambridge University Press, New York 2010.

Tilted-potential Photonic Crystal Cavities for Integrated Quantum Photonics

(Student Paper)

A. Delgoffe, A. Miranda, B. Rigal, A. Lyasota, A. Rudra, B. Dwir and E. Kapon
Laboratory of Physics of Nanostructures, Institute of Physics,
Ecole Polytechnique Fédérale de Lausanne (EPFL),
Route Cantonale – 1015, Lausanne - Switzerland
Tel: +41216933387, e-mail: antoine.delgoffe@epfl.ch

ABSTRACT

We demonstrate a novel, tailored-index photonic crystal cavity designed for optimal extraction and propagation of single photons in integrated quantum photonic chips. The structure consists in a line-defect photonic crystal waveguide with linear effective-index profile supporting Airy-function photonic modes. The observed modes are analyzed theoretically and experimentally using site-controlled quantum dot systems. Selective excitation of Airy-modes by properly positioned single quantum dots is demonstrated.

Keywords: photonic crystal cavities, tailored refractive index, optical disorder, single photon sources.

1. INTRODUCTION

Integration of semiconductor quantum dots (QDs) and photonic crystal (PhC) membrane cavities and waveguides is a promising platform for the realization of integrated quantum photonics circuits for generation and processing of single photons on-chip [1-2]. Basic functions in such systems are efficient extraction of photons from single QDs and their routing to specific destinations on the circuit. This can be accomplished using Purcell enhancement of the single photon emission in a photonic nano-cavity [3], which is optically coupled in an optimal way to waveguides [4] free of mode-localization effects [5]. We propose and demonstrate a novel PhC tailored-index cavity in which the characteristic Airy-function modes can fulfill both objectives.

2. CONCEPT

The tailored-index cavity consists of a PhC line-defect membrane-waveguide in which the two rows of border holes are shifted outwards by an amount s(x) proportional to their position, up to a maximum value of s_{max}. This yields an approximately linear variation of the effective index n_{eff} of the waveguide mode along its axis. A photonic cavity with a linear index variation is thus formed, in which several modes with characteristic resonance frequencies ω_l (and photon energy $E_l = \hbar\omega_l$) are confined, as shown in Fig. 1(a).

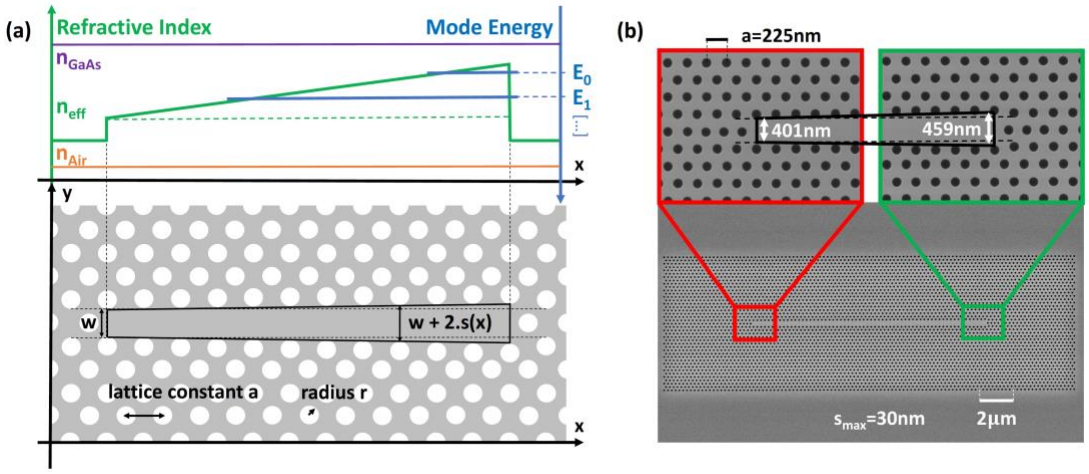


Figure 1. (a) Schematic illustration of the tilted-index cavity (bottom) and the effective index variation showing the resonant mode energies (top). (b) Scanning electron microscope images of a fabricated structure, with magnified view of the two cavity edges. Designed s_{max}=30nm.

The work was supported by the Swiss National Science Foundation.

Such structures were first studied numerically using a 2D finite-difference method (FDM), based on a 250nm-thick GaAs suspended membrane, a triangular PhC hole array of pitch a=225nm and various hole-radius to pitch (r/a) ratios. The tilted-index structures are variants of a uniform L_{61} line-defect cavity in which the hole shift s(x) is introduced (see Fig. 1). An example of the calculated modes for a cavity of total length of 62a=13.95μm and a maximum hole shift of s_{max}=10nm is shown in Fig. 2. The confined modes exhibit Airy-function envelopes similar to those of quantum mechanical particles confined in linearly-graded potential wells [6], superposed on the waveguide Bloch patterns. Each mode, of characteristic energy, consists of a main lobe systematically shifted in x according to the mode energy, to which an oscillating extended "tail" is attached. The main lobes of these wavefunctions can serve for efficient photon extraction from QDs placed there, together with controlled coupling to a distant location via the mode tail. Note that even a slight maximal shift (10nm) of the end holes produces a dramatic difference in mode structure with respect to the uniform-index L_{61} base cavities. The exact slope of the shifted holes determines the energy-position configuration of the spectrally-resolved near-field patterns.

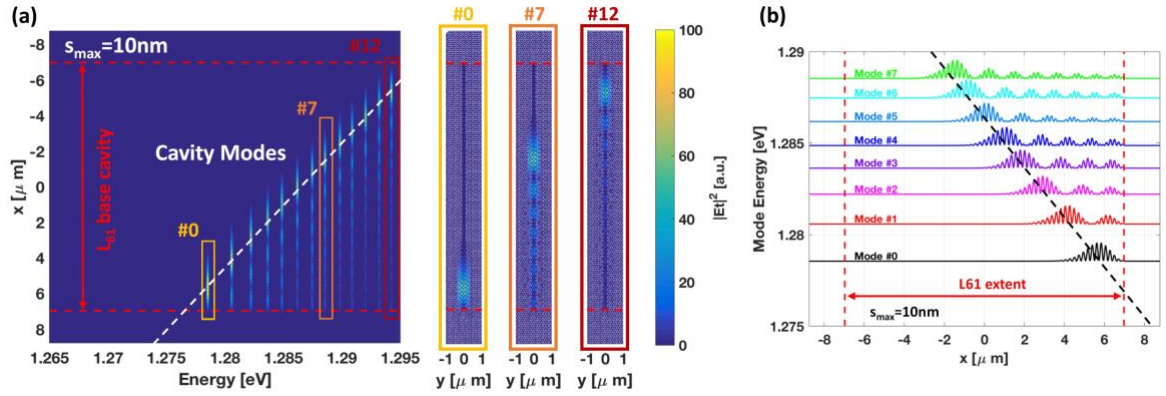


Figure 2. (a) Numerical simulation of in-plane electric field of the confined modes of a tilted-index cavity displayed in position-energy plane. Magnified view of three selected modes in x-y plane are shown. (b) Cross sections of the corresponding PhC Airy-modes. Parameters are s_{max}=10nm, pitch a=225nm, hole radii r=72.5nm, membrane thickness 250nm.

3. DEMONSTRATION

The tilted-index structures were produced on 250nm-GaAs suspended membranes in which the designed PhC hole patterns were fabricated using electron beam lithography. Site-controlled InGaAs/GaAs multiple QDs grown by metallorganic vapour phase epitaxy on substrates patterned with pyramid recesses served as internal light sources [7-8]. The structures were optically characterized by measuring their photoluminescence (PL) spectra and imaging their spectrally-resolved near field patterns at 10K [9]. Examples of the measured spectrally resolved (diffraction limited) near field patterns are shown in Fig. 3. Airy-mode patterns are clearly observed, with energy-position configurations closely matching the simulated results. Simulations and measurements of structures with different maximal hole shifts s_{max} indicate reduced effects of fabrication disorder with increasing effective-index slopes.

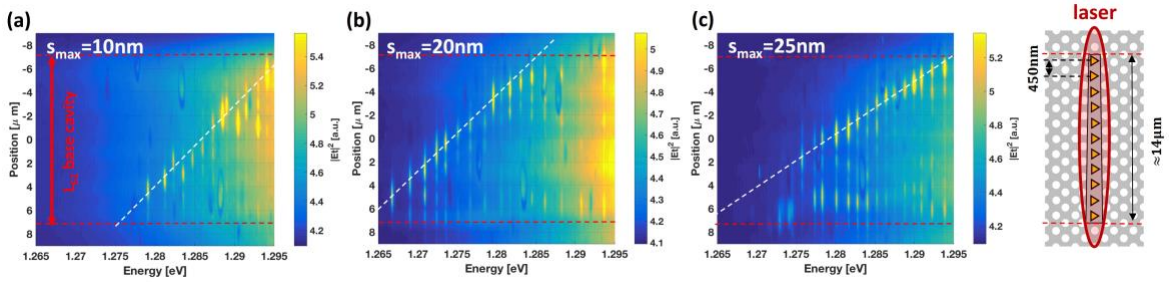


Figure 3. Experimental spectrally-resolved near-field patterns of tilted-index cavities for (a) s_{max}=10nm, (b) s_{max}=20nm and (c) s_{max}=25nm. Arrays of 450nm-spaced QDs serve to excite all cavity modes. Laser spot used for excitation depicted schematically.

In a second series of structures, single QDs were positioned at prescribed locations along the cavity, for matching the position of the main lobe of an Airy-mode of particular photon energy. In a specific configuration, two QDs, separated by ≈ 9.5μm, were positioned near the two edges of the cavities (see Fig. 4). Excitation of each QD separately was possible using a micro-PL setup with an excitation spot of 1-2μm-diameter. Thus, it was possible to excite the Airy-modes of the cavity with a point-like source (each QD is ~20nm wide), with a

relatively broadband spectrum due to emission from the QD barriers at the high power levels (~1mW) of the exciting laser. As evident from the spectrally resolved near field patterns (Fig. 4), only the Airy modes with sufficient overlap with the point-like sources are excited. This demonstrates the possibility of coupling the emission of single QDs to selected Airy modes by proper positioning of the QD with respect to the spatial mode patterns.

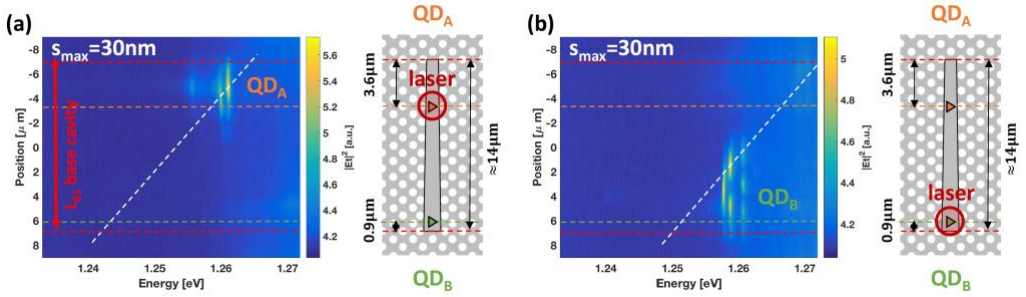


Figure 4. Experimental spectrally-resolved near-field patterns of tilted-index cavities with only 2 QDs located at specific positions at both ends, s_{max}=30nm: (a) excitation with QD_A; (b) excitation with QD_B. Laser spot used for excitation is depicted schematically.

4. CONCLUSIONS

By proper tailoring of the effective index in PhC membrane cavities, it is possible to shape the spatial mode envelope patterns in the form of Airy-functions. These mode shapes make possible the combination of efficient extraction of single photons and their guiding to remote on-chip destinations by precise placement of the QDs. Using site-controlled QDs, the feasibility of such QD-Airy function coupling (and subsequent extraction and guiding of single photons) was demonstrated.

ACKNOWLEDGEMENTS

The present work was partly supported by the French RENATECH network: we thank A. Arnoult for MBE growth of the (111)B GaAs/AlGaAs membrane wafers employed. We also thank M. Zimmermann for participation in preliminary numerical studies of the device.

REFERENCES

[1] J. L. O'Brien, *et al.*: Photonic quantum technologies, *Nature Photonics*, vol. 26. pp. 1532-1539, June 2008.
[2] P. Lodahl, *et al.*: Interfacing single photons and single quantum dots with photonic nanostructures, *Reviews of Modern Physics*, vol. 87 issue 2 pp. 347-400, May 2015.
[3] D. Englund, *et al.*: Controlling the spontaneous emission rate of single quantum dots in a two-dimensional photonic crystal, *Physical Review Letters*, *95 013904*, July 2005.
[4] A. Faraon, *et al.*: Efficient photonic crystal cavity-waveguide couplers, *Applied Physics Letters*, 90 073102, February 2007.
[5] R. Faggiani, *et al.*: Lower bound for the spatial extent of localized modes in photonic crystal waveguides with small random imperfections, *Scientifc Reports*, 6 27037, June 2016.
[6] L. Landau, E. Lifshitz: Quantum Mechanics, New York: Addison-Wesley, 1958.
[7] P. Gallo, *et al.*: Integration of site-controlled pyramidal quantum dots and photonic crystal membranes cavities, *Applied Physics Letters*, 92 263101, June 2008.
[8] A. Surrente, *et al.*: Dense arrays of site-controlled quantum dots with tailored wavelength: Growth mechanisms and optical properties, *Applied Physics Letters*, 111 221102, November 2017.
[9] B. Rigal, *et al.*: Probing disorder and mode localization in photonic crystal cavities using site-controlled quantum dots, *Journal of Applied Physics*, in print (2018).

Photonic integration of quantum entropy sources

(Invited paper)

C. Abellan[1*], W. Amaya[1], M. Rudé, D. Tulli[1], M. W. Mitchell[2,3] and V. Pruneri[2,3]
[1]Quside Technologies S.L., C/Esteve Terradas 1, 08860 Castelldefels (Barcelona), Spain
[2]ICFO-The Institute of Photonic Sciences, The Barcelona Institute of Science and Technology, 08860 Castelldefels (Barcelona), Spain
[3]ICREA-Institució Catalana de Recerca i Estudis Avançats, Lluis Companys 23, 08010 Barcelona, Spain

ABSTRACT

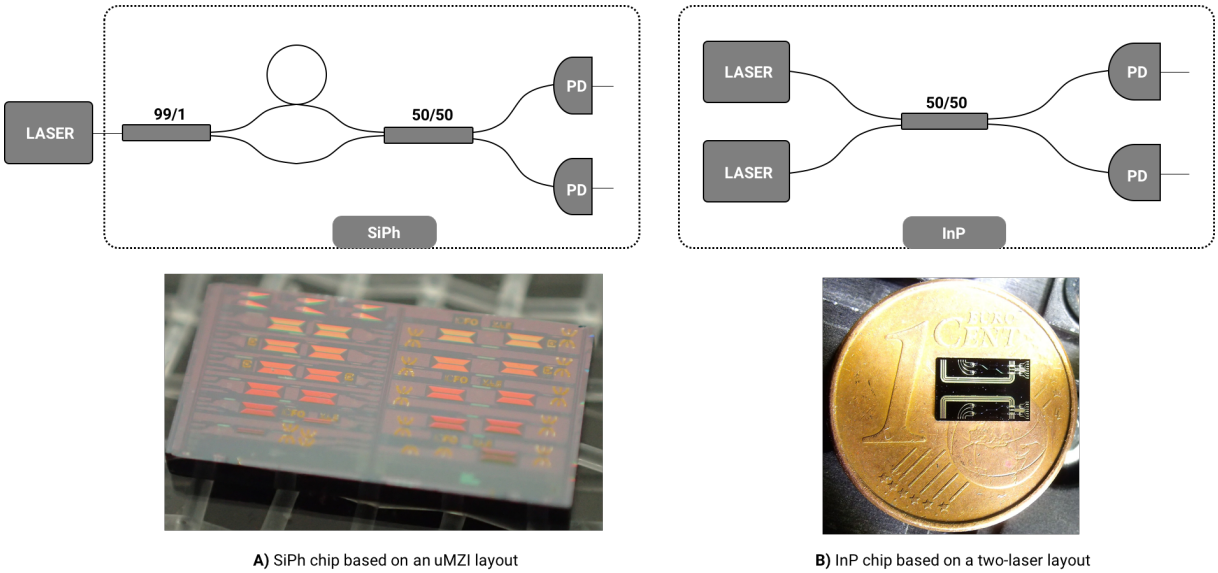
In this talk, we will discuss recent progress on the miniaturisation of ultrafast quantum entropy sources based on the phase-diffusion mechanism present in pulsed semiconductor lasers. Recent results of the integration in silicon photonics and indium phosphide platforms will be presented, demonstrating that Gb/s quantum random number generation is feasible with current photonic integration technologies. This shows potential towards mass scale adoption of quantum and photonic components for cyber-security and super-computation.

Keywords: quantum technologies, integrated photonics, quantum entropy sources.

1. INTRODUCTION

Random number generators play a crucial role in many information technologies, such as cryptography, numerical simulations in engineering, science or finance, and gambling. Historically, multiple techniques have been used to produce random bits, including algorithmic processes, known as pseudo-random number generators. However, only through the detection of quantum mechanical dynamics one can generate truly unpredictable random numbers. Various quantum random number generators (QRNGs) have been proposed during the last 30 years, mostly based on photonic approaches. Some examples include single photons splitting, the measurement of arrival time of single photons or the detection of vacuum fluctuations using homodyne measurements. To date, schemes based on the phase diffusion (PD) process in semiconductor lasers have achieved the fastest bit rates (up to tens of Gb/s) [1]. Randomness metrology procedures have been applied to PD-QRNGs to make quantitative statements about the unpredictability of this type of devices [2], and multiple prototypes have been built to be used in stringent environments, such as in the case of the 2015 loophole-free Bell test experiments [3]. Discrete optical components and optical fibres have been mostly utilised so far, posing limitations to the integration levels that can be achieved, and thus limiting the applicability of the technology to niche markets only. Remarkably, recent progress in the photonic industry can now be exploited to build compact and cost-effective devices with the potential to extend the market reach of quantum random number generators. Here, we present recent results towards the miniaturisation of phase diffusion quantum entropy sources (PD-QES) using Silicon Photonics [4] and Indium Phosphide [5] platforms.

The PD-QESs described in this manuscript are based on the phase diffusion process present in pulsed semiconductor lasers. By pulsing a laser from well below to well above its threshold level, a stream of phase-randomised optical pulses, with nearly identical intensity profiles, is generated [1-3]. When the laser is in its on state, stimulated emission dominates and coherence is created inside of the cavity. However, during the off-time, large phase diffusion is experienced and full randomisation occurs. This macroscopic phase diffusion process is a result of spontaneous emission events occurring inside of the laser cavity, and has therefore a quantum mechanical nature. After a string of phase-random pulses is created, an interferometric setup can be used to convert this now macroscopic phase information into the amplitude domain. In this way, one can obtain a stream of macroscopic amplitude-random pulses. This signal can be detected with standard high-bandwidth telecommunications photodetectors and digitised using commercial analog-to-digital converters. A quantum random number generator is therefore a device that produces random bits starting from a quantum mechanical process, or more precisely, a device that produces random numbers after taking samples directly from a quantum entropy source component.



A) SiPh chip based on an uMZI layout

B) InP chip based on a two-laser layout

Fig. 1. Integrated phase diffusion quantum entropy sources. (A) Silicon Photonics layout and chip based on an unbalanced Mach-Zehnder interfererence scheme. (B) All-optical integration in Indium Phosphide using a novel two-laser interference scheme.

2. PHOTONIC INTEGRATION

Two material platforms dominate the design and development of advanced photonic integrated circuits to date: Silicon Photonics (SiPh) and Indium Phosphide (InP). The key driving force behind SiPh is the ability to use CMOS like fabrication resulting in high-volume production at low cost. Besides CMOS compatibility, SiPh also offers high levels of integration. However, SiPh does not count with an easy integration of a laser source, limiting therefore the scope of the functionalities that can be pursued with this material platform. Alternatively, InP offers efficient integration of laser sources, opening the door to a whole new range of applications that can be monolithically integrated. In this section, we describe the development of two integrated quantum entropy sources in the two main integrated photonic platforms.

In Fig. 1A), the SiPh integration of a PD-QES based on an unbalanced Mach-Zehnder interferometer (uMZI) is shown [4]. In this configuration, the long path of the uMZI delays the pulse train by one period with respect to the short path, effectively achieving the interference of subsequent optical pulses at the output of the interferometer. The chip was designed to operate at 1 GHz frequencies, thus requiring a delay line of ~7 cm. At the output of the interferometer, fast germanium photodiodes are integrated on-chip to detect the interfered signal. An external 10 GHz gain-switched DFB laser was used as a light source to generate the input string of phase-randomised optical pulses. The uMZI is built with two cascaded multimode interferometers (MMIs) and a spiral delay line. Due to the relatively long 7-cm delay line, a ~20 dB loss is incurred by the signal travelling the long path of the uMZI, causing a significant loss unbalance between the two arms of the Mach-Zehnder . To compensate for such a loss unbalance, a 99/1 MMI was used at the input of the MMI to pre-compensate the loss incurred in the long path. Thus, the signal travelling the short path experiences a ~20 dB loss after the first MMI compared to the signal in the long arm, which will accumulate the ~20 dBs when travelling the spiral structure. Finally, when both signals reach the second 50/50 MMI, they both accumulate a 20 dB loss, thus optimising the interference visibility. The interfered signal is detected by the integrated photodetectors, demonstrating the functionality of the chip at an operating frequency of 1 GHz. The SiPh die area is below 1mm x 0.5mm. Future steps include the integration of the laser source on-chip using hybrid or heterogeneous techniques.

In Fig. 1B), the integration of a PD-QES on InP is depicted. In this case, and with the objective to reduce the losses introduced by long delay lines, a new design based on a two-laser scheme is introduced [5]. In this InP chip, all the photonic components are monolithically integrated on the chip, thus achieving full optical integration of the quantum device. In this new heterodyne detection configuration, one of the two lasers is operated in gain-switching mode to produce a string of phase-random pulses, whereas the other is operated in continuous wave (CW) mode

and acts as a local oscillator. The output from the two lasers is combined at a 50/50 MMI. By tuning the central frequency using metallic contacts on the laser structures, and by bringing the frequency detuning within the detection bandwidth of the integrated photodetectors, the random beat note between the GS and the CW lasers can be detected. The integrated device is tested for time intervals of up to 12-hours, finding high operation and statistical stability. The full optical integration in InP is achieved in a die size below 6mm x 2mm. In contrast to the uMZI layout described in the SiPh chip, the two-laser scheme can be operated at an arbitrary frequency, thus enabling full speed tunability. The chip has been tested at 200 MHz due to digitisation limitations, but pulsing rates above the GHz regime have been successfully observed, thus enabling multi-Gb/s entropy production in a fully integrated chip.

3. CONCLUSIONS

We have demonstrated the integration of phase-diffusion quantum entropy sources using standard chip production processes in Indium Phosphide and Silicon Photonics. Bit-rates above Gb/s have been obtained in both cases, showing progress towards mass-scalable ultrafast quantum entropy sources. These devices can be used to generate high-speed and high-quality unpredictable bits, which are of fundamental importance in cryptography, super-computation and gambling applications.

REFERENCES

[1] C. Abellan, W. Amaya, M. Jofre, M. Curty, A. Acin, J. Capmany, V. Pruneri, and M. W. Mitchell, "Ultra-fast quantum randomness generation by accelerated phase diffusion in a pulsed laser diode", Optics express **22**, 2, 1645–1654 (2014)

[2] M. W. Mitchell et al., "Strong experimental guarantees in ultrafast quantum random number generation", Phys. Rev. A **91**, 012314 (2015)

[3] C. Abellán, W. Amaya, D. Mitrani, V. Pruneri, and M. W. Mitchell, "Generation of Fresh and Pure Random Numbers for Loophole-Free Bell Tests", Phys. Rev. Lett. **115**, 250403 (2015)

[4] M. Rudé, C. Abellan, A. Capdevila, D. Domenech, M.W. Mitchell, W. Amaya and V. Pruneri, "Phase diffusion quantum entropy source on a silicon chip", arXiv:1804.04482v1 (2018)

[5] Abellan, C., W. Amaya, D. Domenech, P. Muñoz, J. Capmany, S. Longhi, M. Mitchell, and V. Pruneri: "Quantum entropy source on an InP photonic integrated circuit for random number generation", Optica **3** (9), 989–994 (2016)

Integrated Quantum Photonics on Silicon Chips

(Invited paper)

Carsten Schuck[1,2]
[1] Westfälische Wilhelms-Universität Münster, *Wilhelm-Klemm-Straße 10 – 48149, Münster - Germany*
Tel: +49 251 83 63948, e-mail: carsten.schuck@uni-muenster.de
[2] *Center for NanoTechnology (CeNTech), Heisenbergstraße 11 – 48149, Münster - Germany*
Tel: +49 251 83 63948, e-mail: carsten.schuck@uni-muenster.de

ABSTRACT
Quantum technology that utilizes single-photons as information carriers promises more efficient computing and higher security in communication. The realization of such novel photonic quantum information processing systems requires the implementation of large numbers of single-photon sources, linear optical circuitry and efficient single-photon detectors. To overcome scalability limitations and interface with established telecommunication architecture, we develop a nanophotonic quantum technology platform on silicon chips, employing standard semiconductor thin-film processing. We generate non-classical photon-pairs at telecom wavelengths via spontaneous parametric down conversion in aluminum nitride micro-ring resonators. Antibunching of heralded single-photons with high modal purity highlights the suitability of this second-order nonlinear source for nanoscale quantum optics. Further, we developed a toolbox of nanophotonic components for integrated quantum circuits. Employing balanced directional couplers we demonstrate quantum interference with 97% visibility when measuring photon statistics with waveguide-coupled detectors directly on-chip. Embedding superconducting nanowire single-photon detectors with nanophotonic circuits enables us to count individual photons with high efficiency, negligible dark count rate and high timing accuracy, as desired for applications in quantum technology. Advanced nanofabrication routines allow for straightforward replication of such sources, circuits and detectors in large numbers on silicon chips, thus paving the way for scalable integrated quantum photonics.

Keywords: quantum interference, superconducting single-photon detectors, spontaneous parametric down conversion, nanophotonic waveguides.

1. INTRODUCTION

Single photons are ideal carriers of quantum information and allow for realizing a broad range of applications in quantum communication, quantum computation and quantum sensing. The implementation of corresponding quantum photonic processing units require the generation, manipulation and detection of single photons. While proof-of-principle demonstrations were realized with bulk optic components the stability and scalability demands of complex quantum photonic circuitry will require an integrated solution. This can be achieved with nanophotonic waveguides and superconducting single-photon detectors on a silicon chip. Modern nanofabrication techniques then allow for replicating and combining functional units for photon generation, manipulation and detection in large numbers on a chip, thus enabling the construction of a programmable photonic quantum information processing system.

Here we employ aluminium nitride microring resonators that feature strong second-order optical nonlinearity to demonstrate the generation of single photons in pure quantum states. Nanophotonic circuit components allow for realizing high-visibility quantum interference of indistinguishable photons, which underlies the implementation of crucial quantum gate operations. Current-biased superconducting nanowires enable efficient detection of single photons with high signal-to-noise ratio. The integration of all these building blocks on a silicon chip holds great promise for photonic quantum technology.

2. PHOTON PAIR GENERATION IN MICRORING RESONATORS

Sources of indistinguishable photons are a key prerequisite for any quantum photonic information processing system. The generation of suitable photon pairs has recently been realized via the third-order nonlinear process of spontaneous four wave mixing (SFWM) in silicon waveguides. However, in SFWM schemes it is not straightforward to separate the resulting correlated signal and idler photons from the co-propagating classical pump field directly on chip, casting a fully integrated quantum photonic solution with waveguide-coupled single-photon detectors into doubt. Here we realize the generation of photon pairs in the second-order nonlinear process of spontaneous parametric down conversion instead, because larger spectral separation between pump und signal (idler) fields benefits efficient filtering.

We achieve phase-matching between higher-order visible-wavelength (775 nm) transverse magnetic pump modes and telecom-wavelengths (1550 nm) signal and idler fields in aluminium nitride (AlN) microring resonators via geometric dispersion engineering. The strong intrinsic second-order nonlinear of the AlN material system allows for generating degenerate photon pairs within 1.1 GHz bandwidth at rates of 3 MHz per milliwatt pump power. We confirm the quantum nature of the down-converted photons by analysing their statistical properties in time-correlated single-photon counting experiments [1]. A measurement of the second order auto-correlation function of idler photons heralded by the detection of their alleged signal partner photon shows high-visibility antibunching with $g^{(2)}(\tau=0) = 0.09$, which has no classical analogue. We further find high modal purity of the generated idler photons in a self-correlation measurement yielding a Schmidt number of K = 1.07, thus underlining the benefits of nanophotonic waveguide implementations for quantum photonics.

3. NANOPHOTONIC CIRCUIT COMPONENTS

Linear optic circuits are sufficient for implementing universal quantum information processing if they can be combined with single-photon sources and efficient detectors, as envisioned here. Crucial circuit components that allow for realizing quantum logic gate operations include beam splitters and optical phase shifters [2]. The latter can be realized via electrostatic actuation of optomechanical nanophotonic devices, which is preferable over thermo-optic and carrier-injection based methods that are challenging the integration with superconducting detectors and single-photons in dielectric waveguides, respectively. On-chip beam splitters on the other hand can be realized as directional couplers of evanescently coupled waveguides allowing for precisely controlled splitting ratios.

Here we show quantum interference of telecom wavelength photons from spontaneous parametric down conversion on a directional coupler fabricated from silicon nitride waveguides. Controlling the pump field characteristics allows for tuning the degree to which signal and idler photons are spectrally distinguishable via phase matching conditions. We observe two-photon interference with visibility of up to 97% using superconducting nanowire single-photon detectors embedded directly within the photonic integrated circuit [3]. Such high-visibility quantum interference will benefit the implementation of two-qubit quantum logic gate operations, which are a prerequisite for realizing universal quantum computing.

4. SUPERCONDUCTING NANOWIRE SINGLE-PHOTON DETECTORS

The overwhelming part of optical quantum technologies critically relies on the detection of single-photons in order to extract information from a quantum system. To perform such measurements both efficiently and accurately detectors are required that count single-photons with low noise, high timing accuracy and speed as well as high detection efficiency. Integrated quantum technology further benefits from efficient interfaces between detectors and nanophotonic circuits as well as operation at telecom wavelengths.

Here we show how superconducting nanowires are coupled with optical waveguides in traveling wave geometry for detection of near-infrared single-photons [4]. Efficient absorption of photons along their direction of propagation and high internal quantum efficiency nanowires biased close to their critical current yield on-chip detection efficiencies above 80%. Short nanowire length further allows for operation speed up to GHz rates, jitter performance of tens of picoseconds and sub-Hz dark count rates. We exploit these highly attractive performance characteristics for detecting quantum signatures of correlated single-photons directly on chip. High yield of hundreds of superconducting nanowire single-photon detectors on a single chip highlights the suitability of our approach for scalable quantum technology.

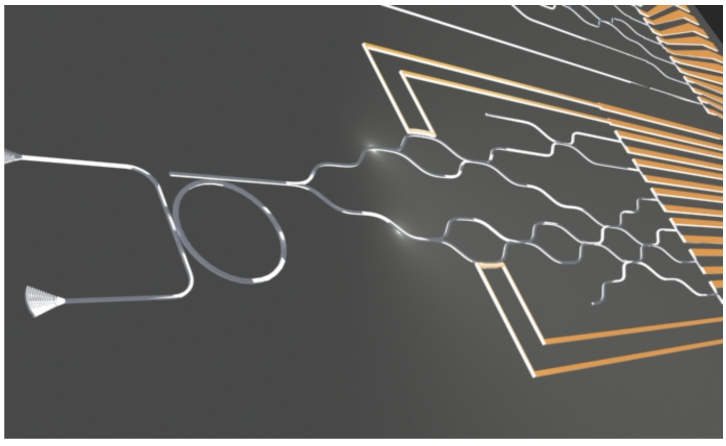


Figure 1. Schematic of quantum photonic circuits on a silicon chip.

5. CONCLUSIONS

We realize a quantum light source based on the second-order nonlinear process of spontaneous parametric down conversion in a microring resonator on a silicon chip. High visibility quantum interference in photonic integrated circuits and efficient single-photon counting with waveguide-coupled superconducting nanowire detectors demonstrates the suitability of our platform for integrated quantum optics. We have taken first steps towards the integration of large numbers of non-classical light sources, nanophotonic circuit components and single-photon detectors on a monolithic silicon chip (see Fig. 1) that satisfies the stability and scalability requirements of complex quantum technology. Future work will rely on these building blocks for realizing quantum logic gates that can be combined into a quantum algorithm as well as quantum communication and sensing schemes.

REFERENCES

[1] X. Guo, C. Schuck, *et al.*: Parametric down-conversion photon-pair source on a nanophotonic chip, *Light: Science & Applications*, vol. 6, pp. e16249 (2017).

[2] M. Poot, C. Schuck, *et al.*: Design and characterization of integrated components for SiN photonic quantum circuits, *Optics Express*, vol. 24, pp. 6843-6860 (2016).

[3] C. Schuck, X. Guo, *et al.*: Quantum interference in heterogeneous superconducting-photonic circuits on a silicon chip, *Nature Communications*, vol. 7, pp. 10352 (2016).

[4] W. H. P. Perncie, C. Schuck, H. X. Tang: Waveguide integrated superconducting nanowire single photon detectors on silicon, in *Superconducting Devices in Quantum Optics*, R. Hadfield, G. Johansson, Eds., Springer, Cham, 2016.

Developments in 300mm Low-Power Si Capacitive Modulators

Invited paper

Charles Baudot[1], I. Charlet[1,2], M. Douix[1,2], S. Guerber[1,2], S. Crémer[1], N. Vulliet[1], J. Planchot[1], R. Blanc[1], L. Babaud[1], C. Alonso-Ramos[2], D. Benedikovich[2], S. Messaoudène[3], S. Kerdiles[3], P. Acosta-Alba[3], C. Euvrard-Colnat[3], E. Cassan[2], D. Marris-Morini[2], L. Vivien[2], and F. Boeuf[1]

[1] Technology R&D, STMicroelectronics SAS, *850 rue Jean Monnet - 38920 Crolles France*

[2] Centre de Nanosciences et de Nanotechnologies, Univ. Paris Sud, Paris Saclay, CNRS - *91405 Orsay, France*

[3] 3Université Grenoble Alpes - CEA, LETI, MINATEC Campus, *38054 Grenoble, France*

Tel: +33438923492, e-mail: charles.baudot@st.com

ABSTRACT

We report on the development of high speed phase shifters for next generation of Si photonics transceivers, based on capacitive structures. Experimental measurements show a $V_\pi L_\pi$ of 0.5V.cm in accumulation regime. We also show that the addition of a SiGe layer at the capacitive interface leads to an improvement of 25 % of the phase shifter efficiency.

Keywords: Silicon capacitive modulators, damascene process, poly silicon, SiGe booster

INTRODUCTION

Silicon photonics has emerged industrially more than a decade ago and is now a well-established technology. Currently, the main application addressed is data-communication, essentially providing active optical transceiver cables for data-centres and metro interconnection networks. The vast deployment of data-centres across the World and its expansion into hyper-data-centres triggers the needs to increase the data-rate transmission, improve the power consumption efficiency and reduce optical signal losses to achieve faster and longer-reach cables.

A key component used in silicon photonics is the modulator found in the transmitter section. It consists of applying a signal amplitude modulation on the optical carrier using an electro-optical effect. PN junctions put in a Mach-Zehnder interferometer (MZI) configuration are the common components used to perform that operation. However, the poor electro-optical efficiency of the diodes result in millimetre long MZI sub-systems. High power consumption of the electronic driver, which controls the MZI diodes, is the principal consequence of that low-efficiency and high footprint [1].

In this paper, we propose a new electro-optical device architecture based on a capacitive structure. Various experimental studies were reported on capacitive structures in silicon platforms [3], [4], [4]. However, our focus is to integrate the device within a transceiver system. We develop a fabrication scheme that makes it possible to co-integrate a Crystal-Si, Oxide, Poly-Si Accumulator (COPA) with other active devices such as Si pn and pin junctions, Ge photodiodes and a complex, 4 layer electrical interconnection back-end of line (BEOL). Our strategy is to insert a new process module within in photonics fabrication flow without any alteration to other devices.

1. CAPACITIVE MODULATOR DESIGN

Figure 1a-b shows the capacitive phase-shifter cross-section. The COPA structure is formed by a P-doped crystalline Si layer, on top of which SiO_2 and N-doped poly Si layers are deposited. As a function of the voltage applied on the P^{++}/N^{++} contacts, carrier accumulation occurs around the oxide layer, leading to refractive index variations in the centre of the waveguide, and phase modulation of the guided mode. The performances of the COPA structure are simulated by solving Poisson equation within Synopsys Device module [5] and the optical mode profile with Lumerical MODE [6]. The impact of the oxide thickness (noted t_{ox}) and the doping levels (D) are simulated. The t_{ox} variation is between [5 – 15]nm and D between [5.2E^{17}- 1.7E^{18}]cm^{-3}. The voltage swing V_{pp} is of only 0.9V to ensure ow power consumption. Previous simulations indicated that the best efficiency is thus obtained for an applied voltage between [0.9 – 1.8]V, keeping the capacitive structure in the accumulation regime.

To evaluate the phase shifter performance, the optical modulation amplitude (OMA) is considered. It depends on the phase shift per unit length $\Delta\phi$ (rad/mm), and on the optical loss per unit length α (mm^{-1}). For an optical input power of 1mW, the OMA of a L-long phase shifter is given by (1).

$$\mathrm{OMA} = e^{-\alpha L} \left| \sin(L \cdot \Delta\phi) \right| \quad (1)$$

From (1) we can see that OMA depends on the phase shifter length. From the derivative of (1), we can deduce the optimal length L_{opt} that maximizes OMA [7]:

$$L_{opt} = \frac{1}{\Delta\phi} \cdot \mathrm{atan}\left(\frac{\Delta\phi}{\alpha}\right) \quad (2)$$

Figure 1c shows the evolution of $\Delta\phi$ and L_{opt} as a function of D and t_{ox}. The largest phase shift efficiency are obtained for thin oxide and for the lowest values of the doping level. However higher D reduces the device footprint, while device speed which is limited by RC product decreases when the oxide thickness and doping level decreases. The operating range for 25 Gbit/s and 56 Gbit/s are coloured in Fig 1c, showing that $t_{ox} \geq 7$nm and $t_{ox} \geq 12$nm are required for 25 Gbit/s and 56 Gbit/s respectively.

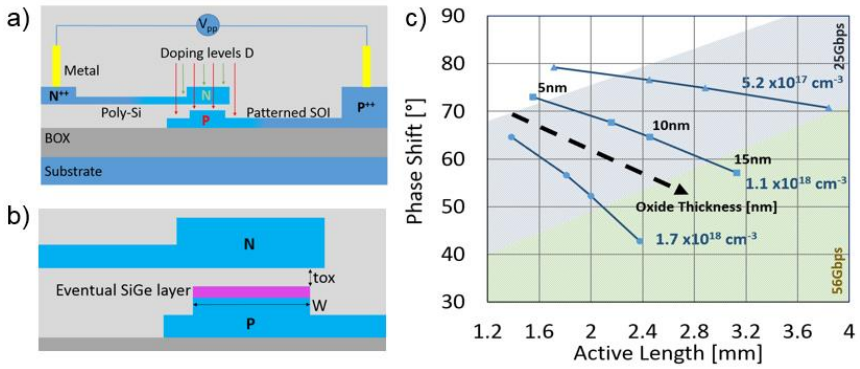


Figure 1: (a) Phase-shifter cross-section showing the capacitive structure. (b) Detailed cross-section of the COPA waveguide. A thin layer of p-type SiGe can eventually be grown above the SOI layer. (c) Simulated features of the capacitive structure.

2. FABRICATION PROCESS

The fabrication scheme has been defined in order to be able to co-integrate the COPA structure with the other active devices already present in Si transceivers. The module which has been added in the process flow consists of conventional Si CMOS process steps (Fig. 2). First, the SOI layer is patterned, encapsulated and doped using boron. Then the encapsulating SiO_2 is partially etched, forming a cavity where the SiO_2 interface, the poly-Si and eventually the $Si_{0.71}Ge_{0.29}$ layers are deposited. The mono-crystalline $Si_{0.71}Ge_{0.29}$ alloy is obtained by selective epitaxial growth using Si as seed layer. Accordingly, we then use high temperature SiO_2 deposition for the dielectric interface. Otherwise, in the absence of SiGe, we use rapid thermal oxidation of the SOI layer at temperatures between 850°C and 1050°C to generate the capacitive interface. A thick layer of amorphous Si deposited by LPCVD, followed by a CMP and a crystallisation anneal generates the poly-Si branch of the device [8]. Finally, the poly-Si is patterned and doped by phosphorous implantation. Figure 2b shows a cross-section TEM of the fabricated structure with the relevant BEOL metallization. Further TEM analysis done on dedicated samples also shows the grown SiGe at the capacitive interface (Fig. 2c-d).

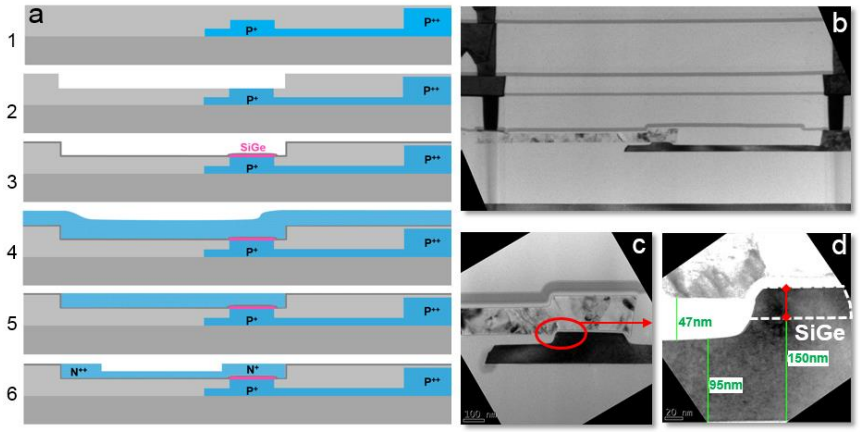


Figure 2: (a) Fabrication steps of the module inserted in the standard flow to generate a capacitive structure. The six main steps consist of a damascene approach to generate the second opto-electrical branch of the device. (b) TEM cross-section showing the patterned capacitive structure and metal interconnections. (c & d) Close-up of the optical section of the device showing both SiGe and oxide interfaces.

3. EXPERIMENTAL CHARACTERIZATION

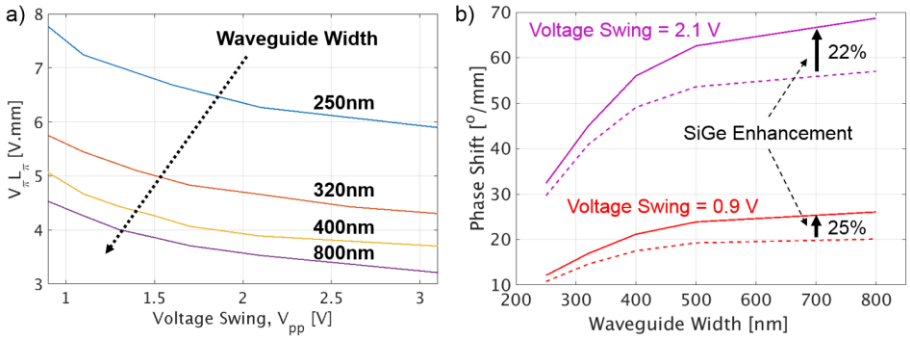


Figure 3: (a) Evolution of $V_\pi L_\pi$ for different waveguide widths as a function of the applied voltage. (b) Effect on the phase-shift of a thin SiGe layer above the SOI.

The static features of the modulator are assessed at $\lambda = 1310$nmn using 700 µm phase shifter embedded in a Mach Zehnder interferometer. The modulator efficiency is measured for different waveguide widths (W on Fig.1b) at fixed t_{ox}= 7.5nm (Figure 3a). Estimations, using the RC product and the $V_\pi L_\pi$ for W = 400nm and V_{pp}= 0.9V suggest 25 Gbit/s operation feasibility. Such a configuration leads to $V_\pi L_\pi = 5V.mm$. Comparatively, this COPA modulator would be 8 times more efficient than a typical pn junction at 25 Gbit/s [1].

SiGe exhibits a stronger electro-optic effect than Si [9]. Modulators with t_{ox}=13nm and including a 15-nm $Si_{0.71}Ge_{0.29}$ layer below the oxide layer (Fig. 1a) are also characterized (Fig. 4b). The capacitance value is 10% higher as compared with a full Si equivalent structure, while the phase-shift is 25% better (Fig. 3b) but the optical losses are 40% higher. Thus, we observe that the effect of the SiGe layer is significant but not optimized yet. Consequently, we can expect to improve COPA modulators by integrating a well-designed SiGe layer.

CONCLUSION

We demonstrate the fabrication of a capacitive structure compatible with a full transceiver integration. Experimental characterizations show the high efficiency obtained of the COPA structure, which is 8 times better than using a standard pn-junction. Such a high efficiency allows a reduction of the phase shifter length and required voltage swing which paves the way towards high speed and low power consumption modulators. Furthermore the integration of a SiGe layer below the oxide layer is promising as a 25% improvement of the phase shift has been already obtained

ACKNOWLEDGEMENTS

This work was partially funded by the European Commission through the H2020-ICT-27-2017 COSMICC project under the grant agreement n°688516.

REFERENCES

[1] E. Temporiti *et al.*: Insights into silicon photonics Mach-Zehnder based optical transmitter architectures, *IEEE Journal of Solid-State Circuits*, vol. 51, pp. 3178-91, Dec. 2016.
[2] J. V. Campenhout *et al.*: Low-voltage, low-loss multi-Gbps silicon micro-ring modulator based on a MOS capacitor, *in IEEE International Conference on Group IV Photonics*, 2012, pp. 10-12.
[3] A. Liu et al.: A high-speed silicon optical modulator based on a metal-oxide-semiconductor capacitor, *Nature*, vol. 427, no. 6975, pp. 615-8, Feb. 2004.
[4] M. Webster *et al.*: An efficient MOS-capacitor based silicon modulator and CMOS drivers for optical transmitters, *in 11th International Conference on Group IV Photonics (GFP)*, Aug. 2014.
[5] Synopsys Tcad Tools, http://www.synopsys.com/Tools/TCAD/
[6] Lumerical Mode Solutions, http://www.lumerical.com.
[7] F. Boeuf et al.: Benchmarking Si, SiGe, and III-V/Si hybrid SIS optical modulators for datacenter applications, Journal of Lightwave Technology, 2017.
[8] M. Douix *et al.*: Low loss poly-silicon for high performance capacitive silicon modulators, *Optics Express*, vol. 26, no. 5, pp. 5983-5990, Mar. 2018.
[9] M. Takenaka and S. Takagi: Strain engineering of plasma dispersion effect for SiGe optical modulators, *IEEE J. Quantum Electron.*, vol. 48, no. 1, pp. 8–16, Jan. 2012.

Low-threshold and High-speed Quantum-dot Microring Lasers on Silicon

Chong Zhang, Di Liang, Geza Kurzcveil, Raymond G. Beausoleil
System Architecture Lab, Hewlett Packard Labs, Hewlett Packard Enterprise
Palo Alto, CA 94304 – *United States*
Tel: +18058866378, e-mail: chong.zhang@hpe.com

ABSTRACT

We report the demonstration of the first hybrid quantum-dot (QD) microring lasers integrated on silicon. By transferring 1.3 μm InAs/GaAs QD gain layers to prepatterned SOI substrate, low threshold-current hybrid ring lasers are realized on silicon. High-speed direct current modulation of over 10 Gbps is achieved as well.

Keywords: Quantum dot laser, hybrid integration, direct laser modulation, silicon photonics.

1. INTRODUCTION

Next-generation high-performance computers (HPCs) demand few Tb/s communication bandwidth between switch hubs and hundreds of Gb/s bandwidth between nodes and hubs to overcome the challenge with rapid growing traffic. Integrated photonic interconnect is believed to be the solution for its advantages in high volume, low power and low cost, and high capacity with unique signal multiplexing techniques, e.g. wavelength division multiplexing (WDM). We have been developing a number of key photonic components, including low-threshold hybrid quantum well (QWs) microring lasers on silicon [1], and a new concept of integrated hybrid metal-oxide-semiconductor (MOS) capacitor for wavelength tuning [2] and data modulation. To further reducing device power consumption and enhancing high-temperature robustness, we have successfully transferred QD laser epitaxial material on this platform recently [3].

QDs lasers have drawn great attention due to their tolerance to material defects and higher radiative recombination efficiency at high temperature compared with QWs [3]. High-quality QDs materials can be epitaxially grown on silicon wafer and record-high laser output power [4] and sub-mA threshold lasing [5] have been reported, however, thick buffer layers still pose a big challenge to interact with silicon photonics. In this paper, we for the first time demonstrate the QD microring lasers on silicon with hybrid integration approach. Low threshold currents down to 2.5 mA at room temperature were achieved in devices with 50 μm in diameter. The RF performance as well as the direct modulation bandwidth are investigated and discussed in this paper.

2. DEVICE DESIGN

The device structure of the hybrid microring lasers is schematically shown in Fig. 1. The microring laser mainly consists of two parts: silicon waveguide (WG) and III-V mesa. The ring waveguide on silicon defines the laser cavity, while the bus waveguide couples out the emitted light from the ring. The III-V mesa consists of multiple layers of InAs/GaAs QDs with center photoluminescence wavelength around 1.3 μm. p- and n-doped GaAs/AlGaAs layers sandwiches the QDs stack to confine the optical mode as well as to offer electrode contacts. Intentional lateral offset between III-V mesa with silicon ring waveguide and curved bus waveguide are designed to adjust the optical coupling strength between ring and bus waveguide which represents the mirror loss of the laser cavity.

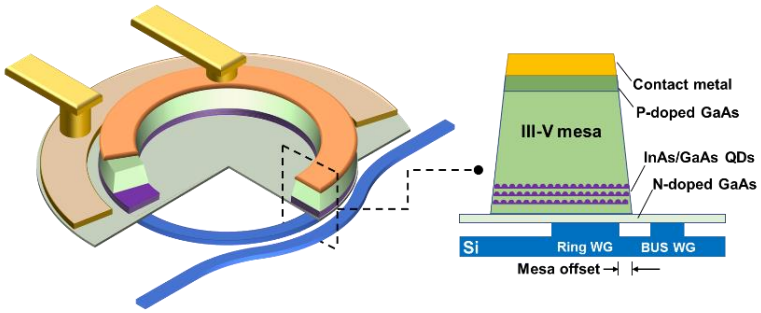


Figure 1. Diagram of hybrid microring laser on silicon and its cross-section structure.

The laser chip was fabricated with a complementary metal–oxide–semiconductor (CMOS) compatible process. The silicon-on-insulator (SOI) used this work has a 400 nm device layer and 1 μm buried-oxide layer. Unlike the previous reported self-aligned fabrication process [6], the silicon waveguide on the SOI substrate was

firstly patterned and etched, together with the grating couplers (GCs) used for coupling the light out with a single-mode fiber. Then the GaAs substrate with QDs layer stack was bonded to the SOI substrate followed with substrate removal. The standard III-V process defines the III-V mesa, n- and p- contact metallization, followed with passivation, via etch and probe-metal contact. Fig. 2(a) shows the scanning electron microscopic (SEM) image of the ring mesa after dry etch, with the p-type contact metal on top of the mesa. Fig. 2(b) shows the top-view of the device after process. The III-V mesa width is 5 μm, and the ring diameter is 50 μm. Fig. 2 (c) shows the cross-section after focus ion beam etching across the bus waveguide. The dry etch-resulted sloped sidewall of the III-V mesa contributes to a higher optical coupling strength to the bus waveguide. Two Si GCs at the end of the bus waveguide are used to collect lasers' clock-wise (CW) and counterclockwise (CCW) output.

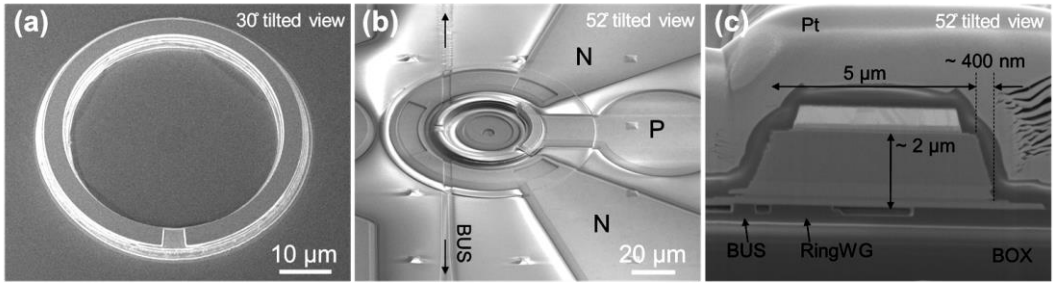


Figure 2. SEM images of the (a) III-V ring mesa, (b) the device after process, and (c) cross-section at the BUS waveguide.

3. MEASUREMENT RESULTS

The device characterizations were performed at room temperature without active temperature control. The microring designs tested in this work have 50 μm diameter and 5 μm wide III-V mesa, but different mesa lateral offset and bus coupling length. Fig. 3(a) shows the light-current-voltage (LIV) curve of a microring laser under continues-wave (cw) pumping. With optimized electrode contact, the series resistance of the microring laser is as low as 16 Ω. Low threshold current was achieved around 2.5 mA at room temperature, equivalent to a 320 A/cm^2 threshold current density. Reasonable optical power over 0.6 mW was out-emitted into the bus waveguide in the CCW direction. The ripples on the LI curve represents both modes competition among longitude modes and the direction switch between CW and CCW directions. The output power didn't show thermal rollover until 35 mA (14× threshold) injection, indicating much better temperature stability in QD gain region. The lasing spectrum at 31.63 mA in Fig. 3(b) shows excellent extinction ratio of 50 dB (limited by the instrument) for the primary lasing mode and a high side-mode suppression ratio (SMSR) of 33 dB over the O band. Due to large and relatively flat optical gain envelop in QD gain region and reflection feedback from the imperfect GCs designs, multiple spectral mode lasing with <10 dB SMSR and free spectral range ~3 nm is common in many injection levels (Fig. 4(c)). Smaller device dimension will help to achieve >30 dB SMSR in more injection range, which is equivalent to single-mode operation. A small wavelength drifting coefficient of 0.037 nm/mW because of self-heating is observed as well.

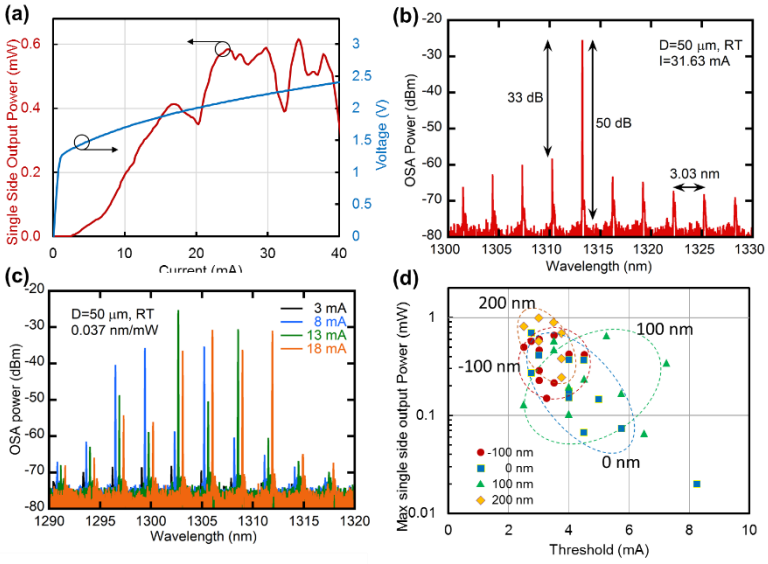


Figure 3. (a) LIV curves of 50 μm hybrid QD ring laser, and (b) (c) the output spectrum under different injection current. (d) Threshold current – maximum power analysis of QD ring lasers with different mesa offset.

We also tested different microring structure designs with different mesa offset, and bus waveguide coupling length. Those devices are fabricated side by side on the same chip, showing high process yield but different lasing performance. Their maximum single side output power and threshold current are analyzed in Fig. 3(c). Depending on the curved section length in bus waveguide, i.e., effective mirror loss, lasing took place between 2.5 to 8 mA with maximum output single-side output power from tens of μW to 1 mW. Due to the sloped sidewall of the III-V mesa, the optimum mesa offset distance is either -100 nm or 200 nm, which have both lower threshold current and higher output power. This indicates that these two configurations have lower optical mode loss at the ring-bus coupler, that is equivalent to a lower cavity leakage loss that is preferred by the limited gain value from the thin QD layers.

The direct modulation bandwidth of the hybrid ring lasers was characterized at uncooled circumstance with a 20 GHz lightwave component analyzer. The frequency response of the 50 QD microring laser is shown in Fig. 4(a). The 3-dB bandwidth is about 3 GHz under small signal condition with 25 mA injection current, and 6 GHz with 35 mA injection current. The communication test was performed with an external high-speed photodetector. A semiconductor optical amplifier and optical filter were used to compensate the coupling loss from the GCs. With 2^7-1 non-return-to-zero pseudorandom binary sequence data input, clear open eye was seen up to 10 Gb/s data rate by directly modulating the laser driving current, as shown in Fig. 4(b). No signal pre-emphasis or equalizer was used in the communication test.

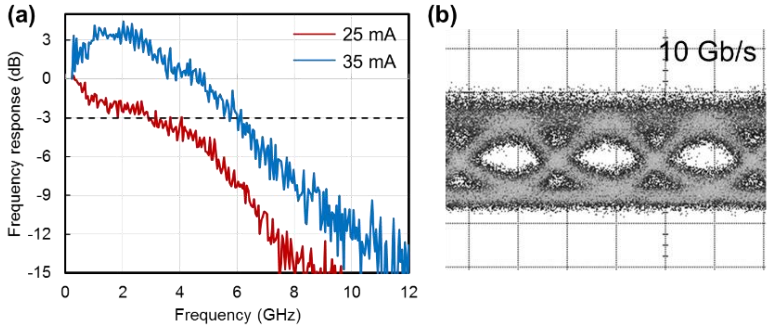


Figure 4. (a) Frequency response of QDs microring under direct current modulation, and (b) eye diagram of direct modulation of the QDs microring at 10 Gb/s.

4. CONCLUSIONS

To our best knowledge, this is the first time that the QDs microring lasers are demonstrated on silicon with the hybrid integration approach. Those microring lasers show low threshold current of few mA and high output power of around 1 mW. High speed current modulation up to 10 Gb/s data rate was also demonstrated, which provides a promising on-chip laser solution in the node-to-node WDM links in future HPCs and other datacom applications.

ACKNOWLEDGEMENTS

The authors thank the Nanofabrication facility at University of California Santa Barbara for the support on device process.

REFERENCES

[1] D. Liang, M. Fiorentino, R. G. Beausoleil, Silicon Photonics III: Systems and Applications, Chap. 18, Springer Science & Business Media, 2016.

[2] D. Liang, *et al.*: Integrated finely tunable microring laser on silicon, *Nat. Photonics*, vol. 10, pp. 719, Nov. 2016.

[3] Geza, *et al.*: Robust hybrid quantum dot laser for integrated silicon photonics, *Opt. Express*, vol. 24, pp. 16167, Jul. 2016.

[4] A. Liu, *et al.*: High performance continuous wave 1.3 μ m quantum dot lasers on silicon, *Appl. Phys. Lett.*, vol. 104, pp. 041104, Jan. 2014.

[5] Y. Wan, *et al.*: 1.3 μm submilliamp threshold quantum dot micro-lasers on Si, *Optica*, vol. 4, pp. 940, Aug. 2017.

[6] C. Zhang, *et al.*: Thermal management of hybrid silicon ring lasers for high temperature operation, *IEEE J. Sel. Top. Quantum Electron*, vol. 21, pp. 385, Nov. 2015.

InAs/GaAs quantum dot 1.3 μm DFB laser heterogeneously integrated on a silicon waveguide circuit

Sarah Uvin[1,2,3], Sulakshna Kumari[1,2], Andreas De Groote[1,2], Steven Verstuyft[1,2], Geert Morthier[1,2], Dries Van Thourhout[1,2] and Gunther Roelkens[1,2]
[1]*Photonics Research Group, Department of Information Technology, Ghent University - imec iGent, Technologiepark-Zwijnaarde 15 - 9052 Ghent - Belgium*
[2]*Center for Nano- and Biophotonics (NB-Photonics), Ghent University - Ghent - Belgium*
[3] *e-mail: sarah.uvin@ugent.be*

ABSTRACT

We demonstrate the first single mode InAs/GaAs quantum dot distributed feedback laser at 1.3 μm wavelength heterogeneously integrated on a Si photonics waveguide circuit. High temperature operation with continuous wave lasing up to 100°C is shown. Threshold current densities as low as 353 A/cm^2 were measured. Single mode lasing around 1320 nm with a side-mode suppression ratio of 40 dB is obtained. These devices are attractive candidates for uncooled wavelength division multiplexing (WDM) transceivers in data centers.

Keywords: Quantum dot lasers, silicon photonics, distributed feedback laser

1 INTRODUCTION

In the present Big Data era, the demand for higher bandwidths is increasing at an unprecedented pace. This trend requires high-performance interconnects that can sustain this high bandwidth without consuming excessive energy. Silicon photonics is emerging as an important platform for the realization of high-speed, power-efficient optical transceivers. However, currently the cost-effective integration of the light source limits silicon-based photonic integrated circuits (PIC) deployment in these fields. On-chip lasers operating at high ambient temperature and with low-loss coupling to the silicon waveguide circuits are essential in order to become a competitive technology for that matter.

Due to the three dimensional confinement of carriers, InAs/GaAs quantum dot (QD) lasers inherently have a more stable performance over the 20°C-100°C temperature range compared to quantum well lasers [1]. Furthermore, they can achieve very low threshold current densities [2] and because of the way QDs are grown they have a wider gain spectrum compared to conventional quantum well lasers making this material system an excellent candidate for creating multi-wavelength transmitters.

The integration of QD lasers on the silicon photonics platform, leveraging the well-developed CMOS fabrication infrastructure and its economy of scale, can provide a distinct cost advantage over other optical technologies. At the same time it allows lower power consumption and enables the scaling of the aggregate bandwidth of transceivers to the Terabit/s range.

There are many possible ways to integrate lasers with silicon optical circuits ranging from hetero-epitaxy of III-V materials [3] to flip-chip bonding [4] and wafer bonding [5]. Many wafer-bonded approaches use a metal layer between the silicon and the GaAs wafers to facilitate bonding [6], which complicates the coupling to an underlying silicon waveguide circuit. Wafer-bonded QD lasers without a metal layer have recently been demonstrated [7]. Since both electrical contacts are now formed on the III-V, low-loss coupling of the laser light to a silicon waveguide is possible. This allows for the integration of heterogeneous III-V-on-Si quantum dot lasers with high-quality Si photonic components.

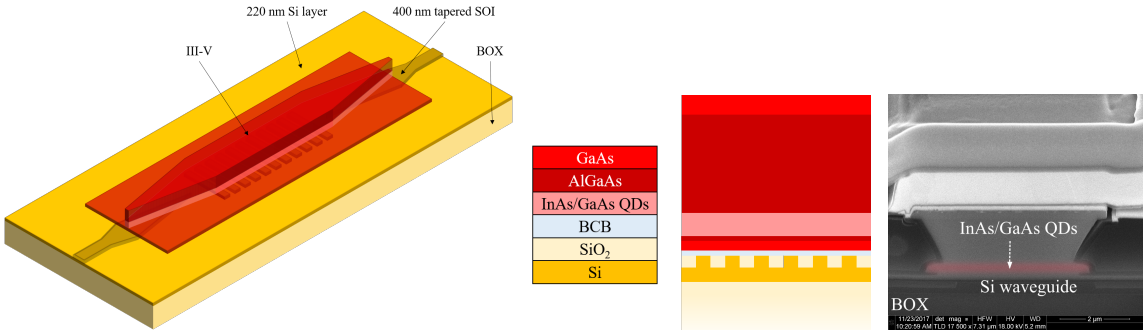
Distributed-feedback (DFB) lasers are crucial devices, providing longitudinal single-mode emission with a narrow line width. They are indispensable for wavelength division multiplexing (WDM) systems. In this paper we demonstrate the first single mode InAs/GaAs quantum dot DFB laser on a silicon substrate with coupling to a silicon waveguide. The DFB laser structure reported in this paper is based on second order gratings defined in the silicon circuit with a Bragg wavelength around 1320 nm.

2 DEVICE DESIGN AND FABRICATION

The device geometry of the DFB laser is shown in Fig. 1(a). The laser cavity consists of a DFB grating defined in the silicon waveguide layer with the III–V gain region bonded on top. The III-V gain section is 1000 μm long (not including the 215 μm-long spotsize converters on each side). Second order DFB gratings were used with a grating period of 400 nm and a duty cycle of 70%, which corresponds with a Bragg wavelength of 1320 nm. The confinement factor of the optical mode in the quantum dot active region is around 8.9 %. A 215 μm-long tapered spotsize converter is used to couple the light from the hybrid gain section into the passive silicon waveguides. The III-V taper is a piecewise linear taper that quickly tapers (L = 35 μm) from a

3.7 μm mesa width to an 1.7 μm wide waveguide width after which a slower adiabatic taper (L = 180 μm) is implemented by tapering both the III-V and silicon waveguide structure.

A cross-sectional diagram of the III-V-on-silicon waveguide structure is depicted in Fig. 1(b). It consists of a planarized SOI wafer containing the silicon waveguides and gratings defined in a 400 nm thick silicon waveguide layer using 193 nm deep UV lithography (180 nm etch depth). The GaAs quantum dot epitaxial layer stack is adhesively bonded to the planarized silicon-on-insulator (SOI) using a 60 nm-thick divinylsiloxane-bisbenzocyclobutene (DVS-BCB) bonding layer. The III-V active region consists of 9 layers of InAs QDs, with a total thickness of 352 nm. The InAs/GaAs QD core region is clad in p-type and n-type $Al_{0.4}Ga_{0.6}As$/GaAs layers, 1.8 μm and 220 nm thick respectively. The epitaxial layer stack was grown by Innolume.



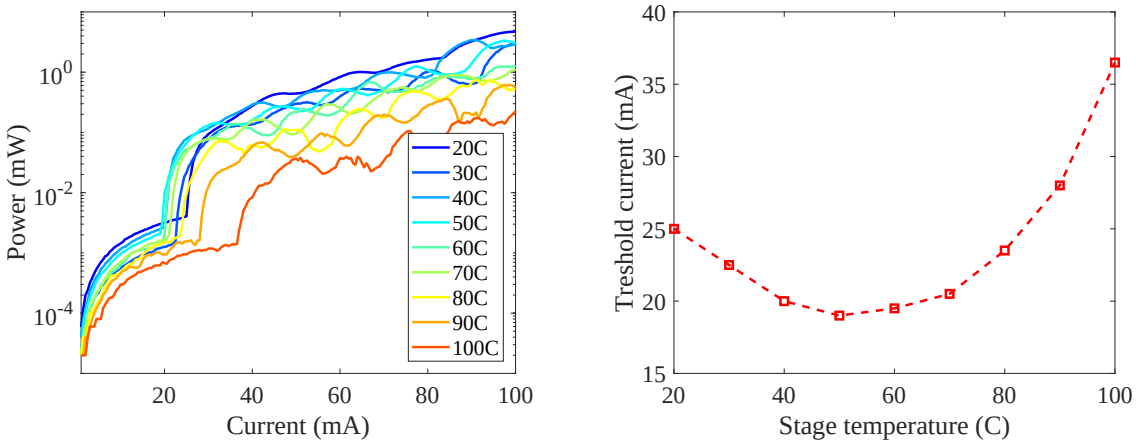
(a) (b) (c)

Figure 1. III-V/Si distributed feedback laser design: (a) 3D view of the III-V-on-silicon DFB laser; (b) schematic cross-section of the laser structure; (c) SEM picture of the actual device.

To fabricate the DFB lasers the III-V mesa and spotsize converter are defined through wet etching, using Citric acid:H_2O_2 and KI:I_2:H_2O for the GaAs/InAs and AlGaAs layers, respectively. This wet etching technique allows creating undercut structures in the spot-size converter, which relaxes the lithography requirements in the definition of the III-V spotsize converter, which was realized using 300 nm UV contact lithography. A scanning electron microscope picture of the reverse trapezoidal III-V mesa is shown in Fig. 1(c).

3 DEVICE CHARACTERIZATION

The laser characterization is carried out by coupling the output of the DFB laser to a standard single mode fiber through a fiber-to-chip grating coupler. The measurements were carried out with the device on a thermo-electric heater set at temperatures ranging from 20°C to 100°C.



(a) (b)

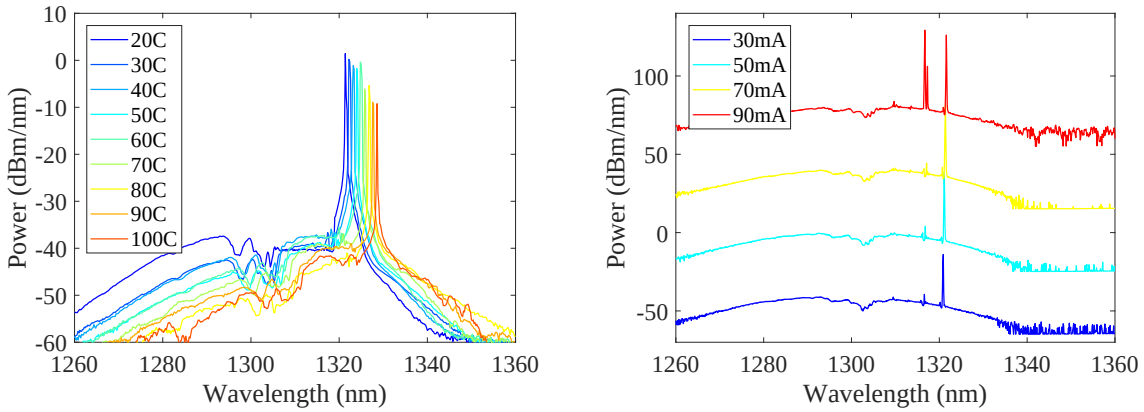
Figure 2. (a) LI curve as a function of temperature. Power in the waveguide is plotted. (b) Threshold current data as a function of stage temperature.

The continuous wave (CW) light-current (LI) characteristic of the DFB laser is shown in Fig. 2(a), as a function of temperature. Lasing is observed up to 100°C. We measure output powers up to 2.5 mW in the waveguide at room temperature. The ripple observed in the LI characteristics are attributed to parasitic reflections from the grating coupler used for fiber coupling and reflections at the taper tip of the III-V material.

The CW threshold current as a function of stage temperature is shown in Fig. 2(b). The lowest threshold current is 19 mA, reached at 50°C. This corresponds with a threshold current density of 353 A/cm^2. At lower

temperatures the threshold current decreases with increasing temperature. This is due to the detuning of the Bragg wavelength and the gain peak: when increasing the temperature, the gain shifts to longer wavelengths and by this matches better with the Bragg wavelength of the grating. At temperatures above 55°C, the threshold current starts increasing with increasing temperature.

The optical spectrum as a function of temperature for a drive current of 50 mA is plotted in Fig. 3(a). Laser emission at 20°C is observed around 1321 nm. With increasing temperature the laser output wavelength shifts to longer wavelengths with a temperature coefficient of 0.1nm/°C. We see single mode operation and a side-mode suppression ratio of 40 dB. Fig. 3(b) shows the optical spectrum as a function of drive current at room temperature. At higher drive currents (e.g. from 90 mA at 20°C) higher order modes appear. This is due to lateral higher order modes that exist in the laser mesa. These modes have a similar optical confinement in the active region and therefore experience a similar level of gain. They have a slightly lower effective index and thus a lower Bragg wavelength than the fundamental mode. At high drive currents these higher order modes start to couple to the fundamental mode in the silicon waveguide due to an imperfect taper in the III-V.



(a) (b)

Figure 3. (a) Optical spectrum for a drive current of 50 mA as a function of temperature: single mode operation with a SMSR of 40 dB; (b) Optical spectrum for different drive currents at room temperature. The different spectra are shifted 40 dB apart.

4 CONCLUSION

This paper demonstrated the first single mode quantum dot DFB laser on a silicon substrate with efficient coupling of light to a silicon waveguide. We demonstrated high temperature operation with CW lasing up to 100°C. Threshold current densities as low as 353 A/cm^2 were measured. The laser showed single mode behavior with a side-mode suppression ratio of 40 dB. The device performance is currently limited by the suboptimal III-V tapers, resulting in residual reflections, extra losses and the existence of higher order modes. We expect significant improvement with better III-V tapers. These devices are attractive candidates for uncooled WDM systems in data centers.

ACKNOWLEDGMENT

Sarah Uvin thanks the Agency for Innovation by Science and Technology in Flanders (IWT) for a PhD grant.

REFERENCES

[1] M. Sugawara and M. Usami, "Quantum dot devices: Handling the heat," *Nature Photonics*, vol. 3, no. 1, pp. 30–31, 2009.

[2] H. Liu, D. Childs, T. Badcock, K. Groom, I. Sellers, M. Hopkinson, R. Hogg, D. Robbins, D. Mowbray, and M. Skolnick, "High-performance three-layer 1.3-μm inas-gaas quantum-dot lasers with very low continuous-wave room-temperature threshold currents," *Photonics Technology Letters, IEEE*, vol. 17, no. 6, pp. 1139–1141, 2005.

[3] A. Y. Liu, J. Peters, X. Huang, D. Jung, J. Norman, M. L. Lee, A. C. Gossard, and J. E. Bowers, "Electrically pumped continuous-wave 1.3 μm quantum-dot lasers epitaxially grown on on-axis (001) gap/si," *Optics Letters*, vol. 42, no. 2, pp. 338–341, 2017.

[4] N. Hatori, Y. Urino, T. Shimizu, M. Okano, T. Yamamoto, M. Mori, T. Nakamura, and Y. Arakawa, "Quantum dot laser for a light source of an athermal silicon optical interposer," in *Photonics*, vol. 2, no. 2. Multidisciplinary Digital Publishing Institute, 2015, pp. 355–364.

[5] K. Tanabe, K. Watanabe, and Y. Arakawa, "Iii-v/si hybrid photonic devices by direct fusion bonding," *Scientific reports*, vol. 2, 2012.

[6] Y.-H. Jhang, K. Tanabe, S. Iwamoto, and Y. Arakawa, "Inas/gaas quantum dot lasers on silicon-on-insulator substrates by metal-stripe wafer bonding," *Photonics Technology Letters, IEEE*, vol. 27, no. 8, pp. 875–878, 2015.

[7] G. Kurczveil, D. Liang, M. Fiorentino, and R. G. Beausoleil, "Robust hybrid quantum dot laser for integrated silicon photonics," *Optics Express*, vol. 24, no. 14, pp. 16 167–16 174, 2016.

Next Generation Silicon Photonics

(Invited paper)

Michal Lipson
Department of Electrical Engineering, Columbia University, New York, NY
Email:michal.lipson@columbia.edu

ABSTRACT

In the past decade, silicon photonics has been shown as a platform for high-performance massively integrated optical devices that can be integrated with state-of-the-art microelectronics. The toolbox of integrated nanophotonics today is rich: from the ability to modulate, guide and amplify at GHz bandwidths, to opto-mechanical and nonlinear devices. The explosion of silicon photonics enabled components with high performance and opened the door to a variety of applications. Recently new atomically thin materials integrated on silicon photonics platform as a post-process have shown the ability to tailor optical properties of integrated devices by simultaneously tailoring the geometry of the device structures and the intrinsic electronic excitations of the material.

Keywords: Silicon photonics, integrated optics

INTRODUCTION

We are now experiencing a revolution in optical technologies, where one can print optical circuits with hundreds of thousands of optical elements on a silicon wafer. These optical circuits can be modified on demand- one can now control the optical properties of hundreds of different optical paths defined in a mm-sized chip. This revolution is ongoing –new materials and technologies are emerging that can manipulate the flow of light in unprecedented ways.

EMERGING APPLICATIONS OF SILICON PHOTONICS PLATFORM

The revolution in optical technologies is opening the door to applications that only a decade ago were unimaginable. Extremely complex systems based on silicon photonics can now be implemented. We have recently demonstrated the largest array of independently controllable silicon waveguides on a chip for Solid-state beam steering applications[1]. Solid-state beam steering using large-scale optical phased arrays is of great interest for LIDAR and free-space communication systems, enabling wide-angle, long distance ranging or transmission of data in a robust platform [2-5]. Ideally, a widely steerable narrow output beam that can reach to long distances requires a large aperture containing a large number of independently phase-controlled elements while remaining at a reasonable total power consumption. Applications at distances of tens to hundreds of meters require element-counts of several thousands, such that independent phase control overwhelmingly dominates power consumption and has prohibited larger element-count demonstrations thus far. We demonstrate the highest yet-reported element count in an actively steered optical phased array while simultaneously achieving record low power consumption of less than 1.8W for the whole array. The array shows steering in two dimensions over a 70 degree by 14 degree field of view while pumped by an InP/silicon laser fabricated on the same platform.

INTEGRATION OF ATOMICALLY THIN MATERIALS ON SILICON PHOTONICS PLATFORM

Recently new atomically thin materials integrated on silicon photonics platform post-processing have shown the ability to tailor optical properties of integrated devices by simultaneously tailoring their geometry and their intrinsic electronic excitations. These materials could enable unprecedented scalability of silicon photonics systems that are bandwidth and/or power limited. Similarly to Graphene, that has already been integrated on photonic waveguides [6] we have shown recently that 2D materials such as monolayer transition-metal dichalcogenides (TMD) can be used to tune drastically the optical properties of waveguides without affecting its absorption properties, therefore providing electro-optic properties to traditionally passive optical materials. Recently discovered TMDs are atomically thin semiconductors with unique electrical and optical properties [7]. These materials enable strong light–matter coupling, with optical absorption around 10–20% in layers as thin as 0.6 nm [8] at visible wavelengths and extremely efficient Coulomb interactions, as manifested in the exciton binding energies on the order of 0.5 eV [9]. In [10] we show a giant index change beyond 60% in monolayer

WS, index under applied voltage. Figure 1a shows a fabricated Mach Zender Interferometer consisting of Si_3N_4 waveguides clad with WS2 2D TMD material. Figure 1b shows the transmission response of device for different applied voltages. One can see that the transmission spectra shift drastically due to the change in the real part of the dielectric.

CONCLUSION

Silicon photonics is continuing to evolve. New materials that can be integrated on silicon photonics post-process are emerging, as well as a plethora of new applications that reach beyond data communications.

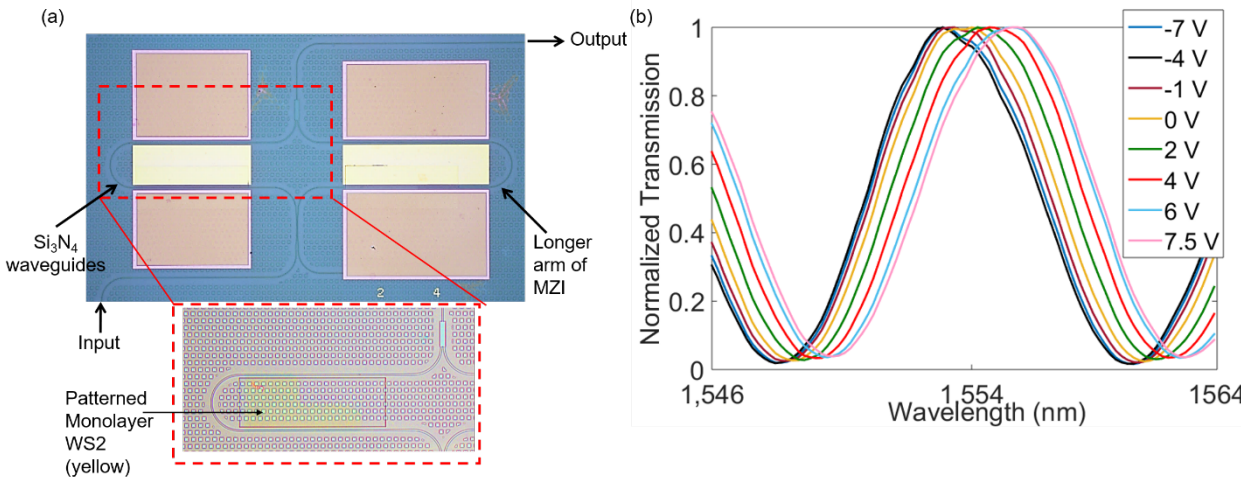


Fig. 1: (a) Optical micrograph of the fabricated MZI with Si_3N_4 waveguides (b) Transmission response of device showing MZI fringes at different voltages

REFERENCES

[1] Steven A. Miller et al, Christopher T. Phare, You-Chia Chang, Moshe Zadka, Aseema Mohanty, Min Chul Shin, Brian Stern, Xingchen Ji, and Michal Lipson, "512-Element Actively Steered Silicon Phased Array for Low-Power LIDAR"

[2] Christopher V. Poulton et al., "Large-scale silicon nitride nanophotonics phased arrays at infrared and visible wavelengths." Opt. Lett. 42, 21-24 (2017).

[3] SungWon Chung, Hooman Adediasl, and Hossein Hashemi, "A Monolithically Integrated Large-Scale Optical Phased Array in Silicon-on-Insulator CMOS." IEEE J. Solid-State Circuits 53, 275-296 (2018).

[4] D.N. Hutchison et al., "High-resolution aliasing-free optical beam steering." Optica 3, 887-890 (2016).

[5] Christopher T. Phare, Min Chul Shin, Steven A. Miller, Brian Stern, and Michal Lipson, "Silicon Optical Phased Array with High-Efficiency Beam Formation over 180 Degree Field of View." arXiv:1802.04624 (2018).

[6] C.T. Phare, Y.-H. D. Lee, J. Cardenas, and M. Lipson, "Graphene electro-optic modulator with 30 GHz bandwidth," Nat Photon, vol. 9, no. 8, pp. 511–514, 2015.

[7] Li, Y. et al. Measurement of the optical dielectric function of monolayer transition-metal dichalcogenides: MoS2 , MoSe2 , WS2 , and WSe2. Phys. Rev. B 90 (2014).

[8] He, K. et al. Tightly bound excitons in monolayer WSe2. Phys. Rev. Lett. 113, 026803 (2014).

[9] Chernikov, A. et al. Population inversion and giant bandgap renormalization in atomically thin WS2 layers. Nat. Photonics 9, 466-470 (2015).

[10] Ipshita Datta1, Sang Hoon Chae2, Gaurang R. Bhatt1, Bichang Li2, Yiling Yu3, Linyou Cao3, James Hone2 and Michal Lipson1, "Giant electro-refractive modulation of monolayer WS2 embedded in photonic structures , Lasers and Electro-Optics (CLEO), 2018 Conference

O-Band QPSK modulation based on a silicon dual-drive Mach-Zehnder

Diego Pérez-Galacho[1,2], Laurent Bramerie[3], Charles Baudot[4], Mohamed Chaibi[3,4], Sonia Messaoudène[4], Nathalie Vulliet[4], Laurent Vivien[2], Christophe Peucheret[3] and Delphine Marris-Morini[2]

[1] Universitat Politènica de València, *c/ Camino de Vera s/n – 46022, Valencia - Spain*
Tel: +34963879735, e-mail: diepega@upv.es

[2] *Centre de Nanosciences et de Nanotechnologies, CNRS, Univ. Paris-Sud, Université Paris-Saclay, C2N-Orsay, 91405 Orsay cedex, France*

[3] *Univ Rennes, CNRS, FOTON – UMR 6082, F-22305 Lannion, France*

[4] *STMicroelectronics, 850 rue Jean Monnet, 38920 Crolles, France*

ABSTRACT

Advanced modulation formats will be required in next generation optical interconnects in order to keep up with future bandwidth demand. In this work QPSK modulation in the O-band is experimentally demonstrated using a silicon-based dual-drive Mach-Zehnder modulator.

Keywords: Silicon modulators, silicon photonics, integrated optics, advanced modulation formats, coherent optical communications.

1. INTRODUCTION

Significant research effort has been dedicated over the past years to the development of silicon based photonic technologies. Nowadays, it is believed that silicon photonics is the best suited for next generation short range optical fiber communications [1], [2]. Developing high performance silicon modulators based on the free-carrier plasma dispersion (FCPD) effect [3] has been an important milestone. These modulators are commonly based on carrier depletion in PN junctions and outstanding performances have already been demonstrated [4]–[8]. However, in order to keep up with the growing bandwidth demand in datacom applications, it is necessary to move from binary on-off keying (OOK) modulation formats to more advanced formats such as 4-level pulse amplitude modulation (PAM-4) or quadrature phase-shift keying (QPSK) [9]. Advanced modulation formats using silicon modulators have already been demonstrated [6]–[8]. However, most of these demonstrations have been carried out in the C-band of optical communication systems (1530 nm – 1565 nm) where the FCPD is stronger. Nevertheless, current standards for short range optical fiber communications favour the use of the O-band (1260 nm – 1360 nm) in order to exploit the zero dispersion region of standard single-mode fibers [10]. In this work we present for the first time a QPSK silicon-based dual-drive Mach-Zehnder modulator (DDMZM) operating in the O-band. QPSK generation is normally based on nested MZM structures, therefore requiring four driving signals. However, the QPSK generation based on DDMZM requires only two driving signals, exhibiting a better power efficiency. As first demonstration, 10 GBd (20 Gbps) is shown.

2. MODULATOR DESIGN AND PRINCIPLE OF OPERATION

The cross-section of the designed phase shifter is depicted in Fig. 1(a). It comprises a PN junction implemented in a rib waveguide. It was designed following the simplified modeling approach proposed in [11]. The targeted doping concentrations of the junction were $P = 5 \cdot 10^{17} cm^{-3}$ and $N = 1.4 \cdot 10^{18} cm^{-3}$. The designed phase shifter was integrated in both arms of a Mach-Zehnder interferometer in order to form a DDMZM, schematically represented in Fig. 1(b) in which the Δn_i boxes represent the phase shifting elements and the Φ box symbolizes a fixed phase shift intended to set the operation point of the DDMZM.

In order to generate QPSK modulation using this architecture it is necessary to bias the modulator at the quadrature point ($\Phi = \pi/2$) and to apply the binary in-phase and quadrature-phase modulating signals to each phase shifter so that a phase shift of π can be achieved in each arm [12]. In the designed DDMZM a 1×2 MMI coupler was used as combiner whereas the input splitter was implemented by means of a 2×2 MMI, naturally setting the modulator to the quadrature point. Heaters were introduced in each arm of the DDMZM in order to compensate for fabrication errors and fine tune the bias of the modulator to the quadrature point. GSGSG coplanar traveling wave electrodes were used to apply the two modulating signals to the phase shifters. The active length of the DDMZM was 2 mm. The modulator was fabricated using the 300 mm technological platform from STMicroelectronics [13].

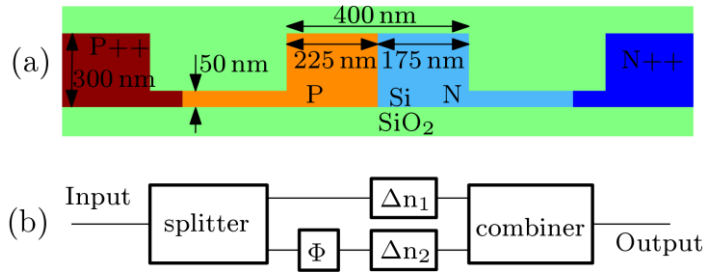


Figure 1. Cross section of the phase shifter (a) and schematic representation of the dual drive Mach-Zehnder modulator (b).

3. CHARACTERIZATION SETUP

In order to assess QPSK modulation, the setup of Fig. 2 was used. TE-polarized light from an O-band external laser was injected in/out of the fabricated chip using grating couplers. RF and DC electrical probes were used to electrically drive the phase shifters and heaters, respectively. Two 2^{15}-1 long de-correlated pseudo random binary sequence (PRBSs) at 10 Gbps were used as modulating signals. The two PRBSs modulating signal were amplified and then a DC bias was added to ensure that the PN junctions were operated in depletion. The driving signals applied to the phase-shifters had peak-to-peak voltages of $7V_{pp}$ with a DC bias of 4V. 50Ω loads were added at the end of the GSGSG coplanar electrodes. The signal at the output of the modulator was then input to an integrated coherent receiver through a variable optical attenuator in order to control the received power. For the purpose of this first demonstration, the same laser was used as local oscillator in the receiver, therefore implementing an homodyne detection scheme. The I/Q output signals of the receiver were fed to a 40 Gsps digital sampling oscilloscope. 10^5 symbols were acquired and then processed offline. For digital processing, an adaptive finite impulse response (FIR) filter with decision-directed least mean square (DD-LMS) tracking was used.

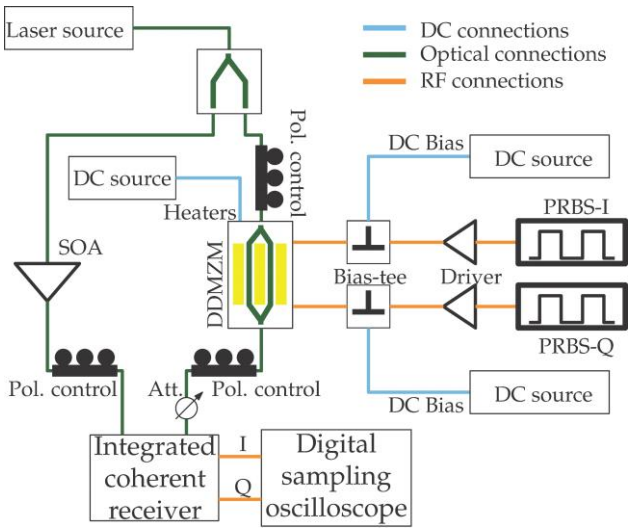


Figure 2. Experimental setup employed for QPSK signal characterization.

4. CHARACTERIZATION SETUP

The DDMZM was first characterized in DC. The measured fiber-to-fiber attenuation was 17 dB, including the loss of the grating couplers, on-chip passive losses and modulator insertion loss (IL). Using a straight waveguide on the chip as normalization, the IL of the modulator was estimated to be 3.8 dB. The V_π of each phase shifter was measured to be between 6 V and 7 V. Taking into account the 2 mm active length, this leads to a modulation efficiency between 1.2 V·cm and 1.4 V·cm.

High-speed measurements were then performed on the modulator. Using the setup previously described, the bit error rate (BER) was measured as a function of the signal average received power, as shown in Fig. 3(a). Each point in the BER curve of Fig. 3(a) is the result of the averaging of five BER measurements, each carried out on 10^5 transmitted symbols. Using a BER value of 10^{-3} as the limit for error free transmission based on forward error correction, the required received power is of -20dBm. The received constellation diagram after offline digital signal processing is shown in Fig. 3(b) for a received power of -22 dBm. A clear QPSK constellation diagram can be seen, and the measured EVM for this constellation is 33%.

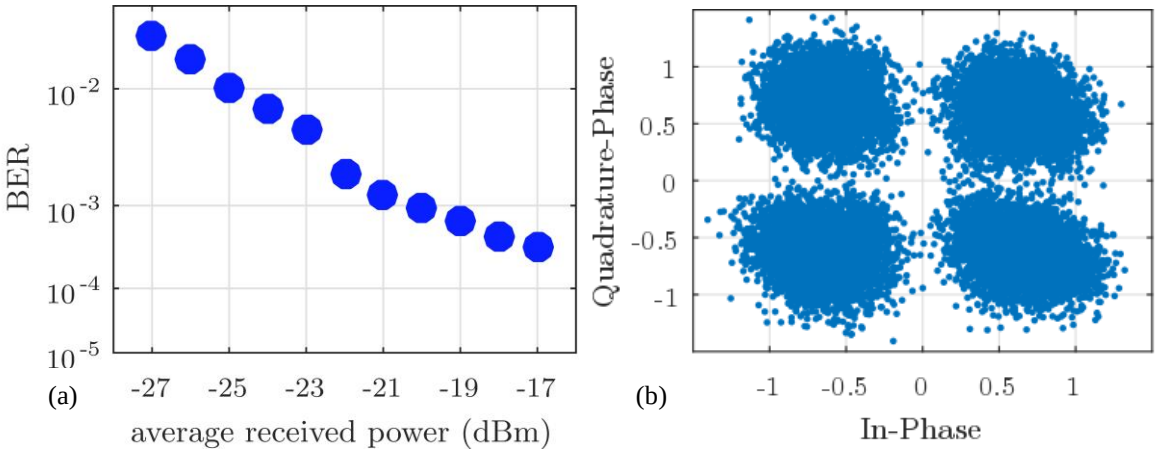


Figure 3 BER as a function of the received power (a) and measured constellation diagram for a received power of -22dBm (b).

5. CONCLUSIONS

Short range optical communication systems in the O-Band are facing important demands of bandwidth nowadays. As a first step towards more efficient modulation schemes, QPSK modulation in the O-band using a silicon modulator has been proposed and experimentally demonstrated at 10GBd (20GBps) for the first time using a DDMZM. The benefit of this modulator is that, relying on a single Mach-Zehnder interferometer, it only requires two driving signals, whereas standard QPSK modulation based on nested MZMs require four driving signals. This reduction on power consumption will be an important advantage in framework of short range communications.

ACKNOWLEDGEMENTS

This work was supported by the European projects Plat4m (FP7-2012-318178), Cosmicc (H2020-ICT-27-2015-688516). We acknowledge the support of French Industry Ministry/DGE through the Nano2017 program.

REFERENCES

[1] B. Jalali and S. Fathpour: Silicon photonics, *J. Lightw. Technol.*, vol. 24, no. 12, pp. 4600–4615, 2006.
[2] M. J. Paniccia: A perfect marriage: optics and silicon, *Optik & Photonik*, vol. 6, no. 2, pp. 34–38, 2011.
[3] R. A. Soref and B. R. Bennett: Electrooptical effects in silicon, *IEEE J. Quantum Electron*., vol. 23, no. 1, pp. 123–129, 1987.
[4] D. Perez-Galacho *et al.*: Low voltage 25Gbps silicon Mach-Zehnder modulator in the O-band, *Opt. Express* 25, 11217-11222 (2017)
[5] D. J. Thomson *et al.*: Silicon carrier depletion modulator with 10 Gbit/s driver realized in high-performance photonic biCMOS, *Laser & Photonics Reviews*, vol. 8, no. 1, pp. 180–187, 2014.
[6] J. Wang *et al.*: Silicon high-speed binary phase-shift keying modulator with a single-drive push–pull high-speed traveling wave electrode, *Photon. Res.*, vol. 3, no. 3, pp. 58–62, 2015.
[7] P. Dong *et al.*: Silicon in-phase/quadrature modulator with on-chip optical equalizer, *J. Lightw. Technol.*, vol. 33, no. 6, pp. 1191–1196, 2015.
[8] Q. Li *et al.*: High-speed BPSK modulation in silicon, *IEEE Photon. Technol. Lett.*, vol. 27, no. 12, pp. 1329–1332, 2015.
[9] A. Shacham *et al.*: Photonic networks-on-chip for future generations of chip multiprocessors, *IEEE Trans. Comput.*, vol. 57, no. 9, pp. 1246–1260, 2008.
[10] Physical Layer Specifications and Management Parameters for 40 Gb/s and 100 Gb/s Operation over Fiber Optic Cables, IEEE Standard for Ethernet Std.
[11] D. Perez-Galacho *et al.*: Simplified modeling and optimization of silicon modulators based on free-carrier plasma dispersion effect, *Opt. Express*, vol. 24, no. 23, pp. 26 332–26 337, Nov 2016.
[12] K.-P. Ho and H.-W Cuei: Generation of arbitrary quadrature signals using one dual-drive modulator, *J. Lightw. Technol.*, vol. 23, no. 2, pp. 764–770, 2006.
[13] C. Baudot *et al.*: DAPHNE silicon photonics technological platform for research and development on WDM applications, *in SPIE Photonics Europe*. 2016, pp. 98 911D–98 911D.

Dual-polarization O-band silicon nitride Bragg filters with high extinction ration

Elena Durán-Valdeiglesias[1], Carlos Alonso-Ramos[1,*], Sylvain Guerber[1,2], Dorian Oser[1], Xavier Le Roux[1], Daniel Benedikovic[1], Nathalie Vulliet[2], Eric Cassan[1], Delphine Marris-Morini[1], Charles Baudot[2], Frédéric Boeuf[2], Laurent Vivien[1]

[1] Centre de Nanoscience et Nanotechnologies, CNRS, Université Paris-Sud, Université Paris-Saclay, C2N – Orsay, 91405 Orsay cedex, France
[2] STMicroelectronics SAS –850 rue Jean Monnet –38920 Crolles, France
Tel: +33169126306, e-mail: carlos.ramos @u-psud.fr

ABSTRACT

Silicon nitride (SiN) photonic circuits operating in the original communication band (O-band) have a great potential to complement the Silicon (Si) photonic platform for the implementation of high-performance transceivers for Datacom applications. The low thermal coefficient, the reduced refractive index contrast, and the CMOS compatibility of SiN, make it an ideal solution to address certain key challenges in the Si photonic circuits. These particularly includes large thermal drift, tight fabrication tolerances, and strong polarization dependence. In this paper, we propose and experimentally demonstrate a SiN Bragg filter designed for dual-polarization operation. By optimizing the dimensions of a triangularly-shaped lateral corrugation, we yielded Bragg gratings with a quasi-square transversal geometry that minimizes filter birefringence. Exploiting this concept, we experimentally demonstrated SiN Bragg filters, fabricated with a single-etch step process in 300 mm Si photonics platform, exhibiting an experimental polarization independent rejection close to 40 dB in the O-band, with a bandwidth of 15 nm and negligible off-band excess loss.

Keywords: silicon nitride, silicon photonics, Bragg gratings, dual-polarization, wavelength filters

1. INTRODUCTION

Silicon photonics is being extensively developed for Datacom applications in big data centers. Following current standardization trends, this work is being focused on the O-band communications, at a wavelength of around 1310 nm. While Si photonics can benefit from large-volume fabrication processes in CMOS foundries, its performance may be limited by stringent requirements in terms of fabrication tolerances, temperature control, and polarization management. Silicon nitride (SiN), a CMOS compatible material, provides a seven-fold reduction in thermo-optic coefficient, compared to silicon [1,2], and a lower index contrast that substantially relaxes fabrication tolerances. Thus, SiN has been identified as a promising material choice to complement the Si photonics platform [3]. In addition, leveraging the reduced index contrast, proper geometry design can be exploited to reduce the birefringence of SiN devices, opening a new route to develop dual-polarization photonic circuits.

Here, we propose and experimentally demonstrate a novel SiN Bragg grating that provides high rejection simultaneously for both transverse electric (TE) and transverse magnetic (TM) polarizations, respectively. We implemented a triangularly-shaped lateral grating (see Fig. 1), with engineered corrugation dimensions to yield an average width that equals the SiN thickness. We also carried out a filter with an effectively square transversal geometry allowing a dual polarization behavior.

2. FILTER DESIGN

Bragg grating waveguides are a key component in the silicon photonics library, allowing the realization of wavelength filters [4], sensors [5], and advanced functionalities for dispersion engineering [6]. Bragg gratings rely on constructive interference of partial back-reflections in a periodic perturbation to implement a waveguide mirror. Bragg reflection occurs when the following phase-matching condition is met:

$$\lambda_c^{TE/TM} = \Lambda n_{BF}^{TE/TM}, \quad (1)$$

where the superscript denotes TE or TM polarization, $\lambda_c^{TE/TM}$ is the central Bragg wavelength, $n_{BF}^{TE/TM}$ is the effective index of the Bloch-Floquet mode that propagates along the periodic waveguide, and Λ is the grating period. From equation (1), it is evident that matching the central Bragg wavelength for TE and TM polarizations requires having similar Bloch-Floquet effective indices ($n_{BF}^{TE} \sim n_{BF}^{TM}$). One way to meet this requirement is to have

Bragg grating with square transversal geometry and homogeneous upper and bottom cladding, i.e. having the same index distribution along the horizontal (x) and vertical (y) axes.

For the filter design, we considered a 600-nm-thick SiN guiding layer surrounded by silicon dioxide (see Fig. 1a). To implement the Bragg grating, we used a triangularly-shaped lateral corrugation, depicted in Fig. 1b. We denote the filter period as Λ, the average grating waveguide width as W_{Ave} and the corrugation width as W_C. This geometry allows a single-etch process and relaxes minimum feature size requirements for short periods.

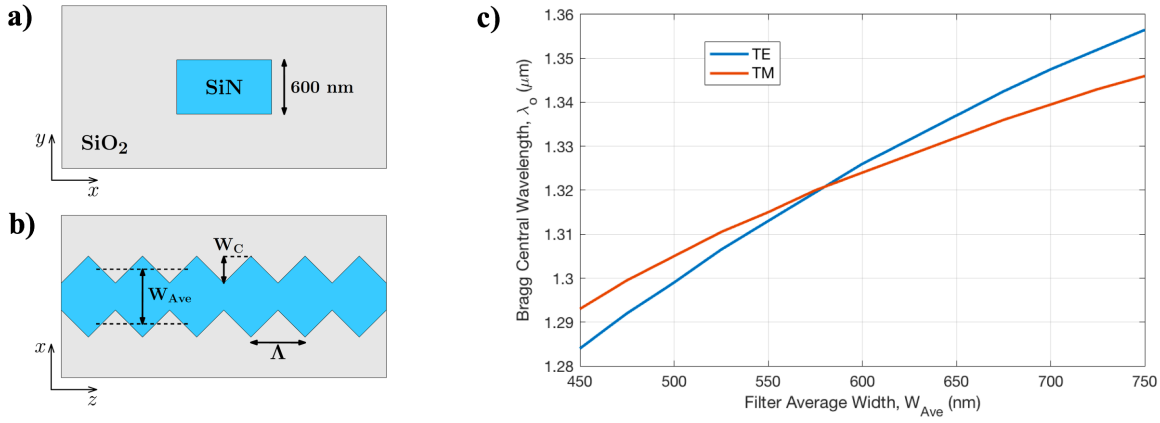


Figure 1. Schematic representation of a) transversal geometry of the strip waveguide, and b) longitudinal geometry of the proposed triangularly-corrugated Bragg filter. c) Central filter wavelength calculated with FDTD as a function of the filter average width (W_{Ave}) for a corrugation width of W_C = 200 nm, a period of Λ = 410 nm, and a total filter length of 20 μm.

We have studied the performance of our filter using finite difference time domain (FDTD) tools [6]. In Fig. 1c, it is shown the central Bragg wavelength, calculated for both TE and TM polarizations as a function of the filter average width, W_{Ave}. We considered a corrugation width of W_C = 200 nm, a pitch of Λ = 410 nm, and a filter length of 20 μm. It can be seen that Bragg central wavelengths for TE and TM polarizations have similar values for filter average widths between 550 nm and 600 nm. This region corresponds to quasi-square filter transversal geometries, where the average grating width approaches the waveguide thickness of 600 nm.

3. EXPERIMENTAL RESULTS

The devices were fabricated on the 300 mm silicon photonics R&D platform DAPHNE in ST Crolles (France) [3,8], using Si wafers with a 1.4 μm-thick buried oxide (BOX) layer, and a 600-nm-thick SiN guiding layer, deposited at low temperature via Plasma Enhanced Chemical Vapor Deposition (PECVD). Input and output grating couplers, access and reference waveguides and triangular filters were defined with 248 nm deep-ultraviolet (deep-UV) optical photolithography and dry etching. Finally, the chip was encapsulated with a 1.5 μm-thick SiO_2 layer. Figure 2a shows the scanning electron microscope (SEM) image of one of the fabricated filters, without encapsulation.

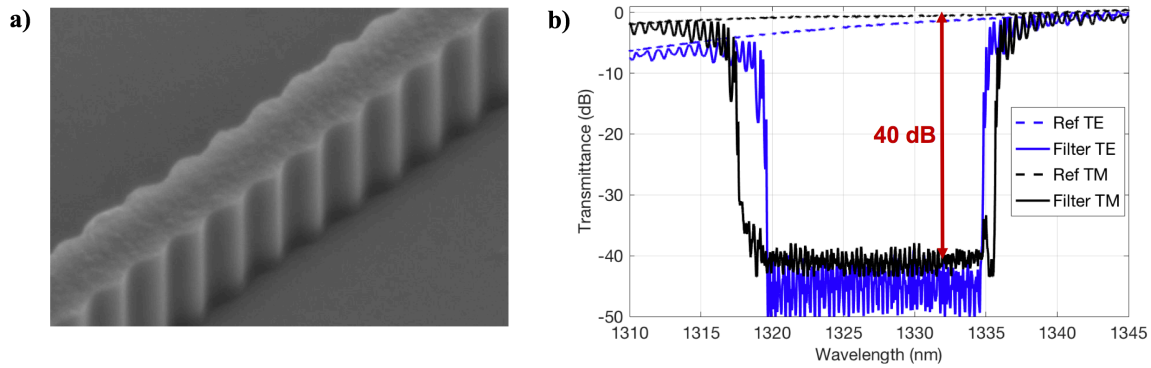


Figure 2. a) Scanning electron microscope (SEM) image of one of the fabricated filters, without encapsulation. b) Measured transmission spectrum for optimized triangular Bragg filter with 500 μm length, and reference strip waveguide.

The triangular filter has an average grating width of W_{Ave} = 600 nm, corrugation width of W_C = 200 nm, pitch of Λ = 410 nm, and length of 500 μm. Figure 2b shows the experimental response for both TE and TM polarizations for the same optimized Bragg filter, compared with a reference strip waveguide of the same length and corresponding polarization. We subtracted the insertion loss of the grating couplers. Our filter exhibits a

polarization-independent extinction ratio close to 40 dB in a bandwidth of ~ 15 nm. The difference in bandwidth for TE and TM polarizations is only 3 nm. In addition, the filter shows negligible off-band excess propagation loss, compared to the reference strip waveguide.

4. CONCLUSIONS

In summary, we have designed and experimentally validated dual-polarization SiN Bragg filters operating in the O-band, based on a triangularly-shaped lateral corrugation geometry. We have shown by simulation that the difference between the central filter wavelength for TE and TM polarizations can be minimized by choosing an average filter width similar to the waveguide thickness, i.e. by implementing a quasi-square transversal filter geometry. We fabricated the filters in the 300 mm silicon photonics R&D platform DAPHNE in ST Crolles, using 248 nm deep-UV optical photolithography in a single-step etch process. We have experimentally demonstrated a polarization independent Bragg rejection of ~ 40 dB, with a 15 nm bandwidth around 1327 nm wavelength, and negligible off-band loss. These results open exciting perspectives for the realization of dual-polarization SiN photonic circuits with a great potential for Datacom applications.

ACKNOWLEDGEMENTS

This work was funded by the European Research Council (ERC POPSTAR) (647342), the European Commission H2020-ICT-27-2017 COSMICC (688516) and the French Industry Ministry Nano2017 program.

REFERENCES

[1] Z. Zhang, M. Yako, K. Ju, N. Kawai, K. Wada: A silicon nitride platform by PVD for dense wavelength division multiplexing on chip, *in Proc. IEEE International Conference on Group IV Photonics*, Paris, France, Aug. 2014.

[2] T. Domínguez-Bucio, A. Z. Khokar, G. Z. Machanovich, F. Y. Gardes: Athermal silicon nitride angled MMI wavelength division (de)multiplexers for the near-infrared, *Opt. Express*, vol. 25 pp. 27310-27320, Oct. 2017.

[3] C. Baudot, M. Douix, S. Guerber, S. Crémer, N. Vulliet, J. Planchot, R. Blanc, L. Babaud, C. Alonso-Ramos, D. Benedikovich, D. Pérez-Galacho, S. Messaoudène, S. Kerdiles, P. Acosta-Alba, C. Euvrard-Colnat, E. Cassan, D. Marris-Morini, L. Vivien, F. Boeuf: Developments in 300 mm silicon photonics using traditional CMOS fabrication methods and materials, *in Proc. IEEE International Electron Devices Meeting (IEDM 2017)*, San Francisco, USA, Dec. 2017.

[4] A. D. Simard, Y. Painchaud, S. LaRochelle: Integrated Bragg gratings in spiral waveguides, *Opt. Express*, vol. 21 pp. 8953-8963, Apr. 2013.

[5] Wang, J. Flueckiger, S. Schmidt, S. Grist, S. T. Fard, J. Kirk, M. Doerfler, K. C. Cheung, D. M. Ratner, L. Chrostowski: A silicon photonic biosensor using phase-shifted Bragg gratings in slot waveguide, *J. Biophotonics*, vol. 6 pp. 821-828, Oct. 2013.

[6] D. T. H. Tan, K. Ikeda, R. E. Saperstein, B. Slutsky, Y. Fainman: Chip-scale dispersion engineering using chirped vertical gratings, *Opt. Lett.*, vol. 33 pp. 3013-3015, Dec. 2015.

[7] FDTD Solutions, Lumerical Solutions, Inc., http://www.lumerical.com

[8] S. Guerber, C. Alonso-Ramos, D. Pérez-Galacho, X. Le Roux, N. Vulliet, S. Crémer, D. Marris-Morini, F. Boeuf, L. Vivien, C. Baudot, "Design and integration of an O-band silicon nitride AWG for CWDM applications", *in Proc. IEEE International Conference on Group IV Photonics*, Berlin, Germany, Aug. 2017.

The performance of High-Index-Contrast Photonics Platforms for On-Chip Raman Spectroscopy

A. Raza,[1,2*] S. Clemmen,[1,2] M. de Goede,[3] R. Ali,[4] P. Hua,[5] S. M. Garcia-Blanco,[3] S. Honkanen,[4] J. S. Wilkinson, [5] and R. Baets[1,2]

[1]Photonics Research Group, INTEC Department, Ghent University-imec, Technologiepark—Zwijnaarde, 9052 Ghent, Belgium
[2]Center of Nano and Biophotonics, Ghent University, Belgium
[3]Optical Sciences Group, MESA+ Institute of Nanotechnology, University of Twente, 4617, The Netherlands
[4]Institute of Photonics, University of Eastern Finland, 80101, Finland
[5]Optoelectronics Research Centre (ORC), University of Southampton, Highfield, Southampton, SO17 1BJ, United Kingdom
**Corresponding author: ali.raza@ugent.be*

Various photonic platforms exist that may be suitable for on-chip Raman spectroscopy. Here we compare 4 of them focusing on their intrinsic photon background and their capability for collecting Raman signal from liquid analytes. These two parameters define the complete figure of merit for waveguide enhanced Raman spectroscopy.

Keywords: Raman spectroscopy, Waveguide enhanced Raman sensing, HIC waveguides

Enhancing the light mater interaction is highly desirable for Raman spectroscopy because of the fundamentally weak Raman scattering cross sections. Hollow optical fibers and more recently nanophotonic waveguides have exhibited enhancement in Raman signal by many orders of magnitude over traditional Raman microscope [1, 2]. Rib waveguides can be used as easily as cover slides and have therefore been used for Raman spectroscopy of various analytes such as bulk liquids [3-5], adsorbed monolayers [6] as well as in gaseous state [7]. Many photonics platforms exist that may seem suitable for a Raman spectroscopy sensor, but a good waveguide-based Raman sensor requires qualities that may contradict each other. The waveguide need to be low loss to maximize the effective interaction length. At the same time, it needs to have a large index to be able to push a significant part of the field into the analyte out of the waveguide while still keeping good guiding properties. The waveguide must also handle large optical power. Finally, it should not induce any photon background that may overlap spectrally with the Raman signal. All these properties impact directly on the signal to noise ratio and may relax strongly the otherwise tight specifications required for light sources and photodetectors of a Raman spectroscopy system. In this report, we compare 4 photonic platforms and present measurements of their broadband photon background. The four platforms under investigation are PECVD Si_3N_4, ALD grown TiO_2, sputtered Ta_2O_5 and reactive co-sputtered Al_2O_3. To measure the Raman background of these waveguide materials, strip waveguides were fabricated on top of a silica substrate using traditional fabrication techniques e.g. Al_2O_3, Si_3N_4 and Ta_2O_5 waveguides were fabricated using deep UV lithography while ALD grown TiO_2 were patterned using e-beam lithography. The fabrication details of each waveguide can be found in [8-11]. The fabricated waveguide geometries, refractive indices and corresponding waveguide losses are presented in Table 1. It is worth noting that those geometries are not optimized for a use in Raman spectroscopy that typically requires smaller dimensions so that the field couples evanescently to an analyte. Therefore, scattering loss for an optimized waveguide may be underestimated. The total backscattered background P_s normalized by total guided power P_0 can be estimated by assuming it has a Raman origin. In a waveguide of length *L*, width *w* and height *h* and propagation loss α can be computed using

$$\frac{P_s}{P_0} = \frac{1}{2} \times \rho\sigma\eta_{BG}\,\gamma^2 \times \left(\frac{e^{-2\alpha L} - 1}{2\alpha}\right)$$

where ρ and σ are respectively the molecular density and Raman cross section of the waveguide material, γ is the coupling efficiency. η_{BG} is background conversion efficiency that quantifies the amount of a background signal collected in a waveguide mode. The values of η_{BG} depends on the geometry and the index contrast of the waveguide. Using COMSOL Multiphysics mode solver, we deduced η_{BG} for the 4 waveguides assuming 785 nm pump wavelength and 820 cm^{-1} stokes shift (Table 1).

The background spectra are measured from the 4 waveguides using a confocal setup [12]. A 785 nm pump is used to excite the TE fundamental mode in a waveguide using high NA 0.9/100× objective. The backscattered signal is collected using the same objective and the Raman Stokes scattered signal is sent to -73°C cooled Andor

IDUS 401 CCD camera after the remaining pump is rejected by a spectral filter. Furthermore, an integrating sphere at the output side of the waveguide is used to measure the transmission and the coupling efficiency.

Waveguide	Cross section (width (nm) × (nm) height)	Refractive index	Waveguide loss (dB/cm)	η_{BG}
Al_2O_3	2400 × 550	1.64	2.2	0.2114
Si_3N_4	700 × 220	1.90	4.3	0.5405
Ta_2O_5	1000 × 550	2.11	4.0	0.6321
TiO_2	1000 × 450	2.36	8.2	0.6901

Table 1.The optical properties of different photonics plat forms under discussion.

The measured Raman spectra σ* are plotted in Fig. 1 and are normalized by ɣ, η_{BG} and length factor. The error bar in Fig 1. represents the deviation of signal over five different waveguide on same chip. TiO_2 exhibits a large Raman background that is an order of magnitude stronger as compared to other three materials. The other three waveguide materials are in close competition and outperform each other depending on the Raman frequency under interest. Therefore, Al_2O_3 may suffer from low collection efficiency from an analyte lying uniformly over the waveguide length. However, Si_3N_4 and Ta_2O_5 seem to have similar performance in term of the Raman background.

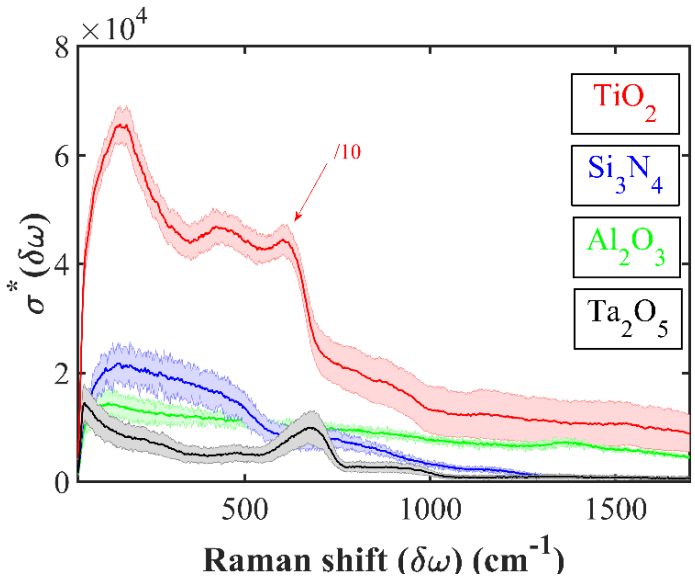


Figure 1. The normalized Raman background of four photonics platform. . The TiO_2 Raman spectrum is normalized by 10 for visual guidance.

In the latter part, we have computed the analyte signal collection efficiency $\eta_{Analyte}$ [2] for all the four photonics platforms. For this purpose, we assume a uniform covering of the waveguides with an analyte having refractive index 1.37 and a Raman mode around 819 cm^{-1} i.e. isopropanol [2]. The Raman collection efficiency $\eta_{Analyte}$ for each is material is maximized by adjusting the geometry of the waveguide assuming the same pump wavelength of 785 nm and 819 cm^{-1} Raman shift. The results of these simulations are summarized in Table 2. Owing to high index contrast, TiO_2 waveguide leads to the high collection efficiency while the Al_2O_3 waveguide suffers due to low index contrast. On the other hand Si_3N_4, and Ta_2O_5 offers similar magnitude of collection efficiency.

Waveguide	Cross section (width (nm) × height (nm))	$\eta_{Analyte}$
Al_2O_3	325 × 1200	0.0395
Si_3N_4	200 × 550	0.1721
Ta_2O_5	175 × 425	0.2667
TiO_2	150 × 375	0.3745

Table 2.The signal collection efficiency $\eta_{Analyte}$ from an analyte lying uniformly on a waveguide.

As a conclusion, we have presented the performance of four different high index contrast photonic platforms in term of photon background and signal collection efficiency. TiO_2 has the higher collection efficiency but its performance suffers due to huge photon background. On the other hand, Al_2O_3, Si_3N_4 and Ta_2O_5 have same photon

background that is an order of magnitude less than TiO_2. Si_3N_4 and Ta_2O_5 looks equally promising as their photon background is low and similar high index contrasts leads to high signal collection efficiency.

Acknowledgement

The authors acknowledge Prof. N. Le Thomas and Dr. Pieter Wuytens for useful feedback. The authors would like to thank the FWO and ERC-InSpectra for their financial support.

REFERENCES

[1] S. O. Konorov, et al. "Hollow-core photonics crystal fiber-optic probes for Raman spectroscopy," Opt. Lett. 31(12), 1911-1913, (2006).

[2] A. Dhakal, et al. "Efficiency of evanescent excitation and collection of spontaneous Raman scattering near high index contrast channel waveguides," Optics Express 23(21), pp.27391-27404 (2014).

[3] A. Dhakal, et al. "Evanescent excitation and collection of spontaneous Raman spectra using silicon nitride nanophotonic waveguides," Opt. Lett. 39(13), pp.4025-4028 (2014).

[4] C. C. Evans, et al. "TiO_2 Nanophotonic Sensors for Efficient Integrated Evanescent Raman Spectroscopy," ACS Photonics 3(9), pp.1662 (2016).

[5] Z. WANG, et al. "Surface and waveguide collection of Raman emission in waveguide-enhanced Raman spectroscopy," Opt. Lett. 41(17), 4146-4149 (2016).

[6] A. Dhakal, et al. "Nanophotonics waveguide enhanced Raman spectroscopy of biological sub monolayers," ACS Photonics 3(11), 2141 (2016).

[7] S. A. Holmstrom, et al. "Trace gas Raman spectroscopy using functionalized waveguides," Optica 3(8), 891-896 (2016).

[8] A. Subramanian, et al. "Low-Loss Single mode PECVD silicon nitride photonic wire waveguides for 532-900 nm wavelength window fabricated within a CMOS pilot line," IEEE Photonics Journal 5(6), 2202809 (2013).

[9] B. S. Ahluwalia, et al. "Fabrication of Submicrometer High Refractive Index Tantalum Pentoxide Waveguides for Optical Propulsion of Microparticles," IEEE Phot. Tech. Lett. 21, 1408 (2009).

[10] M. Hayrinen, et al. "Titanium dioxide slot waveguides for visible wavelengths," Applied Optics 12, 2653-2657 (2015).

[11] J. D. B. Bradley, et al. "Fabrication of low-loss channel waveguides in Al_2O_3 and Y_2O_3 layers by inductively coupled plasma reactive ion etchng," Appl. Phys. B 89, 311-318 (2007).

[12] P. Wuytens, et al. "On-chip surface-enhanced Raman spectroscopy using Nano sphere-lithography patterned antennas on silicon nitride waveguides". Optics Express, 25(11), 12926–12934 (2017).

On-Chip Vernier Filtering of Colliding Pulse Mode-Locked Laser Coupled with Fabry-Pérot Feedback Cavity via MMI Reflector

Mu-Chieh Lo, Robinson Guzmán, and Guillermo Carpintero
Universidad Carlos III de Madrid, Avda. Universidad, 30, 28911 Leganés, Spain
e-mail: mlo@ing.uc3m.es

ABSTRACT

Optical frequency comb spacing multiplication through on-chip Vernier filtering is proposed, based on an InP colliding pulse mode-locked laser coupled with a fractionally matched Fabry-Pérot feedback cavity. These two cavities are defined by and coupled via multimode interference reflector. The deliberately set laser-cavity repetition rate and coupled-feedback cavity FSR give rise to Vernier effect whereby the 6th harmonic generation (150 GHz) of fundamental cavity round-trip frequency (25 GHz) is experimentally demonstrated.

Keywords: Laser mode locking, Semiconductor lasers, Cavity resonators

1 INTRODUCTION

Mode-Locked laser (MLLs) emit ultrafast pulse trains and optical frequency combs have attracted interest in communications and sensing. MLL diodes (MLLDs) provide much higher mode locking (ML) repetition rates that have potential applications as radio-frequency (RF) oscillators, thanks to the typical short cavity length between 0.5 and 1 mm. Harmonic ML (HML) techniques further push the repetition rate above fundamental round-trip frequency up to millimeter-wave (mmW) and even terahertz (THz) ranges, where an optical pulse train at a higher order harmonic of the fundamental round-trip frequency of the laser diode is generated by means of (sub-)harmonic hybrid ML, colliding-pulse ML, coupled-cavity ML, and methods based on the wavelength selectivity of distributed Bragg reflector (DBR) [1] and cascaded asymmetric Mach-Zehnder interferometer (MZI) [2]. In coupled-cavity ML, a primary cavity is coupled with a secondary cavity incorporating an intra-cavity mirror. The secondary cavity can be regarded as a feedback cavity that is able to manipulate the primary laser performance as reported recently [3][4][5].

In this paper, colliding-pulse ML and coupled-cavity ML are combined of which the intentionally mismatched cavity lengths lead to Vernier effect that has been extensively utilized for widely tunable single-wavelength laser [6][7][8]. To the best of our knowledge, it is the first time such Vernier effect is utilized for optical frequency comb spacing multiplication. To define the coupled cavity, standardized multimode interference reflector (MMI-R) [9] building blocks provided by the InP-based generic foundry platform [10] are used as on-chip reflectors.

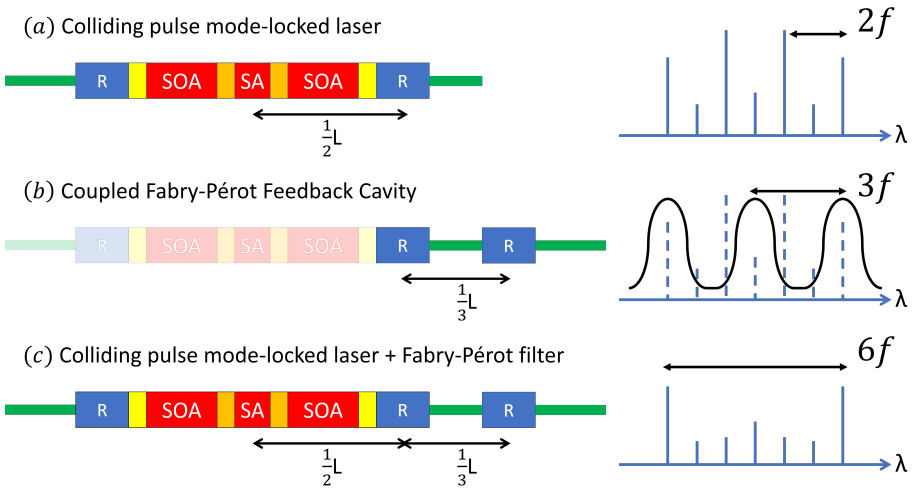


Figure 1: Operation principles of Vernier filtering with colliding-pulse and coupled-cavity mode locking. R: reflector, SOA: semiconductor optical amplifier, SA: saturable absorber. L: cavity length, f: fundamental round-trip frequency. f is inversely proportional to L. (a) Colliding pulse mode-locked laser. Repetition rate: 2f. (b) Coupled Fabry-Pérot feedback cavity. FSR: 3f. (c) Colliding pulse mode-locked laser + Fabry-Pérot feedback cavity for 6th harmonic generation.

2 DEVICE DESIGN AND FABRICATION

The concept of proposed approach is depicted in Fig. 1. With a primary cavity length of L, the laser modes spaced by 2f (2nd harmonic colliding-pulse repetition rate) as shown in Fig. 1(a) are filtered through the passbands of secondary Fabry-Pérot coupled cavity spaced by 3f as shown in Fig. 1(b). Thus, a mode separation of 6f (6th harmonic) is obtained as shown in Fig. 1(c). The photograph and layout of proposed photonic integrated circuit (PIC) presented in Fig. 2(a) and Fig. 2(b), respectively, is a folded version of the schematic depicted in Fig.1(c). It comprises two cavities. The primary cavity is a colliding pulse mode-lock laser combining a saturable absorber (SA), semiconductor optical amplifiers (SOA), multimode interference reflectors (MMI-R) as on-chip reflectors (R) as well as straight passive waveguides in a symmetric geometry with respect to the SA. The cavity length is ∼1.62 mm corresponding to a fundamental round-trip frequency of 25 GHz, and 50-GHz repetition rate under colliding-pulse mode locking operation. The 30 µm SA is surround by two 200 µm SOAs, both bonded to the same electrical contact track fed by a laser driver current source and the SA is reverse-biased by an external voltage. To form a complete cavity passive straight waveguides are inserted incorporating MMI-Rs placed at the ends as mirrors.

The secondary passive cavity is 0.54-mm long, approximately one third the length of primary cavity. It is terminated by MMI-Rs and coupled to the primary cavity via one of the MMI-Rs. Passive shallowly etched waveguides are used to guide the optical signal out of the cavity towards the left edge of chip. The passive waveguides (dark blue) and MMI-Rs are made using deeply etched waveguides that have propagation loss of 5 dB/cm and allow smaller bending radius of 100 µm. Between the shallowly (light blue) and deeply etched waveguides, transition sections (green blocks) must be used to minimize the butt-joint coupling loss and back reflection. Fig. 3 reveals that a 2×2 MMI coupler forms the basis for a 2-port MMI reflector. The dashed shape shows the original 2×2 MMI coupler. The solid shape is the resulting 2-port MIR used in the proposed PIC. Low loss operation can be achieved with nearly 50% transmission and 50% reflection. The proposed PIC is fabricated within a multi-project wafer (MPW) run by SMART Photonics [11].

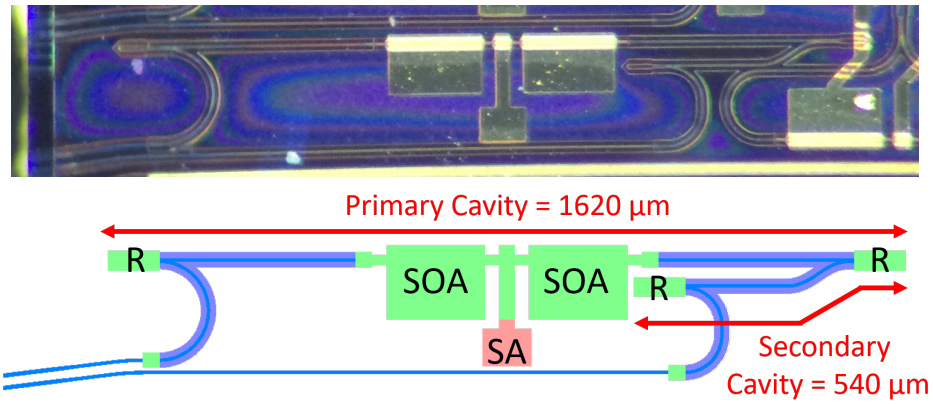


Figure 2: (a) Photograph (b) Layout of the proposed PIC. The primary cavity length is 1.62 mm and the secondary cavity length is 0.54 mm. R: reflector, SOA: semiconductor optical amplifier, SA: saturable absorber. The reflectors are realized using the multimode interference mirrors (MMI-Rs).

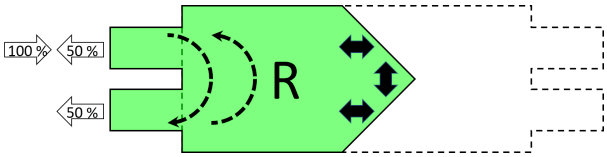


Figure 3: Schematic of multimode interference reflector.

3 RESULTS AND DISCUSSION

The optical spectrum collected from one of the waveguide outputs is presented in Fig. 4. The two highest modes separated by 1.268 nm (150 GHz) around 1572 nm, and the side-mode-suppression ratio (SMSR) is about 30 dB. The suppressed modes separated by 0.210 nm (25 GHz) correspond to the fundamental modes and the 25-GHz-spacing is related to the round-trip frequency of primary cavity. The spacing between highest and partially suppressed modes is 0.632 nm (75 GHz) is attributed to the FSR of secondary cavity. The experimental result agrees with the operation principle as shown in Fig. 1. However, the two highest modes are not equal in intensity and with a power ratio of $<$10 dB. And the number of excited modes is limited. The spectrum reveals a

dual wavelength emission operation rather than a optical frequency comb, indicating that further investigation is required on the actual lasing spectrum of primary cavity and spectral response of secondary cavity individually.

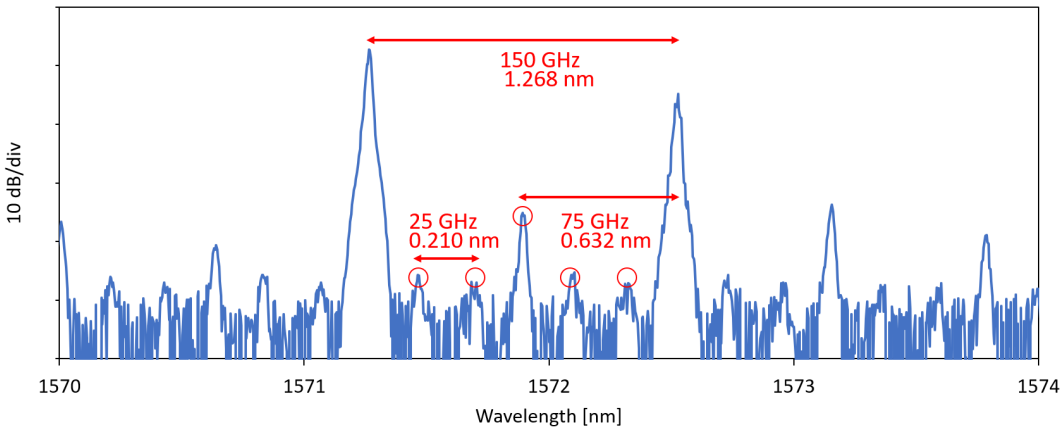


Figure 4: Optical spectrum of the proposed PIC. Mode spacing is 150 GHz with suppressed fundamental cavity modes separated by 25 GHz. 75-GHz mode spacing between highest and partially modes is related to the secondary coupled Fabry-Pérot feedback cavity.

4 CONCLUSION

A new semiconductor laser structure for comb's harmonic generation technique has been demonstrated. Two cavities are coupled via one of the multimode interference reflectors. The primary cavity is a colliding pulse mode-locked laser and the secondary one is a Fabry-Pérot filter. The cavity lengths are fractionally designed such that the mismatched lasing modes and filtering bands give rise to Vernier effect. The result agrees with the theoretically expected mode spacing, 6th harmonic (150 GHz) of fundamental cavity round-trip frequency (25 GHz). The spectral bandwidth and number of lasing modes (comb lines) should be improved.

ACKNOWLEDGMENT

This work has been supported by European Union's Horizon 2020 research and innovation programme under the Marie Skłodowska-Curie grant agreement No. 642355 FiWiN5G.

REFERENCES

[1] J. H. Marsh and L. Hou, "Mode-locked laser diodes and their monolithic integration," *IEEE Journal of Selected Topics in Quantum Electronics*, vol. 23, no. 6, pp. 1–11, Nov 2017.

[2] M.-C. Lo, R. Guzmán, C. Gordón, and G. Carpintero, "Mode-locked laser with pulse interleavers in a monolithic photonic integrated circuit for millimeter wave and terahertz carrier generation," *Opt. Lett.*, vol. 42, no. 8, pp. 1532–1535, Apr 2017.

[3] S. Srinivasan, E. Norberg, T. Komljenovic, M. Davenport, G. Fish, and J. E. Bowers, "Hybrid silicon colliding-pulse mode-locked lasers with on-chip stabilization," *IEEE Journal of Selected Topics in Quantum Electronics*, vol. 21, no. 6, pp. 24–29, Nov 2015.

[4] T. Thiessen and J. K. S. Poon, "20 ghz mode-locked laser diodes with integrated optical feedback cavities in a generic monolithic inp photonics platform," *IEEE Photonics Journal*, vol. 9, no. 5, pp. 1–10, Oct 2017.

[5] M.-C. Lo, R. Guzmán, and G. Carpintero, "Inp femtosecond mode-locked laser in compound feedback cavity with switchable repetition rate," *Opt. Lett.*, vol. 43, no. 3, pp. 1532–1535, Feb 2018.

[6] L. A. Coldren, "Multi-section tunable laser with differing multi-element mirrors," Jan. 23 1990, uS Patent 4,896,325.

[7] S. Keyvaninia, G. Roelkens, D. V. Thourhout, C. Jany, M. Lamponi, A. L. Liepvre, F. Lelarge, D. Make, G.-H. Duan, D. Bordel, and J.-M. Fedeli, "Demonstration of a heterogeneously integrated iii-v/soi single wavelength tunable laser," *Opt. Express*, vol. 21, no. 3, pp. 3784–3792, Feb 2013.

[8] J. C. Hulme, J. K. Doylend, and J. E. Bowers, "Widely tunable vernier ring laser on hybrid silicon," *Opt. Express*, vol. 21, no. 17, pp. 19 718–19 722, Aug 2013.

[9] E. Kleijn, M. K. Smit, and X. J. M. Leijtens, "Multimode interference reflectors: A new class of components for photonic integrated circuits," *Journal of Lightwave Technology*, vol. 31, no. 18, pp. 3055–3063, Sept 2013.

[10] M. Smit, X. Leijtens, H. Ambrosius, E. Bente, J. van der Tol, B. Smalbrugge, T. de Vries, E.-J. Geluk, J. Bolk, R. van Veldhoven, L. Augustin, P. Thijs, D. D'Agostino, H. Rabbani, K. Lawniczuk, S. Stopinski, S. Tahvili, A. Corradi, E. Kleijn, D. Dzibrou, M. Felicetti, E. Bitincka, V. Moskalenko, J. Zhao, R. Santos, G. Gilardi, W. Yao, K. Williams, P. Stabile, P. Kuindersma, J. Pello, S. Bhat, Y. Jiao, D. Heiss, G. Roelkens, M. Wale, P. Firth, F. Soares, N. Grote, M. Schell, H. Debregeas, M. Achouche, J.-L. Gentner, A. Bakker, T. Korthorst, D. Gallagher, A. Dabbs, A. Melloni, F. Morichetti, D. Melati, A. Wonfor, R. Penty, R. Broeke, B. Musk, and D. Robbins, "An introduction to inp-based generic integration technology," *Semiconductor Science and Technology*, vol. 29, no. 8, p. 083001, 2014.

[11] L. M. Augustin, R. Santos, E. den Haan, S. Kleijn, P. J. A. Thijs, S. Latkowski, D. Zhao, W. Yao, J. Bolk, H. Ambrosius, S. Mingaleev, A. Richter, A. Bakker, and T. Korthorst, "Inp-based generic foundry platform for photonic integrated circuits," *IEEE Journal of Selected Topics in Quantum Electronics*, vol. 24, no. 1, pp. 1–10, Jan 2018.

A Compressive Sensing Integrated Fourier Raman Spectrometer

(Invited paper)

Alan Scott[1,2], Hugh Podmore[1]
[1] Honeywell International, *303 Terry Fox Dr., Ottawa, Ontario - Canada*
[2]*Tel: +01 613 591 7777, Fax: +01 613 591 7789, e-mail: alan.scott@honeywell.com*

ABSTRACT

We have built a novel planar-waveguide Fourier-transform spectrometer (FTS) with several innovative design features to achieve high throughput Raman spectroscopy in a compact layout. This waveguide FTS consists of a set of independent Mach-Zehnder interferometers (MZIs) on a photonic chip. An array of microlenses is bonded to the 'bottom' surface of the chip, transforming a normally incident collimated beam into an array of focal spots near the waveguide surface. These micro-beams are deflected using an array of focused ion-beam (FIB) etched 45 degree mirrors into an array of single mode waveguides. Because the features of a Raman spectrum are sparsely distributed in frequency space, we are able to adapt techniques of compressive-sensing (CS) spectroscopy to significantly undersample the interferogram at our chosen bandwidth and resolution. The resulting system reduces the number of waveguides (MZIs) required by a factor of 4 while simultaneously reducing the size of the spectrometer and concentrating the Raman signal in a smaller number of detector pixels for further signal to noise enhancement. Because the interferogram samples are gathered simultaneously, a gated detector can be used to separate Raman peaks from sample fluorescence.

Keywords: Fourier, Raman, Compressive Sensing, Free Space, Microlenses, Silica Waveguides.

1. INTRODUCTION

Raman spectrometers measure inelastic scattering intensity as a function of energy shift of light scattered from a bright monochromatic source such as a laser. Optically, they are most efficient in the UV and visible (UVVis) optical regimes as Raman cross-section is enhanced at short wavelengths by a factor of $1/\lambda^4$. Raman spectra typically consist of sparsely distributed spectral peaks corresponding to the energy difference between discrete states. Dispersive Raman spectrometers require a narrow input slit to achieve high spectral resolution. Fourier-transform spectrometers (FTS) can achieve greater optical throughput for a given bandwidth and resolution, which may improve the signal to noise ratio (SNR) in a Raman system. Unfortunately, traditional Michelson FTS devices based on linearly-translating mirrors are not well-suited for applications in the UVVis as the short optical wavelengths impose strict requirements on jitter and mirror parallelism. Moreover, in a Michelson FTS the spectral information is captured over time, making it susceptible to errors induced by dynamic changes in the target such as laser-induced fluorescence.

The limitations of Michelson interferometry may be overcome using spatially heterodyned Fourier-transform spectrometers (SHFTS). SHFTS devices achieve high optical throughput in the UVVis while maintaining the capability to capture a full spectrum in a single shot [1]. In an SHFTS, light in each arm of an interferometer is spatially-dispersed using gratings, and recombined to produce a spatially-modulated interference pattern along a linear detector. SHFTS devices contain no moving parts, and have been successfully implemented in UVVis [2]. Despite their potential advantages as Raman spectrometers, present SHFTS implementations are difficult to miniaturize and are limited by their detectors to bandwidths of 2000 cm^{-1}.

2. THEORY

2.1 Waveguide SHFTS

Planar waveguide on-chip SHFTS devices may be implemented as an array of Mach-Zehnder interferometers (MZIs) with linearly increasing OPDs [3] as shown in *Figure 1*. This array of MZIs constitutes a discrete Fourier-transform (DFT), wherein the output of each MZI corresponds to a sampling point in the spatial interferogram. These MZI outputs may be sampled independently via a linear detector array bonded to the chip, or by on-chip photodiodes implanted in the substrate. A fast Fourier-transform (FFT) or inverse matrix operation may be used to invert the interferogram and retrieve the input spectrum. These devices achieve snapshot acquisition in a miniaturized package, and may be designed to operate in any wavelength range that is supported by the optical waveguide material.

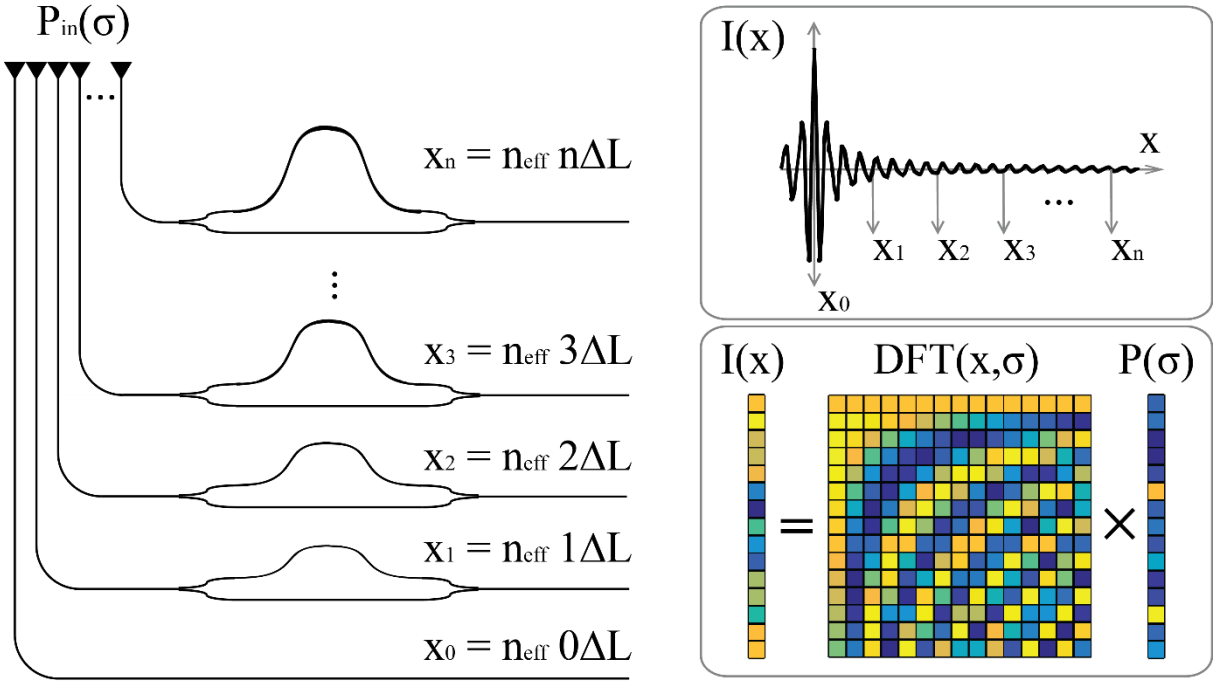


Figure 1. Diagram showing SHFTS operating principle. MZIs implemented as U-bends (left) collect a discrete sampling of the Fourier-transform of the input spectrum (upper right), equivalent to a discretely sampled Michelson interferometer. This may be expressed as a matrix operation y = Ax, where each row of the DFT matrix, A, corresponds to the spectral modulation function of a particular MZI multiplied by the input spectrum x to produce interferogram y (lower right) [5].

Planar waveguide on-chip SHFTS may also achieve greater bandwidths than traditional SHFTS, enabling their use in Raman spectroscopy. Recently, we have demonstrated that the bandwidth of planar-waveguide SHFTS devices may be increased fourfold via implementation as a compressive sensing instrument [4].

2.2 Compressive Sensing

The mathematical formulation of compressive sensing is given elsewhere [6]. The premise of this approach is that a signal that is sparse in frequency space can be fully represented, and retrieved, by a correspondingly sparse number of Fourier components or measurements. The sparser the spectrum, the fewer independent measurements needed to retrieve it. A random set of time domain measurements can be used to efficiently sample the incoming light. A l1-norm minimization method is used, based on the assumption of sparsity, to retrieve a spectrum that best reproduces the sparse measurement set using the least number of spectral elements.

We have previously demonstrated that such a configuration may form the basis for a compressive sensing SHFTS, wherein the number of MZIs is reduced by a factor of four over a fully Nyquist-sampled system [4]. In this spectrometer we randomly select 120 rows (MZIs) from the full DFT matrix to be fabricated on the wafer. This approach allows us to capture a full 2850 cm^{-1} spectrum at <10 cm^{-1} resolution with a manageable chip size using a small linear detector for readout.

Compressive sensing techniques may only be applied in the case that a spectrum is known to be sparse and therefore cannot be applied in the presence of a smooth background continuum. To overcome this limitation, in addition to the 120 compressive sensing MZIs we include a set of 40 fully-sampled low-frequency MZIs to retrieve an estimate of the background. An observed spectrum may be considered as a linear combination of sparse and non-sparse components. For instance, in Raman spectroscopy the signal will consist of a set of spectrally narrow Raman emission lines, as well as spectrally broad fluorescence. Treating these components independently, by using the low-frequency MZIs to generate an estimate of the background fluorescence, and using the high-frequency MZIs to perform a compressive sensing retrieval on a residual interferogram, we may perform a retrieval even in the presence of background contamination. This novel hybridization of standard and compressive spectral retrievals allows us to overcome a traditional limitation of compressive sensing schemes. Without this corrective step, background fluorescence would make accurate compressive sensing retrieval of Raman components impossible.

3. SPECTROMETER OVERVIEW

We present a miniaturized high-resolution planar waveguide visible-wavelength SHFTS for Raman spectroscopy with many innovative aspects. The SHFTS leverages compressive sensing retrieval methods to undersample its interferogram by a factor of c = 1/4, expanding its operational bandwidth without sacrificing resolution. We use a subset of low-resolution MZIs to provide a fully-sampled estimate of non-sparse background signals, to demonstrate, for the first time, the use of compressive sensing methods to retrieve spectra even in the presence of broadband background light. We implement a novel multi-aperture vertical coupling scheme to achieve high-throughput broadband input coupling to 83 independent apertures. Finally, we demonstrate a novel method for snapshot waveguide characterization via white-light hyperspectral imaging at the waveguide outputs.

We have demonstrated, for the first time, a Fourier microspectrometer able to retrieve input spectra using compressive sensing techniques for emission spectroscopy. Initial results are shown in *Figure 2*, significantly outperforming the matrix pseudo-inverse retrieval method.

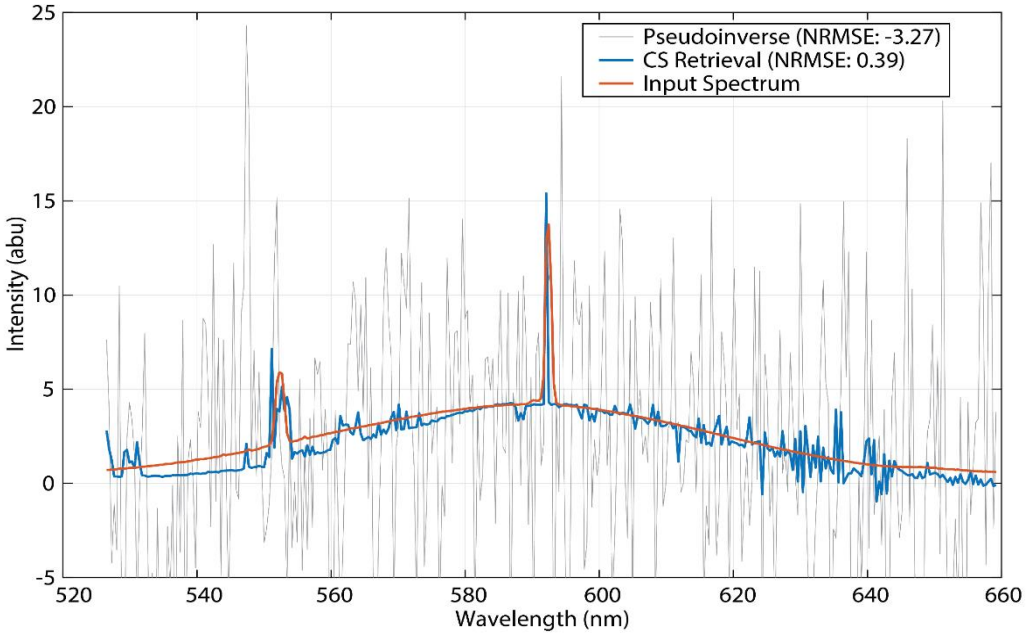


Figure 2. Experimental retrieval of sparse spectra in the presence of non-sparse background signal. The sparse spectra consists of two narrowband filter lines located at 552 nm and 592 nm, while the background light, centered at 590 nm, spans nearly the full bandwidth of the spectrometer. A compressive sensing retrieval (blue) is plotted against a matrix pseudoinverse retrieval (grey), as well as the input spectrum (orange). Minimizing the l1-norm correctly retrieves the input spectrum with a normalized root mean square error (NRMSE) of 0.39 [5].

ACKNOWLEDGEMENTS

This work was performed with funding from the Canadian Space Agency, NSERC, and Honeywell International.

REFERENCES

[1] J. Harlander, R.J Reynolds, and F.L. Roesler: Spatial Heterodyne spectroscopy for the Exploration of Diffuse Interstellar Emission Lines at Far-Ultraviolet Wavelengths, *Ap. J.*, vol. 396. pp. 730-740, 1992.

[2] J. M. Harlander, H.T. Tran, F.L. Roesler: Field-Widened Spatial Heterodyne Spectroscopy: Correcting for Optical Defects and New Vacuum Ultraviolet Performance Tests, *Proc. SPIE*, vol. 2280, pp. 310-319, 1994.

[3] M. Florjańczyk, *et al.*: Multiaperture Planar Waveguide Spectrometer Formed by Arrayed Mach-Zehnder Interferometers, *Opt. Express*, vol. 15(26), pp. 18176-18189, 2007.

[4] H. Podmore, *et al.*: Demonstration of a Compressive-Sensing Fourier-Transform On-Chip Spectrometer, *Opt. Lett.*, vol. 42, pp. 1440-1443, 2017.

[5] H. Podmore, A. Scott, and R. Lee: A Compressive-Sensing Fourier-Transform On-Chip Raman Spectrometer, *Proc. SPIE*, vol. 10539, 2018.

[6] E.J. Candes, J. Romberg, and T. Tao: Robust Uncertainty Principles: Exact Signal Reconstruction From Highly Incomplete Frequency Information, *IEEE Trans. Inf. Theory*, vol. 52, pp. 489-509, 2006.

Integrated Silicon-on-Insulator AWG Spectrometer with Single Pixel Readout for 2.3 um Spectroscopy Applications

(Student Paper)

Anton Vasiliev[1], Muhammad Muneeb[1], Jeroen Allaert[1], Roel Baets[1] and Günther Roelkens[1]
[1]*Photonics Research Group, Ghent University-imec and Center for Nano- and Biophotonics, Technologiepark-Zwijnaarde 15 - 9052 Ghent - Belgium*
Tel: +3293314815, e-mail: anton.vasiliev@ugent.be

ABSTRACT

A compact and cheap mid-infrared spectrometer is realized by integrating a Silicon-on-Insulator (SOI) Arrayed Waveguide Grating (AWG) spectrometer operating in the 2.3 μm wavelength range with a high performance photodiode. The AWG has twelve output channels with a spacing of 225 GHz (4 nm) and a free spectral range (FSR) of 3150 GHz (56 nm), which are simultaneously collected by a single, transistor outline (TO)-packaged extended InGaAs PIN photodiode. The response of each AWG channel is discerned by time-sequentially modulating the optical power in each output channel using integrated Mach-Zehnder based (MZI) thermo-optic modulators with a π-phase shift power consumption of 50 mW. The photonic chip is interfaced using off-the-shelf electronic components and a standard 9/125 single-mode fiber. The response of the AWG is limited to one FSR using a 50 nm Full Width Half-Maximum (FWHM) bandpass interference filter. Using 31 μW optical power in the fiber, the absorption spectrum of a 0.5 mm thick polydimethylsiloxane sheet (PDMS) is sampled and compared to a benchtop spectrometer to good agreement.

Keywords: integrated spectrometer, silicon photonics, arrayed waveguide grating, mid-infrared spectroscopy

1 INTRODUCTION

Silicon photonics is expanding its application areas beyond optical communication. In particular, it is possible to access longer wavelengths in the same Silicon-on-Insulator (SOI) waveguide platform for novel compact sensing applications while still leveraging the well-established CMOS fabrication technology [1]. The mid-infrared wavelength range from 2-4 μm is of interest for spectroscopic detection of various substances in solid, liquid or gas phase. There are several approaches towards the realization of a compact and cheap spectroscopic system. For spectroscopy of gases, a high resolution spectrum in a narrow wavelength range is typically required. This can be realized with mid-infrared distributed feedback (DFB) laser sources which can be thermally tuned over a narrow wavelength range [2].
Spectroscopy of liquids and solids involves broad absorption features and an integrated dispersive spectrometer together with detectors and a broadband source would be a more cost-efficient solution. An integrated wavelength (de)multiplexer such as an arrayed waveguide grating (AWG) is needed. The free spectral range (FSR) and channel spacing can be tailored to fit the application. It is possible to heteregeneously integrate III-V-on-Silicon detectors on the photonic IC with the spectrometer [3]. However, existing packaged (cooled) mid-infrared photodetectors currently outperform the on-chip solutions. We present an approach for integrating a single standard TO-can packaged InGaAs PIN photodiode with a twelve channel AWG with 225 GHz (4 nm) channel spacing. The AWG output arms are modulated using on-chip balanced Mach-Zehnder interferometers (MZIs) by thermal tuning [4]. As an example, the absorption spectrum of polydimethylsiloxane (PDMS) in the 2.3 μm wavelength range is recovered.

2 EXPERIMENTS

The AWG is fabricated on a 200 mm SOI wafer with a 400 nm thick crystalline Si device layer and 2 μm buried oxide layer thickness. Rib waveguides and grating couplers are defined with a 180 nm deep etch and are cladded with SiO_2 and planarized down to the silicon device layer. A thin 0.9 μm layer of SiO_x is deposited on top. 100/10 nm thick Ti/Au resistors are defined on the arms of the modulators. The resistors measure 200x2 μm^2 and realize a π-phase shift with $\approx$ 50 mW of power dissipation. As a final step, the chip is passivated with a thin layer of BCB. The circuit is designed for 2.3 μm wavelength and TE polarized light. The AWG has twelve channels with 225 GHz (4 nm) channel spacing and an FSR of 3150 GHz (56 nm). The MZI modulators of the photonic chip are wirebonded to a printed circuit board (PCB) and are addressed by a home-built 16-bit current source through USB. A Hamamatsu G12183-010K PIN photodiode is fixed to a pre-amplifier PCB with a variable gain up to 10^6 V/A. The PD is manually positioned and fixed 0.5 mm above the output grating coupler array of the AWG, see Fig. 1(a). The output grating array covers an area of 300x140

A. Vasiliev thanks Research Foundation - Flanders (FWO) for a PhD fellowship.

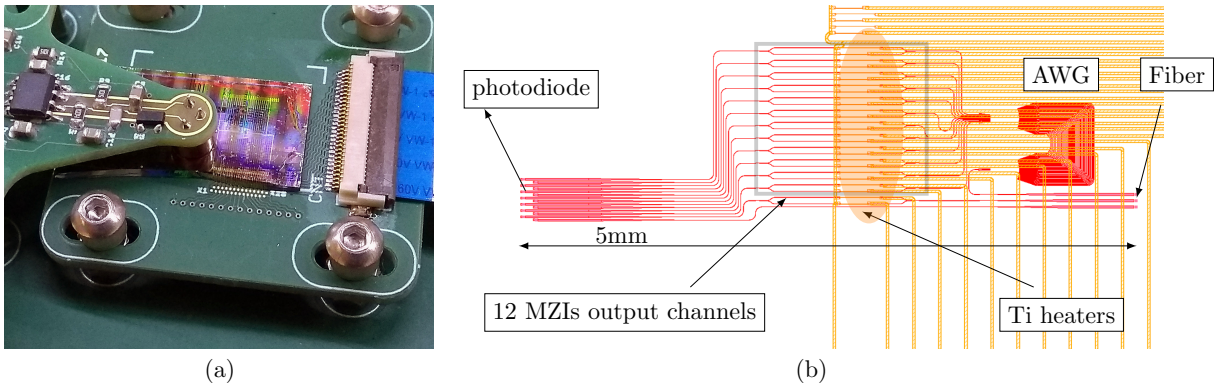


Figure 1. Photograph showing the photonic chip wirebonded to a PCB. The TO-can with the photodiode is positioned directly on top of the output grating couplers of the chip (a). Design layout of the AWG (b). The output channels of the AWG are modulated time-sequentially using (balanced) MZI thermo-optic modulators. A π-phase shift in each channel is achieved by dissipating $\approx$ 50 mW in the metal (Ti/Au) resistor placed 0.9 µm above the optical waveguide.

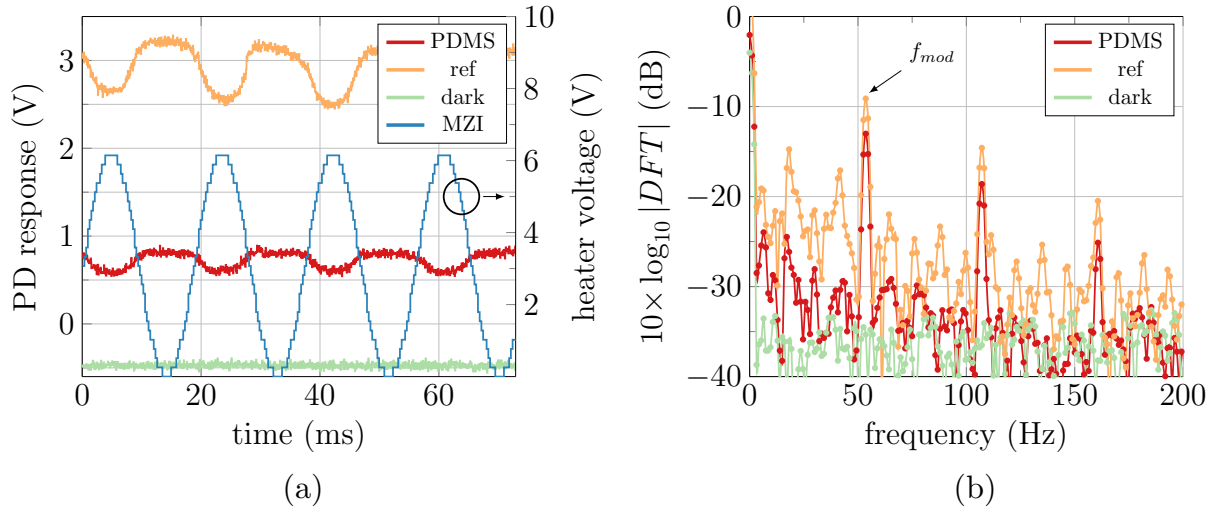


Figure 2. Response of the photodiode to a sinusoidal modulation of one AWG channel. The modulation is done using a MZI thermo-optic modulator. The first thousand sample points are shown for three cases: prior to the chip, the light passes through a 0.5 mm thick PDMS sheet, a reference measurement without PDMS and a dark measurement without the light source (a). The logarithmic DFT spectrum of the PD response is shown (b). The difference in maxima between the 'PDMS' and 'ref' measurement at the modulation frequency f_{mod} is used to determine the spectral response of PDMS at the peak wavelength of this AWG channel.

µm^2 and all the channels are simultaneously collected by the photosensitive area of the PD, 1 mm in diameter. The PD response is read-out using the aforementioned 16-bit ADC with a sampling rate of 24 kSa/s.

A Cr^{2+}:ZnS solid state laser from IPG Photonics working in amplified spontaneous emission (ASE) mode is coupled to a standard 9/125 single mode fiber. The spectrum of the source is filtered in free space prior to coupling using a 50 nm FWHM interference bandpass filter in order to isolate one FSR of the AWG at 2310 nm. After filtering, the total power in the fiber is 31 µW. For the spectroscopy experiment, a 0.5 mm thick Sylgard (1:10) PDMS foil is sandwiched between two 5 mm thick CaF_2 windows and is placed in the free space beam path after the bandpass filter and before the light is coupled into the fiber.

The light from the fiber is vertically coupled to the chip using a grating coupler with a coupling efficiency of 10% at the grating peak wavelength of 2350 nm. The combined output from the channels of the AWG results in a PD signal of 3.2 V for the reference measurement and 0.9 V when PDMS is introduced. The optical power inside each channel can be recovered by modulating each channel time-sequentially [4]. The modulators are nominally transmitting light when no power is dissipated. The modulation depth of the heaters is chosen such that it corresponds to a π-phase shift of each MZI. Slight differences in fabrication lead to drive voltages V_π that are spread between 6 and 7 V and the switching power is about 50 mW. An example of modulation of one such channel is shown in Fig. 2. The PD output is collected for 1 second for each channel with a sampling rate of 24 kHz. The discrete Fourier Transform (DFT) of the signal is performed on the output using the fast-fourier transform (FFT) algorithm with a Kaiser smoothing window. The result for one channel is shown in Fig. 2(b). The absolute value of the DFT spectrum at the modulation frequency is proportional to the optical power modulation of that channel. This value is obtained for each of the twelve channels for the case when

there is no PDMS in the free space beam path and when it is introduced. The difference between the two is a measure for the absorption spectrum of PDMS, sampled at the peak wavelengths of the AWG channels. The AWG channel response is characterized using a single-mode tunable laser and normalized to a reference waveguide. The channel spacing is 225 GHz (4 nm) and one FSR spans 3150 GHz (56 nm). The insertion loss is around 2 dB and the crosstalk between channels is 20 dB.
The absorption spectrum of PDMS obtained in this manner corresponds well to a benchmark measurement. A Yokogawa AQ6375 Optical Spectrum Analyzer (OSA) was used to record the optical spectrum in the fiber before and after introducing PDMS in the free space beam path. The results from the AWG agree well with the OSA measurement, see Fig. 3(b). A slight discrepancy for the longer wavelength channels is observed. This is due to the fact that the central wavelength of the bandpass filter is not exactly centered to one FSR of the AWG.

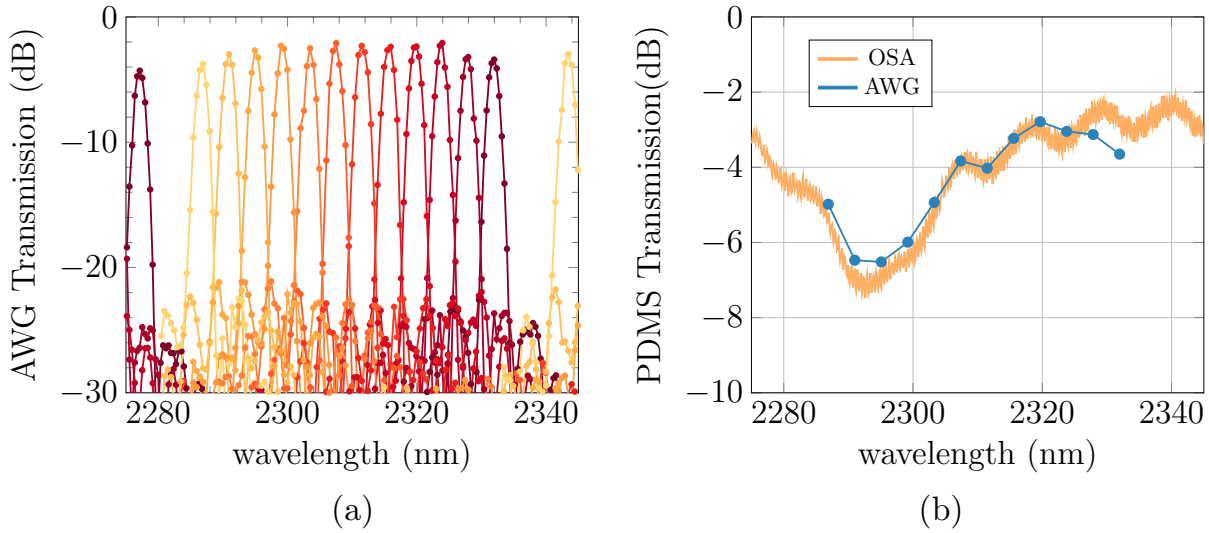


Figure 3. The AWG channels are characterized using a single-mode tunable laser and normalized to a reference waveguide (a). The channel spacing is 225 GHz (4 nm) and one FSR spans 3150 GHz (56 nm). The insertion loss is around 2 dB and the crosstalk between channels is 20 dB. The AWG response is limited to within one FSR with a bandpass filter of 50 nm FWHM at 2305 nm. The optical modulation depth difference of the PD between the PDMS and reference measurement is plotted for each AWG channel with the corresponding channel peak wavelength (b). The results agree well with the results obtained by measuring the PDMS transmission using a Yokogawa AQ6375 OSA.

3 CONCLUSIONS

Low-cost and miniaturized spectrometers can be realized by combining a discrete off-the-shelf mid-infrared photodetector with SOI wavelength demultiplexer circuits. A novel approach is shown where a single discrete photodetector is used to characterize the response of a twelve channel mid-infrared AWG at 2.3 μm. The different AWG channels are discerned by time-sequentially modulating the output arms with MZI-based thermo-optic modulators. The driving and read-out of the spectrometer is performed using low-cost standard electronic components. The absorption spectrum of PDMS is recovered at 2.3 μm to good agreement with bench-top OSA measurements. This is a promising approach which can be applied to longer wavelength SOI spectrometers for the 3-4 μm wavelength range where high-performance cooled detectors are needed.

ACKNOWLEDGMENT

The authors thank Barry Smalbrugge from TU/e for wirebonding and CMST, Ghent University for providing the PDMS sample.

REFERENCES

[1] G. Roelkens et al., “Silicon-based heterogeneous photonic integrated circuits for the mid-infrared,” Opt. Mater. Express 3, no. 9 (2013): 1523-1536.

[2] R. Wang et al., “Broad wavelength coverage 2.3 um III-V-on-silicon DFB laser array,” Optica, 4(8), (2017), p.972-975.

[3] M. Muneeb et al., ”III-V-on-Silicon integrated micro-spectrometer for the 3 um wavelength range,” Opt. Express, 24(9), (2016), p.9465-9472.

[4] R. Baets, D. Delbeke, G. Roelkens and W. Bogaerts, ”Integrated spectrometers with single pixel detector,” WO Patent 2015/162197, October 29, 2015.

Integrated $Al_2O_3:Yb^{3+}$ Microring Laser for On-Chip Active Sensing in an Aqueous Environment

Michiel de Goede, Lanthian Chang, Meindert Dijkstra, Sonia M. García-Blanco
Optical Sciences Group, MESA+ Institute for Nanotechnology, University Twente, P.O. Box 217, 7500 AE Enschede, The Netherlands
Tel: +31 53 489 2640, e-mail:m.degoede@utwente.nl

ABSTRACT

This paper presents an integrated on-chip $Al_2O_3:Yb^{3+}$ microring resonator laser that operates in an aqueous environment. By varying the refractive index of the bulk cladding, the lasing wavelength can be tuned, allowing this device to operate as an active refractive index sensor. In this manner, the lasing modes could be tuned over 15 nm with a sensitivity of 590 nm/RIU. In combination with the wavelength resolution of the detector (100 pm), a limit of detection of 1.5×10^{-4} RIU was achieved. The intrinsic limit of detection was not determined due to the incapability of measuring the laser linewidth. This work demonstrates the viability of realizing very sensitive, laser-based active sensors in an aqueous environment on the $Al_2O_3:Yb^{3+}$ material platform.

Keywords: $Al_2O_3:Yb^{3+}$, laser, microring resonator, sensor.

1. INTRODUCTION

Microring resonators are very often integrated on-chip for the realization of refractive index sensors. Such sensors typically operate by monitoring the wavelength shift of a resonance induced by a dielectric perturbation in the evanescent field region. Microring resonators sensors in the SOI [1], Si_3N_4 [2] and SiON [3] passive material platforms. Generally, wavelength tracking requires a setup containing a tunable laser to repeatedly scan the spectral position of the resonance, which leads to relatively expensive sensing modules

Al_2O_3 is an alternative material platform that can be doped with rare-earth ions to achieve gain [4] and to realize lasers [5]. On this material platform, an active sensor was already demonstrated that could detect particles through a variation of the beat note of a distributed feedback laser [6]. This type of active sensing has the attractive feature that it only requires simple hardware to transduce the sensing-induced change of the optical beat note of the laser output into an electronic signal. Furthermore, due to the high quality factors of this type of Al_2O_3-based lasers [7], a very low intrinsic limit of detection (*iLOD*) of an active sensor could be in principle realized.

In this paper, we present an integrated double microring resonator made out of $Al_2O_3:Yb^{3+}$ waveguides that operates in an aqueous environment. Upon optical pumping, the lasing wavelength could be tuned by varying the refractive index of the liquid flown over it. In this manner a bulk refractive index sensor was realized with a sensitivity of 590 nm/RIU, which, combined with the resolution of the spectral analyzer detector of 100 pm gave a limit of detection of 1.5×10^{-4} RIU. However, it is expected that the *iLOD* is lower due to the linewidth being much narrower than the detector resolution. The presented results, together with this consideration, demonstrate the viability of realizing ultrasensitive sensors on the $Al_2O_3:Yb^{3+}$ material platform that could lead to simple detection methods.

2. MICRORING RESONATOR LASER

The fabrication of the laser started with the reactive cosputtering of Al and Yb to deposit an $Al_2O_3:Yb^{3+}$ layer onto a SiO_2 substrate with an AJA ATC 1500 sputter coater. By controlling the ratio of applied power to both targets the Yb doping concentration can be tuned. The power was chosen to achieve a Yb content of 5×10^{-20} cm^{-3}. The waveguides and microring resonators were patterned with contact UV lithography and etched with an Oxford Plasmalab System 100 inductively coupled plasma reactive ion etcher. Then, a local cladding of SiO_2 was deposited onto the device to cover the input and output waveguides while leaving the microrings open to be addressed by the various liquids. To this end a PDMS microfluidic channel was bonded to the chip. Figure 1a shows the resulting devices inside the microfluidic channel.

After submerging the devices in water they were optically pumped by a diode laser at a wavelength of 976 nm and demonstrated lasing in the spectral range of 1010—1070 nm. The lasing spectrum obtained with an optical spectrum analyser of one of the devices contains three laser modes separated by the Vernier free spectral range, as shown in Fig. 1b. The spectrum of the first lasing mode in Fig. 1b as function of current injected into the diode laser is shown in Fig. 1c. It can be seen that its threshold lies around 200 mA of diode laser current, after which the spectral power increases upon increasing the current. Figure 1d shows the light-light curves of all three lasing modes, indicating the onset of lasing when the diode laser current exceeds the threshold.

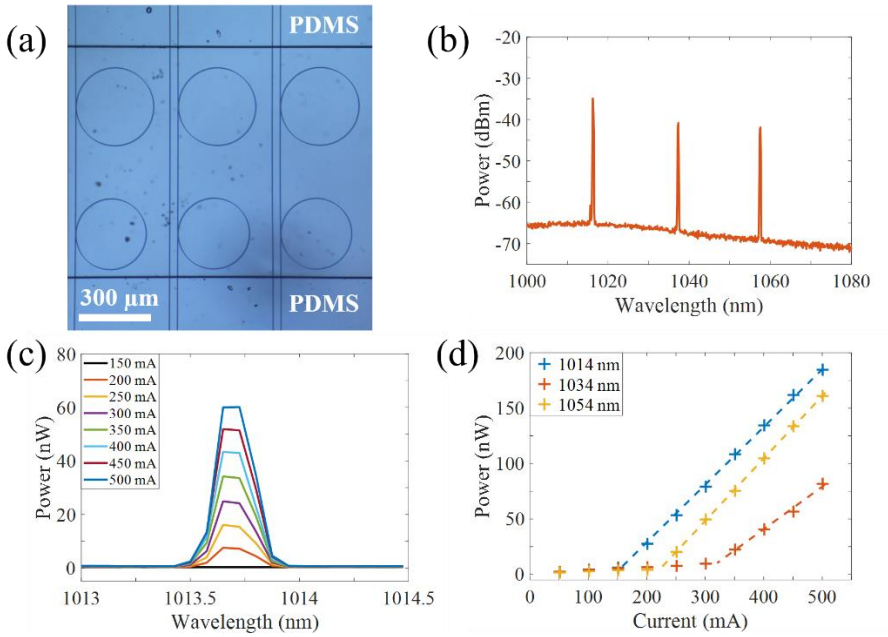


Figure 1. $Al_2O_3:Yb^{3+}$ microring resonator laser operating in aqueous environment. (a), Optical microscope image of circuits containing the double microring resonator in a microfluidic channel. (b), Lasing spectra of the double microring resonator laser. (c), Lasing spectra of the first mode for varying input power. (d), Power characteristic of the laser.

3. ACTIVE SENSING

The laser was used as an active sensor by flowing varying concentrations of NaCl dissolved in water. By changing the refractive index of the top cladding, the optical path length of the microring resonator changes and shifts the lasing wavelength. This was done by flowing water over the active sensor containing NaCl concentrations of 0, 5, 10 and 15 wt%. Figure 2a shows the lasing spectrum of the first mode for these variations. By monitoring the lasing spectrum continuously, the lasing wavelength of all three modes was monitored in real time as shown in Fig 2b and 2c. Furthermore, by reversing the order of the flown liquids the lasing wavelength returned to its original wavelength, indicating reversible operation. Figure 2d shows the measured slope sensitivity of the active sensor that has a value averaged over all three modes of 590 nm/RIU.

The limit of detection (*LOD*) of the sensor is the smallest variation of bulk refractive index change that yields a detectable lasing wavelength shift and is given by [8]:

$$LOD = \frac{3\sigma}{S} \tag{1}$$

where σ is the standard deviation in the position of the lasing wavelength and *S* is the sensitivity of the active sensor. In this case the *LOD* is limited by the resolution of the used optical spectrum analyser of 100 pm, which has a σ of 29 pm. Combining this value with the measured sensitivity gives a LOD = 1.5×10^{-4}. However, the intrinsic limit of detection (*iLOD*) of the system is given by [8]:

$$iLOD = \frac{\lambda_{FWHM}}{S} \tag{2}$$

where λ_{FWHM} is the laser linewidth of the active sensor. With the currently used optical spectrum analyser a maximum laser quality factor of ~10^4 can be measured due to the limited resolution, although the actual value of similar, previously measured $Al_2O_3:Yb^{3+}$ lasers lies much higher due to their narrow linewidth [7]. The true *iLOD* could be obtained by measuring the laser linewidth and it is expected that the *iLOD* is much lower than the currently reported *LOD*. These results could allow for sensitive, active sensor applications integrated on chip on this material platform.

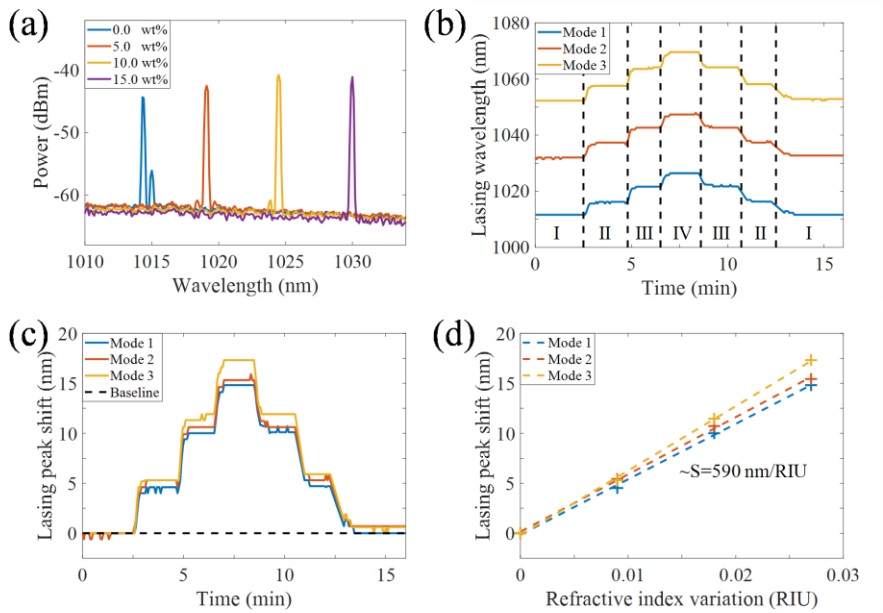


Figure 2. Active sensing experiment. (a), Lasing wavelength shift of the first lasing mode. (b), Real-time monitoring of the lasing wavelengths while flowing water (I), water containing 5.0 wt% NaCl (II),water containing 10.0 wt% NaCl (III) and water containing 15.0 wt% NaCl (IIV). (c), Relative lasing wavelength shift of data in (b). (d), Slope sensitivity of the active sensing experiment. Sensitivity is an average of the three modes.

4. CONCLUSIONS

A double microring resonator of Al_2O_3:Yb^{3+} was realized that had three lasing modes separated by the Vernier free spectral range of the system. This laser was used as a sensor to monitor the refractive index of its liquid cladding. A sensitivity of 590 nm/RIU and LOD of 1.5×10^{-4} RIU was achieved. It is expected that the sensor has a lower *iLOD* and can be used for sensitive sensing. These results indicate that the active sensor could be used for sensitive, active biosensing with the prospects of simple detection schemes.

ACKNOWLEDGEMENTS

This project has received funding from the European Union's Seventh Programme for research, technological development and demonstration under grant agreement No 634928.

REFERENCES

[1] W. Bogaerts, *et al.*: Silicon Microring Resonators. *Laser Photon. Rev.*, vol. 6. pp. 47-73, Sept 2011.

[2] K. Wörhoff, *et al.*: TriPleX: A Versatile Dielectric Photonic Platform. *Adv. Opt. Technol.*, vol. 4. pp. 189-207, Apr 2015.

[3] A. Samusenko, *et al.*: A SiON Microring Resonator-Based Platform for Biosensing at 850 nm. *J. Light. Technol.*, vol. 34. pp. 969-977, Feb 2016.

[4] K. Worhoff, *et al.*: Reliable Low-Cost Fabrication of Low-Loss Al_2O_3:Er^{3+} Waveguides With 5.4-dB Optical Gain. *IEEE J. Quantum Electron.*, vol. 45. pp. 454-461, May 2009.

[5] J. Bradley, *et al.*: Integrated Al_2O_3:Er^{3+} Ring Lasers on Silicon with Wide Wavelength Selectivity. *Opt. Lett.*vol. 35. pp. 73-75, Jan. 2010.

[6] E. Bernhardi, *et al.*: Intra-Laser-Cavity Microparticle Sensing with a Dual-Wavelength Distributed-Feedback Laser. *Laser Photonics Rev.*, vol 7. pp. 589-598, Apr 2013.

[7] E. Bernhardi, *et al.*: Photonic generation of stable microwave signals from a dual-wavelength Al_2O_3:Yb^{3+} distributed-feedback waveguide laser. *Opt. Lett.*, vol. 37. pp 181-183, Jan 2012.

[8] S. Schmidt, *et al.*: Improving the performance of silicon photonic rings, disks and Bragg gratings for use in label-free biosensing. *in Proc. of SPIE 9166*, San Diego, United States of America, Aug 2014.

Water-loaded plasmonic stripe integrated with Si_3N_4 waveguide using gold and CMOS compatible metals

A. Manolis[1], G. Dabos[1], D. Ketzaki[1], E. Chatzianagnostou[1], N. Pleros[1], L. Markey[2], J.C. Weeber[2], A. Dereux[2], A.L. Giesecke[3], C. Porschatis[3], B. Chmielak[3] and D. Tsiokos[1]

[1] Department of Informatics - Center for Interdisciplinary Research and Innovation, Aristotle University of Thessaloniki, Greece, Tel: +302310990588, e-mail: dtsiokos@csd.auth.gr,

[2]Laboratoire Interdisciplinaire Carnot de Bourgogne, CNRS-Université de Bourgogne, Dijon, France

[3]AMO GmbH, Advanced Microelectronic Center Aachen (AMICA), Otto-Blumenthal-Strasse, Aachen, Germany,

ABSTRACT

In this work, we report the integration of low loss Si_3N_4 waveguides with water-loaded thin plasmonic stripes. Experimental measurements revealed a photonic to plasmonic insertion loss of 2.3dB per transition and a propagation length of 75μm at 1550nm when using gold as plasmonic metal. With the aid of numerical simulations we also demonstrate how CMOS compatible metals may be used to realize such structures at low cost. The proposed waveguide scheme holds promise as an optical transducer in future plasmonics-augmented biosensors.

Keywords: Surface plasmons, thin-film plasmonics, silicon nitride, photonic integrated circuits. CMOS metals.

1. INTRODUCTION

Plasmonic technology may revolutionize photonic-integrated-circuits (PICs), unleashing unprecedented performance breakthroughs. Harnessing the unique capability of plasmonic waveguides to guide light at metal surfaces can offer sub-wavelength confinement and increased light–matter interaction at the metal surface [1]. However, the inherent high propagation losses of SPP waveguide configurations impede their broad utilization in more complicated PICs. To lower this barrier, plasmonic structures may be selectively co-integrated with low-loss photonic waveguides therefore minimizing chip losses coming from plasmonic sections while reaping the benefits of guiding light over metal surfaces. Merging plasmonics with photonics in a common integration platform has been so far demonstrated in a range of waveguide configurations and functional devices [2]-[5] however, only a limited number of plasmo-photonic interface structures has been proposed when plasmonic propagation in aqueous environment is required [4], [5] as is typically the case when biochemical sensing applications are targeted. In this paper, we demonstrate the co-integration of water-loaded gold-based plasmonic stripe waveguide with a Si_3N_4 waveguide, utilizing a butt-coupled interface for potential application in future biosensing applications. Following the same design methodology we evaluate the performance of the proposed structures when relying on CMOS-compatible metals such aluminium and copper.

2. GOLD-BASED PLASMONIC STRIPE ON Si_3N_4

2.1 Design and simulation

Figure 1(a) illustrates the proposed plasmo-photonic structure. A Si_3N_4 photonic waveguide and a gold-based plasmonic stripe waveguide are interfaced in a butt coupled scheme via photonic linear tapers. The test structure exploits Si_3N_4 TM grating couplers (GCs) to achieve coupling in and out of the chip [6]. Figure1(b) depicts a more detailed side-view geometry of the proposed interface. The main challenge of interfacing the silicon nitride and the gold stripe waveguides was to spatially match photonic and plasmonic mode profiles. Our design process was based on the optimization of two parameters: Longitudinal Offset (LO) and Vertical Offset (VO) between the photonic and plasmonic waveguide facets, as shown in Fig.1(b). LO and VO were optimized via numerical simulations, in terms of coupling efficiency, to the values of 500nm and 400nm respectively, as described in [8].

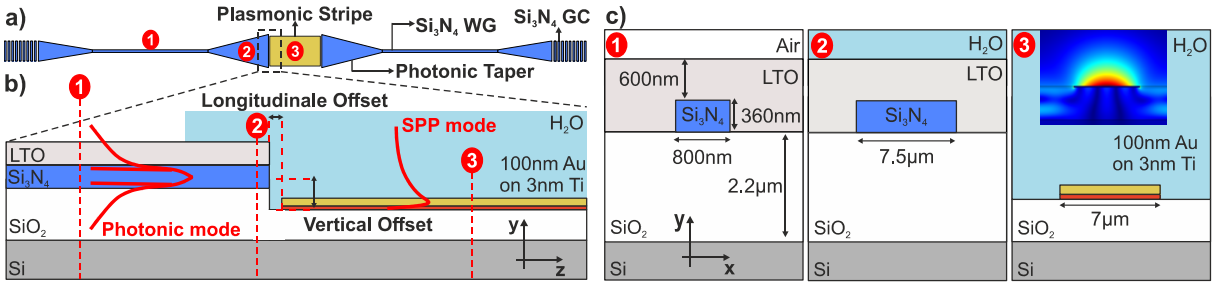


Figure 1. (a) Schematic representation of the proposed interface structure. (b) Sideview of the proposed interface illustrating Vertical Offset (VO) and Longitudinal Offset (LO) parameters. (c) Cross-section and dimensions of the photonic and the plasmonic waveguides.

The different cross-sections across the structure including the photonic waveguide (1) the taper end facet (2) and the plasmonic waveguide (3) are depicted in Fig.1(c). A 360nm × 800nm Si_3N_4 photonic waveguide core is cladded with 600nm of LTO on a 2.2μm thick SiO_2 substrate layer (Fig.1(c)(1)). The photonic waveguide is linearly tapered to 7.5μm width forming a photonic taper waveguide (Fig.1(c)(2)) which is interfaced with a 100nm × 7μm plasmonic stripe exposed to the surrounding medium. The plasmonic waveguide resides on a Ti layer located between the gold film and the SiO_2 layer (Fig.1(c)(3)). As illustrated in Fig.1(c), the plasmonic waveguide and the photonic taper are surrounded by water in order to evaluate coupling performance in conditions encountered in potential biosensing-related applications. Numerical simulations for the proposed structure predicted a coupling loss equal to 2.2dB and an L_{SPP} reaching 86μm at 1550nm [7].

2.2 Fabrication and characterization

For the fabrication of the proposed interface structure, a standard 6'' silicon wafer with 2.2μm of thermally grown SiO_2 has been employed as substrate. The Si_3N_4 waveguide was deposited in low pressure chemical vapor deposition process (LPCVD). Optical projection lithography with a CANON i-line stepper tool was used to define markers, waveguides and GCs. Reactive-ion-etching (RIE) based on CHF_3 and He chemistry was exploited for the structure transfer of the waveguides. Following this, 600nm of SiO_2 were deposited in a low temperature LPCVD furnace (LTO). A subsequent annealing process for several hours at 1000°C minimized hydrogen content and absorption of the LTO cladding to reduce the waveguide propagation losses. Afterwards, cavities for the plasmonic material were defined by the i-line stepper tool and etched 1.36μm deep through LTO, Si_3N_4 and SiO_2 as well by RIE with CHF_3 and He chemistry. In the final fabrication stage, the metallic plasmonic stripes were deposited into the cavities by a lift-off process using e-beam lithography, thermal evaporation of gold and lift-off dissolution. A very thin (3nm) titanium layer was deposited by e-gun evaporation prior to gold for an improved adhesion of gold on the sample. SEM images of the fabricated structure are shown in Figure 2(a).

Characterization measurements were carried out to evaluate propagation losses as well as the photonic to plasmonic coupling loss. Broadband measurements were carried out by sweeping the wavelength of a tunable laser source from 1500nm to 1580nm to launch light into Si_3N_4 GCs of the cut-back sections. By performing linear fitting process on the measured data, we calculated 0.058dB/μm propagation losses at 1550nm corresponding to an L_{SPP} equal to 75μm, showing good agreement with the simulation predicted value of 86μm. Blue scatter points in Fig.2(b) indicate the broadband operation of the structure by maintaining similar propagation losses measured for a wavelength range over 80nm. Red scatter points in Fig.2(c) illustrate the calculated photonic-to-plasmonic coupling loss, revealing broadband operation with a value of 2.3dB at 1550nm, for a single transition adequately matching the value of 2.2dB predicted numerically.

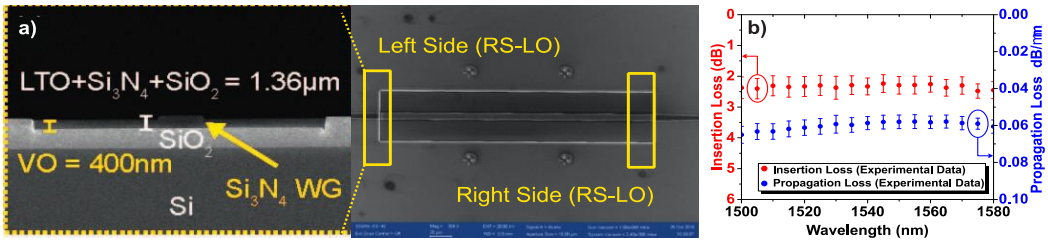


Figure 2. (a) SEM images of the interface structure in cross section and stripe top view. (b) Broadband experimental data for the insertion and propagation loss.

3. MODELLING OF CMOS-COMPATIBLE STRUCTURES

Successful matching of the numerical predictions with the experimental results for the Au-based plasmonic structure allowed us to use the same simulation methodology for the design of CMOS compatible plasmonic waveguides by replacing gold with low cost Aluminium (Al) and Copper (Cu). As in the case of the Au-based thin-film configuration reported in [7], the design study for the CMOS-based thin-film structure begins with a 2D eigenvalue analysis on the cross-sections of the waveguides under investigation. The coupling mechanism for this end-fire structure is expected to be governed by the same principles as the case of Au, so spatial mode matching should be achieved in order to efficiently transfer the light from the photonic to the plasmonic waveguide. The power overlap integral analysis led to similar results for the dimensions of the two waveguide structures under study (Si_3N_4 photonic and thin-film plasmonic waveguide) both for Al- based (n_Al=1.42-15.1i) and Cu-based (n_Cu=0.26-9.8i) [9] plasmonic metals.

To have a fair comparison between the different metal materials the same dimensions for the Si_3N_4 photonic and Au-based thin-film plasmonic waveguides have been retained i.e. 360nm×7.5μm for the Si_3N_4 photonic core and 100nm×7μm for the metallic thin-film stripe. It is shown that, for these dimensions at the wavelength of interest (1550nm), the fundamental TM plasmonic mode is supported by both the Al- and the Cu-based thin-film waveguides having an electric field distribution similar to the one of the Au-based structure. The effective indices derived from this 2D eigenmode study were neff_Al=1.312-0.00196i and neff_Cu=1.319-0.00156i corresponding to propagation lengths (L_{SPP}) of 63μm and 79μm for the Al- and the Cu-based structure, respectively.

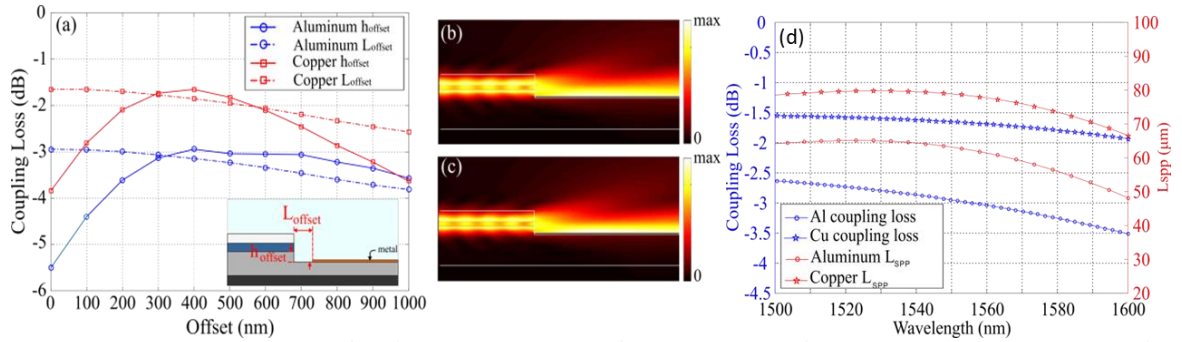


Figure 3. (a) Coupling loss versus h_{offset} for a fixed L_{offset}=0μm and L_{offset} for the optimum h_{offset} for both CMOS metals. (b), (c) Electric field distribution along the light propagation direction for optimal (L_{offset} =0nm, h_{offset} =400nm) Al-based structure and Cu-based structure respectively, (d) Coupling loss (blue curves) and plasmonic propagation length (red curves) versus wavelength for the end-fire configurations.

An end-fire interface configuration as the one depicted in the inset of Figure 3(a) was analysed by means of 3D FDTD numerical simulations adopting Al and Cu as the plasmonic metal material. The effect of both vertical (h_{offset}) and lateral (L_{offset}) offset distances on induced coupling loss of the plasmo-photonic interface has been investigated. Figure 3(a) shows the results of this numerical analysis both for Al and Cu. For both the Al- and the Cu-based structures the variation of coupling loss with respect to h_{offset} exhibits a local minimum around h_{offset}=400nm corresponding to stronger coupling. At the same time, the variation of coupling loss versus L_{offset} exhibits a monotonically decreasing behavior signifying that the minimum achieved coupling loss is obtained for L_{offset}=0 for both CMOS metal materials yet coupling excess loss remains always below 1dB for an L_{offset} up to 1μm. Moreover, the end-fire structure based on Cu seems to have better performance in terms of coupling efficiency when compared to Al. As such, the minimum achieved coupling loss for L_{offset} =0 and h_{offset} =400nm has been calculated at -2.94dB and -1.65dB for Al and Cu, respectively. Figures 3(b) and 3(c) illustrate the electric field distributions along the light propagation direction for both CMOS metals.

The broadband functionality of the CMOS end-fire structures was also investigated in the wavelength region 1500nm-1600nm. As illustrated in Fig. 3(d), small deviations in coupling loss and in L_{SPP} are observed for both metals when the wavelength deviates from 1550nm to 1600nm rendering the CMOS end-fire configurations functionally tolerant in this wavelength range indicating again a 1-dB bandwidth greater than 100nm.

4. CONCLUSIONS

We demonstrate a butt-coupled scheme for efficiently integrating low loss Si_3N_4 waveguides and water-loaded plasmonic stripes with experimentally measured insertion loss of 2.3dB per transition and an Lspp of 75μm at 1550nm. The same design methodology was used to draw a clear path for replacing noble metals in plasmonics with low cost, CMOS-compatible metals such as Al or Cu for mass manufacturing integrated biosensors.

ACKNOWLEDGEMENTS

This work was supported by the European H2020, PLASMOfab project (Co. No. 688166).

REFERENCES

[1] D. K. Gramotnev and S. I. Bozhevolnyi, Plasmonics beyond the diffraction limit, *Nat. Photonics* vol.4 pp. 83–91, 2010.

[2] O. Tsilipakos, et al, Interfacing dielectric-loaded plasmonic and siliconphotonic waveguides: theoretical analysis and experimental demonstration, *IEEE J. Quantum Electron*. vol.48, pp. 678–687, 2012.

[3] C. Delacour et al, Efficient directional coupling between silicon and copper plasmonic nanoslot waveguides: toward metal− oxide−silicon nanophotonics, *Nano Lett*., vol. 10, pp. 2922-2926, 2010.

[4] Xu Sun et al., High-sensitivity liquid refractive-index sensor based on a Mach-Zehnder interferometer with a double-slot hybrid plasmonic waveguide, *Opt. Express*, vol.23, pp.25688-25699, 2015.

[5] B. Y. Fan et al, Refractive index sensor based on hybrid coupler with short-range surface plasmon polariton and dielectric waveguide, *Appl. Phys. Lett*. vol. 100, 111108, 2012.

[6] G. Dabos et al., TM grating coupler on low-loss LPCVD based Si_3N_4 waveguide platform, *Opt. Com.*, vol. 405, pp. 35-38, 2017.

[7] G. Dabos et al., Butt-coupled interface between stoichiometric Si_3N_4 and thin-film plasmonic waveguides, *in Proc. SPIE P.W.*, p.10106-41, San Francisco, USA, 2017.

[8] G. Dabos et al., Plasmonic stripes in aqueous environment co-integrated with Si3N4 photonics, *in IEEE Photonics Journal*, vol. PP, no. 99, pp. 1-1.

[9] J.-C. Weeber, et al, Characterization of CMOS metal based dielectric loaded surface plasmon waveguides at telecom wavelengths, *Opt. Express*, vol. 25, pp. 394–408, 2017.

Surface enhanced Raman spectroscopy via isolated plasmonic nanoantennas integrated on silicon nitride waveguides

Ali Raza[1,2], Javier Losada[3], Stephane Clemmen[1,2], Roel Baets[1,2], Amadeu Griol[3] and Alejandro Martínez[3]
[1] Photonics Research Group, INTEC Department, Ghent University-imec, Technologiepark-Zwijnaarde, 9052 Ghent - Belgium
[2] Center for Nano- and Biophotonics, Ghent University – Belgium
[3] Nanophotonics Technology Center, Universitat Politècnica de València, Camino de Vera s/n, 46022, Valencia - Spain
e-mail: amartinez@ntc.upv.es

ABSTRACT

In this work, we demonstrate experimentally surface enhanced Raman spectroscopy (SERS) via bowtie metallic nanoantennas integrated in silicon nitride waveguides. Two different configurations are considered: nanoantenna on top of the waveguide and nanoantenna inside a gap created in the waveguide. Even though both configurations allow for observing the Raman peaks of 4-nitrothiophenol (NTP), the latter shows higher peaks as a result of a better coupling from the Raman active centres to the fundamental TE waveguide mode. Our results pave the way towards the realization of massive SERS detectors on silicon-compatible photonic chips.

Keywords: silicon photonics; SERS; nanoantennas; hybrid photonic circuits.

1. INTRODUCTION

Recently, there has been a growing interest on the integration of plasmonic nanostructures in silicon waveguides. The main reason is that this hybrid plasmonic-photonic approach [1] reunites the best of two worlds: on one side, the extreme optical properties of plasmonic nanostructures enabling optical functionalities (sensing, modulation, non-linear processing) at low power and in sub-micron foot-prints; on the other side, the possibility of massive fabrication of photonic integrated circuits (PICs) using silicon-compatible technologies.

One of the possible plasmonic structures to be integrated in silicon-based PICs is a metallic nanoantenna supporting a localized surface plasmon resonance (LSPR) either in the near-infrared [2] or in the visible [3]. Silicon and silicon nitride waveguides are chosen respectively for each wavelength regime. In the simples approach, plasmonic nanoantennas are built on top of the dielectric waveguides so that they are excited via coupling between the evanescent part of the waveguide mode (typically, the fundamental TE-like mode) and the nanoantenna LSPR. Although this approach has enabled different interesting experimental results, the weak coupling (~10%) between the waveguide mode and the LSPR makes typically necessary to include a set of nanoantennas for an efficient detection (for instance, in the demonstration of on-chip surface-enhanced Raman scattering (SERS) [4]). Stronger coupling (and as a result, larger amplitude contrast at the waveguide output) can be obtained if the nanoantenna is placed in a subwavelength gap created in the silicon waveguide, so that the nanoantenna is perfectly aligned with the waveguide optical axis [5]. In both cases, the nanoantenna – supporting strongly localized fields in its surroundings - would act as an efficient transducer between the Raman-active centres of a certain substance and the waveguide modes, thus ultimately enabling massive SERS detectors in a silicon-compatible PIC.

In this work, we demonstrate SERS via isolated bow-tie Au nanoantennas integrated in silicon nitride waveguides using the previous approaches and establish a comparison between them from numerical and experimental results.

2. NUMERICAL SIMULATIONS

Figure 1 shows a sketch of the two different configurations to be considered in this work: bow-tie Au nanoantenna on top of a silicon nitride waveguide (CONF1) and inside a subwavelength gap etched in a silicon nitride waveguide (CONF2). Notice that CONF2 requires first etching the waveguides (and the gap), then depositing SiO_2 so that the nanoantenna can be aligned with the waveguide axis and then building the nanoantenna inside the gap [5]. Full 3D numerical simulations using the software *CST Microwave Studio* were used to analyse the performance both devices. Two parameters have been considered in the simulations in order to know about the performance of the system: the β-factor, which is determined by the ratio of the Stokes power coupled into the fundamental TE-like mode of the waveguide; and the intensity enhancement, which is obtained by monitoring the local electric field enhancement in the middle of the nanoantenna gap when the waveguide is fed by the fundamental TE-like waveguide mode.

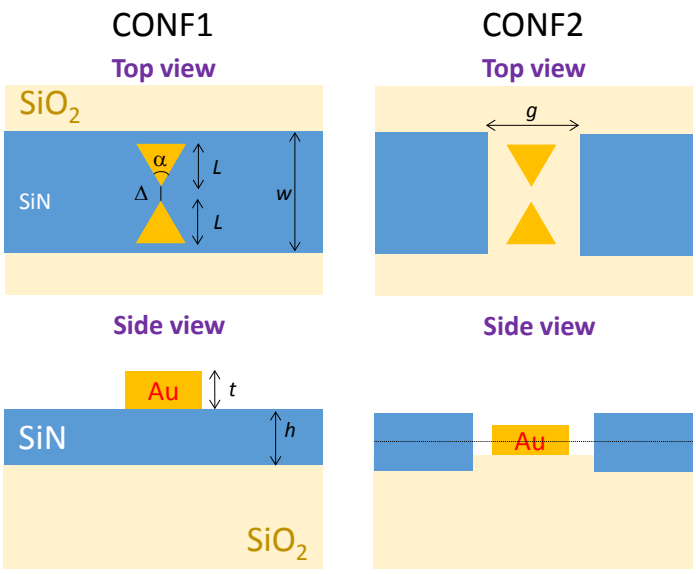


Figure 1. Sketches of the two devices under study in this work: nanoantenna on top of the waveguide (left-hand side) and nanoantenna in a gap created in the waveguide (right-hand side).

We started by simulating CONF1 using the nominal parameters of the system that was used in Ref. [4] to measure SERS in a chain of nanoantennas. These parameters are: α=60º, L=100 nm, Δ=50 nm, w=700 nm, h=220 nm, and t = 30 nm (plus 3 nm of Ti for adhesion). Figure 2 shows on the left the β-factor and intensity enhancement as a function of the wavelength for this structure. Notice that we have observed that the LSPR of the nanoantenna is redshifted with respect to the laser wavelength to be used in the experimental system (λ=785 nm) as well as with respect to the expected Stokes peaks. Then, we simulated CONF2 and optimized the parameters in order to maximize both the β-factor and intensity enhancement. The results are shown in Fig. 2 (right column) for an optimized device with α=64º, L=120 nm, Δ=20 nm, w=700 nm, h=220 nm, g= 250 nm and t = 30 nm (again plus 3 nm of Ti for adhesion). In Fig. 2 we have also included the results for the fabricated structures after extracting the dimensions from scanning electron microscope images (see Fig. 3). Notice that, in general, CONF2 can lead to one order of magnitude larger values of the β-factor and the intensity enhancement as a result of the improved interaction between the waveguide mode and the nanoantenna. However, we want to highlight here that CONF1 could be further optimized to improve its response.

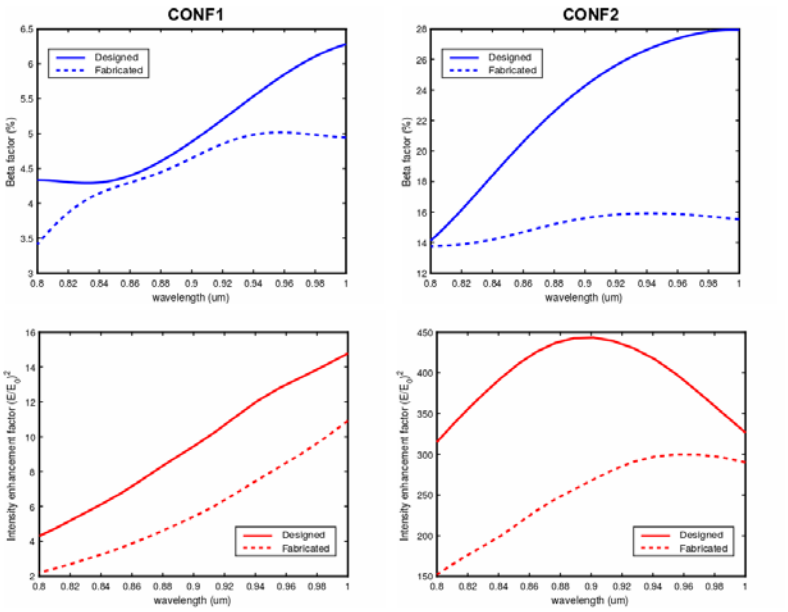


Figure 2. Numerical results obtained with CST Microwave Studio: β-factor (top) and intensity enhancement (bottom) for CONF1 (left) and CONF2 (right). Solid (dashed) lines show the results for the nominal (fabricated) parameters of the devices.

3. EXPERIMENTAL RESULTS

Samples with devices for both CONF and CONF2 were fabricated and teste in the lab. Details about the fabrication methods can be found in Ref.[4] (For CONF1 devices) and in Ref. [5] (for CONF2 devices). Both chips were coated with gold binding layer of 4-nitrothiophenol (NTP) using full night immersion in 1.55 g/L solution of NTP in ethanol. We recorded the Raman spectra in a back reflection configuration using a confocal Raman microscope (WITEC Alpha 300 R+, equipped with 40× 0.6 NA objective, 785 nm wavelength and -70°C cooled ANDOR IDUS CCD camera). Both spectra shown in Fig 3 are recorded using 1mW power and 1 Sec integration time. Raman peaks are detected in both approaches, which shows the potential of the hybrid approach for on-chip SERS. Moreover, the Raman peaks – especially the one at 1,340 cm^{-1} - can be more clearly distinguished in CONF2, in good agreement with the numerical simulations. We believe that larger signal-to-noise ratio in the Raman spectrum can be achieved by further design of the systems.

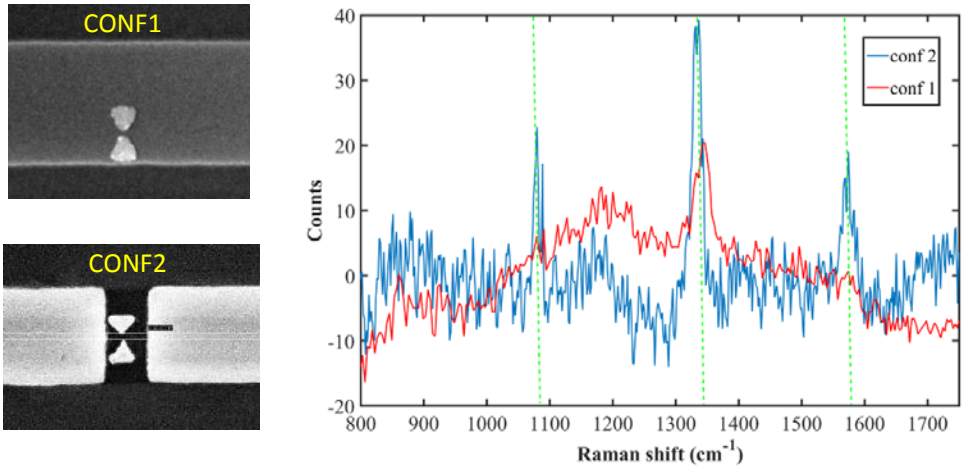


Figure 3. Background subtracted NTP Raman spectrum measured using CONF 1 (red) and CONF2 (blue) Green dotted lines corresponds to the position of three Raman modes of NTP. Scanning electron microscope images of the fabricated samples for both configurations are shown on the left.

4. CONCLUSIONS

We have demonstrated experimentally on-chip SERS in the 700−1000 nm region using isolated bow-tie nanoantennas integrated either on top or inside a gap of a silicon nitride waveguide. Remarkably, the active area of the sensing region is much less than 1 μm^2, which should prospects for miniaturization well beyond what can be achieved using dielectric photonics. This finding shows that integration of plasmonic elements into silicon-based waveguides can pave the way towards hybrid PICs to be used in multiple applications in the classical and quantum domains.

ACKNOWLEDGEMENTS

A. M. acknowledges support from the Spanish Ministry of Economy and Competiveness (MINECO) under grants TEC2014-51902-C2-1-R and TEC2014-61906-EXP. The authors also acknowledge FWO and ERC-InSpectra for their financial support. We also acknowledge Dr. Frederic Peyskens for his useful discussion.

REFERENCES

[1] F. J. Rodriguez-Fortuño, A. Espinosa-Soria, A. Martínez: Exploiting metamaterials, plasmonics and nanoantennas concepts in silicon Photonics, *J. Opt.* vol. 18, 123001, 2016.

[2] I. Alepuz-Benache, C. García-Meca, F. J. Rodríguez-Fortuño, R. Ortuño, M. Lorente-Crespo, A. Griol, A. Martínez: Strong magnetic resonance of coupled aluminum nanodisks on top of a silicon waveguide, *Proc. SPIE* 8424, 84242J, 2012.

[3] F. Peyskens, A. Z. Subramanian, P. Neutens, A. Dhakal, P. Van Dorpe, N. Le Thomas, R. Baets: Bright and dark plasmon resonances of nanoplasmonic antennas evanescently coupled with a silicon nitride waveguide, *Opt. Express* vol. 23, no. 3, pp. 3088–3101, 2015.

[4] F. Peyskens, A. Dhakal, P. Van Dorpe, N. Le Thomas, R. Baets: Surface enhanced Raman spectroscopy using a single mode nanophotonic-plasmonic platform, *ACS Photon.* vol. 3, no. 1, pp. 102–108, 2016.

[5] A. Espinosa-Soria, A. Griol, A. Martínez, Experimental measurement of plasmonic nanostructures embedded in silicon waveguide gaps, *Opt. Express* vol. 24, no. 9592-9601, 2016.

Subwavelength metamaterials structures for applications in silicon photonics

(Invited paper)

J. H. Schmid,[1] P. Cheben,[1] D. Melati,[1] D.-X. Xu,[1] S. Janz,[1] J. Lapointe,[1] S. Wang,[1] M. Vachon,[1] R. Halir,[2] A. Ortega-Moñux,[2] G. Wangüemert-Pérez,[2] I. Molina-Fernández,[2] A. Sánchez-Postigo,[2] J.M. Luque-Gonzalez,[2] J.D. Sarmiento-Merenguel,[2] Jiří Čtyroký[3]

[1] Advanced Electronics and Photonics Research Centre, National Research Council Canada,
1200 Montreal Road, Ottawa, Ontario, Canada
e-mail: jens.schmid@nrc-cnrc.gc.ca
[2] Universidad de Málaga, Dpto. de Ingeniería Comunicaciones, ETSI Telecomunicación,
Campus de Teatinos s/n, 29071 Málaga, Spain
[3] Institute of Photonics and Electronics, CAS,
Chaberská 57, 182 51 Prague, Czech Republic

ABSTRACT

Subwavelength engineering in silicon photonic integrated circuits is a powerful design tool that allows one to adjust the waveguide core effective refractive index by periodically patterning the silicon waveguide layer at the subwavelength scale. This creates a new degree of freedom in photonic circuit design. In recent years, the subwavelength metamaterial concept has been demonstrated and applied to many silicon photonic devices such as fiber-chip couplers, waveguide crossings, microspectrometers, ultra-fast optical switches, athermal waveguides, evanescent field sensors, polarization rotators and colorless interference couplers. Here we report our advances in the development of subwavelength engineered dielectric metamaterial structures for silicon photonic devices with a special emphasis on the practical performance of fiber-chip coupling structures and the possibility to affect the spectral bandwidth of silicon photonic devices by subwavelength engineering. In particular, we will present our results in developing highly efficient and broadband fiber-chip and laser-chip couplers for silicon photonic wire waveguides using subwavelength engineered structures, a broadband prism assisted grating coupler, an ultra-broadband multi-mode interference (MMI) coupler device and narrow-band Bragg spectral filters in subwavelength grating (SWG) waveguides.

Keywords: Silicon photonics, subwavelength structures, metamaterials, Bragg gratings

1. INTRODUCTION

In recent years, the research field of subwavelength photonics has seen tremendous progress, particularly in nanostructured engineered materials: metamaterials, metallic and dielectric subwavelength structures and subwavelength engineered waveguides. The novel optical properties found in these structures, along with the capability, through advanced fabrication techniques, to control their optical responses with unprecedented accuracy, has opened new prospects for controlling and manipulating light in planar waveguide circuits at the subwavelength scale. Since the first demonstrations of an optical waveguide with a periodic subwavelength grating metamaterial core [1-3], metamaterial SWG waveguides have attracted a strong research interest in academia and industry because of their unique potential to control light propagation in planar waveguides [4] and subwavelength engineered structures are likely to become key building blocks for the next generation of integrated photonic circuits.

2. FIBER-CHIP COUPLING

Efficient input and output coupling interfaces between silicon photonic chip and optical fiber or lasers are a fundamental prerequisite for successful implementations of such photonic chips for processing, modulating and detecting light. Here we demonstrate that tapered SWG edge couplers, as shown in the SEM micrograph in Fig. 1, can outperform inverse taper couplers in efficiency and polarization dependent loss. Specifically, as we have

previously reported in [5], by optimizing the coupler design, we experimentally demonstrated an SWG coupler with a loss of 0.4 dB and negligible polarization dependence fabricated on a silicon-on-insulator chip with a standard 220 nm silicon thickness and silicon dioxide cladding. In this work we used lensed optical fiber tips with a mode field diameter of 3 μm.

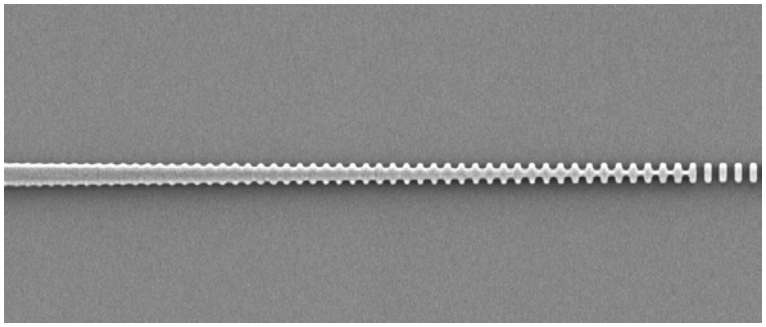


Figure 1. SEM micrograph of SWG fiber-chip edge coupling structure.

It is highly desirable to increase the mode size at the interface between SWG coupling structure and the optical fiber to improve alignment tolerance of the fiber to the chip. However, for large mode sizes, optical loss of the waveguide mode through the buried oxide (BOX) layer to the substrate becomes a serious limitation to the coupling efficiency. Minimizing the SWG taper length helps alleviate this source of optical loss. In Fig. 2 we show an example eigenmode expansion propagation calculation of the effect of substrate loss as a function of length of an optimized taper shape for a facet mode size diameter of 6 μm. It can be seen that even for this relatively large mode size and standard BOX thickness of 2 μm coupling efficiencies >90% are feasible.

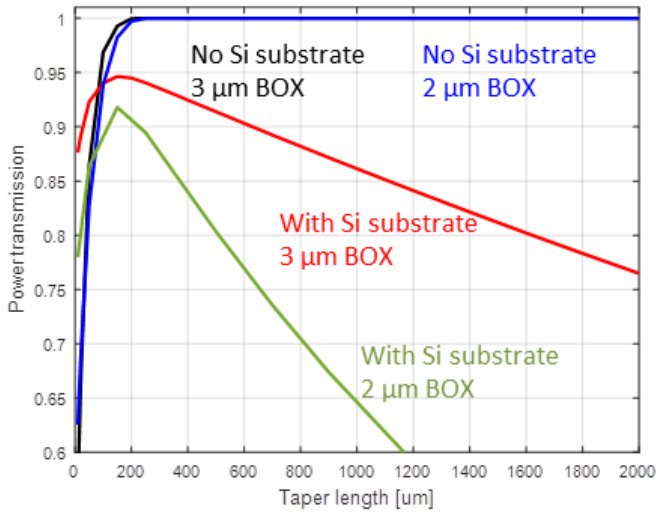


Figure 2. Eigenmode expansion propagation calculation of power transmission through an optimized SWG taper structure as a function of length in the presence of substrate leakage losses for a facet mode size diameter of 6 μm.

3. NARROWBAND BRAGG FILTERS

We have recently presented the first systematic theoretical and numerical study of narrowband reflection and transmission spectral filters in silicon-on-insulator SWG waveguides comprising Bragg gratings with lateral loading segments [6]. Such narrowband reflection filters can potentially find applications as components providing wavelength selective feedback for a narrow linewidth hybrid III-V-silicon laser system or as sensing elements. The combination of waveguide core refractive index engineering and evanescent coupling of the waveguide mode with the Bragg grating loading segments makes it possible to design long and weakly coupled grating structures as required for narrowband operation, which is otherwise hard to achieve in the silicon-on-insulator high-index contrast material system. The results of the theoretical study indicated a narrow Bragg

reflection bandwidth of 50 pm is attainable for realistic grating parameters with critical dimensions larger than 100 nm. An example of a fabricated structure is shown in Fig. 3. In optical transmission measurements we have found Bragg peaks as narrow as 50 pm with an extinction ratio of 10 dB or 250 pm with an extinction ratio of 30 dB.

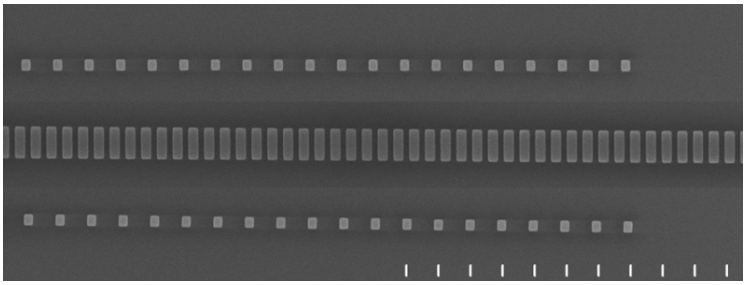


Figure 3. SEM micrograph of a fabricated SWG Bragg grating structure with lateral loading segments.

4. CONCLUSIONS

Subwavelength engineering provides a new degree of freedom in the design of silicon photonic components. We have provided examples of the application of this powerful technique in two areas that are of particular practical importance, namely fiber-chip coupling and bandwidth engineering of components. We presented an optimized fiber-chip coupler with broadband and polarization-independent coupling with high efficiency and discussed design strategies for increasing the mode size while minimizing substrate leakage loss. We also showed the design of narrowband Bragg filters including first experimental results demonstrating a 3-dB reflection bandwidth of 50 pm.

REFERENCES

[1] P. Cheben, *et al.*, Subwavelength waveguide grating for mode conversion and light coupling in integrated optics, *Opt. Express* **14,** 4695–4702 (2006).

[2] J. H. Schmid, *et al.* Gradient-index antireflective subwavelength structures for planar waveguide facets. *Opt. Lett.* **32,** 1794–1796 (2007).

[3] P. Cheben, *et al.*, Refractive index engineering with subwavelength gratings for efficient microphotonic couplers and planar waveguide multiplexers, *Opt. Lett.* **35,** 2526–2528 (2010).

[4] R. Halir, *et al.*, Waveguide sub-wavelength structures: a review of principles and applications, *Laser Photonics Rev.* **9**, 25–49 (2015).

[5] P. Cheben, *et al.* Broadband polarization independent nanophotonic coupler for silicon waveguides with ultra-high efficiency, *Opt. Express* **23,** 22553–22563 (2015).

[6] J. Čtyroký, *et al.*, Design of narrowband Bragg spectral filters in subwavelength grating metamaterial waveguides, *Opt. Express* **26,** 171-194 (2018).

High performance and small footprint spot size converters based on SWG metamaterial lenses

(Student Paper)

José Manuel Luque-González[1,*], Alejandro Ortega-Moñux[1], Robert Halir[1], Iñigo Molina-Fernández[1], J. Gonzalo Wangüemert-Pérez[1], Jens H. Schmid[2] and Pavel Cheben[2]

[1] *Universidad de Málaga, Dept. de Ingeniería de Comunicaciones, ETSI Telecomunicación, Campus de Teatinos s/n, 29071 Málaga, España*

[2] *National Research Council Canada, 1200 Montreal Road, Bldg. M50, Ottawa K1A 0R6, Canada*

**Corresponding author: jmlg@ic.uma.es*

ABSTRACT

Spot size converters with high expansion ratio are required in a variety of situations. This is the case of non-focusing Silicon on Insulator (SOI) fiber-to-chip grating couplers, which typically require long adiabatic tapers (L_{taper} >100μm) from the narrow single-mode waveguides ($W_{Si\text{-}wire}$ ~ 500nm) to the wide grating region ($W_{grating}$ ~ 15μm). Here, we explore the potential of subwavelength grating (SWG) dielectric metamaterials to implement integrated GRaded INdex (GRIN) lenses to expand the mode field. Our designs achieve the desired Beam Expansion (BE) with insertion losses below 1dB over a distance of only L_{BE} ~ 17μm.

Keywords: Subwavelength grating, Graded Index, Beam expander, Silicon-On-Insulator, Grating coupler.

1. INTRODUCTION

Silicon-on-insulator is emerging as a promising fabrication platform for integrated optical systems, as it enables high-volume fabrication, with existing CMOS infrastructure, and highly compact devices, owing to the high index contrast between the core and cladding materials ($n_{Si} = 3.476$ and $n_{SiO_2} = 1.444$). These materials set the dimensions of typical SOI single-mode waveguides to ~ $500 \times 220\text{nm}^2$ at telecom wavelengths. However, these small dimensions make direct coupling to standard optical fibers, with a mode field diameter of 10.4μm, very challenging, which is why grating couplers are widely used for low-loss coupling [1]. Since grating couplers are about 30 times wider than single mode waveguides ($W_{grating}$ ~ 15μm vs. $W_{Si\text{-}wire}$ ~ 500nm), some kind of beam expansion between them is required. Adiabatic linear tapers are conventionally used for this purpose but, to keep losses low, a length of 100-200 μm is required [2] which makes this a bulky solution. Other solutions such as adiabatic parabolic tapers [2] only achieve a slight reduction of the device length. Recently proposed non-adiabatic tapers [3] achieve a substantial length saving at the expense of reducing the bandwidth.

In this work we present two different realizations of GRaded INdex (GRIN) lens beam expanders, using SubWavelength Gratings (SWG) [4,5]. As illustrated in Fig. 1 the parabolic GRIN lens is implemented with a subwavelength structure in the transversal x-direction in Design I (Fig. 1.a) and in the longitudinal z-direction in Design II (Fig. 1.b). In both cases, we have kept the pitch Λ constant and we have designed the duty cycle (DC) to achieve the desired parabolic profile $n_{eq}(x) \sim n_0(1-\alpha\, x^2)$. Design I was originally proposed in [4] for a different application, but it has been redesigned here to improve its performance. With respect to Design II, to the authors´ knowledge this is the first time that an integrated beam expander has been implemented using this approach (i.e. using a z-periodic SWG based GRIN lens). We have demonstrated by rigorous 3D full-vectorial FDTD simulations that both designs achieve less than 1dB coupling losses between a silicon wire and a conventional grating coupler, with lengths < 20μm, for the TE polarization. This is much shorter than the conventional solution based on linear adiabatic tapers, which requires lengths greater than 100μm to obtain the same performance.

2. DESIGN OF THE SWG BASED GRIN LENS

First, the lens width is set to the desired grating width, i.e. $W_{GRIN} \sim W_{grating} \sim 15\mu m$. Then, as it was previously stated, we implement the parabolic refractive index profile of the lenses controlling the duty cycle of the periodic structure. This can be done by mapping the desired parabolic refractive index profile $n_{eq}(x)$ into a duty cycle profile DC(x), benefiting from the relation between the duty cycle and the equivalent refractive index n_{eq} (DC) of the SWG structure. This can be seen in Figure 2.a) which represents the duty cycle in Design I as a function of the transverse position x (x = 0 is the centre of the lens). The nearly parabolic shape of this curve is due to the almost linear dependence of the equivalent refractive index of the SWG structure with the duty cycle, as shown in the figure 2.a) inset. It must be noticed that, as the pitch has been fixed to Λ_x = 400nm and the duty cycles used to synthetize the parabolic refractive index range from $DC_{x,min}$ = 30% to $DC_{x,max}$ = 70%, the minimum feature size (MFS) for this design is ~ 120 nm.

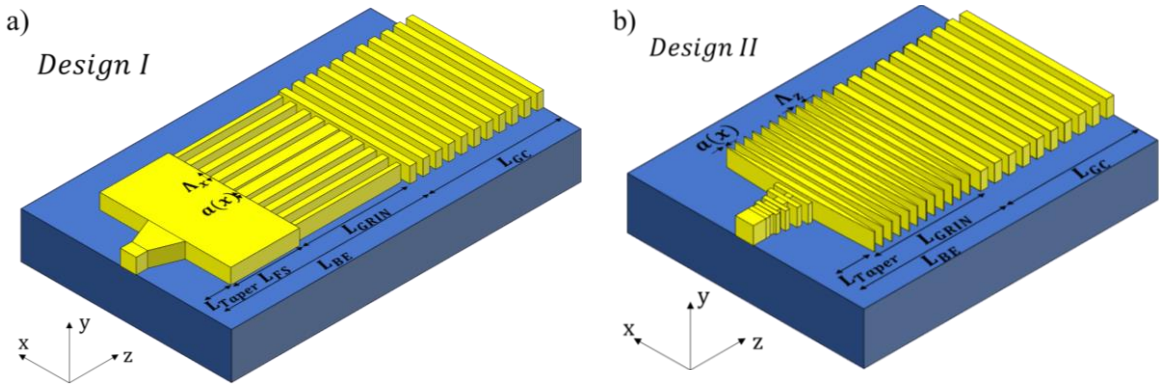


Figure 1: Schematic drawing of the beam expanders based on SWG GRIN lenses proposed in this work. For the sake of clarity, the figure includes not only the beam expander but also the input access waveguide and taper and the output chip to fiber grating coupler. The equivalent parabolic index of the lenses $n_{eq}(x)$ is implemented in both cases by maintaining the pitch constant and optimizing the duty cycle. a) Design I is composed of an input adaptation taper, a free-space propagation zone, a quasi-periodic in x SWG lens working as a collimator, and the grating coupler. The SWG is arranged along the x-direction, so the duty cycle is defined as $DC_x(x) = a(x) / \Lambda_x$ b) Design II comprises an adaptation taper, a z-periodic SWG lens and the grating coupler. The SWG is arranged along the z-direction, so the duty cycle is defined as $DC_z(x) = a(x) / \Lambda_z$.

As proposed in [4], the total length of the beam expander can be reduced if light first diffracts in a free-space propagation zone (i.e. a slab waveguide) before being collimated by the GRIN lens (see Fig, 1.a). Short adiabatic taper has been also included at the input to optimize the excitation of the free-space zone. Figure 3.a) shows the field propagation through the beam expander with Design I, which exhibits insertion losses below 1dB and a total length of L_{BE}~17µm.

The next design of the beam expander is based on a z-periodic SWG parabolic lens (Design II). The function $DC_z(x)$ that defines the lens has been drawn in Fig 2.b). We have chosen a period Λ_z = 220nm (much smaller than in the previous case) to avoid Bragg reflections within all the wavelength operation range of the device [5]. Once again, the relation between the synthetized effective index and the duty cycle is almost linear (see inset of Fig. 2.b)), so the function $DC_z(x)$ is roughly parabolic. The MFS of this design is ~100nm in the centre of the lens and larger than 80nm for |x| <5µm, where most of the optical intensity is confined. The total length of the beam expander (including a short adaptation taper at the input) is L_{BE} ~17µm, whereas the insertion losses are again below 1dB. Figure 3.b) represents the simulated field propagation through the designed device.

These designs are therefore much shorter than linear adiabatic tapers L_{taper} >100µm (see Fig. 3c) typically used in grating designs.

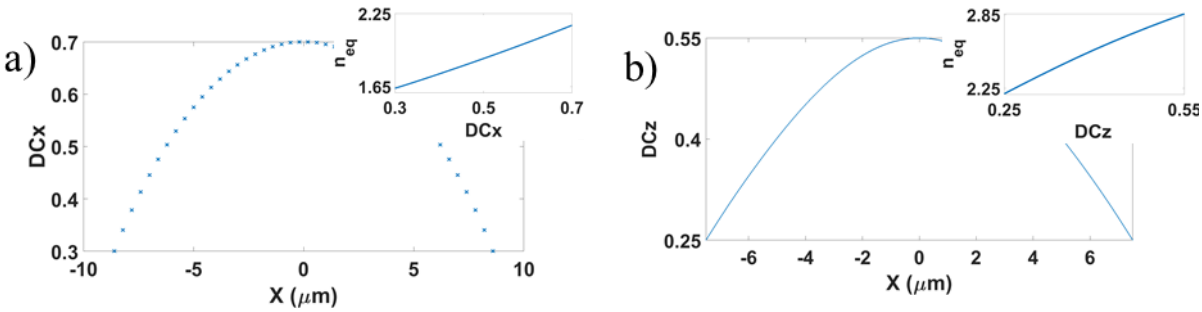


Figure 2: Duty cycle as a function of the transverse x-position within the lenses (x = 0 is the centre of the lens). a) Design I - $DC_x(x)$, b) Design II- $DC_z(x)$. Insets: Equivalent index of the SWG metamaterial as a function of the duty cycle ($n_{eq}(DC_x)$ and $n_{eq}(DC_z)$ respectively). It should be noticed that in both cases $n_{eq}(DC)$ are nearly linear, so the duty cycle shapes are parabolic.

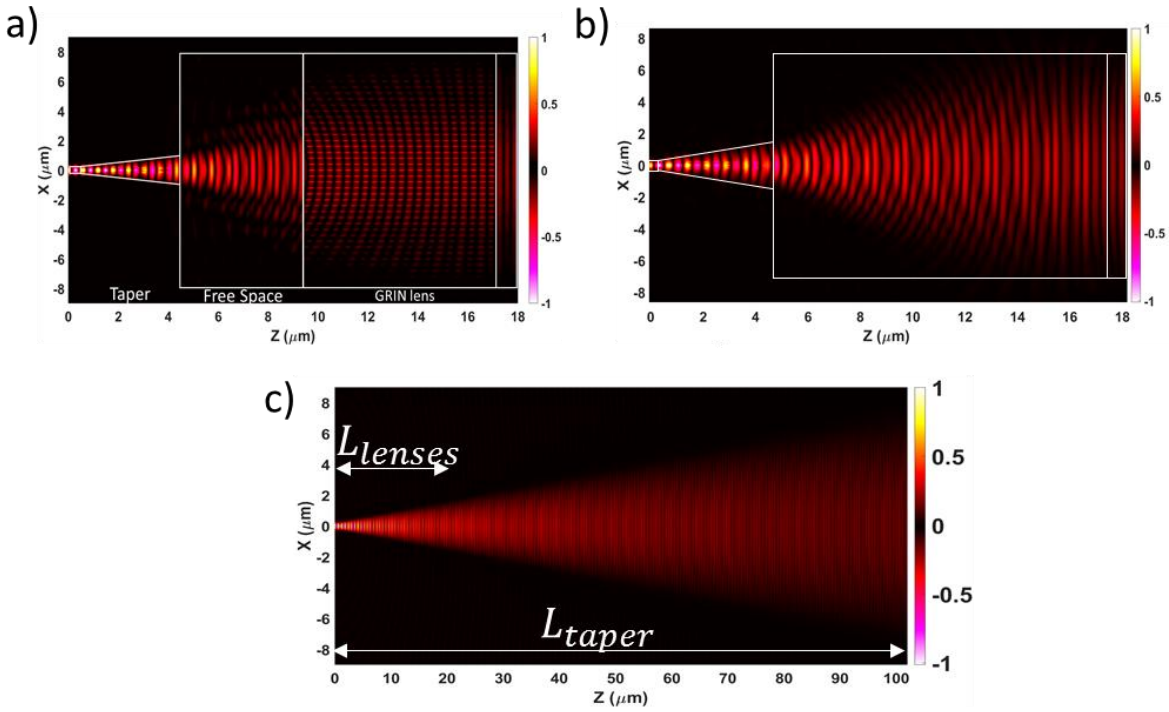


Figure 3: Electric field (real part) propagation through the two beam expanders proposed in this work. a) Design I, based on a quasi-x-periodic SWG GRIN lens working as a collimator. b) Design II, based on a z-periodic SWG GRIN lens. c) Electric field propagation through an adiabatic linear taper with the same beam expansion and similar losses.

3. CONCLUSIONS

In this work we have explored the potential of subwavelength grating dielectric metamaterials to implement GRIN integrated devices in a conventional SOI platform. We have presented two different SWG-based parabolic GRIN lenses working as beam expanders in the plane of the chip. Our designs achieve a huge spot-size lateral expansion (~30×) with a very reduced length (L_{BE} ~ 17µm) maintaining the insertions losses below 1dB. These results pave the way to the development of more involved integrated GRIN metamaterials based on SWG periodic structures.

ACKNOWLEDGEMENTS

We acknowledge funding from the Ministerio de Economía y Competitividad, Programa Estatal de Investigación, Desarrollo e Innovación Orientada a los Retos de la Sociedad (cofinanciado FEDER), (TEC2016-80718-R); Universidad de Málaga. Ministerio de Educación, Cultura y Deporte (MECD) (FPU16/06121);

REFERENCES

[1] Tamir, T., & Peng, S. T. (1977). Analysis and design of grating couplers. *Applied Physics A: Materials Science & Processing*, *14*(3), 235-254.

[2] Fu, Y., Ye, T., Tang, W., & Chu, T. (2014). Efficient adiabatic silicon-on-insulator waveguide taper. *Photonics Research*, *2*(3), A41-A44.

[3] Zou, J., Yu, Y., Ye, M., Liu, L., Deng, S., Xu, X., & Zhang, X. (2014). Short and efficient mode-size converter designed by segmented-stepwise method. *Optics letters*, *39*(21), 6273-6276.

[4] Levy, U., Abashin, M., Ikeda, K., Krishnamoorthy, A., Cunningham, J., & Fainman, Y. (2007). Inhomogenous dielectric metamaterials with space-variant polarizability. *Physical review letters*, *98*(24), 243901.

[5] Halir, R. *et al* (2015). Waveguide subwavelength structures: a review of principles and applications. *Laser & Photonics Reviews*, *9*(1), 25-49.

Coherent control of the absorption and scattering of an isolated plasmonic nanoantenna integrated in a silicon waveguide

Alba Espinosa-Soria[1], Amadeu Griol[1] and Alejandro Martínez[1]
[1] *Nanophotonics Technology Center, Universitat Politècnica de València, Camino de Vera s/n, 46022, Valencia - Spain*
e-mail: amartinez@nrtc.upv.es

ABSTRACT

In this paper, we use an on-chip approach to experimentally demonstrate that the absorption and scattering of a subwavelength plasmonic nanoantenna can be manipulated by using coherent illumination. To do so, we integrate the nanoantenna in a gap separating two silicon photonic waveguides so that it can be illuminated from its both sides by two coherent beams with controlled amplitude and phase. We show experimentally that scattering can be modulated by about one order of magnitude, whilst higher values could be obtained by further optimization. This finding paves the way towards coherent all-optical data processing in subwavelength devices integrated on silicon-compatible chips.

Keywords: silicon photonics; coherent perfect absorption; nanoantennas; hybrid photonic circuits.

1. INTRODUCTION

Interference between counter-propagating monochromatic waves incident upon an absorbing medium can result in either enhanced or suppressed absorption and scattering, ultimately enabling the regime known as coherent perfect absorption [1]-[2]. This provides a very suitable way towards all-optical processing without nonlinearities, which therefore may be performed at low levels of optical power and ultra-high speed [3]. Although most demonstrations of this phenomenon have made use of thin absorbing layers formed by arrays of plasmonic nanoantennas operated under normal free-space excitation, the principles of coherent manipulation of absorption and scattering are also applicable to individual nanoantennas, which could result in all-optical processing in subwavelength scales. However, coherent illumination of individual nanoantennas from free-space is highly challenging, which has prevented the demonstration of the coherent manipulation of single subwavelength entities. Here, we demonstrate experimentally the coherent control of an isolated plasmonic nanoantenna with foot-print much smaller than the wavelength. In particular, we show how the scattering and absorption of the nanoantenna, whose response is dominated by a dipolar electric resonance, are deeply modulated when the phase difference between the feeding counter-propagating signals is changed.

2. DESCRIPTION OF THE STRUCTURE

Figure 1(a) sketches the nanophotonic structure we address in this work: a strip nanoantenna is built on a subwavelength gap separating two silicon waveguides [4], which provide the guided paths for counter-directional illumination with controlled phase. We consider that the nanoantenna (centred at z=0) is perfectly aligned with the waveguide axis to maximize optical interaction. Such interaction will mainly consist of scattered radiation (part of which will be guided and directed towards the output ports, *s*, and the rest will be scattered out of the system, *s'*) and absorption (*a*). The extinction of the system will therefore consist of two terms: *s'* and *a*. If the input fields have the same amplitude and the phase difference between them is $\Delta\phi = 0$ at z=0 (Fig. 1(b)) there will be constructive interference at the position of the nanoantenna (green curve in Fig. 1(e)) and both scattering (*s* and *s'*) and absorption (*a*) will be maximized. Indeed, under the proper conditions, such output fields can be completely suppressed, reaching a regime of coherent perfect extinction, for which the signals at the two output ports of the system vanish. If the amplitude is the same but $\Delta\phi=\pi$ at z=0 (Fig. 1(c)), there is destructive interference at the position of the nanostructure, and the local fields are zero (blue curve in Fig. 1(e)). As a result, both absorption and scattering will be extremely minimized. Assuming a nanostructure with very small dimensions we can reach the condition of coherent perfect transmission since the guided fields do not "see" the nanostructure. Finally, if one of the inputs (B) is eliminated (Fig. 1(d)) we get single-beam illumination. In this case, the square of the electric field at the particle position is the average of the previous cases, so we will have both scattering and absorption. Backward scattering will produce guided waves towards the input port and forward scattering will interfere with part of the incoming guided field (the portion that is not absorbed or scattered) to produce a certain output signal at port B. In general, it can be seen that not only the scattering and the absorption of the nanoantenna can be modulated by controlling the phase difference, but also the transmission and reflection along the waveguides, which could be employed for on-chip coherent data processing.

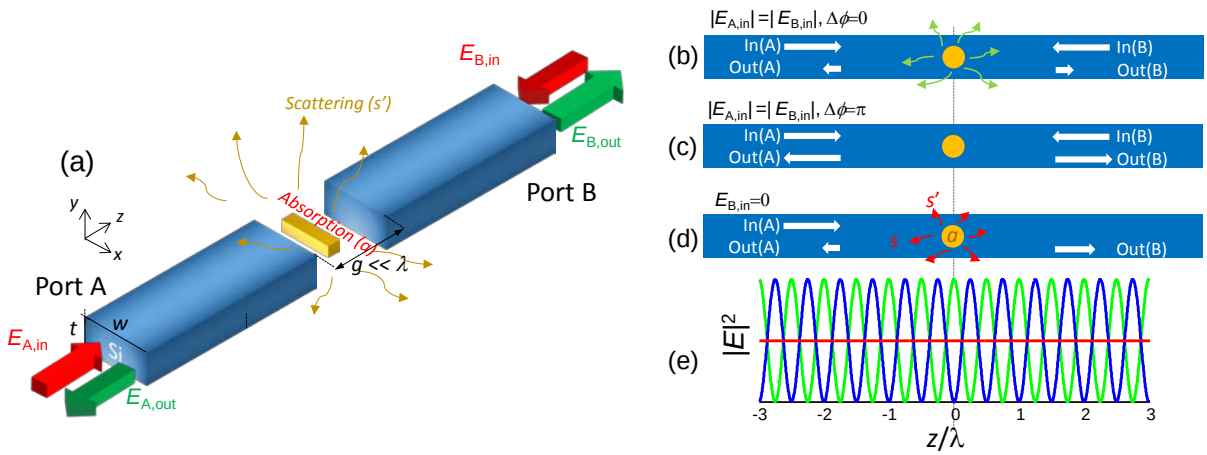


Figure 1. Coherent manipulation of a plasmonic nanoantenna. (a) In our practical implementation, the plasmonic nanoantenna is inserted in a subwavelength gap created in a dielectric (silicon) waveguide. (b)–(d) Schematic representation of a waveguide (blue) with two ports (A and B) having a metallic nanoantenna (orange circle) positioned in its optical axis and at z=0. Scattering, absorption and transmission will depend on the amplitude and phase relation between counter-propagating guided waves, leading to enhanced scattering/absorption and reduced transmission for constructive interference at z=0 (b), reduced scattering/absorption and enhanced transmission for destructive interference at z=0 (c) and standard single-beam scattering, absorption and transmission when one of the input signals (B) is switched off. (e) $|E|^2$ along the waveguide – without the nanoantenna - for the three cases: green (b), blue (c) and red curve (d).

3. EXPERIMENTAL RESULTS

We demonstrate the proposed system using a silicon photonic circuit as shown in Fig. 2. In brief, light enters the system via an integrated silicon waveguide, which is the spilt up in two paths that will feed the plasmonic nanoantenna (inset in Fig. 2) in opposite directions. The nanoantenna is designed to support an electric-dipole plasmonic resonance at telecom wavelengths [4]. There is a path length difference ΔL between both feeding waveguides so, provided that the effective index of the TE-like waveguide mode is n the phase difference between both input ports can be simply obtained as $\varphi = 2\pi n \Delta L/\lambda$. The scattered intensity will be proportional to $2\cos^2(\varphi/2)$. In particular, the fabricated chip had $\Delta L \approx 20$ μm. This way, we implement a wavelength-dependent phase shift without modifying the amplitudes of the paths. Notice that such a phase shift can also be obtained by other means, for instance, by inserting a phase-modulator – which in silicon can operate a speeds of tens of GHz - in one of the waveguides. This approach would allow to dynamically change the phase shift at a single wavelength.

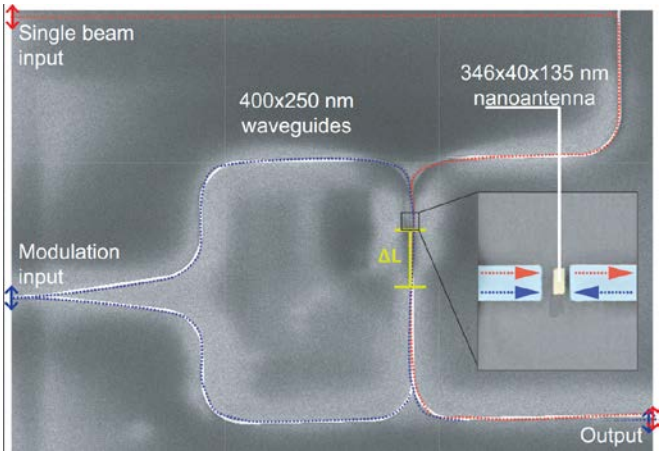


Figure 2. Scanning electron images of the silicon photonic circuit to demonstrate coherent control of isolated nanoantenna. Inset: detail of the nanoantenna inserted in the gap. Blue (red) lines indicate the paths followed by the guided light for dual-beam (single-beam) illumination). The chip was fabricated using silicon-compatible nanofabrication tools (details can be found in [4]).

The circuit was experimentally characterized at telecom wavelengths using a set-up similar to that described in [5]. Therefore, we were able to measure both on-chip transmission as well as normal scattering in a single shot. Moreover, by careful selection of the input and output ports, the chip shown in Fig. 2(a) allows for measurement of both transmission and normal scattering for one-way as well as two-way excitation of the nanoantenna. Experimental results for both transmission and scattering are shown in Figs. 3(a) and 3(b) respectively. Notice that absorption (a) is not directly measurable in our system, but it can be considered as proportional to scattering (s'),

as it is the case in plasmonic nanostructures whose response is dominated by an electric dipole resonance, so its spectrum should look similar to that depicted in Fig. 3(b). In transmission (Fig. 3(a)), we see a modulation of the response for dual-beam illumination of ~3 dB in a broad bandwidth. Larger contrast could be obtained by an optimized design of the system, so all-optical coherent data processing with this approach seems feasible. The peaks observed in the single-beam transmission can be attributed to the creation of undesired recirculation paths in the circuit (see Fig. 2) but we do not observed them in our measurements in Ref. [4]. In scattering measurements (Fig. 3(b)) we observe that the dual-beam response shows an intensity modulation in comparison with the single-beam response (showing a peak at ~1.5 μm, which correspond to the nanoantenna plasmonic resonance). Such modulation, with about one order of magnitude in depth, is attributed to constructive (maxima) and destructive (minima) interference of the counter-propagating beams at the nanoantenna position. In general, the measured spectrum agrees well with the expected $2\cos^2(\varphi/2)$ response. A similar modulation should be expected for the nanoantenna absorption.

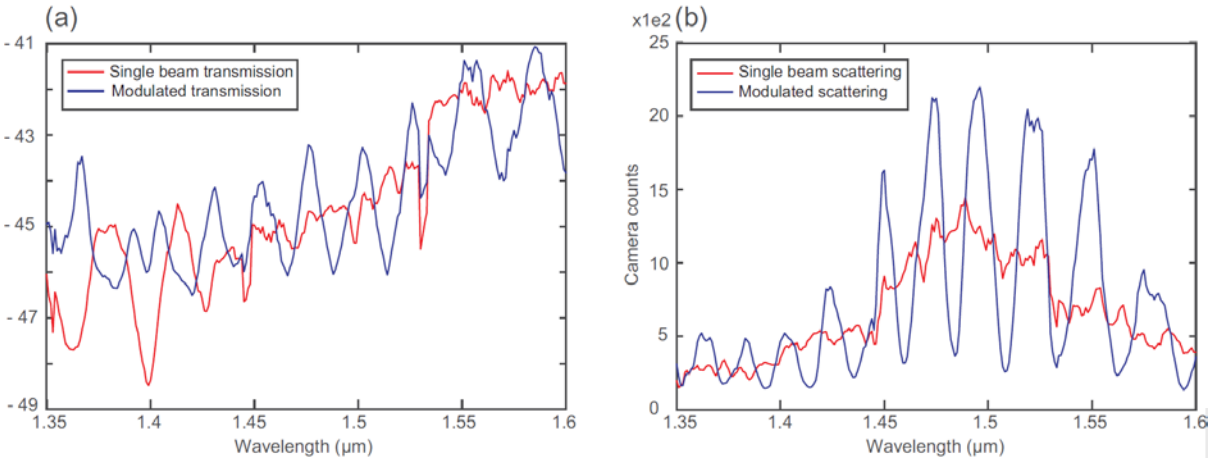


Figure 3. Experimental results. (a) Transmission and (b) normal scattering measured spectra for the single-beam (red) and dual-beam (blue) transmission paths. Waveguides are fed by using the fundamental TE mode of the silicon waveguide.

4. CONCLUSIONS

In conclusion, we have demonstrated coherent control of the scattering and absorption of a single plasmonic nanoantenna integrated in a silicon chip at telecom wavelengths. Using standard silicon circuitry, we are able to illuminate the nanoantenna using counter-propagation light beams whose phase is wavelength-dependent as a consequence of the waveguide dispersion. We show that the scattering – and, as a result, also the absorption - of the nanoantenna can be either enhanced or suppressed depending on the phase shift between counter-directional beams. Moreover, port-to-port transmission is also modulated depending on the phase shift. A modulation contrast of about one order of magnitude (~10 dB) in scattering and ~3 dB in transmission is observed over a 15 nm bandwidth, as a result of the broad resonance of the employed nanoantenna. Being our system suitable for dense integration of multiple nanoantennas on a chip, this approach could lead to massive ultrafast coherent all-optical signal processing in silicon.

ACKNOWLEDGEMENTS

A. M. acknowledges support from the Spanish Ministry of Economy and Competiveness (MINECO) under grants TEC2014-51902-C2-1-R and TEC2014-61906-EXP.

REFERENCES

[1] W. Wan , Y. Chong , L. Ge , H. Noh , A. D. Stone , H. Cao: Time-Reversed Lasing and Interferometric Control of Absorption, *Science* vol. 331, 889-891, 2011.

[2] D. G. Baranov, A. Krasnok, T. Shegai, A. Alù, Y. Chong: Coherent perfect absorbers: linear control of light with light, *Nature Rev. Mat.* vol. 2, 17064, 2017.

[3] X. Fang, K. F. MacDonald and N. I. Zheludev, Controlling light with light using coherent metadevices: all-optical transistor, summator and invertor, Light Sci. Appl. 4, e292 (2015).

[4] A. Espinosa-Soria, A. Griol, A. Martínez: Experimental measurement of plasmonic nanostructures embedded in silicon waveguide gaps, *Opt. Express* vol. 24, pp. 9592-9601, 2016.

[5] A. Espinosa-Soria, F. J. Rodríguez-Fortuño, A. Griol, A. Martínez: On-chip optimal Stokes nanopolarimetry based on spin-orbit interaction of light, *Nano Lett.* vol. 17, pp. 3139-3144, 2017.

Plasmonics for integrated optics

Invited paper

Pierre Berini[1,2,3]
[1] *School of Electrical Engineering and Computer Science, University of Ottawa, 25 Templeton St., Ottawa, Ontario K1N 6N5, Canada, e-mail: berini@eecs.uottawa.ca*
[2] *Department of Physics, University of Ottawa, Ottawa, Ontario K1N 6N5, Canada*
[3] *Centre for Research in Photonics at the University of Ottawa, Ottawa, Ontario K1N 6N5, Canada*

ABSTRACT

We review work on integrated optical components and devices operating with surface plasmons. The properties of long-range surface plasmon waveguides are discussed, followed by their application to elements such as S-bends, Y-junction splitters, couplers and Mach-Zehnder interferometers. Such passive elements are then used to underpin advanced active devices, such as surface-plasmon amplifiers, lasers and biosensors.

Keywords: Surface plasmon waveguides, passive components, active devices, lasers, amplifiers, biosensors.

1. INTRODUCTION

Long-range surface plasmon polaritons (LRSPPs) are transverse magnetic (TM) surface waves that propagate on a thin metal slab or stripe cladded by dielectrics of similar refractive index [1]. LRSPPs can propagate up to centimeters in the infrared, which is significantly further than the propagation length of single-interface SPPs. The increased propagation length of LRSPPs is due to reduced confinement to the metal, but the increased length enables a long optical interaction between these surface waves and the surrounding claddings. LRSPPs propagating along thin narrow metal stripes are of particular interest because they are confined in the plane transverse to the direction of propagation, thereby enabling integrated optical elements as shown in Fig. 1.

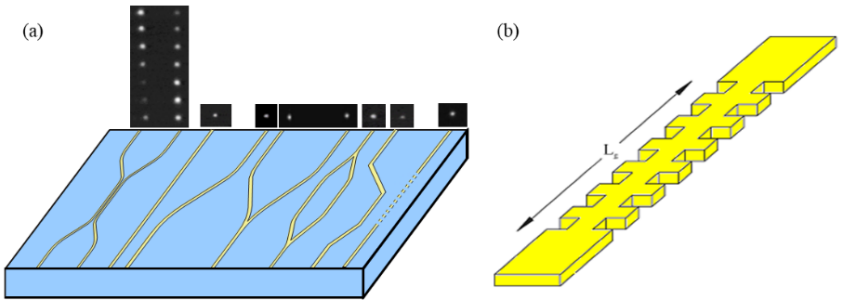


Figure 1. (a) Sketch of integrated optical elements implemented with LRSPP waveguides along with a mosaic of measured mode outputs. Left to right: edge couplers, straight segment, S-bend segment, Y-junction splitter, Mach-Zehnder interferometer (MZI), sharp bends, waveguide Bragg grating [1]. (b) Sketch of a waveguide Bragg grating implemented as a step-in-width metal stripe structure.

Integrated optical elements based on LRSPPs have compelling performance characteristics and are easy to fabricate. Many of the required elements have been fabricated and demonstrated experimentally, and are used in applications. Fig. 1(a) summarises some of the elements of interest, including parallel waveguide couplers, a straight waveguide, S-bend, Y-junction splitter, single-output Mach-Zehnder interferometer (MZI), sharp bends, and a waveguide Bragg grating. The latter is typically implemented as a step-in-width metal stripe structure, as sketched in Fig. 1(b). Mode outputs from typical structures captured using an infrared camera are also shown in Fig. 1(a); the structures were fabricated as thin (20 nm) Au stripes on SiO_2 and covered by an index-matched medium [1]. Low attenuation values of a few dB/mm are routinely achievable in the infrared (*e.g.*, λ_0 ~ 1310 and 1550 nm) along with near-perfect end-fire coupling (>90% efficiency) to dielectric waveguides and optical fibre.

2. ACTIVE PLASMONIC DEVICES

Significant theoretical and experimental work has been conducted over the past decade to compensate for surface plasmon loss or even produce amplification and lasing with surface plasmons [2]. Lasing with surface plasmons is of strong current interest because the structures can be miniaturized, offering compact coherent sources for integrated photonic or plasmonic circuits [3,4]. LRSPPs with their low attenuation are attractive for active plasmonic applications because many active materials have sufficient gain to overcome the losses so demonstrations and proof-of-principle studies are readily undertaken. Also, LRSPP amplifiers and lasers can be integrated with passive elements (*e.g.*, Fig. 1) to enable advanced functionality circuits.

One of the first demonstrations of surface plasmon amplification was carried out using LRSPPs on a thin Au stripe on SiO_2, cladded by an optically-pumped dipolar gain medium (IR-140 dye molecules in solvent), where a modal gain of about 10 dB/mm was measured [5]. Work was also carried out to incorporate the same dye molecules (IR-140) into PMMA to produce a solid-state gain medium that could be readily spin-coated onto substrates, integrated with other materials, and structured using e-beam litho [6,7]. Optimisation of the medium led to optically-pumped gain of 80 to 300 cm^{-1} at 880 nm [7]. The medium can provide long-term (low-bleaching) gain as long as the pump repetition period is greater that the thermal characteristic time of the medium. The medium structured by e-beam litho retains much of its gain as long as the dose is not too high [7].

LRSPP laser concepts were proposed theoretically and the requirements for single-mode lasing investigated [8]. LRSPP distributed feedback (DFB) lasers were then realized and demonstrated [9], as summarised in Fig. 2. The lasers consist of a 20 nm thick Au stripe on a thick silica layer, covered with 600 nm of PMMA doped with IR-140 as the active medium. The Au stripe was stepped in width in a pitch of $\Lambda \sim 300$ nm (*cf.* Fig. 1(b)), forming a Bragg grating with a centre wavelength of $\lambda_B \sim 880$ nm, corresponding to the peak emission wavelength of IR-140 dye molecules. The laser was pumped from the top and the emission emerged from a facet, as shown in Fig. 2(a). Fig. 2(b) shows the measured peak emission intensity *vs.* pump power density for such a laser, from which a clear lasing threshold is identified (I_p = 1.04 MW/cm^2). Fig. 2(c) shows the evolution of the output spectrum beyond threshold as the pump power density is increased, revealing lasing in a single mode and significant linewidth narrowing (the spectrum measured for I_p = 2.88 MW/cm^2 is spectrograph-limited). The inset to Fig. 2(b) shows an output mode beyond threshold captured on an IR camera. DFB lasers such as this are compact and easy to fabricate and integrate with other optical elements (*cf.* Fig. 1(a)).

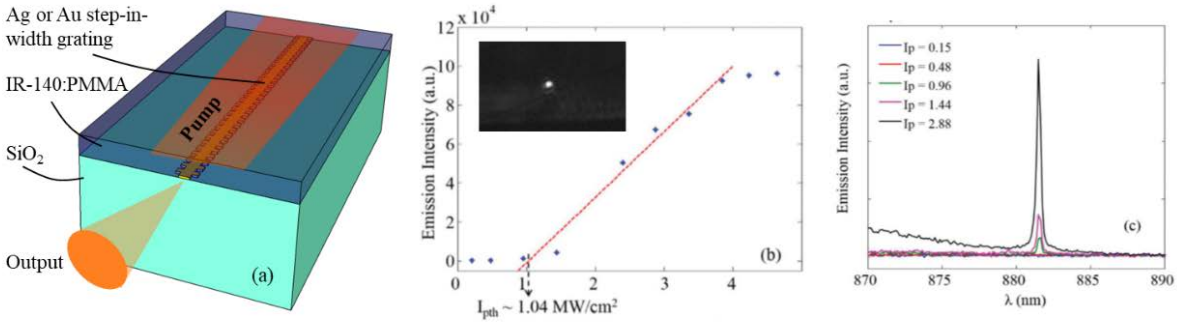


Figure 2. (a) Sketch an LRSPP DFB waveguide laser. (b) Measured peak emission intensity vs. pump power density (MW/cm^2) for a Au DFB laser; the lasing threshold is 1.04 MW/cm^2 [9]. (c) Linewidth narrowing with increasing pump power density (Ip in MW/cm^2) [9].

3. BIOSENSORS

LRSPPs on metal stripe waveguides are attractive for biosensing applications because an integrated optical geometry (*cf.* Fig. 1) can be used as a transducer, and the low attenuation enables a long interaction length with the sensing medium. Furthermore, the biosensors are compact and mass manufacturable using semiconductor fabrication tools and processes. An LRPP waveguide biosensor is shown Fig. 3(a), which illustrates a Au stripe on Cytop within a fluidic channel filled with sensing solution [10]. The thin red region models a biochemical adlayer forming on the metal stripe during sensing. The LRSPP propagates over a broad range of wavelengths with the field distribution shown in Fig. 3(b). This field distribution is symmetric-like, leading to efficient butt-coupling to a TM-polarised optical fibre or beam. Fig. 3(c) shows a SEM of fabricated structures and Figs. 3(d)-(e) fluidic fixturing and interfacing. Figs. 3(f)-(h) show single-output [11], dual-output [12] and triple-output [13] (MZIs), where one of the arms is exposed to the sensing fluid via a microfluidic channel of length L_F. LRSPP waveguide biosensors were used successfully for disease detection in complex fluids [14], including Dengue infection in patient blood plasma [15], leukemia in patient blood sera [16], and bacteria in urine [14].

Sensing occurs as biomaterial binds selectively to the top surface of the stripe functionalised with appropriate recognition chemistry - *e.g.*, antigen immobilised on the waveguide to capture antibodies in a patient sample. As binding occurs, a biochemical adlayer forms on the surface of the stripe (red region, Fig. 3(a)), which perturbs the propagation of the LRSPP, leading to changes in its intensity and phase. Both changes can be measured in real time, the former via a straight waveguide and the latter via a MZI (Figs. 3(f)-(h)). Single-output MZIs (Fig. 3(f)) are simpler, but multiple-output MZIs provide advantages: Dual-output MZIs (Fig. 3(g)) provide twice the dynamic range (twice the sensitivity) when operated in differential mode, as shown in Fig. 3(i), and the ability to suppress the effects of common perturbations and drift by referencing to the sum of the outputs. Similarly, triple-output MZIs suppress common perturbations and increase the dynamic range, but additionally they mitigate sensitivity fading and resolve directional ambiguity when unwrapping the phase.

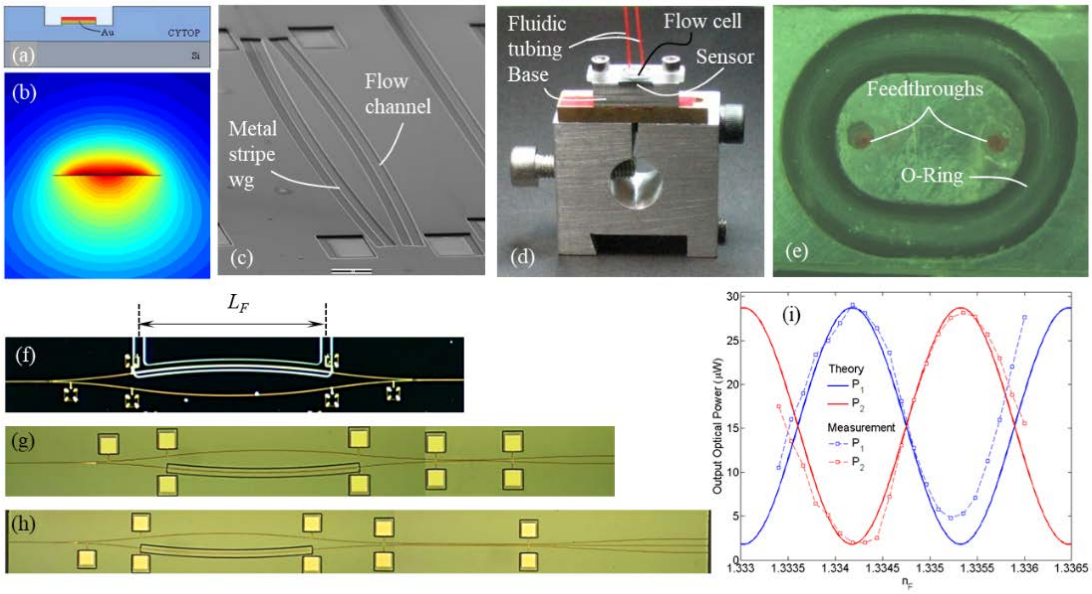


Figure 3. (a) Cross-sectional sketch of an LRSPP waveguide biosensor, (b) LRSPP field distribution, (c) SEM image of biosensors, (d) fixture housing a biosensor, (e) flow cell lid. Microscope images of (f) single-output [11], (g) dual-output [12] and (h) triple-output [13] MZI biosensors, with a microfluidic channel of length L_F. (i) Measured and theoretical responses of a dual-output MZI biosensor [12].

4. CONCLUSIONS

Integrated optics using LRSPPs on metal stripe waveguides is compelling. The low attenuation of LRSPPs enables a long optical interaction length with the claddings as well as amplification using conventional gain materials. The technology is promising for several applications, including amplification, lasing and biosensing.

REFERENCES

[1] Berini, P., "Long-range surface plasmon polaritons," *Adv. Opt. Phot.* 1, 484-588 (2009).
[2] Berini, P. and De Leon, I., "Surface plasmon-polariton amplifiers and lasers," *Nat. Phot.* 6, 16-24 (2012).
[3] Bergman D. J. and Stockman, M. I., "Surface Plasmon amplification by stimulated emission of radiation: Quantum generation of coherent surface plasmons in nanosystems," *Phys. Rev. Lett.* 90, 027402 (2003).
[4] Ma, R. M., Oulton, R. F., Sorger, V. J., Bartal, G., and Zhang, X., "Room-temperature subdiffraction-limited plasmon laser by total internal reflection," *Nat. Mat.* 10, 110-113 (2011).
[5] De Leon, I., and Berini, P., Amplification of long-range surface plasmons by a dipolar gain medium. *Nat. Phot.* 4, 382-387 (2010).
[6] Hahn, C., Song, S. H., Oh, C. H., and Berini, P., "Plasmonic gain in long-range surface plasmon polariton waveguides bounded symmetrically by dye-doped polymer," *Appl. Phys. Lett.* 107, 121107 (2015).
[7] Amyot-Bourgeois, M. *et al.*, "Gain optimization, bleaching and e-beam structuring of IR-140 doped PMMA, and integration with plasmonic waveguides," *Opt. Mat. Exp.* 7, 3963-3978 (2017).
[8] Karami Keshmarzi, E., Tait, R. N., and Berini, P., "Long-range surface plasmon single-mode laser concepts," *J. Appl. Phys.* 112, 063115 (2012).
[9] Karami Keshmarzi, E., Tait, R. N., and Berini, P., "Single-mode surface plasmon distributed feedback lasers," *Nanoscale*, DOI: 10.1039/C7NR09183D
[10] Krupin, O., Asiri, H., Wang, C., Tait, R. N., Berini, P., "Biosensing using straight long-range surface plasmon waveguides," *Opt. Express* 21, 698-709 (2013).
[11] Khan, A., Krupin, O., Lisicka-Skrzek, E., Berini, P., "Mach-Zehnder refractometric sensor using long-range surface plasmon waveguides," *Appl. Phys. Lett.* 103, 111108 (2013).
[12] Fan, H., Berini, P., "Bulk sensing using a long-range surface-plasmon dual-output Mach-Zehnder interferometer," *J. Lightwave Technol.* 34, 2631-2638 (2016).
[13] Fan, H., Berini, P., "Bulk sensing using a long-range surface-plasmon triple-output Mach-Zehnder interferometer," *J. Opt. Soc. Am. B* 33, 1068-1074 (2016).
[14] Krupin, O. *et al.*, "Long-Range Surface Plasmon-Polariton Waveguide Biosensors for Disease Detection," *J. Lightwave Technol.* 34, 4673-4681 (2016).
[15] Wong, W. R. *et al.*, "Serological diagnosis of dengue infection in blood plasma using long-range surface plasmon waveguides," *Anal. Chem.* 86, 1735-1743 (2014).
[16] Krupin, O. *et al.*, "Detection of leukemia markers using long-range surface plasmon waveguides functionalized with protein G," *Lab on a Chip* 15, 4156-4165 (2015).

Synchronization of Modelocked Coupled Microresonator Combs

Jae K. Jang[1], Alexander Klenner[1], Xingchen Ji[2,3], Yoshitomo Okawachi[1], Michal Lipson[3], and Alexander L. Gaeta[1,*]

[1]*Department of Applied Physics and Applied Mathematics, Columbia University, New York, NY 10027, USA*
[2]*School of Electrical and Computer Engineering, Cornell University, Ithaca, NY 14853, USA*
[3]*Department of Electrical Engineering, Columbia University, New York, NY 10027, USA*
**Tel: +1-212-854-6564, e-mail: a.gaeta@columbia.edu*

ABSTRACT

We report the first experimental synchronization of two modelocked chip-based frequency combs. The synchronization is established passively via an optical fiber link for lengths up to 20 m and allows for coherent combining of the generated soliton pulses. Such a system could have applications in data communications, imaging, and clock distribution.

Keywords: microresonator combs, nonlinear photonics, synchronization, four-wave mixing

1. INTRODUCTION

Spontaneous synchronization of coupled nonlinear oscillators is a ubiquitous phenomenon that has been observed in many branches of science, including biology, neuroscience, engineering and physics [1]. In the context of optical physics, extensive studies of this phenomenon have been performed on networks of coupled lasers which have led to the demonstration of their collective phase locking [2] and coherent beam combining [3]. These results have subsequently been extended to the technology of modelocked laser-based optical frequency combs which has resulted in coupled combs with near-identical line spacing. An alternative platform for optical frequency comb generation is based on driven passive nonlinear microresonators [4]. It combines merits of the more conventional laser-based comb technology [5] with additional benefits such as spatial compactness and potential for on-chip integration [6]. Although single microresonator systems have been intensively studied over the past decade [4,6-12], the dynamics of coupled microresonators remain unexplored, and only very recently have there been preliminary numerical results showing evidence of frequency-locking among interacting microresonator combs [11].

2. RESULTS

Here we report the first demonstration of synchronization of two microresonator-based frequency combs, separated by over 20 m of optical fiber. Such a system offers not only a powerful platform for studying synchronization physics, In addition, we demonstrate coherent combining of the output of two frequency-locked combs which could have immediate implications in overcoming the power limitation of microresonator comb technology. Such synchronization offers the possibility of applications such as synchronization of multiple wavelength-division multiplexed sources [13,14].

A schematic of our experiment is shown in Fig. 1. We employ two silicon nitride microresonators with waveguide dimension of 730×1500 nm on two independent chips. A single tunable continuous-wave (CW) laser serves as the pump source for both microresonators. Its output is amplified with an erbium-doped fiber amplifier and split into two beams of equal intensity. Each beam is coupled to the integrated bus waveguide of a microresonator with a lensed fiber. We access the cavity soliton-based coherent frequency comb state [8-10] by electrically tuning the integrated microheaters on chips, as detailed in [12]. The output of one microresonator is collected and a small fraction (<1%) is combined with the CW pump field of the second microresonator. This combined field, which contains a portion ("synch signal") of the first ("master") microresonator comb signal,

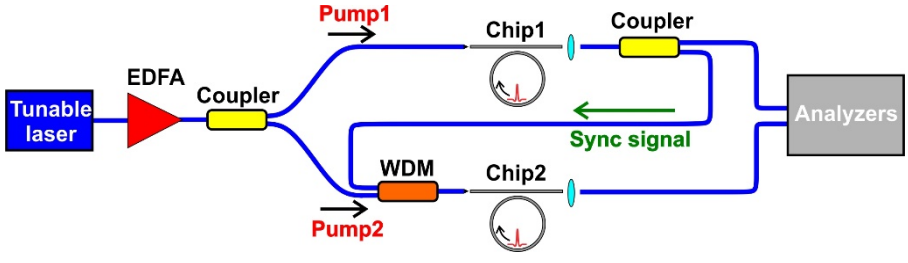


Fig. 1. A simplified schematic of our experimental set-up. EDFA: erbium-doped fiber amplifier, WDM: wavelength division multiplexer.

drives the second ("slave") microresonator. The sync signal goes through several passive fiber components whose cumulative length is over 20 m of optical fiber.

Figure 2 shows our experimental results on the synchronization behavior for our system. All results for the synchronized case are plotted in blue while the results of the unsynchronized case are plotted in red. Figure 2(a) and (d) show the optical spectra of the slave comb measured with an optical spectrum analyzer (OSA). In addition, we measure the *combined* optical spectra [Fig. 2(b) and (e)] with a high resolution (10 MHz) OSA, which allows us to resolve individual comb lines. We observe fringes in the synchronized case in Fig. 2(a) and attribute it to stationary interference between the slave comb and the sync signal which encompasses a fraction of the master comb. This is confirmed both by the complementary radio-frequency beat-note measurements [insets of (a) and (d)] and by the round-trip averaged spectra (green curves) from numerical simulation based on the Lugiato-Lefever equation [8], which are in good agreement with the experiment. Our simulation quantitatively reproduces the interference fringes that manifest during synchronization. It also reveals that the disappearance of the fringes in the absence of synchronization in Fig. 2(d) which is due to a relative drift of the circulating cavity solitons in the two microresonators. In the case of synchronization, the combined spectrum in Fig. 2(b) exhibits clear fringes reminiscent of a multiple cavity soliton state in microresonators [12], which indicates that the relative positions of the intracavity solitons are stably locked, *i.e.* the repetition rates are equal. Outside the synchronization regime, the fringes vanish and the spectral envelope becomes smooth, as in Fig. 2(e). Figure 2(c) presents the zoomed-in plots, extracted from Fig. 2(b) and (e) (black boxes), of the 12th comb lines which are blue-detuned relative to the pump. The blue trace corresponding to synchronized combs only exhibits a single comb line, in contrast to the unsynchronized case in the red trace showing two distinct lines. Finally, we investigate the possibility of coherent comb combining by interfering the two comb outputs with a beam splitter. The red curve in Fig. 2(f) shows the incoherent intensity sum of the individual combs through the splitter. In comparison, the blue curve corresponds to the measured combined spectrum when the combs are synchronized. As expected, the spectral power of the coherently combined spectrum is approximately double that of the incoherent sum. The black dashed curve shows the theoretically expected coherent sum of the individual spectra, which is in good agreement with our experimental data.

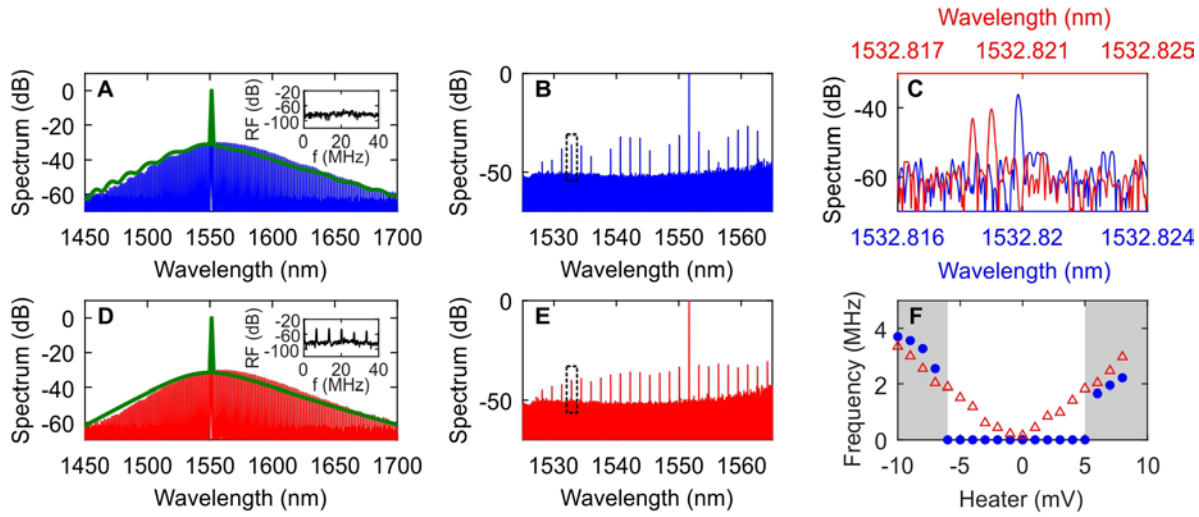


Fig. 2. Synchronization of two coupled microresonator combs. (A) and (B) show the slave comb spectrum and the combined spectrum, respectively, when the two combs are synchronized. The green curve is from numerical simulation and the inset is the complementary frequency down-converted beat-note measurement. The results of the unsynchronized case are presented in an identical manner in (D) and (E). (C) shows the zoomed-in plots of the 12th comb line from the pump, marked by black dashed rectangles in (B) and (E). One of the plots has been displaced along the wavelength axis by 0.001 nm for clarity. (F) First-harmonic beatnote frequency as one of the microresonators is thermally tuned, when the combs are coupled (blue circles) and uncoupled (red circles). Here the calibration factor is approximately 36 MHz/mV, implying synchronization regime can be maintained over a resonance shift of 400 MHz relative to the pump.

3. CONCLUSIONS

These results provide the first experimental demonstration of synchronization between two microresonator combs, which in this case are separated by an optical path length of > 20 m. The passive synchronization technique studied here could further advance coherent communication scheme, offering a means of achieving the required phase coherence between the multi-carrier sources and the local oscillators.

REFERENCES

[1] S. H. Strogatz, "From Kuramoto to Crawford: exploring the onset of synchronization in populations of coupled oscillators," Physica D **143**, 1-20 (2000).

[2] M. Nixon, M. Fridman, E. Ronen, A. A. Friesem, N. Davidson, I. Kanter, "Controlling synchronization in large laser networks," Phys. Rev. Lett. **108**, 214101 (2012).

[3] P. K. Cheo, A. Liu, G. G. King, "A high-brightness laser beam from a phase-locked multicore Yb-doped fiber laser," IEEE Photon. Technol. Lett. **13**, 439-441 (2001).

[4] T. J. Kippenberg *et al*., Science **332,** 555-559 (2011).

[5] S. T. Cundiff and J. Ye, Rev. Mod. Phys. **75**, 325-342 (2003).

[6] J. S. Levy, K. Saha, Y. Okawachi, M. A. Foster, A. L. Gaeta, M. Lipson, "High-performance silicon-nitride-based multiple-wavelength source," Nature Photon. **4**, 37-40 (2010).

[7] Y. K. Chembo and N. Yu, Phys. Rev. A **82**, 033801 (2010).

[8] S. Coen, H. G. Randle, T. Sylvestre, M. Erkintalo, "Modeling of octave-spanning Kerr frequency combs using a generalized mean-field Lugiato-Lefever model," Opt. Lett. **38**, 37-39 (2013).

[9] K. Saha, Y. Okawachi, B. Shim, J. S. Levy, R. Salem, A. R. Johnson, M. A. Foster, M. R. E. Lamont, M. Lipson, A. L. Gaeta, "Modelocking and femtosecond pulse generation in chip-based frequency combs," Opt. Express **21**, 1335-1343 (2013).

[10] T. Herr, V. Brasch, J. D. Jost, C. Y. Wang, N. M. Kondratiev, M. L. Gorodetsky, T. J. Kippenberg, Temporal solitons in optical microresonators," Nature Photon. **8**, 145-152 (2014).

[11] J. H. D. Munns, I. A. Walmsley, Y. H. Wen, "Novel interactions of dissipative Kerr solitons in nonlinear cavity networks," CLEO/Europe-EQEC (2017).

[12] C. Joshi, J. K. Jang, K. Luke, X. Ji, S. A. Miller, A. Klenner, Y. Okawachi, M. Lipson, A. L. Gaeta, Thermally controlled comb generation and soliton modelocking in microresonators," Opt. Lett. **41**, 2565-2568 (2016).

[13] J. S. Levy, K. Saha, Y. Okawachi, M. A. Foster, A. L. Gaeta, M. Lipson, "High-performance silicon-nitride-based multiple-wavelength source," IEEE Photon. Technol. Lett. **24**, 1375-1377 (2012).

[14] P. Marin-Palomo, J. N. Kemal, M. Karpov, A. Kordts, J. Pfeifle, M. H. P. Pfeiffer, P. Trocha, S. Wolf, V. Brasch, M. H. Anderson, R. Rosenberger, K. Vijayan, W. Freude, T. J. Kippenberg, C. Koos, Microresonator-based solitons for massively parallel coherent optical communications," Nature **546**, 274-279 (2017).

Low-loss inverted taper edge coupler in silicon nitride

(Student paper)

Juan Fernández[1,2], Rocío Baños[1], David Doménech[1], Carlos Domínguez[3] and Pascual Muñoz[2]

[1] *VLC Photonics S.L, c/ Camino de Vera s/n – 46022, Valencia – Spain – david.domenech@vlcphotonics.com*

[2] Universitat Politènica de València, c/ Camino de Vera s/n – 46022, Valencia – Spain – *pascual.munoz@upv.es*

[3] *Instituto de Microelectrónica de Barcelona (IMB-CNM), CSIC – Bellaterra 08193 - Spain*

ABSTRACT

An inverted lateral taper with one vertical discrete step was designed for a medium confinement silicon nitride waveguide platform in the C-band, as chip edge coupler, with predicted insertion loss of 0.58 dB. The design is supported by an extensive study to evaluate the impact of fabrication process variations in the performance of such coupler. The device was manufactured and measured, showing an insertion loss of 1.47 dB, which was traced back to fabrication process variations as cross-checked with simulations. To our knowledge, the reported edge coupler is the shortest and among the best performing found for silicon nitride platforms.

Keywords: Silicon nitride, photonic integrated circuits, fiber coupling, inverted taper

1. INTRODUCTION

Silicon Nitride based integration platforms are subject of attention due to the wide wavelength range over which the material is transparent (400-2400 nm) and inherently low-loss [1]. This waveguide technology is based on a combination of silicon nitride as waveguide layers, filled by and encapsulated with silica (SiO_2) as cladding layers grown on a silicon wafer. SiO_2 and Si_3N_4 layers are fabricated with CMOS-compatible industrial standard chemical vapour deposition (both low pressure, LPCVD, and plasma enhanced, PECVD) techniques, that enable cost-effective volume production [2]. Edge coupling to the chips can make use of spot-size converters (SSC) [3]-[4]. Inversely tapered waveguides, either lateral, vertical and combined (3D) [5], waveguides are one type of SSC providing some advantages: simple design, easy fabrication, broad transmission bandwidth, and high coupling efficiency. Silicon nitride SSCs have been previously reported, with 3.3 dB insertion loss, 500 µm length and tip height 100 nm [6] and others with 0.65 dB losses, length of 800 µm [7] 150 nm tip width, and 700 nm tip height. Other papers quote 0.5 dB loss for film heights of 100 nm [8]. In this paper, we report on the design and characterization of an inverted taper with 1.5 dB insertion loss and 150 µm length for a silicon nitride platform with guiding film height of 300 nm and taper tip height of 150 nm.

2. DEVICE DESIGN

The edge coupler proposed makes use of the already existing lithographic steps in our previously developed Si_3N_4 generic integration platforms [2]. That is, it does not resort to specialized additional process steps such as wet etching or more complex lithography approaches as the use of a shadow mask, but it rather markers the use of the different nitride etching levels of our platform. The mode transformer design is made up of two height levels of an adiabatic inverse lateral taper structure in silicon nitride shown in Fig.1.

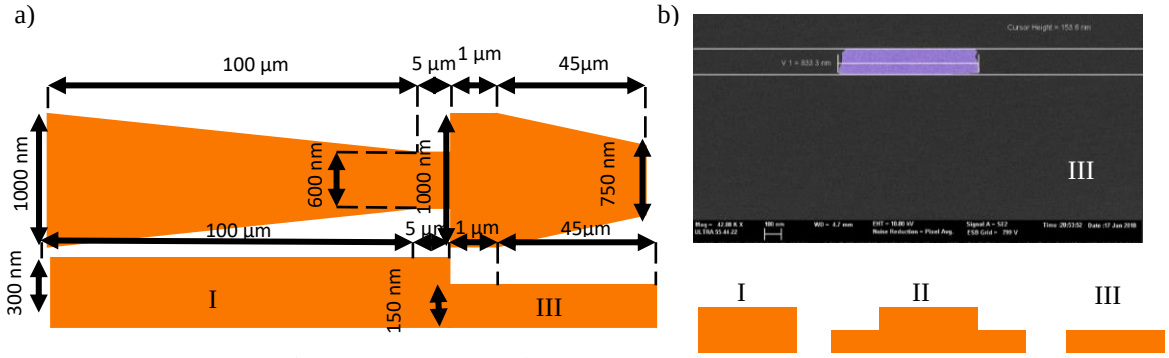


Figure 1. a) Top and side view of the inverted taper, b) platform waveguide cross-sections, I deep, II shallow and III mini-deep and SEM micrograph (in pseudo-color) of the facet tip for one of the measured inverted tapers (tip widths in 0.8-0.9 µm).

The designed device was fabricated in a Silicon Nitride photonics platform compatible with a standard CMOS pilot line Three different waveguide structures are defined by photo-lithography with a I-line stepper (minimum

feature 600 nm) followed by a reactive ion etching (RIE) of the silicon nitride film. The 300 nm silicon nitride layer may be etched: completely to form a strip waveguide structure (deep), partially avoiding core obtaining a rib waveguide structure (shallow) or partially in the core and completely in the sides to form a strip waveguide of 150 nm thickness (mini-deep). To obtain the insertion loss of the device, the overlap integral [9] between different widths of the three possible cross-sections and a 2.5 µm Mode Field Diameter (MFD) that it is typical of lensed fiber has been performed. Firstly, the mini-deep waveguide is the best cross-section to couple power to 2.5 µm MFD as compare with deep or shallow cross-section. There is a local minimum for the power loss of 0.35 dB with a waveguide width of 750 nm. Secondly, to obtain a deep cross-section output of inverted taper, an overlap integral between deep cross-section and mini-deep cross-section must be studied.

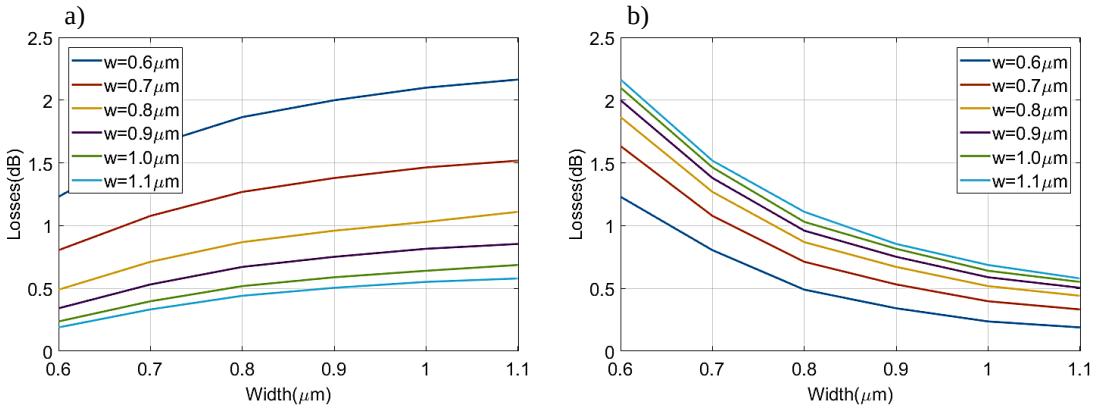


Figure 2. Overlap between deep waveguide and mini-deep waveguide. a) different deep widths vs mini-deep widths, b) different mini-deep widths vs deep widths.

As shown Fig. 2 a), the loss is reduced when the deep waveguide width is decreased and the mini-deep waveguide is decreased. From the graphs, the optimum point is for widths of 1 µm and 0.6 µm for the deep and mini-deep cross-sections respectively. These values ensure single mode operation as well. To optimize the excess loss of the overall device, the tapering losses must be minimized as well. Next, the beam propagation method (BPM) from the FIMMWAVE software package is employed to obtain the taper response and losses.

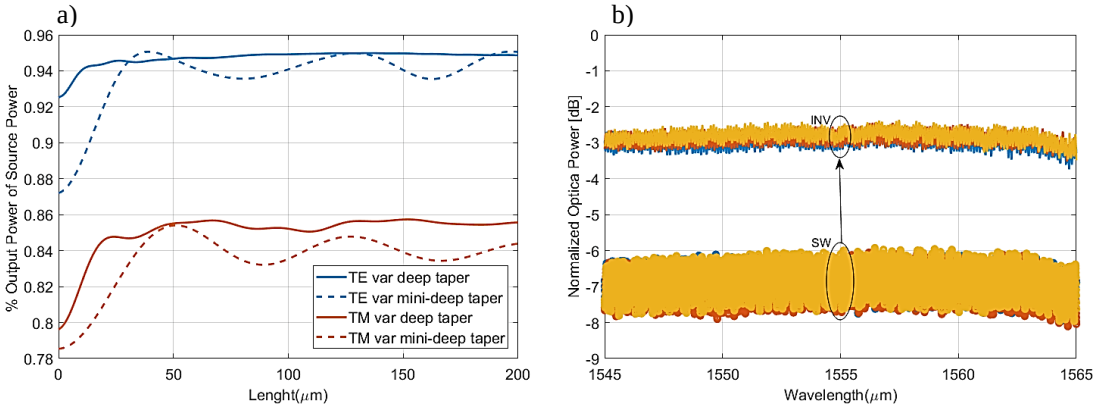


Figure 3. a) Total output power for different taper lengths for mini-deep and for deep cross-sections. b) fiber to fiber TE transmission measurements for test structures with (INV) and without (SW) inverted tapers.

The results are shown in Fig. 3 a), where shows the total power coupled, for different lengths of the first taper in the mini-deep cross-section, for fixed length (100 µm) of the deep cross-section taper. Complementary, Fig. 3 b) shows the results for fixed length (50 µm) of the mini-deep taper, and lengths of the deep section taper. From the graphs, Fig. 3 a) shows how the power coupling oscillates with the mini-deep taper length. At 45 µm taper length TE polarization shows a maximum. Thus, the taper lengths chosen according to all the above and to maximize coupled power are: 45 µm length for the mini-deep taper and 100 µm length for the deep taper. With this configuration, the simulation yields 0.23 dB excess losses with a 20 dB suppression of the higher order modes. Design tolerances were thoroughly analysed, but the mask misalignment between process steps was found to be the most relevant. Defining the deep and mini-deep cross-sections in lithography makes use of two different masks that are to be aligned in different steps. To explore the impact of possible misalignments, a straight deep section is introduced in between the two tapers, as shown in Fig. 1. The misalignment can only happen in the longitudinal direction, since the mini-deep is actually done with same deep mask, but without the shallow mask protection.

The mask alignment errors of 1 µm result into approximately 0.4 dB extra losses for the TE. This design was fabricated in a multi-project wafer run (MPW) offered by IMB-CNM [2] within a 5x5 mm^2 chip die. Instead of use DoE (Design of Experiments), only one design with optimum values is used since fabrication variations were expected, as later detailed, and with the aim of correlating experimental results to the design and simulation flow outcomes.

3. EXPERIMENTAL RESULTS

We used and end-fire measurement setup with microscope objectives with MFD 2.5 µm and with polarizers, in order to inject and collect TE polarization. The test structure is composed of two edge couplers, each at one side of the chip, and a straight deep waveguide of 1 µm width between them. To measure the response a ASE broadband source was employed, together with a OSA. All the measurements are normalized to the spectrum acquired without the chip, that is between the microscope objectives face to. All measurements are with the polarizers set to allow TE to go through to/from the microscope objectives. Fiber collimators are employed, so as to allow fiber connections from the ASE source and to the OSA. The results are shown in Fig. 3 b) both for a straight waveguide with two inverted tapers and without them as detailed. The fiber to fiber loss is 3.635 dB when inverted tapers are employed. The measured propagation loss for the 1 µm width deep straight waveguide is 1.41dB/cm [1]. Each edge coupler has 1.47 dB insertion loss for the TE polarization. This is significantly different from the 0.58 dB predicted by simulation (0.35 dB due to overlap and 0.23 dB due to the tapers, i.e. transition loss). The difference is attributed to the following. Firstly, the wafers were stealth diced 25 µm inside the die. Therefore, the mini-deep taper was no longer 45 µm long, but its length was reduced accordingly. Simulations for the new length and result width of 0.9 µm width in the mini-deep result into additional overlap coupling loss of 0.405 dB insertion losses for TE polarization. Furthermore, the new taper length increases the taper loss up to 0.351 dB. Next, the width variations in the lithographic processes are of the order of 100 nm, which in turn result from simulation into an 0.295 dB in total (overlap and transition). Mask and fabrication alignment errors could add 0.4-0.5 dB as mentioned in section D1 due to misalignment between masks that produce overlap losses. In summary, the overall losses in the worst case, including a width error, may reach 1.051 dB for TE, whereas losses due to mask alignment and fabrication may add an extra 0.4-0.5 dB. This could explain the experimental 1.47 dB vs the 0.58 dB predicted in the design stage.

4. CONCLUSION

A lateral inverted taper was designed for a Silicon Nitride platform, with theoretical insertion loss of 0.58. Experimental results yield 1.47 dB loss, and the difference was studied incorporating into the simulation the known manufacturing variations. This structure as edge coupler is the shortest reported in silicon nitride with a length of 150 µm, and among the ones with the lowest insertion loss in the literature.

REFERENCES

[1] P. Muñoz e.a., "*Silicon Nitride Photonic Integration Platforms for Visible, Near-Infrared and Mid-Infrared Applications*," Sensors, 17(9), 2088 (2017).

[2] Silicon nitride technology at IMB-CNM-CSIC. http://www.imb-cnm.csic.es/index.php/en/clean-room/silicon-nitride-technology

[3] T. Shoji e.a., "*Low loss mode size converter from 0.3 µm square Si wire waveguides to single mode fibres*," Electron. Lett. 38, 1669-1670 (2002).

[4] K. Shiraishi e.a., "*A silicon-based spot-size converter between single-mode fibers and Si-wire waveguides using cascaded tapers*," Appl. Phys. Lett. 91, 141120 (2007).

[5] Moerman, I., Van Daele, P. P., & Demeester, P. M. "*A review on fabrication technologies for the monolithic integration of tapers with III-V semiconductor devices*," IEEE Journal of Selected Topics in Quantum Electronics, 3(6), 1308-1320 (1998).

[6] Y. Shani e.a., "*Efficient coupling of a semiconductor laser to an optical fiber by means of a tapered waveguide on silicon,"* Applied physics letters, 55(23), 2389-2391 (1989)

[7] M.T. Doan e.a., "*Spot size mode converter for efficient coupling to SiN waveguides,"* In Proc. Photonics North International Society for Optics and Photonics, pp. 221-228, December 2004.

[8] L. Zhuang e.a., "*Low-loss, high-index-contrast Si_3N_4/SiO_2 optical waveguides for optical delay lines in microwave photonics signal processing*," Opt. Express 19, 23162-23170 (2011)

[9] H. Kobayashi e.a., "*Narrow-beam divergence 1.3- µm multiple-quantum-well laser diodes with monolithically integrated tapered thickness waveguide*," IEEE Journal of Selected Topics in Quantum Electronics, 1998, vol. 3, no 6, p. 1384-1391.

Mid-infrared Suspended Waveguide Platform and Building Blocks

(Invited paper)

J. G. Wangüemert-Pérez[1,*], A. Sánchez-Postigo[1], J. Soler Penades[2], A. Ortega-Moñux[1], M. Nedeljkovic[2], R. Halir[1], F. El Mokhtari Mimun[1], Y.X. Cheng[2], Z. Qu[2], A.Z. Khokhar[2], A. Osman[2], W. Cao[2], C.G. Littlejohns[2], P. Cheben[3], G. Z. Mashanovich[2], I. Molina-Fernández[1]

[1] *Universidad de Málaga, Dpto. Ingeniería de Comunicaciones, ETSI-Telecomunicación, 29071 Málaga, Spain*

[2] *Optoelectronics Research Centre, University of Southampton, Southampton, SO17 1BJ, United Kingdom*

[3] *National Research Council Canada, Building M-50, Ottawa, K1A 0R6 Canada*

[*] *Corresponding author: gonzalo@ic.uma.es*

ABSTRACT

In this work we present our recent progress in the development of a platform for the mid-infrared wavelength range, based on suspended silicon waveguide with subwavelength metamaterial cladding. The platform has some intrinsic advantages, which make it a very promising candidate for sensing applications in the fingerprint region. Specifically, it can cover the full transparency window of silicon (up to a wavelength of 8 μm), only requires one lithographic etch-step and can be designed for strong light-matter interaction. Design rules, practical aspects of the fabrication process and experimental results of a complete set of elemental building blocks operating at two very different wavelengths, 3.8 μm and 7.67 μm, will be discussed. Propagation losses as low as 0.82 dB/cm at λ_o=3.8 μm and 3.1 dB/cm at λ_o=7.67 μm are attained, for the interconnecting waveguides.

Keywords: Integrated optics, Subwavelength structures, Mid-infrared, Waveguides, Optical devices.

1. INTRODUCTION

The Mid-InfraRed band (MIR, wavelengths from around 2 to 20 μm) is an especially interesting wavelength range because it includes the molecular fingerprint spectral region. Each substance is uniquely identified by a specific absorption spectrum. By measuring these spectra, it is possible to determine the presence and concentration of substances as diverse as greenhouse gases, explosives, food, petroleum products, polluting substances, plastics or even human tissues, among others. Regardless of the final application, to operate with a high degree of integration it is necessary to provide the most appropriate platform for this new band of wavelengths. One of the most successful platforms in the communications band (around 1.55 μm), Silicon-on-Insulator (SOI), could only be used up to a wavelength of 4 μm, given the strong absorption of silicon dioxide at longer wavelengths. Therefore, to be able to increase the wavelength and cover the full range of the MIR band, it is necessary to develop new platforms. The different alternatives that are currently being considered in the bibliography can be grouped into two different types: i) Platforms that combine materials with a greater range of transparency, including, silicon on sapphire, silicon on silicon nitride, chalcogenide crystals, germanium on silicon nitride or germanium on silicon (a summary of their attainable propagation loss can be found in [1]); and ii) Suspended platforms that are based on the selective elimination of the oxide on which silicon rests, producing waveguides known as suspended silicon. In this way, the complete transparency of silicon, up to 8 μm, could be covered, while still benefiting from the consolidated SOI manufacturing processes.

There are two alternatives to achieve the suspension: i) using an array of holes away from the core waveguide, yielding silicon membrane waveguides [2], and ii) using periodic subwavelength metamaterial cladding [3] [4]. In this work we will only focus on the latter, reviewing the current state of development. The operation principle of the elemental suspended waveguide, practical issues and experimental results of essential building blocks (interconnecting waveguides, bends, grating couplers and MMIs) operating at two different wavelengths, 3.8 μm and 7.67 μm, will be covered throughout the present work.

2. THE SUSPENDED SILICON WAVEGUIDES

A schematic representation of the suspended silicon waveguide is shown in Figure 1(a). As can be seen, it is composed of a silicon core of width W_{wg} and thickness t_{Si} which is anchored to the unsuspended lateral silicon areas making use of a subwavelength (SWG) pattern of silicon bars. The periodic cladding thus works as an equivalent homogeneous medium, by means of which it is possible to control the lateral refractive index contrast required for optical waveguiding (see Figure 1(b)). The SWG cladding must also perform two additional crucial functions: i) to have enough mechanical stiffness to support the weight of the wider and therefore heavier waveguides present in the circuit and ii) to allow the flow of the hydrofluoric acid (HF) through the holes to remove the buried oxide layer. This makes the design process to determine the adequate dimensions more intricate than that of conventional photonic waveguides, because each one of the aforementioned functions

imposes its own constraints, and, unfortunately, their respective optimum values move towards opposite directions. Table 1 summarizes towards what values the different geometrical parameters should move to better satisfy the respective constraints imposed by the fabrication process, the optical waveguiding and the mechanical stability. The final chosen values of the interconnecting waveguides at the two operating wavelengths, 3.8 μm and 7.67 μm, are also indicated in Table 1.

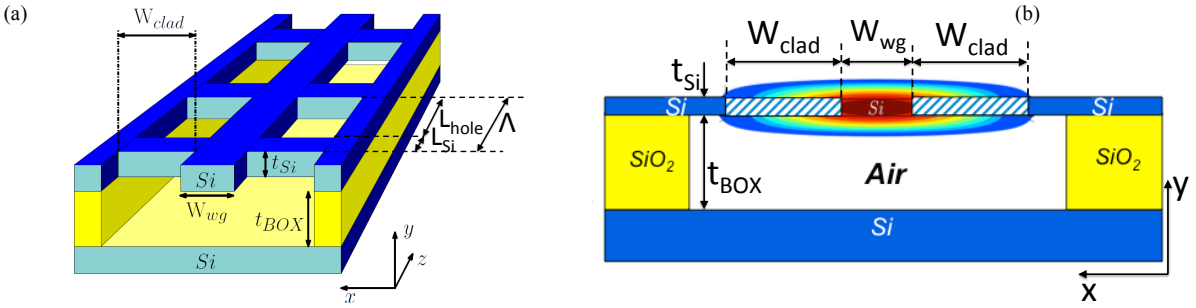


Figure 1. (a) 3D schematic of the suspended silicon waveguide; (b) 2D cross view and electric field spatial distribution of the fundamental mode associated with a specific value of the equivalent metamaterial cladding.

TABLE 1. SUMMARY OF CONSTRAINTS AND FINAL SELECTED VALUES AT λ = 3.8 μm & λ= 7.67 μm.

Parameter	A high value (↑) is good …	A small value (↓) is good…	Selected values at	
			λ= 3.8 μm	*λ=7.67μm*
W_{clad}	• to reduce the lateral leakage	• to reduce the mechanical torque	*2.5 μm*	*3 μm*
W_{wg}	• to reduce the lateral leakage	• to reduce the weight of the waveguide • to avoid the second order horizontal mode	*1.3 μm*	*2.9 μm*
t_{Si}	• to reduce the vertical leakage	• to reduce the weight of the waveguide • to avoid the second order vertical mode	*0.5 μm*	*1.4 μm*
t_{BOX}	• to reduce the vertical leakage		*3 μm*	*3 μm*
L_{Si}	• to assure the mechanical stability	• to increase the lateral index contrast and so reduce the lateral leakage. • to operate in the SWG regime	*0.1 μm*	*0.25 μm*
L_{Hole}	• to facilitate the flow of HF • to increase the lateral index contrast and thereby reduce the lateral leakage	• to operate in the SWG regime	*0.45 μm*	*0.9 μm*

3. FABRICATION

The fabrication process of any device in the proposed suspended platform requires the well-known dry etch to transfer the pattern to the silicon layer plus an additional wet etch to locally remove the BOX. This consists in dipping the chip into a 1:7 HF bath to remove the BOX. The difficulty arises from the required immersion time, which, as is shown in Fig. 2(a), is greater for wide waveguides (e.g. Multimode Interference devices, MMIs) than for narrow ones (e.g. interconnecting waveguides). Although the HF acid is highly selective and, in theory, it should not affect the silicon, in practice the silicon is slightly affected, suffering an over etching which produces a reduction in both the thickness and width of the nominal dimensions (see Fig. 2(b)). This silicon over etching can have dramatic consequences not only in the performance of the device but also in its mechanical stability. To compensate for this effect, required biasing for the dry etch must be accurately known in advance. Figures 2(c) and 2(d) show the effects of the dip time: when it is too short, the BOX is not completely removed, and when it is excessive, the over etching is so large that it ends up breaking the silicon bars. Figure 2 (e), in turn, shows the results of a more optimized dip time.

4. EXPERIMENTAL RESULTS

A complete set of essential building blocks operating at the wavelengths of 3.8 μm and 7.67 μm, respectively, have been designed, fabricated and characterized. Table 2 shows their SEM images and summarizes their dimensions and attained performance.

5. CONCLUSIONS

We have presented and reviewed the current state of a recent platform for the Mid-Infrared band, the suspended silicon waveguide, which would allow us to extend the usage of silicon photonics up to wavelengths of 8 μm. The first results at 3.8 μm and 7.67 μm in waveguides, bends, MMIs, and interferometers are very promising.

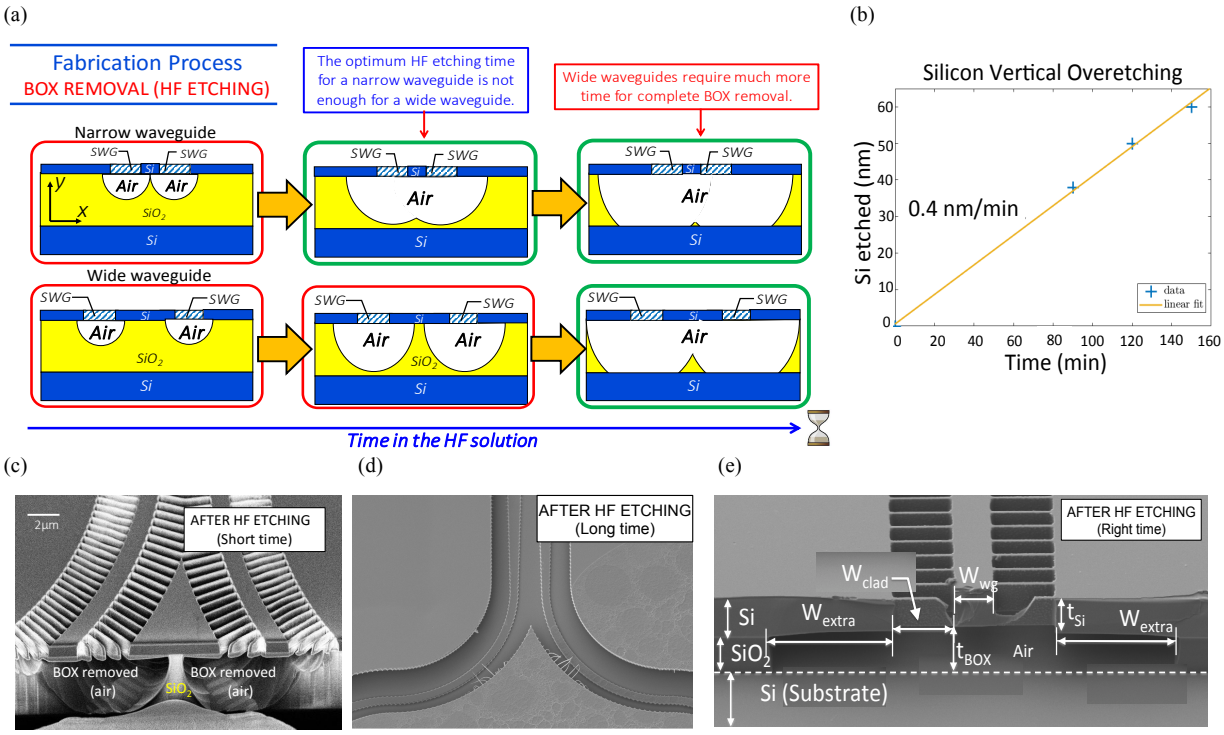
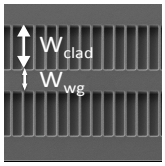
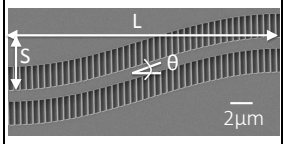
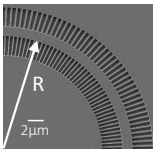
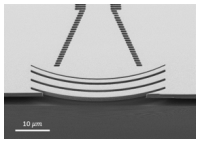
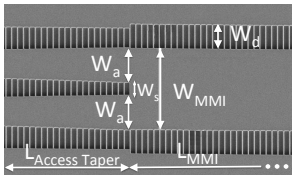


Figure 2. (a) Graphical illustration of the wet etching process to remove the BOX beneath the devices; (b) Undesired reduction of the vertical silicon thickness as a function of the immersion time into the HF acid dissolution; SEM images of fabricated interconnecting waveguides when the immersion time is c) too short; d) too long and e) optimized.

TABLE 2. PERFORMANCE SUMMARY OF SOME BASIC BUILDING BLOCKS AT λ = 3.8 μm & λ= 7.67 μm.

Straight waveguides	S-bends	90º-bends	Focusing grating coupler	MMI
				
@ λ = 3.8 μm W_{wg}= 1.3 μm W_{wg}= 2.5 μm Loss: 0.82 dB/cm	**@ λ = 3.8 μm** S= 7 μm; L= 41 μm; θ = 15º Loss: 0.01 dB/bend	**@ λ = 3.8 μm** R=16 μm; Loss:0.02dB/bend	Not available	**@ λ = 3.8 μm** **(no-biasing was applied)** W_a= 3.1 μm; W_S= 1.3 μm W_d= 2 μm; W_{MMI}= 7.1 μm L_{Taper}= 40 μm; L_{MMI}= 71.5 μm ExcessLoss & Imbalance <0.3 dB (minimum shifted to 3.71 μm)
@ λ = 7.67 μm W_{wg}= 2.9 μm W_{wg}= 3 μm Loss: 3.1 dB/cm	**@ λ = 7.67 μm** S= 5 μm; L= 75 μm; θ = 6º Losses: 0.06 dB/bend	**@ λ = 7.67 μm** R=35 μm; Loss:0.08dB/bend	**@ λ = 7.67 μm** (simulated, fabricated but not yet characterized) Coupling efficien.: 58% $Bandwidth_{1dB}$ = 230 nm Back-Reflections: 0.1% Radiation angle: 19.3º	**@ λ = 7.67 μm** (simulation results, under fabrication) W_a= 5.9 μm; W_S= 1.84 μm W_d= 2 μm; W_{MMI}= 13.38 μm L_{Taper}= 30 μm; L_{MMI}= 136.9 μm ExcessLoss & Imbalance <0.3 dB

ACKNOWLEDGEMENTS

We acknowledge funding from: Ministerio de Economía y Competitividad (TEC2016-80718-R); Ministerio de Educación, Cultura y Deporte (FPU14/06121) and Universidad de Málaga.

REFERENCES

[1] Ting Hu, *et al.*:Silicon photonic platforms for mid-infrared applications, *Photon. Res.*5, pp.417-430 (2017).

[2] Z. Cheng, *et al.*: Mid-infrared suspended membrane waveguide and ring resonator on silicon-on-insulator," *IEEE Photonics J.* 4(5), pp.1510–1519 (2012).

[3] J. Soler Penades, *et al.*: Suspended silicon mid-infrared waveguide devices with subwavelength grating metamaterial cladding, *Opt. Express* 24, pp.22908-22916 (2016).

[4] J. Soler Penadés, *et al.*: Suspended silicon waveguides for long-wave infrared wavelengths, *Opt. Lett.* 43, 795-798 (2018).

A new platform for integrated quantum optics: the short-wave infrared

(Student paper)
Lawrence Rosenfeld[1,2] Joshua W. Silverstone[1], Benjamin Slater[1], Döndü Sahin[1], Alex McMillan[1], Mark G. Thompson[1]
[1]*Quantum Engineering Technology Labs, H. H. Wills Physics Laboratory and Department of Electrical and Electronic Engineering, University of Bristol, Bristol BS8 1FD, UK*
[2]*Quantum Engineering Centre for Doctoral Training, H. H. Wills Physics Laboratory and Department of Electrical and Electronic Engineering, University of Bristol, Bristol BS8 1FD, UK*
e-mail: josh.silverstone@bristol.ac.uk

ABSTRACT

Integrated silicon photonic circuits are a promising candidate for large scale quantum optics experiments. Parasitic nonlinear absorption at near-IR (NIR) can be reduced or entirely eliminated by translating to the short-wave infrared (SWIR) band ca. 2.1 μm. We measure superconducting nanowire single photon detector efficiency, low loss multi-mode waveguides with 0.21 dB/cm attenuation and nonlinear absorption induced by a picosecond pulsed laser to be $\alpha_2 = 0.475 \times 10^{-12}$ m/W - an order of magnitude less than in NIR single-mode waveguides. This work demonstrates the feasibility for large scale integrated quantum photonics.

Keywords: Integrated photonics, mid-infrared optics, quantum optics, nonlinear optics

1. INTRODUCTION

Devices based on the properties of quantum mechanics—superposition and entanglement—stand to revolutionise how we gather, transmit, and process information. From quantum sensors, which overcome the shot noise limit to achieve exquisite sensitivity, to quantum key distribution systems, which allow cryptographic keys to be shared with unconditional secrecy, to tremendously powerful quantum computers, with applications from pharmaceutical and material design to machine learning and cryptography, quantum technology promises improvements across science, engineering, and society at large.
For photonic quantum technology to flourish, high performance is required at unprecedented scale. Silicon quantum photonics [1] offers the scale, mature fabrication capability, and much of the performance needed, and has facilitated exciting proof-of-concept devices from integrated functionality [2], and complex on-chip quantum light sources [3], through to inter-chip Bell tests [4]. Silicon photonics, however, has strong limitations in terms of scattering and nonlinear absorption. Subwavelength roughness on etched high-index-contrast waveguide sidewalls is the dominant source of propagation loss in silicon waveguides. Despite their excellent confinement and strong nonlinearity, silicon waveguides also suffer from strong deleterious two-photon absorption (TPA) at 1.55 μm. Quantum correlated photon-pairs can be generated in silicon via the nonlinear process, spontaneous four-wave mixing (SFWM). TPA limits the input power for nonlinear effects, such as parametric gain and supercontinuum generation, but it also subtly limits SFWM. As pointed out by Husko and colleagues [5], cross-TPA causes a bright pump to stimulate loss on copropagating single-photon channels, fundamentally limiting efficiency.

The short-wave infrared (SWIR) wavelength band, around 2.1 μm, mitigates side-wall scattering and nearly eliminates TPA, and greatly enhances silicon's dispersive nonlinearity (see Fig. 1a). Manufacturability is improved, bringing some subwavelength structures within reach of optical lithography, and free-carrier effects (attenuation, modulation) are enhanced.
With the manufacturing challenge of new TPA-free and lower-nonlinearity materials behind us, we must focus on the optical challenges presented by this new SWIR band.

2. RESULTS

The SWIR presents a number of opportunities, in addition to the suppression of TPA. We will discuss these, as well as the challenges, and outline our progress to date in exploiting this new band for SiQP. We will discuss the design and technical challenges of devices; show results on new passive structures, including waveguide couplers and delay lines; report on our progress towards generating and collecting photon pairs in the mid-IR; and finally outline our development of integrated SWIR-optimised single-photon detectors.

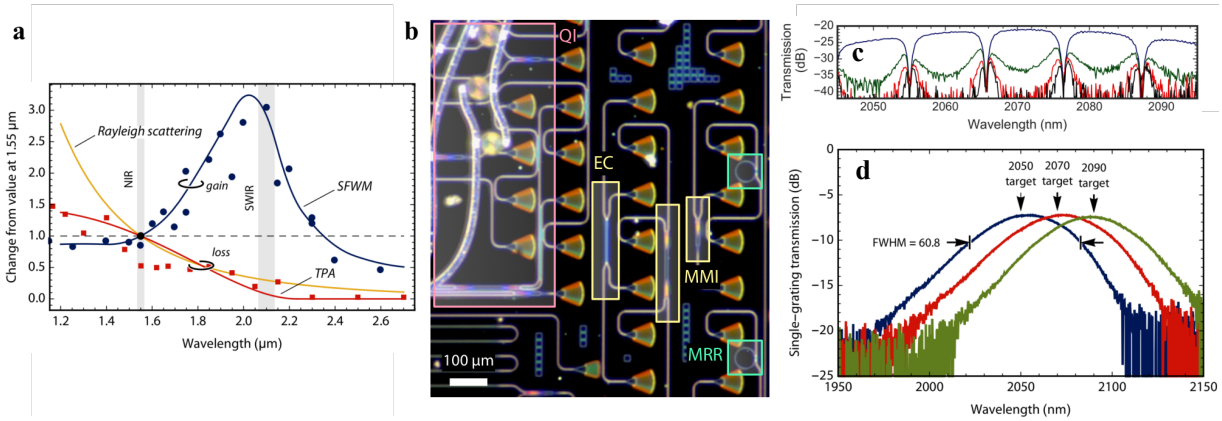


Figure 1a. *Linear, nonlinear loss and gain change in value from 1.55 µm.* ***b.*** *Micrograph of fabricated SWIR SiQP structures.* ***c.*** *Through port transmission spectra of a four stage cascaded racetrack filter.* ***d.*** *Measured single grating coupler transmission spectra.*

Linear loss contributions arise from waveguide wall roughness produced in during fabrication. A way to reduce this is to adiabatically taper between single-mode bends to less confined multi-mode waveguide straight sections, thereby reducing the overlap between the propagating light and the sidewalls. On a 220-nm top-silicon die, we design and fabricate strip waveguides in square spirals with single- and multi-mode bent and straight sections with 650 nm and 1500 nm widths, respectively. Figure 2b shows a cutback measurement of these waveguide spirals, probed with a narrow CW inter-subband quantum cascade laser (QCL) (Eblana Photonics) centred on 2.049 µm. Using linear regression fitting, we estimate the loss and standard error of the fit to be 0.21 ± 0.02 dB/cm with an insertion loss of 7.97 dB per grating.

To investigate the nonlinear response of the multi-mode waveguides spirals, we pump with a Thulium-Holmium doped fibre laser with a central wavelength of 2.07 µm, temporal width of 3 ps and peak power >10 kW. By varying the optical power launched into the waveguide and measuring the output on a InGaAs photodiode (PD), we use a nonlinear fit that accounts for linear loss, free carrier effects and TPA to estimate that the nonlinear absorption coefficient shown in Fig. 2a. The SWIR measurement of $\alpha_2 = 0.048$ cm/GW is an order of magnitude lower than the measured NIR value, $\alpha_2 = 0.37$ cm/GW, and much lower than the ~1 cm/GW reported elsewhere in the literature [6,7]. These comparison measurements were made in a single-mode waveguide spiral (cross-sectional area 500 × 220 nm^2) with a picosecond-pulsed laser operating at 1.55 µm. With the pulsed SWIR fibre laser, we compare the input and output pulses on an optical spectrum analyser (OSA) (Yokogawa AQ6375) and probe the nonlinear response of the longest (11.6 cm) square spiral to find ~3π self-phase accumulated during propagation through the waveguide.

To observe correlated photon pairs produced from SFWM that are co-propagating with a bright pump laser, measures to reject the pump are required. We demonstrate an on-chip filter using four cascaded racetrack resonators with the drop port of ring *i* connected to the input of the ring (*i*+1). We design these racetracks with a cavity length of 100 µm, corresponding to an experimentally measured group index $n_g = 3.965$ and FSR = 756.1 GHz. Characterisation of the device was performed with a supercontinuum source (NKT SuperK-Compact) and OSA the through port spectra is shown in Fig. 1c. Each ring in the filter provides up to 15 dB of extinction between the through and drop ports, giving us a maximum of 60 dB pump suppression - sufficient for observing single photons with additional off-chip bulk filtering.

Superconducting nanowire single photon detectors (SNSPDs) in the NIR are now capable of detection efficiencies around 90%. Single photon detection in the SWIR band is more challenging due to the lower photon energy. We take measurements of NIR SNSPD efficiency with an attenuated CW QCL laser with a central linewidth of 2.049 µm. By first measuring the transmission of several neutral density filters (NDFs) with the QCL, and separately the optical power transmitted from a knife-edge variable optical attenuator on an InGaAs PD, the laser beam is attenuated with the NDFs down to a regime where the SNSPDs are not latched and triggering events have photon arrival times much less than the dead time of the detectors.

The efficiency is estimated by fitting the incident photon to output photon fluxes. We find the best performance of a commercial NIR SNSPD to be up to 6% efficient with the mid-infrared fibre loops filters removed. To push the SWIR as a platform for quantum photonics, far higher detection efficiencies are desirable. Finite-difference time-domain (FDTD) and finite-difference eigenmode simulation results for WSi nanowires are shown in Fig. 2e and Fig. 2c and d respectively, showing the expected the absorption of light in SNSPD nanowire regions.

Development of superconducting WSi films on silicon waveguides are milestones for moving towards full integration of optical circuits, control electronics and detection on the same chip.

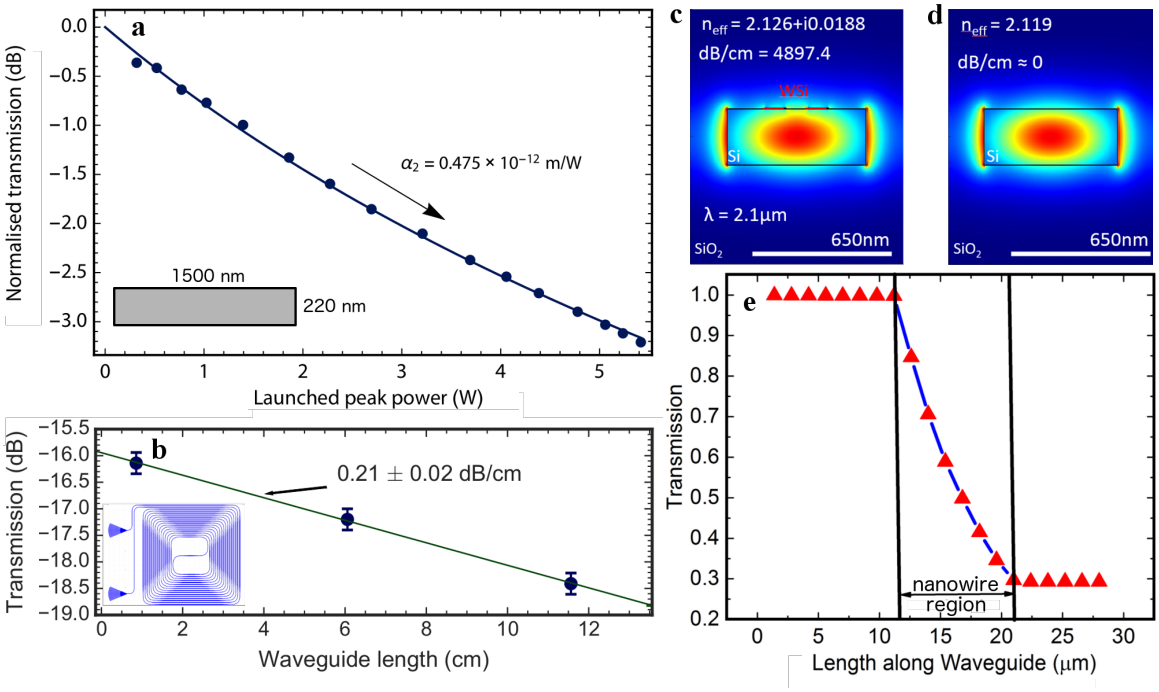


Figure 2a. *Measurement of the TPA coefficient α_2 in the SWIR band* ***b.*** *Cutback measurement of the propagation loss for multi-mode waveguides.* ***c.*** *FDE simulation of the electric field intensity for SWIR waveguides with 4nm thick WSi nanowires* ***d.*** *FDE simulation without WSi at a wavelength of 2.1 μm.* ***e.*** *FDTD simulations of a waveguide with a 10 μm WSi nanowire showing 70% absorption in this region.*

3. CONCLUSIONS

In summary, we have demonstrated the earliest stages of a new technology platform for integrated quantum photonics. First-generation designs of many passive structures perform well, with some showing state-of-the-art performance (e.g. propagation loss). Much remains to be done, however, and the next steps will be to robustly demonstrate photon-pair generation, while simultaneously improving our fibre- and chip-coupled single-photon detection capability.

This work opens the door to a new, fundamentally scalable quantum photonic technology platform, on which useful quantum devices can finally be realised.

ACKNOWLEDGEMENTS

LR was supported by the Bristol Quantum Engineering Centre for Doctoral Training, EPSRC grant EP/L015730/1. This work was supported by the UK EPSRC grant QuPIC EP/N015126/1.

REFERENCES

[1] J.W. Silverstone, et al. 'Silicon Quantum Photonics', IEEE Journal of Selected Topics in Quantum Electronics **22**, 6, 390 (2016) doi: 10.1109/JSTQE.2016.2573218

[2] J.W. Silverstone, et al. 'On-chip quantum interference between silicon photon-pair sources', Nature Photonics **8**, 104–108 (2014) doi: 10.1038/nphoton.2013.339

[3] R. Santagati, et al. 'Silicon photonic processor of two-qubit entangling quantum logic'. Journal of Optics **19**, 114006 (2017) doi:10.1088/2040-8986/aa8d56

[4] J. Wang, et al. 'Chip-to-chip quantum photonic interconnect by path-polarization interconversion'. Optica **3**, 407–413 (2016) doi: 10.1364/OPTICA.3.000407

[5] C. A. Husko, et al. "Multi-photon absorption limits to heralded single photon sources", Scientific Reports **3**, 3087 (2013) doi: 10.1038/srep03087

[6] A.D. Bristow, N. Rotenberg, H.M. van Driel. 'Two-photon absorption and Kerr coefficients of silicon for 850–2200 nm'. Applied Physics Letters **90**, 191104 (2007) doi: 10.1063/1.2737359

[7] T. Wang et al. 'Multi-photon absorption and third-order nonlinearity in silicon at mid-infrared wavelengths. Optics Express **21**, 32192 (2013) doi: 10.1364/oe.21.032192

High-efficiency SiN Grating Fiber-Chip Coupler with Bottom Reflector

Siddharth Nambiar, Abhai Kumar., Rakshitha K., Praveen Ranganath, Shankar Kumar Selvaraja
Center for Nanoscience and Engineering, Indian Institute of Science, Bengaluru -560012
Tel: : +91 80 2293 3342 , e-mail: shankar.ks@iisc.ac.in

ABSTRACT

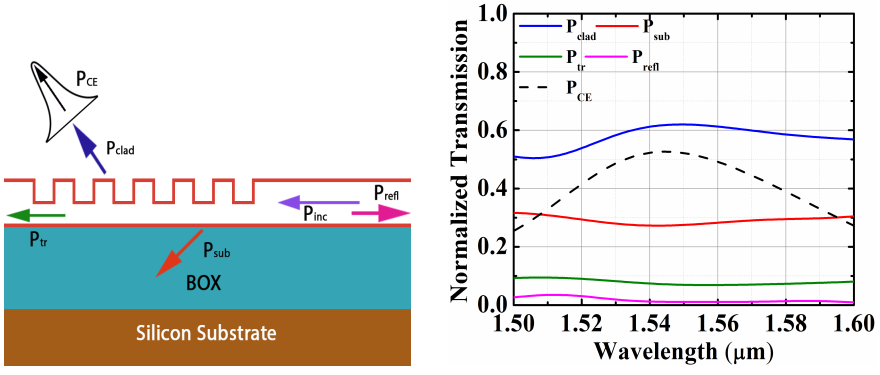
We design and experimentally demonstrate a high efficiency SiN grating coupler on a 500 nm thick platform with distributed Bragg layers as bottom reflectors. Maximum efficiency for the design is calculated to be over 73 % with a 1 dB bandwidth of 56 nm. The experimental peak coupling efficiency is observed to be 2.29 dB/coupler with a 1 dB bandwidth of 49 nm.

Keywords: Grating coupler, photonic-integrated circuits, silicon nitride.

1 INTRODUCTION

Silicon Nitride (SiN) is increasingly garnering interest as an alternative material to the established Silicon-on-Insulator (SOI) platform for building photonic integrated circuits [1], [2]. Apart from being a CMOS compatible material, SiN based devices have higher tolerance to fabrication imperfections given its moderate index contrast. These devices have a lower temperature sensitivity due to the low thermo-optic coefficient of SiN. Also, unlike crystalline silicon, SiN does not suffer from two photon absorption making it suitable for various nonlinear photonic applications. As such there has been a renewed interest to develop surface grating couplers for various Silicon Nitride on Insulator (SNOI) platforms [3], [4], [5]. Most of these couplers were realized with SiN grown using Low Pressure Chemical Vapour Deposition (LPCVD) that required high-temperature processing (>700 C°). In this work, we present a highly efficient grating coupler based on ultra rich silicon nitride film of 500 nm thickness grown using plasma enhanced chemical vapour deposition (PECVD) process. Furthermore, the demonstration is the best efficiency reported yet for a single-mode SiN waveguide configuration.

2 GRATING DESIGN AND SIMULATION



(a) (b)

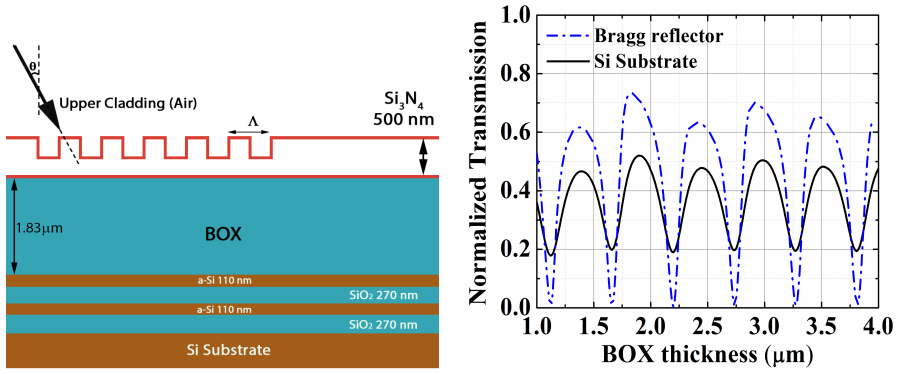
Figure 1: (a) 2D schematic of grating design layout with an illustration of the different loss channels. (b) Simulated normalized transmission or CE at optimized design of 1.05 μm, 9.5° angle, 270 nm etch depth and 55 % duty cycle along with the various associated power loss channels.

Power coupling to any surface grating coupler typically depends on two factors namely the directionality and fiber mode mismatch. While the former defines proportion of total power diffracted upwards to the fiber, the latter signifies the mismatch between the grating field and the Gaussian fiber mode. For our design, we maximize the directionality by plugging substrate leakage through a bottom reflector inserted under the bottom oxide clad layer. Initially, the grating parameters are optimized using 2D FDTD. A schematic of the grating design with its associated loss mechanisms is illustrated in fig. 1(a). Accordingly, the power incident P_{inc} is expressed as:

$$P_{inc} = P_{clad} + P_{sub} + P_{refl} + P_{tr} \quad (1)$$

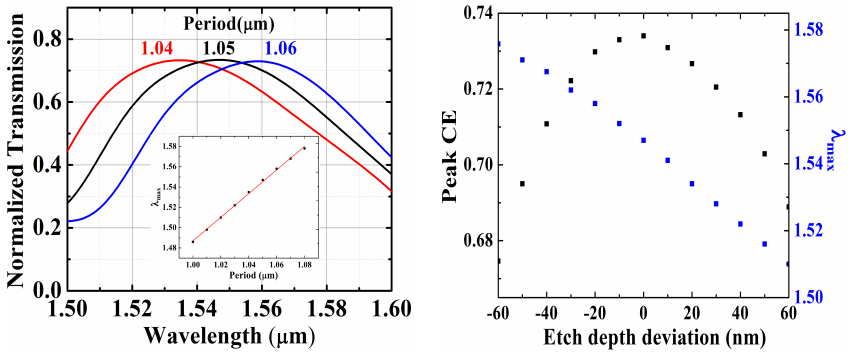
$$P_{CE} = \eta P_{clad} \quad (2)$$

where P_{clad} denotes the power extracted to the top cladding, P_{sub} the substrate leakage, P_{refl} denotes the back reflection and P_{tr} signifies the power transmitted through the grating. And η is the mode field overlap between the diffracted grating field and a Gaussian fiber mode. A parametric optimization sweep of the grating period, duty cycle, etch depth, and inclination angle is done. Maximum efficiency is observed at 52.2 % at a peak wavelength 1.544 μm for inclination angle of 9.5°, 55% duty cycle , etch depth of 270 nm and a period of 1.05 μm. Figure 1(b) summarizes the grating spectrum along with the Coupling Efficiency (CE) for an optimal device. It is observed that a substantial portion of power is leaked into substrate (>20%). To address this, a two layer Bragg reflector is added underneath the oxide (as shown in fig. 2(a)) and a parametric sweep of the oxide thickness is carried out to phase match the diffracted and the reflected field. These results are plotted in fig. 2(b). With the Bragg mirror, the peak efficiency improves to 73 % at a peak wavelength of 1.55 μm. Further optimization reveals the optimum etch depth with the mirror is slightly lower at 260 nm at an incident angle of 10°. The effect of period and etch depth on CE and peak wavelength is showcased in fig. 4. For an



(a) (b)

Figure 2: (a) 2D schematic of the grating design with a 2 layer DBR. (b) Normalized transmission at 1.55 μm wavelength as a function of BOX thickness with and without bottom reflector for optimized design.



(a) (b)

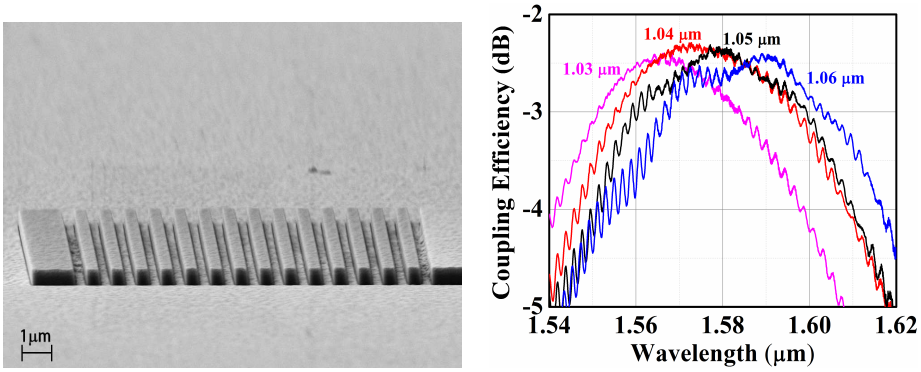
Figure 3: (a) Normalized transmission or CE for different periods. Inset shows variation of peak wavelength with period. (b) Peak CE as well as peak wavelength variation as function of etch depth at optimized period and inclination angle.

etch depth of 80 nm, the peak coupling is observed to be over 70 % with a noticeable red shift in the peak wavelength λ_{max}. Both plots indicate that there is only a marginal shift in power coupling due to deviation from the optimal design which in turn underlines the robustness of design to fabrication process.

3 FABRICATION AND CHARACTERIZATION

A clean Silicon wafer is first deposited with successive layers of SiO_2 and a-Si to from the bottom reflector. The stack consisting of SiO_2/a-Si of 270/110 nm thickness deposited using PECVD. This was followed by eposition of 1.83 μm SiO_2 and the 500 nm SiN layers also done using PECVD. Gratings of periods 1.03-1.07 μm and duty cycle between 50-60 % were written on a sample coated with MaN 2403 resist using electron beam lithography. The patterns were written on patch waveguides of 300 μm length and 12 μm width. These gratings along with patches were etched 260 nm deep in a single step etch process using inductively coupled plasma-reactive ion etching (ICP-RIE).

A SEM image of a fabricated device is depicted in Fig. 4(a). Devices were characterized using a Super-luminescent LED in the C band. Light is coupled into the grating through a polarization controller and the out-coupling fiber to an Optical Spectrum Analyzer (OSA). The device spectrum obtained from OSA is normalized



(a) (b)

Figure 4: (a) SEM cross section of the fabricated device.(b) Measured CE for best devices with different periods at inclination angle 8.5°.

to the source spectrum. The characterization results are presented in fig. 4(b). Best results are obtained for devices of duty cycle of 55 % at an inclination angle of 8.5°. Peak CE for gratings on patches observed to be -2.29 dB at 1572 nm with a 1 dB bandwidth of 49 nm, for a period of 1.04 μm.

TABLE 1: Comparison of different reported uniform SiN grating couplers in literature.

SiN Coupler	Max CE (-dB)		Band -width (nm)		λ_{max} (μm)		t_{SiN} (nm)	Deposition type	Bottom reflector
	Simulated	Experiment	Simulated	Experiment	Simulated	Experiment			
Ref[3]	3.9	4.2	67	67	1.57	1.57	400	LPCVD	N
Ref[4]	2.32	2.5	102	53	1.479	1.49	400	LPCVD	Y
Ref[5]	2.9	3.7	54	54	1.55	1.555	700	LPCVD	N
This work	1.34	2.29	56	49	1.546	1.572	500	PECVD	Y

It is noticed that the peak coupling angle as well as wavelength differs from that of simulated results. This discrepancy in data may be attributed to a less than optimum etch depth and duty cycle for the fabricated devices. Table I gives a comparative summary of selected SiN based uniform grating couplers reported so far.

4 CONCLUSION

We have designed, fabricated and experimentally demonstrated an air-clad SiN grating coupler in a 500 nm PECVD SiN platform. Measured coupling efficiency is observed to be 2.29 dB at 1.572 μm with a 1dB bandwidth of 49 nm. The minimum fabricated grating features are over 500 nm which is compatible with standard optical lithographic systems. Further improvement in the coupling efficiency could be achieved by mode profile matching through apodization.

ACKNOWLEDGMENT

The authors thank Siddharth Nambiar and Rakshitha K for helping us in fabrication. The authors also thank National Nanofabrication Centre and Micro-Nano Characterization Facility at Centre for Nano Science and Engineering. The work is supporting by DST-SERB and MeitY, Government of India

REFERENCES

[1] A. Rahim, E. Ryckeboer, A. Z. Subramanian, S. Clemmen, B. Kuyken, A. Dhakal, A. Raza, A. Hermans, M. Muneeb, and S. Dhoore, Y. Li, U. Dave, P. Bienstman, N. Le Thomas, G. Roelkens, D. V. Thourhout, P. Helin, S. Severi, X. Rottenberg, R. Baets, "Expanding the Silicon Photonics Portfolio With Silicon Nitride Photonic Integrated Circuits", J. Lightwave Technol., vol. 35, pp. 639-649, February 15, 2017.

[2] J. Shainline, S. Buckley, N. Nader, C. Gentry, K. Cossel, J. Cleary, M. Popović, N. Newbury, S. Nam, and R. Mirin, "Room-temperature-deposited dielectrics and superconductors for integrated photonics", Opt. Express, vol. 25, 2017, pp. 10322-10334.

[3] C. R. Doerr, L. Chen, Y. K. Chen, and L. L. Buhl, "Wide Bandwidth Silicon Nitride Grating Coupler", IEEE Phot. Tech Lett., vol. 22, 2010, 1461-1463.

[4] H. Zhang, C. Li, X. Tu, J. Song, H. Zhou, X. Luo, Y. Huang, M. Yu, and G. Lo, "Efficient silicon nitride grating coupler with distributed Bragg reflectors", Opt. Express, vol. 22, 2014, pp. 21800-21805.

[5] X. Zhao, D. Li, C. Zeng, G. Gao, Z. Huang, Q. Huang, Y. Wang and Jinsong Xia, "Grating Coupler for 700-nm Silicon Nitride Strip Waveguides", J. Lightwave Technol., vol. 34, pp. 1322-1327, February 2016.

PIX4life: photonic integrated circuits for bio-photonics

(Invited paper)

Marco A. G. Porcel[1], J. David Domenech[1], Hilde Jans[2], Romano Hoofman[2], Douwe Geuzebroek[3], Pieter Dumon[4], Marcel van der Vliet[5], Jeremy Witzens[6], Eric Bourguignon[7], Iñigo Artundo[1] and Liesbet Lagae[2]

[1]*VLC Photonics S.L., c/ Camino de Vera s/n - 46021 Valencia - Spain*
Tel: +34961337884, e-mail: marco.garcia@vlcphotonics.com
[2]*IMEC, Kapeldreef 75, 3001 Heverlee, Belgium*
[3]*LioniX Int., Hengelosestraat 500 - Enschede - The Netherlands*
[4]*Luceda Photonics, - Noordlaan 21 - Belgium*
[5]*PhoeniX BV, - Capitool 50, 7521 - Enschede - The Netherlands*
[6]*RWTH Aachen University, Aachen - Germany*
[7]*Toptica, - Lochhamer Schlag 19 - 82166 - Grafelfing - Germany*

ABSTRACT

As key enabling technology, photonics has become critical in many fields. Advances in fabrication technologies have realized photonic integrated circuits not only for telecommunication wavelengths but also in the mid-infrared, and very importantly, in the visible. The latter can strongly benefit bio- and life-science applications where visible light is very commonly used in bulky and expensive optical systems. Through PICs Robust optical functionalities can be realized cost-effectively. However, the technology was not openly available until very recently.

The pilot line, PIX4life, was established with the aid of the European Union to facilitate European R&D employing visible light PICs for visible applications, targeting mainly health and bio-science applications.

Keywords: Pilot line, PIX4life, silicon nitride photonics, biophotonics, life sciences, visible wavelength, short near-infrared

1 INTRODUCTION

Nowadays, there is a growing interest in life sciences towards Silicon Nitride (SiN) based Photonic Integrated Circuits (PICs). This has been precipitated thanks to the transparency of SiN which expands from through the visible range of the electromagnetic spectrum up to 2600 nm that is achieved by modern deposition techniques [1]. PICs transparent in the visible and sort near-infrared ranges can be employed in many bio- and life-science applications where traditional bulk optical systems are currently been employed.

The use of SiN-based monolithic PICs in such applications provides very important benefits due to their mechanical, chemical, thermal and electro-optical stability, reduced size and light weight [2]. By integrating these photonic components in a single chip, a miniature system can be developed that often also works faster and more reliable than its larger counterparts. Potentially allowing hundreds of basic building blocks, opening the door to novel complex applications [3, 4].

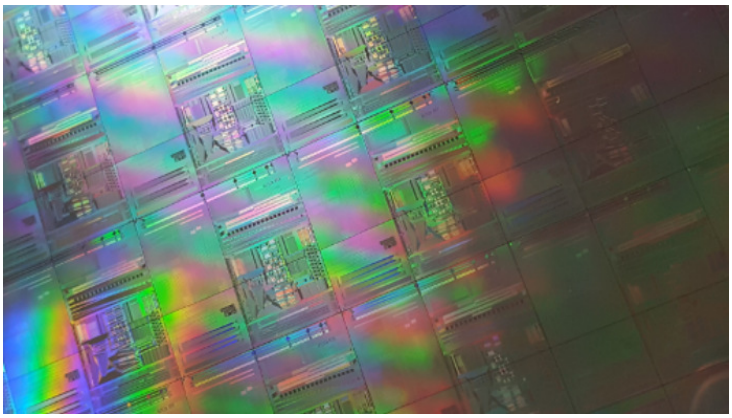


Figure 1. Example of a SiN wafer based on BioPIX technology.

Such photonic integrated circuits (PICs), produced on silicon wafers, in a standardized and automated production flow, also makes this integration technology inexpensive and scalable.

Due to their fast response, small sensing area and accuracy, SiN-based PIC sensors have been employed in research for chemical, biological and medical measurements. Some of these applications are already benefiting from PICs in biophotonics, like:

- Medical instrumentation: confocal and multi-photon imaging, DNA sequencers, optical coherence tomography, respiratory gas monitors, Raman spectroscopy, glucose monitors, flow cytometry, etc.
- Photonic Lab-on-a-chip: rapid and automated analysis of small volume samples, in-vitro and in-vivo monitoring, implantable biofluoroimaging, digital electrowetting, drug discovery, etc.
- Optical sensors to measure chemical properties such as pH changes and trace gas, indirect biosensors via fluorescence, phosphorescence or colorimetric measurements, and direct biosensors of metabolites, enzymes, environmental toxins, etc.

The implantation/adaptation of this technology by the industry has been previously delayed due to the low maturity of the fabrication process, design tools, foundry processes and packaging. In addition, the high cost of prototyping and pilot production resulted in a very slow adoption of photonic integrated circuit (PIC) technology, primarily by applications where applications can benefit from a cost reduction and middle-large scale production.

2 SILICON NITRIDE FOR THE VISIBLE

In PIX4life, we aim to tackle these issues, by maturing a high performance, high yielding and CMOS-fab compatible SiN PIC pilot line. PIX4life offers as well the complete supply chain of services for applications in the visible range (400-700 nm) and sort near-infrared (700-900 nm). Moreover, to lower the cost of prototyping the SiN technology is offered via Multi Project Wafer runs (MPWs), where multiple design from multiple users are place in the same wafer mask, sharing area and therefore costs. While MPWs provide a few copies of each design, PIX4life offers as well dedicated wafers for larger designs, or for larger number of copies of a design.

PIX4life offers services from two different foundries, each offering their own silicon nitride platform BioPIX by the foundry IMEC and TripleX^{TM}by the foundry LioniX Int., and located in Belgium and The Netherlands respectively [5, 6]. An example of a BioPIX MPW wafer is shown in Fig. 1 and an example of a TripleX^{TM}chip for visible light is shown in Fig. 2.

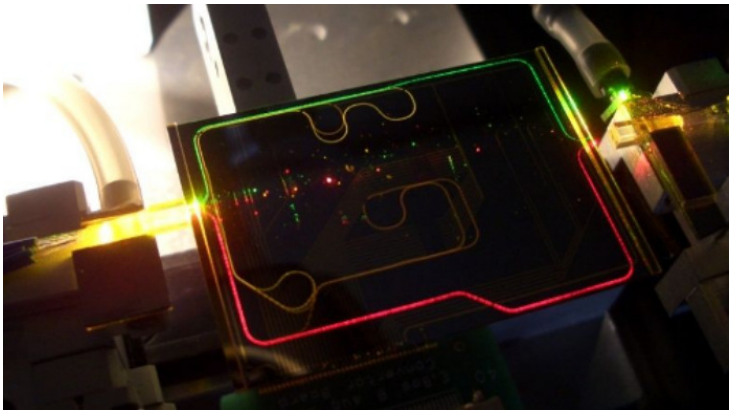


Figure 2. Example of a SiN PIC based on TripleX^{TM}.

In order to generate a SiN PIC design, that will be use to fabricate a photolithographic mask, the photonic desing software companies Phoenix and Luceda, the process design kit (PDK) for PIX4life containing all the building blocks required for most applications. Some of these building blocks have already been reported in biophotonics scientific literature. Among the reported SiN PICs we find ring resonator (RR) filters, microdisk resonators, grating couplers, wavelength combiners, multi-mode interferometers, array waveguide gratings (AWGs), and difraction gratings.

3 DEMONSTRATORS

Within PIX4life, four companies are building demonstrators based on one of the two SiN platforms. These are the following:

- *Toptica: a multispectral light source on chip*. Life science applications in the field of e.g. microscopy or flow cytometry require multiple excitation wavelengths to excite the dyes of interest. To move away from the bulky optics, Toptica is developing a fully integrated multispectral light source. This not only reduces the physical dimensions but also the cost, and it improves robustness.

- *Medlumics: an OCT-on-chip for ophthalmologists*. Medlumics aims to use the SiN photonic pilot line to produce an OCT-on-chip system operating in the near infrared, thus paving the way towards compact and cost-effective medical devices to be used in the daily practice, for example by ophthalmologists. The company's current OCT systems are based on SOI technology and use light at larger wavelengths. This is perfect for its use, among others, in cardiology, gastroenterology or dermatology. But to examine the eye, light in the near infrared is preferable. This is possible using SiN technology.
- *Miltenyi: flow cytometer with innovative laser*. Miltenyi is a German company that makes flow cytometers with a chip-based sorting module. At the moment it uses standard lasers to illuminate the fluorescent labels attached to the cells that flow past in the microfluidic channel and to identify them. The company now wants to start using biophotonics so that this laser light can be better targeted and controlled and hence enhance the sensitivity and robustness of their flow cytometer.
- *Bosch: cheaper sensors for monitoring health parameters*. Bosch wants to start using photonic sensors for monitoring health parameters such as body temperature, the composition of sweat, heartbeat, respiration rate, etc. Interaction between light and the body at the nanoscale, either by absorption or diffraction, will provide valuable information about these parameters. For engineering such a system and in order to create a reliable product, the SiN platform offers the best compromise between chemical resistance and optical performance, enabling the detection of the desired physical and chemical properties, while maintaining the small size and low power.

ACKNOWLEDGMENT

This work was supported by the European Union's Horizon 2020 research and innovations program, under the grant agreement no. 688519 (PIX4life).

REFERENCES

1. Curley, R., McCormack, T. & Phipps, M. *Low-Pressure CVD and Plasma-Enhanced CVD* 2 (2011).
2. Neutens, P. *et al. Development of a CMOS Compatible Biophotonics Platform Based on SiN Nanophotonic Waveguides CLEO: QELS_Fundamental Science* (Optical Society of America, 2014), JTh2A–31.
3. Geuzebroek, D. *et al.* Photonic Integrated Circuits for Visible Light and near Infrared: Controlling Transport and Properties of Light. *Sens. Actuators B Chem.* **223,** 952–956 (Feb. 2016).
4. Van Dorpe, P. *Silicon Nitride Based Planar Integrated Circuits for Biophotonics Applications* (IEEE, 2016), 147–147.
5. Heideman, R. *et al. Large-Scale Integrated Optics Using TriPleX^{TM} Waveguide Technology: From UV to IR* (eds Glebov, A. L. & Chen, R. T.) (2009), 72210R.
6. Subramanian, A. Z. *et al.* Low-Loss Singlemode PECVD Silicon Nitride Photonic Wire Waveguides for 532-900 Nm Wavelength Window Fabricated Within a CMOS Pilot Line. *IEEE Photonics J.* **5,** 2202809 (2013).